Diesel waste gas abatement using alloyed nanoparticles

Dissertation

for the degree of

Doctor of Natural Science

- Dr. rer. nat. –

by

Simon Hartwig

Technical Chemistry I

University of Duisburg-Essen

2024

DOI: 10.17185/duepublico/81882
URN: urn:nbn:de:hbz:465-20240503-082700-6

This thesis was prepared from August 2017 to March 2022 in the group of Dr. Sven Reichenberger, Institute of Technical Chemistry I (headed by Prof. habil. Dr.-Ing Stephan Barcikowski), University of Duisburg-Essen.

Day of examination: 19th April 2024

Referees:

Prof. habil. Dr.-Ing. Stephan Barcikowski
University of Duisburg-Essen

Jun.-Prof. Dr. Corina Andronescu
University of Duisburg-Essen

Chairman:

Jun.-Prof Dr. Anzhela Galstyan
University of Duisburg-Essen

"Only those who dare to fail greatly,
can ever achieve greatly."

Robert F. Kennedy, 1966

Acknowledgements

Many years of hard work lie behind me, and it is time for me to express my gratitude to the people who have been by my side throughout this dissertation and without whom this work would never have been possible.

First of all, I would like to express my sincere gratitude to Prof. Dr. Stephan Barcikowski for making this thesis possible by providing a competitive environment in which to grow, for his support, and for the many lessons he has taught me. Similarly, I would like to thank Dr. Galina Marzun and Dr. habil. Sven Reichenberger for their support, advice and guidance. I am also grateful to Jun. Prof. Dr. Corina Andronescu for taking on the second review and to Jun.-Prof Dr. Anzhela Galstyan for chairing the defence committee.

I would like to extend my thanks to everyone from Umicore: Dr. Franz Dornhaus, Dr. Christoph Hengst, and Bernd Wittek for the fruitful discussions and generally good working atmosphere and for the effort they put into getting accurate results. I am also grateful to Kerstin Neuhahn for the precise sample preparation at Umicore. I would also like to thank the company Umicore AG & Co. KG for the financial support that made this study possible.

I also want to express my gratitude to Dr. Odo Wunnike for allowing me to extend my industry experience by making an internship at Evonik Creavis possible.

This work would not have been possible without my great colleagues: I'd like to extend my gratitude to Dr. Markus Heidelmann and Jurij Jakobi for countless HR-TEM Images and EDX-Scans; Florian de Kock, Dennis Markett, Kai Schott and Dana Krenz for their help in the lab and for the excellent mood they brought with them. In general, I was fortunate to have the best research department I could have hoped for, including its current and former members. Thanks for the great times we had at team building, on work-trips, coffee breaks and for the generally welcoming atmosphere you extended to me.

Also, I can't forget my students: Thanks to Jasmin Beverungen, Manuel Matten and Moritz Materna for all the intense effort and dedication you put into your work that this dissertation profited from.

Finally, I want to thank the people closest to me. First of all, my wife Caroline Hartwig for helping me through hardships and being by my side. And after that, my parents, Uwe and Heike Siebeneicher, for always giving me the feeling that the sky is the limit if I work hard enough while still making me feel accepted if something doesn't work out as planned.

Abstract

Clean air would hardly be possible without catalytic conversion. Since the advent of large-scale combustion, air quality has always been a concern for society because of the adverse health effects of pollutants from combustion processes. Since the 1970s, regulations have been in place to minimise the emission of harmful combustion products, mainly from internal combustion processes. The catalytic converter is one of the most essential devices in meeting these regulations. The converter's activity is mainly based on noble metal nanoparticles, in many cases Pt and Pd. These precious metals are rare and, therefore, expensive. A reduction in the use of precious metals promises not only economic advantages but also improvements in catalytic activity but may also be a way to improve catalytic activity. The only drawback to this solution is the limited research into alloy nanoparticle catalysts. This is possibly due to the fact that the synthesis of alloyed nanoparticles often requires bespoke synthesis protocols for each alloy. This effort can be circumvented by laser-based nanoparticle synthesis, which can be used to produce a wide variety of alloys in the same way. This work aims to fill this gap by preparing 13 alloy systems with 45 different compositions to industry standards using laser-based particle synthesis and testing them in industrially relevant exhaust gas environments. In detail, the work focusses on diesel oxidation catalysis (DOC) and ammonia slip catalysis (ASC). The results show which alloys are best suited in terms of activity and durability and provide design criteria that can be used in the future to design alloys for emission control systems.

Zusammenfassung

Saubere Luft wäre ohne den Einsatz von Katalysatoren kaum möglich. Seitdem in großem Umfang Brennstoffe zur Energiegewinnung verfeuert werden, haben Gesellschaften das Problem von schlechter Luftqualität und daraus resultierenden Gesundheitsproblemen erkannt. Deshalb gibt es seit den 1970er Jahren Vorschriften, die die Emission von Schadstoffen aus Verbrennungsprozessen regulieren. Katalysatoren leisten dabei einen wichtigen Beitrag, durch ihre Fähigkeit die entstehenden Schadgase in unschädliche Produkte umzuwandeln. Die Aktivität der Katalysatoren beruht dabei hauptsächlich auf Nanopartikeln aus Edelmetall, häufig Platin oder Palladium. Durch ihre Seltenheit sind diese Edelmetalle aber teuer. Eine Verringerung des Edelmetalleinsatzes verspricht dabei neben wirtschaftlichen Vorteilen auch Verbesserungen der katalytischen Aktivität. Der einzige Nachteil dieser Lösung ist die begrenzte Forschung zum Thema der legierten Nanopartikel. Dies liegt möglicherweise daran, dass die Synthese legierter Nanopartikel häufig maßgeschneiderte Syntheseprotokolle für jede Legierung benötigt. Dieser Aufwand kann durch die laserbasierte Nanopartikelsynthese umgangen werden, mit Hilfe derer verschiedenste Legierungen auf die gleiche Art und Weise herstellbar sind. Diese Arbeit soll dazu beitragen, diese Lücke zu schließen, indem 13 Legierungssysteme mit 45 verschiedenen Zusammensetzungen nach Industriestandards mithilfe der laserbasierten Partikelsynthese hergestellt und in industriell relevanten Abgasumgebungen getestet werden. Im Detail fokussiert sich die Arbeit dabei auf die Dieseloxidationskatalyse (DOC) und die Ammoniakschlupfkatalyse (ASC). Die Ergebnisse zeigen, welche Legierungen in Bezug auf Aktivität und Durabilität am besten geeignet sind, und liefern Design-Kriterien, die in Zukunft für die Entwicklung von Legierungen für Abgasnachbehandlungssysteme verwendet werden können.

Table of Contents

Abbreviations

ASC	Ammonia Slip Catalyst
DOC	Diesel Oxidation Catalyst
DPF	Diesel Particulate Filter
EDM	Electrical Discharge Machining
EDX	Energy Dispersive X-Ray
HER	Hydrogen Evolution Reaction
HR-TEM	High Resolution Transmission Electron Microscope
ICP-OES	Inductively Couple Plasma – Optical Emission Spectroscopy
IR	Infrared
LASiS	Laser Ablation Synthesis in Solution
MOR	Methanol Oxidation Reaction
OER	Oxygen Evolution Reaction
ORR	Oxygen Reduction Reaction
PGE	Platinum Group Element
PLAL	Pulsed Laser Ablation in Liquids
SCO	Selective catalytic oxidation
SCR	Selective catalytic reduction
TWC	Three Way Catalyts (typically applied in $\lambda = 1$ environments)
YTZ	Yttria stabilized Zircon Oxide
λ	Air-fuel ratio; $\lambda > 1$ oxygen rich, $\lambda < 1$ fuel rich

Table of Figures

1 Introduction

The ability to move goods and people is the foundation of our modern society. For many years, the main means of doing this has been the internal combustion engine. The popularity of this approach has led to problems related to the emissions it produces. This has made it necessary to regulate and limit emissions. Since their introduction, these regulations have become increasingly stringent [1–3], sometimes even leading to the introduction of restricted driving zones [4]. This places greater demands on the emission control systems used by car manufacturers. One of the most important is the catalytic converter [5]. These catalysts must be durable and active, performing from engine cold start to full load conditions [6–9]. In addition, the catalysts are needed to be robust, to withstand the constantly changing temperatures and changes in feed gas composition resulting from engine load changes [10]. Selecting catalysts for these environments is a challenging task, as engine emissions are much more complex than laboratory simulations, which are usually performed with simple mixtures (e.g. $CO + O_2$) used to elucidate mechanisms. Consequently, studies that additionally mimic engine conditions as closely as possible are needed, since interpolation can introduce significant uncertainties. The work in this thesis has therefore been as close to industrial practice as possible, with catalyst preparation and ageing carried out to industry standards and using gas mixtures used in industrial test environments. In addition, efforts will be made to improve upon the state of the art by expanding the compositional knowledge base for diesel exhaust catalysts.

This is done for two reasons - activity improvement and economic optimisation. Firstly, the state of the art in terms of active materials for diesel oxidation catalysts (DOC) are Pt, Pd and combinations of these two elements [10,11]. In ammonia slip catalysts (ASC) these noble metals also play an important role, but their activity is augmented by base metal oxides [12]. Yet, the activity of these catalysts may be improved by considering the Sabatier principle. Montemore et al. have published the activities of several metals in CO oxidation [13], showing that the peak activity divides the active materials into two groups, Pt and Pd, and

Au, Ag and Cu. From this, it may be concluded that combinations of Pt or Pd with Ag, Au or Cu could potentially improve the overall activity. This already illustrates the economic optimizations possible. If an alloy, e.g., Pt-Cu, could give a similar or even better activity than Pt-Pd, the result is a direct and significant reduction in cost. This is particularly interesting given the ever-increasing price of Platinum Group Elements (PGEs). Catalyst optimisation by alloying is not a new approach. Research in this field has been carried out, for example, on electrocatalysts [14–20] and interesting work has been done on high-entropy alloys for application in three-way-catalysts [21,22], where a high activity and durability have been demonstrated. Selective oxidation catalysts based on alloys have also been developed [23]. Unfortunately, many studies on exhaust gas abatement only concentrate on a limited number of alloys [24–28]. This may be attributed to the complexities involved in synthesizing a diverse set of solid solution nanoparticles while maintaining consistent particle size distribution and catalyst loading using conventional techniques. Therefore, a study focusing on a wider composition space of the PGM alloys in diesel emission control and systematically testing a range of alloys in an industrial test regime seems useful. Laser ablation, a technique capable of producing solid solution particles with appropriate size distributions for waste gas abatement, emerges as a suitable method [24]. Furthermore, the particle synthesis process is separate from the deposition process when creating catalysts based on laser-synthesized particles [29]. This implies that, size distribution and loading can be tuned separately, ideally leading to comparable size distributions and loadings over the whole test field. Consequently, this work aims to address this research gap by preparing 45 binary alloys using laser ablation synthesis, mainly consisting of Pt + X. X being a second element either from the platinum group and coin metals or from the group of base metals. These catalysts will then be prepared according to industry standards and tested in three different ageing states (fresh, aged at 650°C and aged at 800°C) in industrially relevant feed gas mixtures. One of which will be a Diesel Oxidation Catalysis (DOC) environment with a feed of CO, C_3H_6, O_2, H_2O, CO_2 and NO in N_2 balance and two mixtures being an Ammonia Slip Catalysis (ASC) environment with a feed consisting of NH_3, O_2 and H_2O in N_2 balance with one mixture additionally containing NO. The alloys used in this study are selected based on this application, with Pt chosen as the common denominator, as this element is ubiquitous in waste gas abatement and it is used either in its pure form or in alloys [9,30,31]. Pt-Pd is chosen as reference for its high activity and durability, the latter of which has been shown to be due to Pd mitigating the particle growth resulting from the volatility of PtO_2 species [32]. This shows that durability enhancement is an effect arising directly from two metals being present. Therefore, in addition to activity, durability will be an important readout and focus and this thesis.

Building upon an extensive literature review to gain comprehensive insights into the applications of various metals and, where available, Pt-based alloys of these metals, the following alloys have been considered for inclusion in this study. Pt-Rh alloys, despite Rh's more common use in three-way catalysis [9], are included due to their similar activation energy for CO oxidation to that of Pt [33], and the potential for improved durability owing to Rh's high melting point. Pt-Au and Pt-Ag alloys have been selected based on evidence from multiple authors indicating that Ag and Au maintain their activity in the presence of a wet gas stream [34–37], and water is a notable part of the gas mixtures used. Alloys of Pt-Cu, Pt-Mn, and Pt-Fe offer the prospect of reducing catalyst costs while retaining activity, particularly in ammonia slip catalysts. This potential arises from the known activity of Cu, Mn, and Fe oxides in ammonia oxidation [38]. In addition to ammonia oxidation, Cu is also expected to be a valuable alloying component for DOC due to Sabatier principle considerations [13]. In addition to a good activity, Fe is also hypothesised to have a high selectivity for N_2 because its high activation energy for N_2-dissociation [39] may prevent the formation of reactive nitrogen species. Ruthenium has been extensively studied for CO-Oxidation and N_2-formation [39]. It hasn't found its way into applications because its activity comes from a thin oxide layer that grows too thick under atmospheric conditions, reducing its activity, and because water adsorption also inhibits the activity [40,41]. While the oxide layer grows on pure Ru, an alloy of Pt-Ru may inhibit this by ennobling with Pt, and the Pt-Ru alloy may also be very durable due to the high melting point of Ru. The high melting point of Nb and Mo is also a major reason for testing Pt-Nb and Pt-Mo alloys. In addition to these Pt based alloys, Pt-Cu and Au-Rh as well as Au-Ir alloys will be tested. Pd-Cu is expected to be active due to similar Sabatier principle considerations as Pt-Cu [37], while the high activity of Rh and Ir is expected to be moderated by the addition of Au, which may improve the selectivity of these active materials by O-Spillover to gold [13,42].

The composition of each alloy is based on the underlying bulk phase diagram and the test field is divided into two categories. Pt-Pd, Pt-Ru, Pt-Cu, Pt-Au, Pt-Ag, Pt-Rh and Pd-Cu, Au-Rh as well as Au-Ir are expected to show a high activity in CO-oxidation and therefore the mixing interval is chosen to be wide (10-99 at% Pt). Deviations from this interval are only made for exceptionally high-priced combinations such as Pt-Rh, Au-Ir and Au-Rh, where the maximum Rh and Ir contents were kept below 50 at%. Pt-Nb, Pt-Mn, Pt-Mo and Pt-Fe were chosen mainly because of the hypothesised ennoblement of the second element by platinum. Therefore, the Pt content was kept above 50 at%.

Screening this wide range of materials and compositions - 13 alloy systems with a total of 45 different alloys - is only possible with a robust synthesis protocol based on laser synthesis

in liquids. This avoids the need to find a chemical synthesis route for each alloy by using high power ultrashort pulsed laser ablation. The ability of this synthesis method to produce colloids and alloys has been widely demonstrated in the literature [14,24,43–53]. The ability to produce high quantities of nanoparticles (~g/h) has also been demonstrated and is also necessary to meet the requirements of industrial testing [24,54,55].

2 State of the Art

The purpose of this chapter is to provide the reader with an insight into the current state of the art of exhaust gas after-treatment using catalytic converters in the context of diesel engine applications. It provides an insight into the formation of pollutants and shows how to avoid the harmful exhaust gases that are typically produced. In particular, it explains how catalytic converters help to clean the exhaust gases. The reader is also given an insight into the state of the art in catalyst synthesis, both chemically and via laser-based synthesis, with a particular focus on the production and importance of alloy metal catalysts.

2.1 Origin of Pollutants in a Diesel Engine

Before fuel is burnt in the engine, it must be fed to the engine in a suitable manner. The aim is to create an ignitable mixture in the combustion chamber. In the diesel engine, this is achieved by injecting fuel into the cylinder shortly before the piston reaches top dead centre (TDC – when the piston is at the highest point of its stroke). There, high temperatures and pressures prevail in the combustion chamber due to the adiabatically compressed air. Mixture formation, therefore only takes place in the combustion chamber milliseconds before ignition conditions for auto-ignition are reached. [56] The time remaining before ignition is insufficient to produce a homogeneous air/fuel mixture. The inhomogeneous mixture eventually causes combustion to take place in a diffusion-controlled regime. Therefore, diesel engines must be operated with a significant excess of air to ensure sufficient combustion. The main emission problems arise from the combination of inhomogeneous mixture and excess oxygen. [6,56]

To be able to explain the origin of the pollutants it is sensible to look at the combustion process in detail. At the start of combustion, only some of the fuel droplets have evaporated and participate in combustion. This creates localised areas of low oxygen content. The mixture there is rich. The local lack of oxygen, together with the already high temperatures, leads to decomposition and incomplete combustion of the fuel. CO, hydrocarbons and soot

are formed. Especially when the engine is cold, e.g., shortly after starting, the cylinder wall causes the mixture close to it to cool down. Here, despite a higher oxygen content, incomplete combustion can occur as well. At the same time, there are areas in the cylinder with a comparatively high oxygen content. Here the heterogeneous mixture is particularly lean. This leads to the formation of nitrogen oxides early in the combustion phase at high temperatures. [56,57]

As combustion progresses, the mixture homogenises and the air/fuel ratio approaches oxygen rich conditions throughout. Incompletely burnt fuel continues to oxidise until the mixture falls below the lower ignition limit and combustion stops. Any incomplete combustion products are then emitted as exhaust gases. The more fuel is burnt in the final phase, the lower the emissions of hydrocarbons, CO and soot. However, as combustion takes place under lean conditions, the flame temperatures are high. As with lean areas in the early stages of combustion, this leads to increased formation of nitrogen oxides. [56–58] The formation of nitrogen oxides can be described in a simplified way with the Zeldovich-mechanism extended by Lavoie and Heywood [59]:

$$\begin{aligned} O + N_2 &\rightleftharpoons NO + N \\ N + O_2 &\rightleftharpoons NO + O \\ N + OH &\rightleftharpoons NO + H \end{aligned} \tag{2.1}$$

Although the reactions are comparatively slow and do not reach thermodynamic equilibrium during the combustion process, they nevertheless produce appreciable nitrogen oxide emissions that would be harmful when released untreated to the environment [56,59]. In addition, nitrogen dioxide is formed in the flame front according to the following reaction scheme [57]:

$$NO + HO_2 \rightleftharpoons NO_2 + OH \tag{2.2}$$

A reduction to NO also occurs, but is significantly slower [57]:

$$NO_2 + O \rightleftharpoons NO + O_2 \tag{2.3}$$

In addition to these main pollutants, also N_2O is formed in the engine by reaction of nitrogen species with oxygen.

Due to the everyday use of combustion engines in high numbers, non-negligible amounts of pollutants are produced. Because these have proven to be harmful to humans and the environment, mandatory compliance with limit values was established with the introduction of exhaust emission standards in 1992. Since then, the limit emission values of carbon monoxide, hydrocarbons, nitrogen oxides, and soot have been continuously regulated by the

EU and other government bodies to limit air pollution particularly in larger cities. (cf. Figure 1). In the coming Euro 7 norm for light duty vehicles N_2O will also be regulated because of its high greenhouse potential [60].

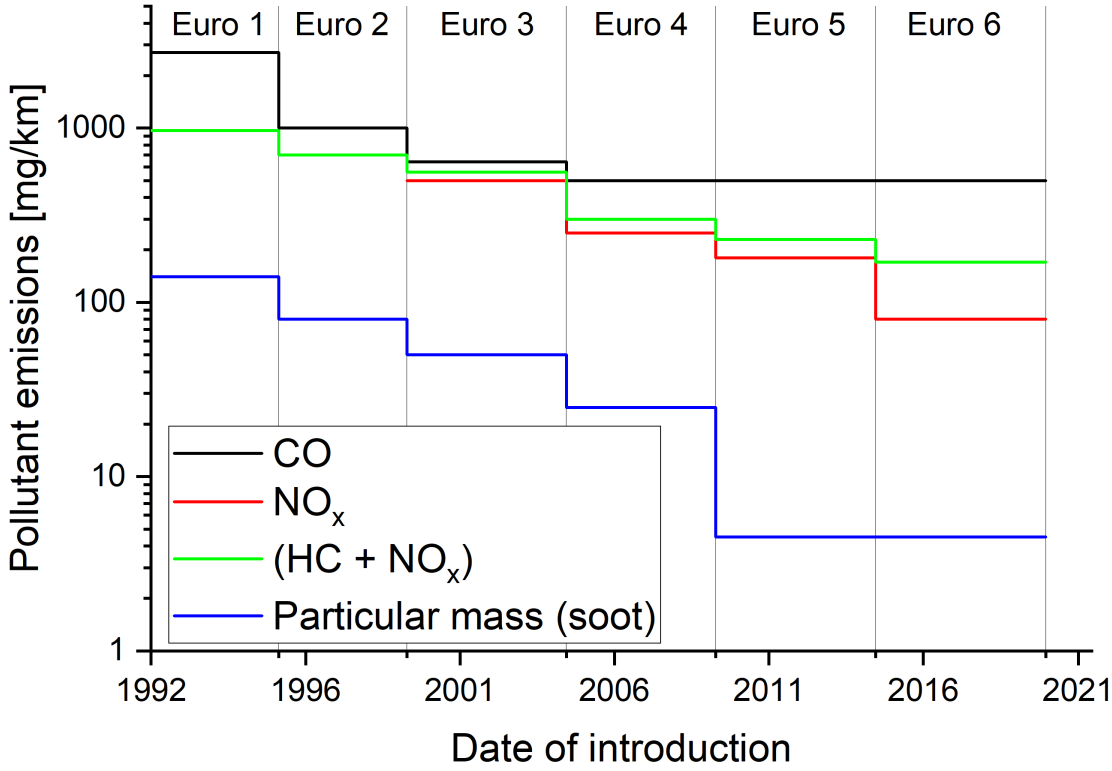

Figure 1 Pollutant limits according to Euro-Norm for diesel-powered vehicles and date of introduction. [1]

In order to comply with these limits, manufacturers have various options. First, the obligations are met by optimising the engine. This involves adjustments to the spatial and temporal injection process, the combustion chamber geometry, exhaust gas recirculation and charge air cooling [6,56]. However, the increasingly stringent emission limits require exhaust gas aftertreatment in addition to the technically complex internal engine measures.

These measures, known as out-of-engine measures, are mainly concerned with the catalytic treatment of exhaust gases. Only this can ensure future compliance with exhaust gas limits. The following chapter deals with the state of the art and the possibilities for innovation in catalytic exhaust gas purification.

2.2 Waste Gas Abatement with Catalysts

As illustrated in the prior chapter, combustion in a diesel engine inevitably leads to pollutant emissions (soot, hydrocarbons, carbon monoxide and nitrogen oxides). The largest proportion of nitrogen oxides is NO. [6,12]

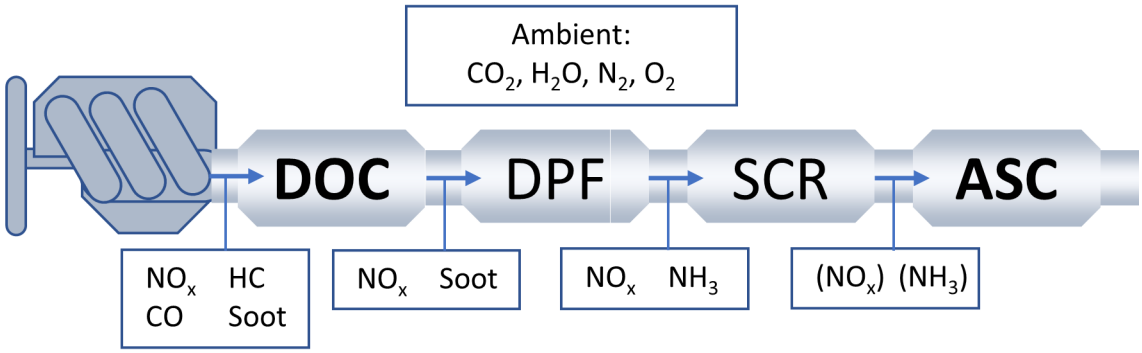

Figure 2 Exemplary catalytic waste gas abatement system. Diesel oxidation catalyst (DOC) removes CO and HC, diesel particulate filter (DPF) removes soot, selective catalytic reduction catalyst (SCR) removes nitrogen oxides and ammonia slip catalyst (ASC) removes excess ammonia.

A wide variety of strategies are used for exhaust gas purification, which differ primarily in the addition of additives and the geometric arrangement of the individual catalytic converters and filters [56]. Basically, exhaust gas purification can be divided into four elementary steps as illustrated in Figure 2 [61]. One of the first treatment steps is the removal of CO and incompletely burnt hydrocarbons. This diesel oxidation catalyst also serves as a catalytic burner that raises the exhaust gas temperature for the downstream soot particle filter [6]. The filter is sometimes also catalytically coated to improve oxidative regeneration. A positive side effect of the oxidation catalyst is that it helps setting the thermodynamic equilibrium between NO and NO_2. The former is particularly useful and important in the following SCR step where nitrogen oxides are catalytically reduced to nitrogen using ammonia. Hereby, the following reactions can take place within the SCR catalyst:

$$4NO + 4NH_3 + O_2 \rightleftharpoons 4N_2 + 6H_2O \tag{2.4}$$

$$NO + 2NH_3 + NO_2 \rightleftharpoons 2N_2 + 3H_2O \tag{2.5}$$

$$8NH_3 + 6NO_2 \rightleftharpoons 7N_2 + 12H_2O \tag{2.6}$$

Here, reaction (2.4) describes the “standard-SCR” reaction, generally taking place above 250°C. Reaction (2.5) is also called “fast-SCR”, as this reaction has an early onset at 170°C and a fast kinetic. When NO_2 dominates, reaction (2.6) is favoured chemically, albeit this reaction is not favoured for the waste gas abatement due to its slow kinetic and high demand on ammonia [9,62]. As can be seen from the SCR reactions, abatement of NO_x requires the dosing of NH_3. In order to ensure the removal of NO_x typically a slight excess of NH_3 is dosed in practice [62]. This allows for the possibility of an ammonia slip and is the reason, why, in a last step, an oxidation catalyst is used again. This fulfils the task of burning excess dosed ammonia to stop the emission of this dangerous gas. It is important that the catalyst

oxidises as selectively as possible to molecular nitrogen. Otherwise, nitrogen oxides may be formed again at this point, which would then be released directly into the environment. [61] In addition to these reactions, there are also side reactions in the DOC and ASC resulting in the formation of N_2O [63–67].

As the main focus of this study is on the oxidation catalysts DOC and ASC, the following chapters will illustrate the reactions in these catalysts in more detail.

2.2.1 Diesel-Oxidation Catalysis

Today's strict exhaust emission limits require the use of catalytic converters in modern diesel vehicles. An essential catalyst component is the diesel oxidation catalyst (DOC). This catalyst is used to oxidise incompletely burnt substances. Substances that are harmful to health and therefore controlled are, for example, CO, NO_x and various hydrocarbons as well as soot particles. The main task of the oxidation catalyst is the combustion of these substances to CO_2, H_2O and the establishing of a thermodynamic equilibrium between NO and NO_2 [6]. Simplified, the main reactions for DOC can be summarised as follows:

$$CO + \frac{1}{2}O_2 \rightleftharpoons CO_2 \tag{2.7}$$

$$C_xH_y + (x + \frac{y}{4})O_2 \rightleftharpoons xCO_2 + \frac{y}{2}H_2O \tag{2.8}$$

$$NO + \frac{1}{2}O_2 \rightleftharpoons NO_2 \tag{2.9}$$

Apart from these main reactions, nitrous oxide (N_2O) is also formed at the catalyst [67] via the following pathway [66]:

$$HC + NO_x \rightleftharpoons N_2O + H_2O + CO_2 \tag{2.10}$$

Since future exhaust gas legislation will also co-regulate this potent climate gas [60,68], emphasis is placed on a low formation rate of this gas. With regard to exhaust gas legislation, reaction (2.9) initially appears counterproductive. Both NO and NO_2 are regulated pollutants whose formation must be avoided. A direct reduction of NO to N_2 and O_2 would be desirable. However, this reduction reaction is not favoured at the oxidation catalyst under lean combustion conditions. Catalytic converters that enable the reduction of nitrogen oxides with the aid of ammonia are more suitable under these ambient conditions [61]. Since this reaction, as illustrated in chapter 2.2, best proceeds according to the fast SCR mechanism, a high proportion of NO_2 in the exhaust gas stream is favoured. The supply of high proportions of NO_2 is hence one of the main tasks of the diesel oxidation catalyst (aside from oxidizing remaining unburnt fuels and CO to CO_2 and doing so while producing as

little nitrous oxide from reaction (2.10)). Additionally, it has to perform this task over a wide temperature range under highly variable ambient conditions.

Diesel engine exhaust temperatures range from 80°C (cold start) to 600°C (full load), with typical operation between 200°C and 500°C [6–9]. Within this temperature interval, the diesel oxidation catalyst must achieve reliable post-combustion of the pollutants. While the thermodynamic equilibrium of reactions (2.7) and (2.8) is on the side of the products throughout the relevant temperature range (strongly negative $\Delta_r G(T)$) [69], the temperature dependence of the equilibrium in the NO oxidation (2.9) leads to a relevant shift towards the educts starting from 350°C [9,70]. Since the catalyst can only accelerate a thermodynamically favoured reaction, higher NO fractions than desired must be expected above this temperature. The most important performance criteria for the exhaust catalyst can be derived from this. It must achieve a complete conversion of CO and hydrocarbons at the lowest possible temperatures and enable a high conversion of NO to NO_2 in the thermodynamically favoured temperature range.

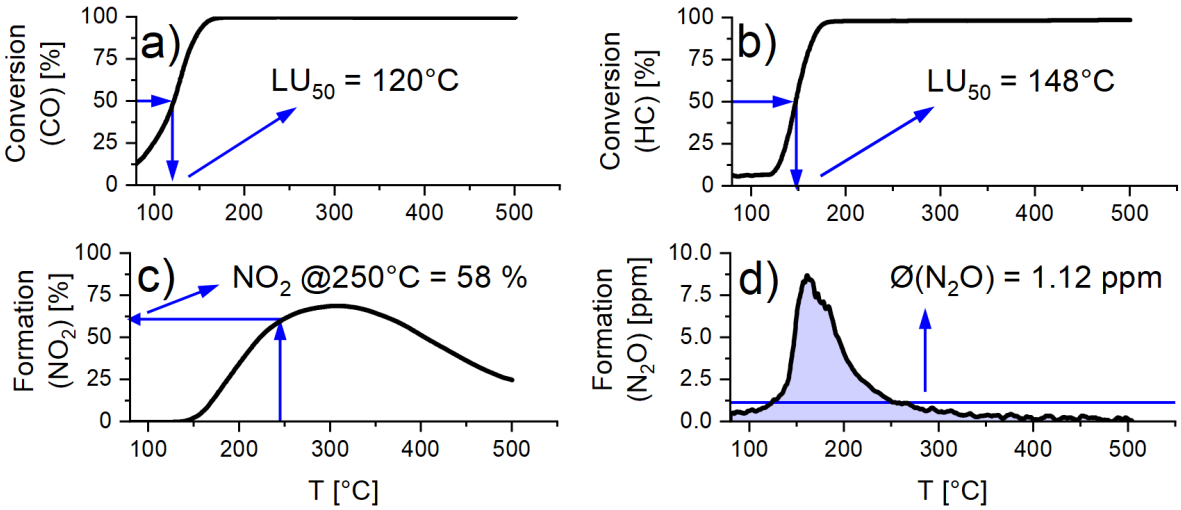

Figure 3 Exemplary results of Pt-Pd for illustrating the standard metric for evaluating catalyst performance. Reprinted with permission from S. Siebeneicher, S. Reichenberger, C. Hengst, F. Dornhaus, B. Wittek, S. Barcikowski, ChemCatChem 2023, DOI: 10.1002/cctc.202300563. Copyright © 2023 Wiley-VCH GmbH.

Industry standard metrics are typically used to assess whether a catalyst is meeting expectations (cf. Figure 3). The conversion of CO and hydrocarbons is determined using the light-up temperature (LU_{50}). This is defined as the temperature at which 50 % conversion is achieved. The lower the LU_{50}, the lower also the required temperature to achieve full conversion will be or in simple terms, the better the catalyst. When evaluating the NO oxidation performance in an application-oriented context, the formation of NO_2 is typically evaluated at 250°C. This temperature is still far enough below the threshold where the back-reaction to NO is thermodynamically favoured and therefore does not significantly affect

the conversion. The higher the conversion at this temperature, the better the catalyst will be classified. The method of N_2O result evaluation isn't as clearly defined. Therefore, in this study, the integral over the whole temperature range is taken and normalized for the temperature difference, giving an average N_2O concentration. The lower this concentration the better the catalyst, because it is more selective towards NO_2 (or N_2).

The active components of the diesel oxidation catalyst are usually precious metal nanoparticles, deposited by wet impregnation onto an oxidic support.[12] Most commonly used in diesel applications are platinum and palladium supported high surface area Al_2O_3 (corundum) [9,12]. This composite material (catalyst) is called washcoat and is applied to a ceramic carrier (typically cordierite honeycomb structures) for use in the exhaust tract. Assuming a Pt-only catalyst, cost estimates can be performed. With a platinum price of 33 €/g (as of May 2023) and a typical noble metal amount of 3 g/l in a DOC,[12] the cost for the precious metal alone ranges in the order of 100 €/l of catalyst volume. For economic reasons, this amount needs to be minimized. Traditionally this has been achieved by downsizing the noble metal particles to maximize the active surface area for a given mass. In order to facilitate a high durability, the particles also need to be distributed homogeneously on the carrier material to slow surface area reduction by sintering. [9,12]

Another promising approach, which has been sparsely researched so far, is to reduce the mass of precious metals by alloying them with less costly metals. One of the main reasons for this is the great challenge of producing alloyed nanoparticles by wet chemical means. Nonetheless, notable work has been done with a limited set of alloys [24–28], in electrochemical applications [14–20] and in the field of three-way catalysts [21,22]. As will be explained in detail in chapter 2.3.2, laser synthesis offers an opportunity to improve the catalysts here. Generally, the potential of the alloys is not limited to cost optimisation, but also promises improvements in catalytic activity and durability, depending on the material (cf. chapter 2.4 and 3.1).

2.2.2 Ammonia-Slip Catalysis

As modern diesel waste gas abatement systems utilize the selective catalytic reaction based on ammonia to reduce the emission of nitrous oxides, excessively dosed ammonia can be released into the environment. Since ammonia is a pungent gas with adverse effects on health and the environment, its emission has been regulated by the EURO 6 norm, particularly for heavy duty vehicles [71] and will also be regulated in future emission regulations for light duty vehicles [68]. With regulations being put into action, car manufacturers had to limit the ammonia slip. This is achieved by using an ammonia slip

catalyst (ASC) that's operating based on selective ammonia oxidation (NH_3-SCO). Ideally every molecule of excess ammonia is converted via the following pathway [12]:

$$NH_3 + 0.75O_2 \rightleftharpoons 0.5N_2 + 1.5H_2O \tag{2.11}$$

Unfortunately, the ammonia will also form nitrous oxides as by-products in an oxygen rich atmosphere [72]:

$$NH_3 + 1.75O_2 \rightleftharpoons NO_2 + 1.5H_2O \tag{2.12}$$

$$NH_3 + 1.25O_2 \rightleftharpoons NO + 1.5H_2O \tag{2.13}$$

$$NH_3 + O_2 \rightleftharpoons 0.5N_2O + 1.5H_2O \tag{2.14}$$

If there is still NO present in the waste gas, also the NO-SCR can take place[6]:

$$4NO + 4NH_3 + O_2 \rightleftharpoons 4N_2 + 6H_2O \tag{2.15}$$

Meanwhile in the ASC, nitrous oxide may be formed via the decomposition of ammonium nitrate as shown by Grossale et al. [73]:

$$2NO_2 + 2NH_3 \rightleftharpoons NH_4NO_3 + N_2 + H_2O \tag{2.16}$$

$$NH_4NO_3 \rightleftharpoons N_2O + 2H_2O \tag{2.17}$$

Also NO and N_2O are a byproduct commonly occurring from the imide and i-SCR mechanism in selective ammonia oxidation [65].

With the ASC being the last waste gas abatement step, it, in principle has to obtain 100% selectivity for molecular nitrogen while also ensuring 100% conversion. In other words, the nitrogen yield of the catalytic process should reach 100% at temperatures that are as low as possible to ensure clean exhaust in cold start conditions. Yet, also at high temperatures (~700°C; high load operation and regeneration of the DPF) 100% nitrogen yield is still imperative, while the catalyst must also remain stable [74]. These requirements are very difficult to be fulfilled by a single catalyst, which is why typically different materials are combined in an ASC. A class of materials that is generally catalytically very active and selective at low temperatures (<300°C) for the respective reactions are noble metals (i.e., Pt, Pd or Pt-Rh). However, while this is mostly true for reactions of hydrocarbons or CO these noble metals show a particularly low selectivity for N_2 (aside their high material costs). Materials that in turn possess a high N_2 selectivity are comprised of transition metal or transition metals and their oxides (i.e., Fe, V, Cu, CuO). These materials are typically active at higher temperatures (300 – 600°C) and come with lower material costs. Consequently, to achieve an early light up and a high selectivity both material classes are

combined on an oxidic support like Al_2O_3 or ZSM-5 in commercial applications. [74,75] This combination can be further augmented by incorporating SCR active catalysts like Cu- or Fe- containing zeolites or V_2O_5; which enable the catalyst to form nitrogen via the SCR routes driven by the formed by-products. Generally the studied metal loadings of Pt, Pd and Pt-Rh lie within 1 – 4.4 wt% and the metals are supported on oxides like Al_2O_3, CeO_2-SiO_2, SiO_2-Al_2O_3, ZrO_2, TiO_2 or ZSM-5. [76–87]. Other studied materials include Ag, Au and Ru, which show a high selectivity, but lack the high activity of commercially used noble metals [74]. Also, literature shows that metallic surfaces appear to enhance the N_2-selectivity, which was demonstrated for Ag-Cu [88]. This is important in the context of this study as alloying of metals can also lead to an reduction in oxides and enable active bimetallic catalysts, similar to the combination of the materials as shown for Pt and Cu [81,83,89–91], Pt and Fe [82,85], Pd and Cu [92] and, Pt and Ag [74].

2.3 Synthesis of Alloy Catalysts

As described earlier, an automotive catalyst generally consists of an active material, which consists of finely divided catalytically active material, usually in the form of nanoparticles, and a support that fixes the nanoparticles and facilitates handling and application. This chapter looks at the methods used to synthesise the active material, both chemically and by laser, before looking at how the nanoparticles are supported.

Literature describes a wealth of different routes for the synthesizes of alloyed nanoparticles. Before this chapter illustrates the most important ones, it is useful to illustrate the particle morphologies that typically occur when mixed element particles are synthesized. In particular, there are five different classes that are briefly described in Figure 4, and which are the result of different approaches to their synthesis.

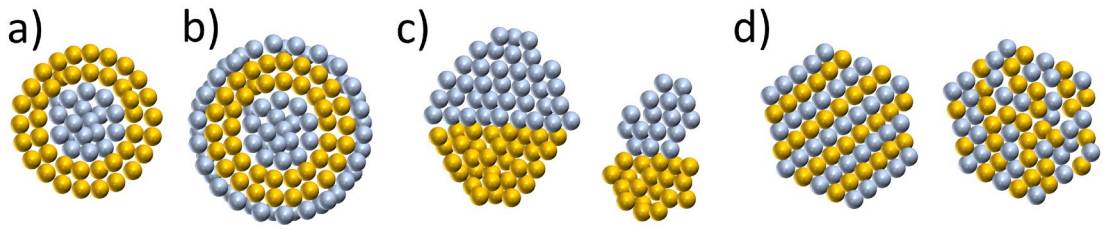

Figure 4 Classes of alloy particle morphologies. Core-Shell particles (a), onion-like (b), Segregated / Janus-Particle (c), intermixed, either orderly or randomly (d). Reprinted and adapted with permission from R. Ferrando, J. Jellinek, R. L. Johnston, Chem. Rev. 2008, 108, 845–910, DOI: 10.1021/cr040090g. Copyright © 2008 American Chemical Society.

Particles can occur in a core-shell configuration, where one element is segregated into the centre of the particle and another forms a shell. It is also possible for the particles to form onion-like structures, but this is usually the result of experimental efforts, as will be illustrated later in this chapter. Another possibility is for the elements to form segregated

mixtures, where the final particle looks like it has been sintered together from two particles of opposite elements. Finally, true solid solutions are also possible. Either the alloyed particles form an ordered mixture or the mixture within the particle follows a random distribution. [93]

2.3.1 Chemical Synthesis

A widely used route to the synthesis of alloyed particles originates from the synthesis of monometallic colloids. First published by Faraday in 1857 [94] and later improved by Turkevich [95] in the 1950s, the synthesis of metallic nanoparticles starts with the reduction of dissolved metallic salts in a solution. The resulting particles are then prevented from condensing into microparticles by the presence of ligands that bind to the surface and stop particle growth. Typically alkyl thiols or thioethers are used as the sulphur binds strongly to the metallic surface, especially for gold. [93]

Bimetallic colloids can be prepared in a similar fashion, by dissolving appropriate mixtures of salt and employing reducing agents like $NaBH_4$, N_2H_4 or H_2 gas [96–100]. Since the reduction starts with the material of the highest standard potential, this route usually leads to core-shell particles, which possess a structure akin to their order of reduction potential, as for example with Pt-Ag [99] or Pd-Pt [101]. Strongly binding ligands can invert this process, or in case of similar redox-potentials and/or high mixing enthalpy, bimetallic solid solution ("alloyed") particles can be obtained [99,102]. A reduction carried out over sufficiently short timeframes, will assist in the formation of alloyed particles as well [103]. Another approach is the synthesis of oxidic particles and the coating of these with oxides of different metals. Subsequent reduction then yields metallic core-shell particles as demonstrated for Mn-Ni and Fe-Sn [96,104,105]. Onion-like particles are synthesised in a similar way, by precipitating a metal salt by reduction in the presence of metal clusters. The condensation yields bimetallic clusters and, if alternated, can produce onion-like structures [98,106–108]. If alloyed particles are desired, the reduction of metal complexes already containing both elements is a possibility [109,110]. Furthermore, transition-metal complexes or labile noble metal salts can be adsorbed unto an oxide like silica and be subjected to thermolysis under vacuum, forming bimetallic nanoparticles [96,98,111–114]. Similarly, colloids are accessible, if ligands are used in the solution based thermal decomposition [115–118]. Further synthesis routes follow an electro- [96,119–123] or sonochemical [124,125] approach, both of which favour the formation of core-shell particles. Finally, a special synthesis method uses radiolysis. In this approach the reduction is triggered by solvated electrons generated by γ-radiation [111,126–130] or e-beam irradiation

[131,132] of an aqueous solution. While lower radiation doses also yield core-shell particles, higher doses appear to favour solid solution particles. [93,127]

Outside of the bounds of bi- or trimetallic nanoparticles, there is a wealth of information on the synthesis of high-entropy alloys (HEA). These materials are typically composed of 5 or more elements, that form a solid solution because of the strong contribution of the mixing entropy. In the case of nanoparticles even 3 elements can be enough to be classified as HEA, as the contribution of the surface entropy can be high enough to stabilize a mixture that would be instable in the bulk. These alloys – e.g., PdRuIr - are accessible by wet-chemical reduction synthesis. [22] The synthesis of high-entropy alloys follows routes similar to the aforementioned ones, like hydrothermal [133] and co-precipitation [134], but extends the toolkit to involve some reaction step on a short or ultrashort timescale like sputtering synthesis [135], ultrasonication [135], and arc discharge [136,137]. Also reduction syntheses sometimes employ extreme conditions like the severe chemical reduction [138,139] or shock based synthesis routes [138,140,141], which helps the elemental mixing [142].

In any case, all chemical synthesis methods can be classified into two categories, successive (condensation onto core material) or simultaneous (precipitation from solution) [143]. If particles are not generated in a simultaneous manner, the formation of solid solution bimetallic particles is highly unlikely. Furthermore, synthesis of solid solution particles by simultaneous methods depends strongly on the chemical properties of the elements. This means that screening a large variety of bimetallic alloys becomes a demanding process that often involves fine-tuning bespoke synthesis protocols for each alloy. An elegant way to escape this is the application of extreme conditions akin to the ones employed in HEA-synthesis, which is why the synthesis of alloys by lasers is discussed in the following chapter.

2.3.2 Laser Synthesis

Laser based synthesis of colloids is a method first reported by Fojtik and Henglein in 1993 [47]. While laser ablation of metals, in gas [144] or in vacuum [145] was used before to generated molecules, atoms and clusters, this method, in which the laser beam is focussed on a metal sheet suspended in a liquid, directly generates stable colloids. With lasers becoming stronger and more affordable, the research on laser synthesis has gotten increasing attention in the past decades [46,146,147]. The laser ablation synthesis in solution (LASiS), sometimes also referred to as pulsed laser ablation in liquids (PLAL) occurs upon irradiation of a target, suspended in liquid, with a short- or ultrashort pulsed laser.

Depending on the length of the laser pulse, energies between about 100 µJ (500 W, 5 MHz, 5 ps pulse) and 20 mJ (100 W, 5 kHz, 10 ns pulse) are radiated into the target material.

Assuming a focussed laser spot on the material of 100 µm diameter, this equals an energy density (fluence) of 1 J/cm² and 255 J/cm² respectively. The material's reaction to this energy can be described using a two-temperature model [148–150]. Here, the energy dissipation is modelled via electron- and phonon-temperature. The electrons of the irradiated material react quickest and reach temperatures of several thousand Kelvin within the first few fs after the pulse [149]. The electrons subsequently transfer their energy to the lattice of the material and thus form lattice vibrations, described as phonons. This thermalization happens on the order of several picoseconds [149]. If the laser pulse length is sufficiently short, all laser energy can be transferred to the electrons before they equilibrate with the lattice. For this reason, fs-pulsed ablation is sometimes referred to as "cold", because the material does not heat up, i.e., no energy is transferred to the lattice, before disintegration. If the pulse length is in the order of ps, some heating occurs, with ns-pulses transferring significant portions of heat energy into the material [151,152]. With the lattice becoming energized, the material heats up and starts to melt, vaporize and given enough fluence even becomes supercritical [153]. This phase change also means a drastic change in local pressure, expelling material from the target. Initially the material expands, forming a sponge like structure with some supercritical material expanding outward into the surrounding liquid layer (cf. Figure 5). The acceleration is slowed by the liquid and after several hundred ps the lifted material collapses back onto the target, forming a molten bed for the next few nanoseconds. During this phase, the first nanoparticles are generated, by condensation from the supercritical state and, depending on the laser fluence, from the disintegration of the sponge like structure into nanoparticles [153]. These two formation mechanisms, originally described by Zhigilei et al. [50,153], also explain the origin of bimodal size distribution of colloids synthesized by fs-, or ps-pulsed laser ablation. After generation, the particles are expelled from the target into the surrounding liquid and thus rapidly cool, initially in the order of 10^{12} K/s, with the largest particles still reaching about 10^{9} K/s. For many particles this means that cooling is too rapid for proper crystallization and the

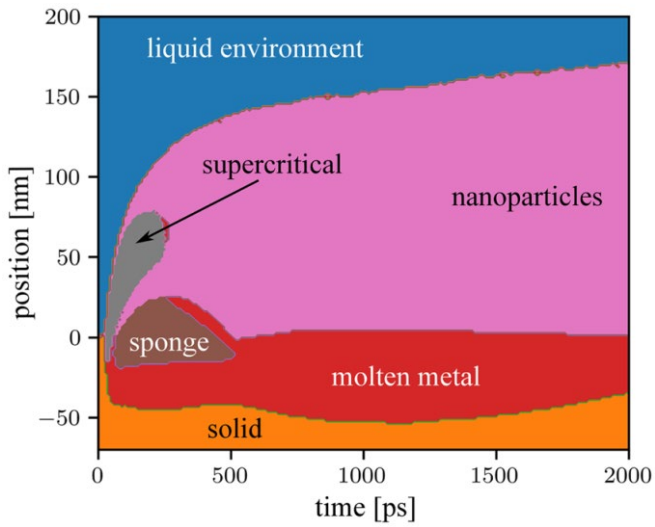

Figure 5 Development of different phases upon ps irradiation of Fe-Ni-Target with a fluence of 3000 J/m². Reprinted with permission from Chen, C., Zhigilei, L.V., Appl. Phys. A 129, 288 (2023). DOI: 10.1007/s00339-023-06525-0.

formation of defect-rich particles results [153]. Depending on the material, even metallic glass nanoparticles can be formed [154]. Most importantly, the strong intermixing and rapid cooling enables the formation of alloy particles, that can even form phases, that are immiscible in the bulk [155–157]. While current technology limits the simulation of the laser ablation process to short timescales and thus to at best ps-pulsed laser irradiation, it can be interpolated to ns-pulsed ablation. In contrast to ps-pulsed irradiation, the energy is deposited into the material on a much longer timescale, enabling the material to heat even further. This possibly leads to reduced formation of sponge-like structures and more supercritically heated material. From the latter phase, the condensation of nanoparticles should occur, similar to the process simulated for ps-pulsed irradiation, also explaining the more monomodal size distribution observed for ns-pulse synthesized colloids. With the nanoparticles being expelled into cold liquid, the cooling rates should be on the same order as simulated for ps-pulse synthesized particles, generally still enabling the synthesis of novel, bulk immiscible, phases. In fact, Waag et al. demonstrated that ns-pulsed ablation appears to be beneficial, if the target is not alloyed prior to ablation, i.e., as a pressed powder mixture. Here, ns pulses generated more alloyed particles from a mixed powder target, than ps-pulsed ablation [52]. Waag et al. attributed this observation to stronger intermixing in the layers that are molten by the laser, illustrating the beneficial thermal influence of the ns-pulsed irradiation.

With the particles being expelled into the surrounding liquid, their energy gets transferred into the liquid, which results in the formation of a cavitation bubble [158]. This bubble expands and collapses several times, before finally releasing the contained nanoparticles. The extreme conditions within the cavitation bubble, especially at the point of collapse, result in the liquid partially disintegrating. In fact, Kalus et al. showed that the reaction products of a decomposing liquid can form persistent microbubbles [159]. Both, the cavitation bubble and the persistent bubbles, contribute to reduced particle synthesis efficiency [159], but more importantly the formed molecules and radicals can have significant influence on the chemistry of the formed nanoparticles. With water generating hydroxyl and oxygen radicals [160], the nanoparticles are subjected to an oxidative environment. This means that materials being ablated in water can form oxides, if their standard potential is sufficiently low. This becomes especially important if the goal is the synthesis of alloys, as the formation of oxides may hinder the formation of an alloy. Literature offers a wide variety of alloys that have been attempted to be synthesized by laser ablation in liquids. They can be classified into two material categories. The first of which is alloys that are synthesized from noble metal mixtures. Of these, e.g. Ag-Au [161,162], Pt-Pd [163] and Pt-Au [156,164] have been synthesized successfully in water or aqueous solutions of varying pH. One

exception to this rule is a trimetallic alloy of Ni-Mn-In, whose constituents are not noble, but synthesis has been reported to be successful in water [165]. The second material category is alloys where at least one constituent is not noble. If these mixtures are synthesized in water, oxidation of at least one constituent or the formation of a bimetallic oxide occurs, as is shown for Zn-Mg [166], Ni-Ti [167], Sn-Zn [168], Cu-Zn [169], Bi-In-Sn [170] or Cu-Zn [171]. Generally, these studies show, that especially small particles are oxidizing, with larger particles often containing a bimetallic core. More success is reported, when organic solvents are employed in the synthesis, as shown for Ni-Fe [172], Au-Fe [173,174], Ag-Fe [175,176], Pd-Y [177,178], Sm-Co [172], Cu-In / Cu-Ga / Cu-In-Ga [179], Nd-Fe-B [180] or a high-entropy alloy like Co-Cr-Fe-Ni-Mn [45]. But even the use of organic solvents does not guarantee successful alloy formation, as was shown for Au-Fe [181], Au-Ni [182] and Ni-Fe [183,184]. These observations can be explained when the decomposition products of organic solvents are considered. When pyrolysis occurs, they tend to form radicals, that possess reductive potential, favouring elemental ablation [146,159,185]. Additionally, there were many studies observing a trend in alloy formation depending on molecularly bound oxygen in the used solvent, like Ni-Mo [14], Fe-Mn [186], Pt-Fe [187]. These studies reported an improved alloy formation if less oxygen is bound in the solvent molecule. As any solvent will also dissolve oxygen, this spurred research into the influence of dissolved oxygen. It was shown, that a reduction in dissolved oxygen also aids alloy formation in the case of Pt-Fe [188] and Pt-Cu [53]. As a rule of thumb, alloy formation will likely occur in a degassed organic solvent, containing as little molecularly bound oxygen as possible, though this will also favour carbon shell or carbide formation [146].

When catalysis is the desired application for the generated nanoparticles, small particle sizes are generally preferrable, as they maximize the active surface area per unit weight. This means, that size control is of high importance. On way to tune the particle size distribution in LASiS is by varying the laser parameters. Using lasers with fs and ps pulses tends to form bimodal size distributions, while ns-pulsed lasers tend to form monomodal size distributions [189–191]. Also, the fluence has an impact on the primary particle size. Considering only the laser ablation, lower fluences seem to favour smaller particles [190–195]. But since high throughput synthesis demands continuous ablation, employing scanning the laser at a suitable repetition rate [55], laser fragmentation after particle generation is inevitable [196]. In this process higher fluences form smaller particles [190,197]. Depending on the setup, it needs to be evaluated, if lower or higher fluences are desirable, all the while considering productivity effects [192,198]. Apart from laser-based variables, synthesis environments can be tuned similar to the chemical synthesis. For example, ions can be used to stabilize the electrostatic charge of the nanoparticles and thus quench particle growth

early during synthesis [190]. This effect can be achieved using a large variety of salts with alkali or alkaline earth metal halides being intensively researched and nitrates as well as citrates also being considered [146,199–204]. NaCl thereby being very common [199,201,205,206] as well as tuning the pH by e.g., NaOH [207–211], though the ionic strength needs to be roughly matched to the colloid's particle concentration. That is, because the ions are acting on the nanoparticle surface and a higher mass and number concentration (i.e., more and or smaller particles) need an equally changed number of ions to stabilize the charge. In effect, too little ions won't affect the particle size distribution and too many ions may even destabilize the colloid. Apart from using ions, surfactants may also be used to tune the resulting particle size distribution. Many different surface active molecules are applied here, for example PVA, PVP, PEG [212], starch [213], albumin [214], gelatine [215], chitosan [216] or other surfactants like SDS [217] or CTAB [218]. Similarly, ablation in organic solvents allows particle size adjustments, as the solvent polarity [219,220] or adsorbed solvent molecules have an impact on the resulting particle size distribution [221,222]. Finally, the adsorption of the synthesized particles onto a support will also hinder ripening and particle growth, stabilizing the particle size. With an in-situ approach, where the support is suspended in the carrier liquid, the particles can be directly adsorbed, yielding small particle sizes [223], while the increased liquid opacity from the suspended support might reduce productivity.

2.3.3 Supporting Laser generated Colloids

With the application of the laser generated particles in automotive catalysts, adsorption onto an oxidic support is necessary. Before a discussion of the supporting strategies, it is imperative to understand the origins of colloid stability because supporting a nanoparticle is intricately linked to its stability in a liquid environment.

At the border of any material, the bonds from the bulk material are broken. This leads to surface reconfiguration and termination by molecules from the surrounding environment. For example, a surface can acquire charge by preferential adsorption of ions or the ionization of surface groups. [224] These phenomena mean, that a surface charge may form on any surface. If the material is sufficiently small, the proportion of surface to volume rises until the properties of the surface start to govern the particle behaviour. In case of colloids, this means that sufficiently small particles suspended in a liquid can exhibit a surface charge that can enable colloid stability. This follows from first principal analysis of the repulsive and attractive forces acting between the particles withing the liquid.
The attraction between two particles can be described using the van-der-waals potential. This attractive force results from the attraction of temporary dipoles, that any material

forms due to oscillations of the charges contained within the molecule above absolute zero temperature. While the attractive force scales with $1/d^6$, if molecules are considered (d being the distance between molecules), geometrical considerations lead to a scaling close to 1/d for particle attraction.

The complete equation is derived by Lauth and Kowalczyk as follows [225]:

$$P_{vdw}(d) = \frac{A_{312}}{6}\left(\frac{2R_1R_2}{f_1(d)} + \frac{2R_1R_2}{f_2(d)} + \ln\left(\frac{f_1(d)}{f_2(d)}\right)\right) \tag{2.18}$$

With R_1 and R_2 describing the radius of nanoparticle and support and f_1 and f_2 as follows:

$$f_1(d) = d^2 + 2R_1d + 2R_2d \tag{2.19}$$

$$f_2(d) = f_1(d) + 4R_1R_2 \tag{2.20}$$

A_{312} represents the Hamaker constant of a particle with the Hamaker constant A_{33} and another particle with the Hamaker constant A_{22} interacting in a liquid with the Hamaker constant A_{11} [224]:

$$A_{312} = \left(\sqrt{A_{33}} - \sqrt{A_{11}}\right)\left(\sqrt{A_{22}} - \sqrt{A_{11}}\right) \tag{2.21}$$

The repulsive force between particles can be estimated by considering the electric field around them. A charged support particle with the charge Q will have an electric field E, which can be described using the gaussian theorem (ε being the permittivity of the medium):

$$Q = \varepsilon \oint \vec{E} d\vec{A} \tag{2.22}$$

In order to describe the electric field on the outside, a closed sphere with the area $A = 4\pi r^2$ is projected onto the particle. Since the electric field will be symmetrical, the integral simplifies to

$$Q = \varepsilon \oint \vec{E}(r) d\vec{A} = \varepsilon \oint \vec{E}(r) d\vec{A}(\varphi,\Theta) = \varepsilon \vec{E}(r) \oint d\vec{A}(\varphi,\Theta) \tag{2.23}$$

Rearranging and solving the integral using the area A, gives a description of the electric field E in dependence of the distance from the surface r:

$$E(r) = \frac{Q}{4\pi\varepsilon r^2} = \frac{Q}{4\pi\varepsilon_o\varepsilon_r r^2} \tag{2.24}$$

Here ε is split into the ε_0, the permittivity of the vacuum, and ε_r, the relative permittivity of the medium. If the charge Q is assumed to be contained on the surface of the particle with radius R, the surface charge density ϱ can be defined:

$$\rho = \frac{Q}{A} = \frac{Q}{4\pi R^2} \tag{2.25}$$

Combining the field (2.24) and the surface charge (2.25) yields an expression for the electric field around the support particle:

$$E(r) = \frac{Q}{4\pi\varepsilon_o\varepsilon_r r^2} = \frac{4\pi R^2\rho}{4\pi\varepsilon_o\varepsilon_r r^2} = \frac{R^2\rho}{\varepsilon_o\varepsilon_r r^2} \tag{2.26}$$

The electric potential around this particle can be obtained by integrating the electric field:

$$\varphi(r) = -\int \vec{E}(r)d\vec{r} = -\int \frac{R^2\rho}{\varepsilon_o\varepsilon_r r^2}d\vec{r} = -\frac{R^2\rho}{\varepsilon_o\varepsilon_r}\int \frac{1}{r^2}d\vec{r} \tag{2.27}$$

With $\varphi(r \to \infty) = 0$ the integration results in:

$$\varphi(r) = \frac{R^2\rho}{\varepsilon_o\varepsilon_r r} \tag{2.28}$$

The potential energy of a particle moving through this electric field, can be described by multiplying the potential by the charge $E_{pot} = q\varphi$. With q representing for example a metallic nanoparticle. This nanoparticle has its own surface charge $q_{NP} = 4\pi R_{NP}{}^2\rho_{NP}$ and thus, after application of some geometric correction, that sets the border of the support particle to be at r=0, the potential can be described as follows:

$$E_{pot}(r) = 4\pi R_{NP}{}^2\rho_{NP}\frac{\rho_s}{\varepsilon_o\varepsilon_r}\frac{R_s{}^2}{(r-R_s)} \tag{2.29}$$

Combining the attractive (2.18) and repulsive (2.29) potentials allows the illustration of the energy barrier that forms and is the reason for a stable colloid, when an aprotic liquid without dissolved ions is considered (cf. Figure 6 b)).

As soon as the liquid contains some ions, the solution for the repulsive potential becomes more complex (cf. Figure 6 a)). Generally, it has been shown, that under these circumstances a rigid layer of counterions adsorbs onto the surface of the charged particle. This layer is termed Stern layer and comprises of an inner and outer Helmholtz layer, both named after their respective discoverers. This layer is followed by more loosely bound ions. If the particle is moved through the surrounding liquid, the shell will be sheared within this layer, which is why it is termed shear layer. It is at its border, where the zeta-potential can be measured. Following this layer, there will be a diffuse layer of even more loosely bound ions until finally the composition of the liquid equates that in the volume of the rest of the liquid. [224–226] Derivation of the repulsive potential relates closely to the one shown previously, while it needs to be considered that the electrochemical double layers are approximated by capacitors.

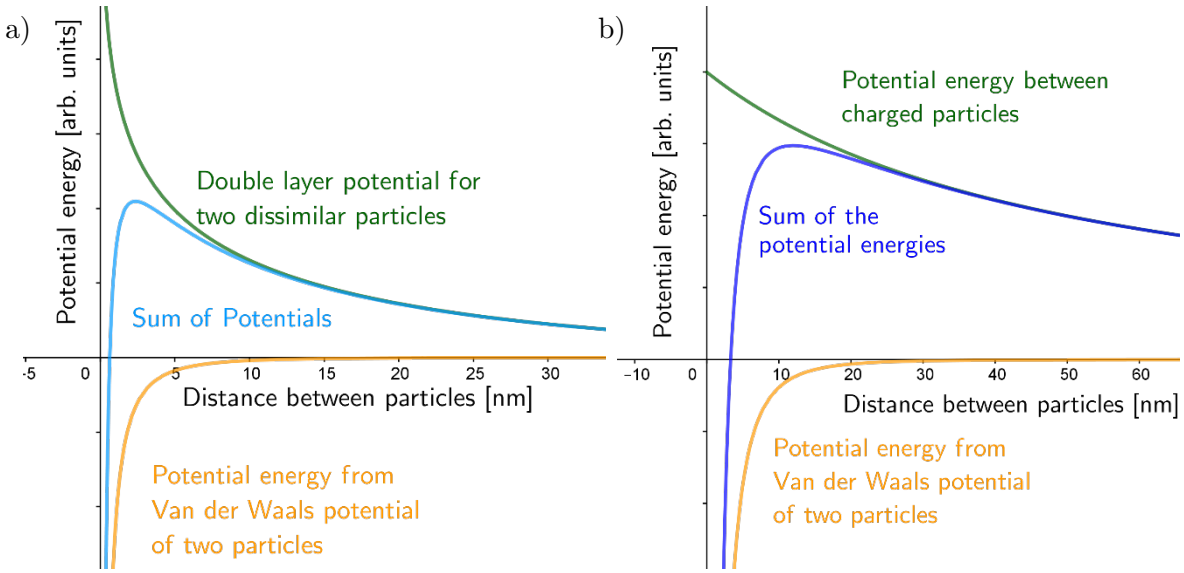

Figure 6 Potentials acting on two approaching particles of different size. a) shows the qualitative potential based on DLVO theory in a liquid with dissolved ions, b) shows how the potential looks like if two charged particles are suspended in an ion-free liquid.

Further geometrical considerations allow for the conclusion of the equations for two particles of unequal radius and thin double layers, approaching each other under the assumption of constant surface charge [224,227]:

$$\Phi_R^\sigma = N_1 \left\{ N_2 f(r) - \ln\left[1 - \exp(-2\kappa r)\right] \right\} \tag{2.30}$$

With

$$N_1 = \pi\varepsilon R_{NP} R_S \frac{\psi_{NP}^2 + \psi_S^2}{R_{NP} + R_S} \tag{2.31}$$

$$N_2 = \frac{2\psi_{NP}\psi_S}{\psi_{NP}^2 + \psi_S^2} \tag{2.32}$$

where R_{NP} and R_S denote the radius of the nanoparticle and support, while $\psi_{NP/S}$ denotes the surface potential and

$$f(r) = \ln\left(\frac{1 + e^{-\kappa r}}{1 - e^{-\kappa r}}\right) \tag{2.33}$$

In these equations, κ is used to model the concentration and charge of the ions within the solution. It is also termed Debye-Hückel parameter:

$$\kappa = \sqrt{\frac{e^2}{\varepsilon k_B T} \sum_i z_i^2 n_{i\infty}} \tag{2.34}$$

Here e denotes the elemental charge, k_B the Boltzmann constant, T the temperature in Kelvin, z_i the charge of the i-th ion and n_i the density of ions within 1 m^3 of solution. Using the relation between molar ([M]=mol/l) and number concentration $n_{i\infty} = 1000 \frac{l}{m^3} N_A M_{i\infty}$, with N_A being Avogadro's constant, the parameter can be modified to allow for more common concentration numbers in mol/l:

$$\kappa = \sqrt{\frac{1000 N_A e^2}{\varepsilon k_B T} \sum_i z_i^2 M_{i\infty}} \tag{2.35}$$

The inverse of κ, κ^{-1}, can be understood as a characteristic distance from the particle surface; here the repulsive force has dropped significantly (to 1/e of the original potential).
When comparing the repulsive force generated by the adsorption of the different ionic layers (Figure 6 a)) to the simple electrostatic force (Figure 6 b)), it can be seen that the simple electrostatic consideration leads to a maximum further away from the surface and a much longer ranging interaction potential. Still, depending on the involved surface charge, both repulsive forces inhibit particle agglomeration. That is, as long as both involved particles have the same polarity of surface charge, i.e., positive or negative. As soon as the polarity differs between particles, no repulsive force exists. In fact, the repulsive force will change to

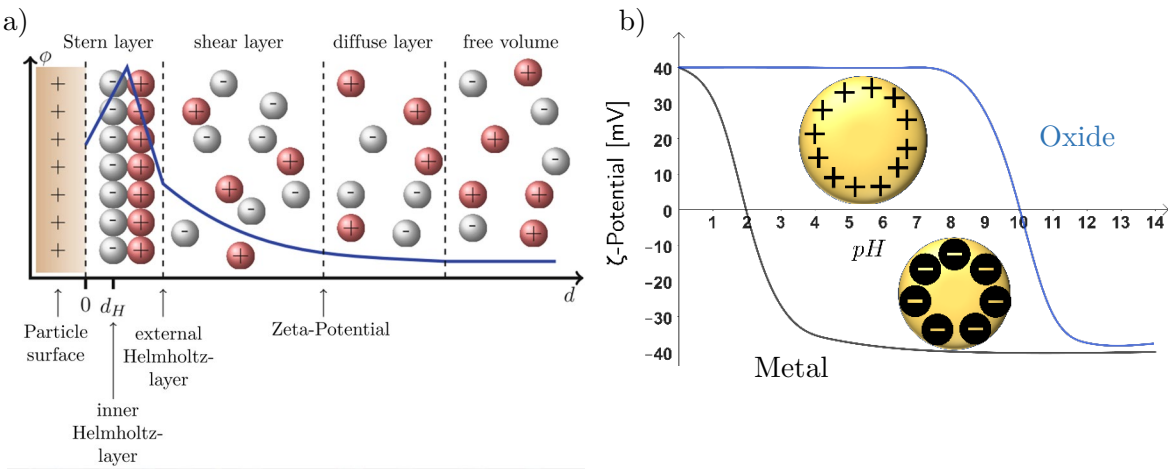

Figure 7 Qualitative illustration of the potentials around a charged particle in a solution containing ions (a) and of the dependence of the zeta potential of two materials (oxide and metal) from the pH (b). The particles show the respective surface charge, if the zeta-potential is positive or negative. (a) Reprinted with permission from G. J. Lauth, J. Kowalczyk, Springer Spektrum Berlin, Heidelberg, Berlin, Heidelberg, 2016, DOI: 10.1007/978-3-662-47018-3. Copyright © 2016 Springer-Verlag Berlin Heidelberg.

an attractive one, allowing barrierless adsorption. One way of flipping the surface charge is to vary the pH of the solution, which can alter the termination on the surface and thus the exhibited surface polarity and charge. Although not every material responds in the same way. For example, metallic nanoparticles tend to have a negative surface charge over a wide range of pH and will only change the surface charge, when subjected to strongly acidic conditions [29], as illustrated in Figure 7 b). The point in this graph, where the zeta-potential crosses zero is termed isoelectric point (IEP), as this is the point where positive and negative charges cancel out and the particle appears neutral. On the other hand, oxidic particles like Al_2O_3 or TiO_2 tend to have their IEP in the slightly caustic region between 7 and 10 [29]. This means that there is a pH area where metallic and oxidic particle have the same surface charge, i.e., $pH > IEP_{support}$, and where both particles have opposing polarity, i.e., $IEP_{particle} < pH < IEP_{support}$. This behaviour then can be used to support the metallic particles. First the colloid is mixed with the support in a caustic region above the IEP of the support material. Then the mixture is stirred and slowly titrated, so that the pH falls between the IEPs of both materials. Here, the adsorption of nanoparticles onto support particles occurs, yielding immobilized nanoparticles, ready for application. This method of supporting particles was first proposed by Wagener et al. [228] and was later supported by experimental evidence for Pt [29,229] and Pd [230].

In its core, this method of supporting is driven by the diffusion of both particle species. In order to adsorb to a surface, the repulsive forces need to be overcome. If the electrostatic environment is favourable, adsorption readily happens at room temperature. But if a pH adjustment is impossible, overcoming the repulsive barriers is much more challenging. This situation arises if the nanoparticles are synthesized in a solvent, as many solvents are aprotic and thus do not allow for pH-adjustments. In those solvents, a different approach needs to be used. In order to overcome the adsorption energy barrier, a higher temperature can be used, as this means that each diffusing particle has a greater kinetic energy, that might exceed the adsorption barrier. Another option is to increase the particle concentration drastically. In the limit, where all solvent is evaporated, the distance between particle and support cannot exceed the tenths of nanometres, where the maximum of the repulsion is located (cf. in Figure 7 b). Thus, the removal of solvent pushes the particles beyond this maximum, facilitating the adsorption. This adsorption is also aided by the fact that the removal of solvent means that the VdW-Potential rises, because of an increase in Hamaker constant as A_{11} approaches zero (cf. Equation (2.21)). Also, an increased concentration maximizes the collision frequency, increasing the chances of particle/support interaction. Both methods can also be combined by distilling the mixture of nanoparticles and support, while stirring, in order to remove the solvent and force the nanoparticles onto the oxidic

support. Apart from the described supporting strategies here, Reichenberger et al. also give an overview over support strategies including electrophoretic deposition, which is only relevant for conductive support materials [231].

2.4 Alloys as Catalysts

The reason for why alloys are employed as catalysts is tightly connected to the knowledge, we have about the basic principles of catalyst operation. Sabatier illustrated in his talk in front of the German chemical society 1911, how the adsorption enthalpy of substance influences the reaction rate [232]. A substance, or product, that binds too strongly to a catalyst surface will hinder the reaction by blocking surface sites and a too light binding will hinder the reaction from occurring in the first place. In 1969 Balandin showed how a catalyst has to follow geometric and energetic considerations and presented the volcano plot by plotting the catalytic activity in dependence of the heat of adsorption, visualizing the Sabatier principle (cf. Figure 8) [233]. Newer concepts take into account the electronic structure of the catalyst. Termed Brønsted-Evans-Polanyi (BEP) relation and discussed by Nørskov in 2008, the catalyst activity can be correlated to the position and width of the d-band centre, which is defined by the catalyst surface [117,234]. Apart from substance, the geometric structure of the surface influences this electronic landscape through the coordination number of the surface atoms, which is a direct function of the size and shape of nanoparticles [235]. A change in coordination number can have drastic effects on the heat of adsorption, as was shown by Bligaard and Nørskov [236] for Pt and the CO adsorption. The heat of chemisorption was

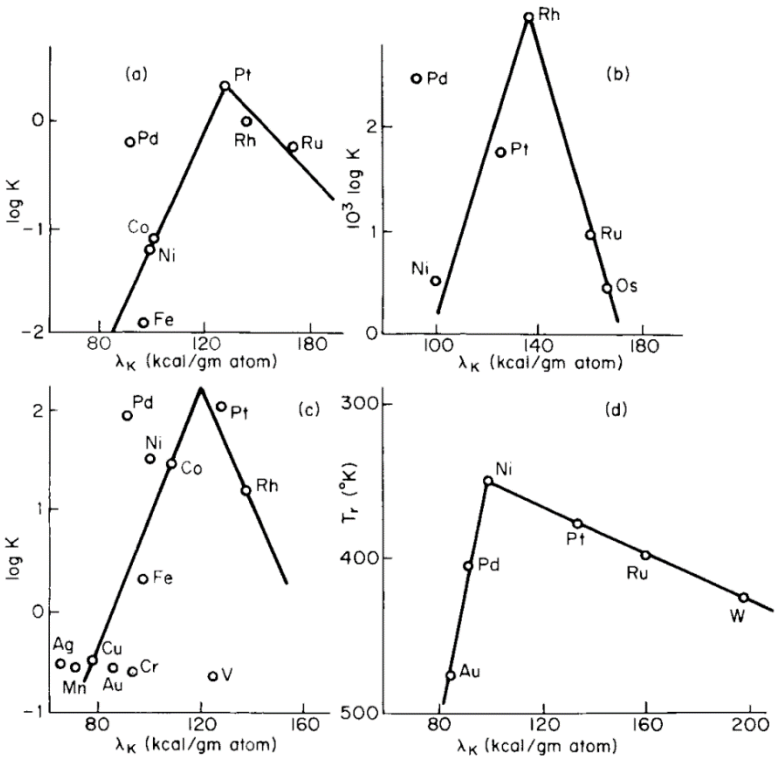

Figure 8 Exemplary volcano dependences when plotting the catalytic activity vs. the heat of sublimation. (a) benzene hydrogenation; (b) cinnamic acid hydrogenation; c) oxygen hydrogenation; d) ethylamine hydrogenolysis. Reprinted with permission from A. A. Balandin, in Adv. Catal., 1969, pp. 1–210, DOI: 10.1016/S0360-0564(08)60029-2. Copyright © 1969 Academic Press Inc. Published by Elsevier Inc.

shown to vary by 1 eV, which has significant effects on the activity of the different surface facets because any change in adsorption enthalpy exponentially influences the reaction rate. Although the parameters that have been found to influence catalyst activity are numerous, an important way of influencing them is through the material that makes up the catalyst particle itself. Material modification, particularly alloying, allows finer tuning than simply changing the catalyst material, and thus makes a large number of tuning variables available [237]. Strasser et al. divided the influence of a second metal into three unique effects, which however, partly influence each other [238]: 1) Ensemble effects; unique ensembles of surface atoms perform specific mechanistic functions. 2) Ligand effects; when dissimilar surface atoms come into contact, a charge transfer occurs, changing the electronic structure and modifying the activity. 3) Geometric effects; the spatial arrangement of surface atoms is altered by alloying, caused by strain, geometry and size. [117]

Apart from improving the reaction rate by proper alloying, economic considerations have also played a significant role in driving the research. Many catalysts are based on noble metals, which demand reduction in use simply due to the high cost per gram. Xu et al. could show that chemically synthesized alloy Pt-Cu particles perform well in the electrochemical oxidation of formic acid. In fact, the alloy with 20 at% Cu showed a higher activity and due to the copper content was cheaper per gram [239]. Similarly Marbella et al demonstrated the same activity improvement and noble metal saving using Au-Cu alloys in the electrochemical reduction of CO_2 [240]. Another improved reaction is the oxygen reduction reaction (ORR) that was shown to benefit from alloying Pt with Ni and showed best reaction rates on the {111} facet [241]. Additionally, core-shell structures of Pd-Pt (core-shell respectively) shave been used to fine tune facets and strain, drastically improving on activity in ORR [117]. Many oxidation reactions have also been improved by alloying. Gu et al. showed that an equimolar alloy of Pt-Ru is better than Pt in the methanol oxidation reaction (MOR) [242]. Similarly Pt-Ni also exceeded Pt when applied in MOR at an equimolar alloy [243]. Equally, the CO-Oxidation also profits from alloying. Chemically synthesized Ag-Au particles were shown to be very active in several studies [244–246]. Abdelsayed was able to rank several alloys on how active they were in CO oxidation (Cu-Pd>Cu-Rh>Au-Pd>Au-Rh>Pt-Rh>Pd-Rh>Au-Pt) and also highlighted the importance of complete removal of capping agents or surfactants which would otherwise poison the catalyst [247]. This points to an important advantage that laser synthesis may have over chemically preparing catalysts. It is possible to synthesize nanoparticle without surfactants, removing the need for complicated purification procedures. In fact, surfactant free alloy nanoparticles have been synthesized and demonstrated to be more active than their single metal counterparts in OER [14] and ORR [248].

3 Method Development

In the following chapter, the selection and design criteria for the choice of alloying elements, target production and synthesis of the catalysts required for the work are derived and described in detail.

3.1 Choice of Alloy Metals

The choice of alloying elements is largely based on their planned use as oxidation catalysts. In simplified terms, the following aftertreatment reactions necessary for diesel engines can be identified:

$$CO + \frac{1}{2}O_2 \rightleftharpoons CO_2 \tag{3.1}$$

$$C_xH_y + (x + \frac{y}{4})O_2 \rightleftharpoons xCO_2 + \frac{y}{2}H_2O \tag{3.2}$$

$$NO + \frac{1}{2}O_2 \rightleftharpoons NO_2 \tag{3.3}$$

$$2NH_3 + \frac{3}{2}O_2 \rightleftharpoons N_2 + 3H_2O \tag{3.4}$$

Reactions (3.1)-(3.3) are examples of the oxidative treatment of engine exhaust gas in the diesel oxidation catalyst (DOC). Reaction (3.4) describes the oxidation of ammonia to prevent ammonia slip after reduction catalytic treatment of the nitrogen oxides (ASC).

The basis of every oxidation reaction is the activation of oxygen on the catalyst. It can be derived from Sabatier's principle that the binding of oxygen (and the reactants) should be neither too strong nor too weak in order to exhibit good catalytic activity. In 2018, Montemore et al. presented a detailed review on the activation of oxygen on metallic surfaces [13]. This also identifies the type of species that form on selected materials. Figure 9 b) shows that the adsorption enthalpies for O_2 are lowest for the noble metals Pt, Pd, Au and Ag. Au can only bind molecular oxygen weakly, which is why only physisorbed

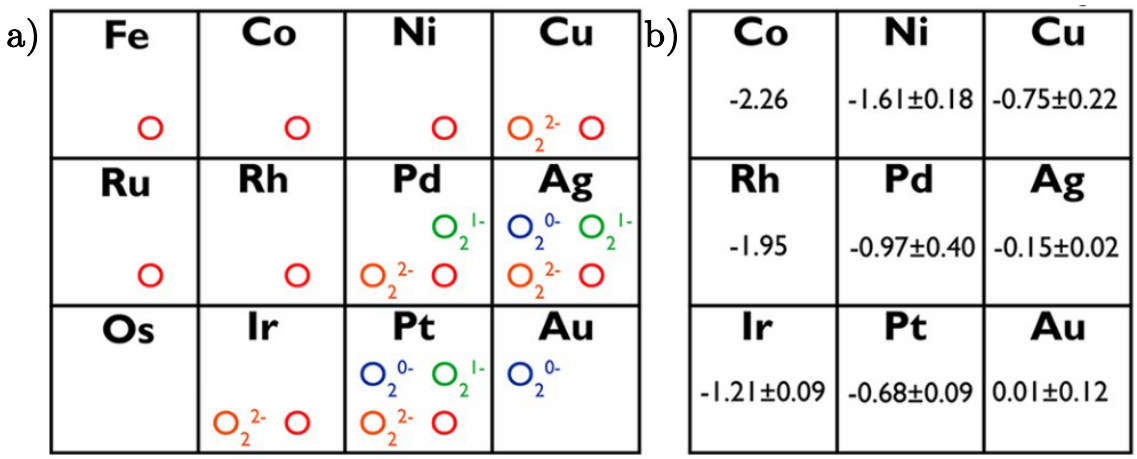

Figure 9 a) Experimentally observed states under ultra-high vacuum and low surface coverings. Physisorbed (O_2^{0-}), superoxo (O_2^{-}), peroxo (O_2^{2-}) and atomic (O) species are entered. b) Adsorption enthalpies for O_2 in eV calculated by DFT. Reprinted with permission from Matthew M. Montemore, Matthijs A. van Spronsen, Robert J. Madix, and Cynthia M. Friend, Chemical Reviews 2018 118 (5), 2816-2862, DOI: 10.1021/acs.chemrev.7b00217. Copyright © 2018 American Chemical Society.

oxygen can be found. Pt, Pd and Ag, on the other hand, can also bind superoxo and peroxo species (Figure 9 a)).

A closer look at CO oxidation reveals a volcano plot-like relationship for these elements (Figure 10). Apart from (111)-terminated surfaces, the adsorption enthalpies of the elements do not lie where the highest reaction rate is expected. A combination of platinum with silver, gold, palladium or copper seems opportune. Ideally, a binary alloy shifts the enthalpies of adsorption in such a way that a higher activity is achieved. Gold and silver also show advantages in the presence of water. Improved oxygen dissociation is observed with silver ([35,36]), which should have a positive effect on CO oxidation in the moist exhaust gas stream. Experiments with gold also showed positive effects of water on CO oxidation [34]. Furthermore, rhodium will also be investigated as an alloying element in this study. As a typical element in the 3-way catalytic converter, rhodium helps to reduce nitrogen oxides and has a positive effect on ageing resistance [9]. It also shows a similarly low activation energy for CO oxidation as platinum [33].

The further away the elements in the periodic table are from the block of noble metals (Pt, Pd, Au, Ag), the more oxygen is directly dissociated and chemically bound. These thin surface oxides are initially active (e.g. for Cu or Ru in CO oxidation) but become inactive as the reaction progresses due to surface restructuring and growth of the surface oxide layer [34,40]. This could be one of the reasons why no breakthroughs were made in the early days of exhaust gas catalysis with base metals [249] and the use of precious metals has taken hold. Another one was their susceptibility to deactivation by sulphur and water [250].

Since the sulphur content of fuel has since drastically decreased [250], base metals and especially alloys of them may be reconsidered for exhaust gas catalysis.

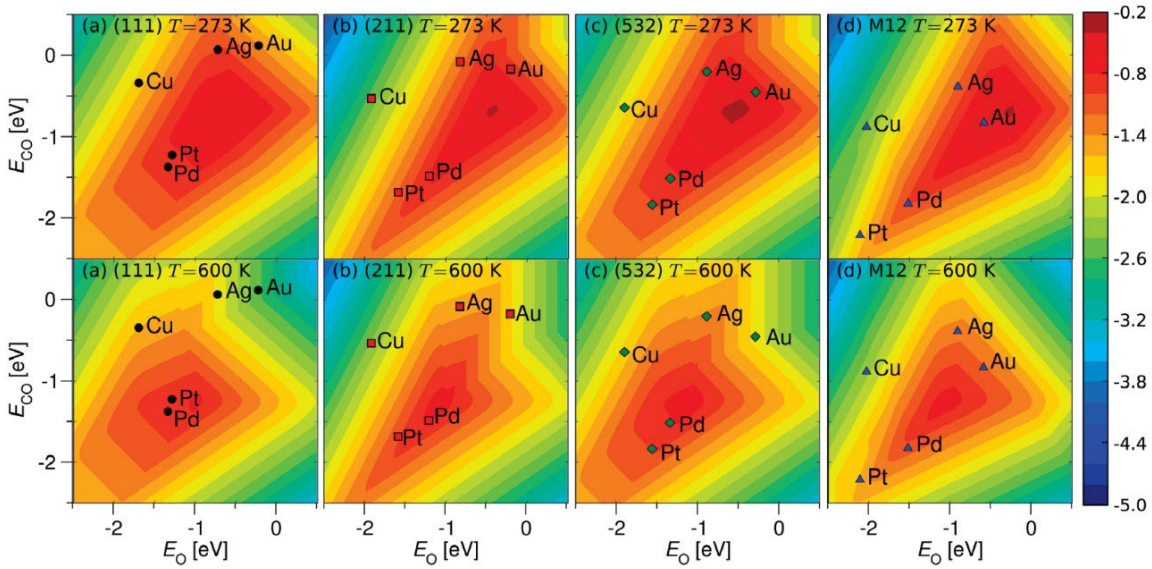

Figure 10 “Sabatier activity" i.e., reaction rate of CO oxidation (logarithmic colour scale) as a function of the adsorption energies of CO and O calculated using microkinetic models. Red indicates high rate, blue low. Upper row at low pressure (0.22 bar) and low temperature, lower row at high pressure (1 bar) and high temperature. Reprinted with permission from T. Jiang, D. J. Mowbray, S. Dobrin, H. Falsig, B. Hvolbæk, T. Bligaard, and J. K. Nørskov, The Journal of Physical Chemistry C 2009 113 (24), 10548-10553, DOI: 10.1021/jp811185g. Copyright © 2009 American Chemical Society.

From studies on the corrosion resistance of stainless steel (Fe, Cr, Mo, Ni) and titanium based materials, it is known that even small additions of precious metals ennoble the materials. This improves the corrosion resistance of the materials. An essential reason for this is assumed to be the prevention of anodic oxidation of the non-ferrous metals. [251]

In anticipation of a similar effect, alloys with base metals (Nb, Mo, Mn, Fe, Cu, Ru) are investigated in this study. Platinum is chosen as the common denominator because it is catalytically very active. As a precious metal, however, platinum is also very expensive and known to undergo particle growth [9,32]. Alloying with other metals promises to improve the economic efficiency of the catalyst and, depending on the metal, also the ageing resistance by inhibiting particle growth. This principle is already being pursued commercially in the form of catalysts based on a Pt-Pd alloy [9]. There, it is known that the alloy suppresses Pt nanoparticle growth [32] and thus improves durability. As a commercially used system, Pt-Pd also forms the reference in this study.

Furthermore, alloying with some base but refractory metals is also thought to improve durability. The growth of Pt nanoparticles based on Ostwald ripening could be slowed down by alloying with refractory metals (Nb, Mo, W, Ru, Re), analogous to stabilisation with

palladium. The production of targets with tungsten and rhenium is a great challenge due to their high melting points.

The successful dissociation of oxygen at the surface is also central to ammonia oxidation. In addition to the advantages of the alloying elements as CO oxidation catalysts, there is some evidence in the literature that the elements selected so far will also have a positive effect on ammonia oxidation. For example, the oxides of iron, manganese and copper are among the more active catalysts of ammonia oxidation [38]. As a product of ammonia oxidation, mainly elemental nitrogen is desired in the slip catalyst. A good catalyst for this has a high activation energy for N_2 dissociation because this promotes the formation of molecular nitrogen under reaction conditions. This property is fulfilled by ruthenium [39] and it has been shown that the oxidation of ammonia on RuO_2 is highly selective to nitrogen [40,41].
In addition to alloys with platinum as the base metal, other combinations should be investigated. A mixture of palladium with copper should give an improvement in CO oxidation analogous to the mixture of platinum with copper. Mixtures of gold with iridium or rhodium could improve selectivity. Rhodium alone, for example, shows a high affinity for the formation of nitrogen oxides in ammonia oxidation, which is why it is also used in nitric acid production [38]. This behaviour is precisely not desired if in the ammonia slip catalyst. Therefore, an alloy with the more inert gold should improve selectivity. A mixture of gold and iridium, on the other hand, promises improved catalytic activity. It is known that oxygen adsorbed on iridium dissociates and is transferred in this form to the alloyed gold. [42] The oxygen, which is not stable there, should be able to transfer particularly well to adsorbed reactants. The system should therefore be highly active [13].

Reasons for the exclusion of certain elements

The reasons for the exclusion of certain materials arise mainly from the broad use of catalytic converters in the automotive sector. Particular attention is paid to avoiding toxic emissions and questionable mining conditions. The elements used should, as far as possible:

1. Not be known to have precarious mining conditions (cobalt)[252–254]
2. Not be radioactive (Technetium)
3. Not form particularly toxic (chromium) or volatile and toxic oxidation products (osmium)
4. Not easily form particularly volatile and toxic carbonyls (nickel)

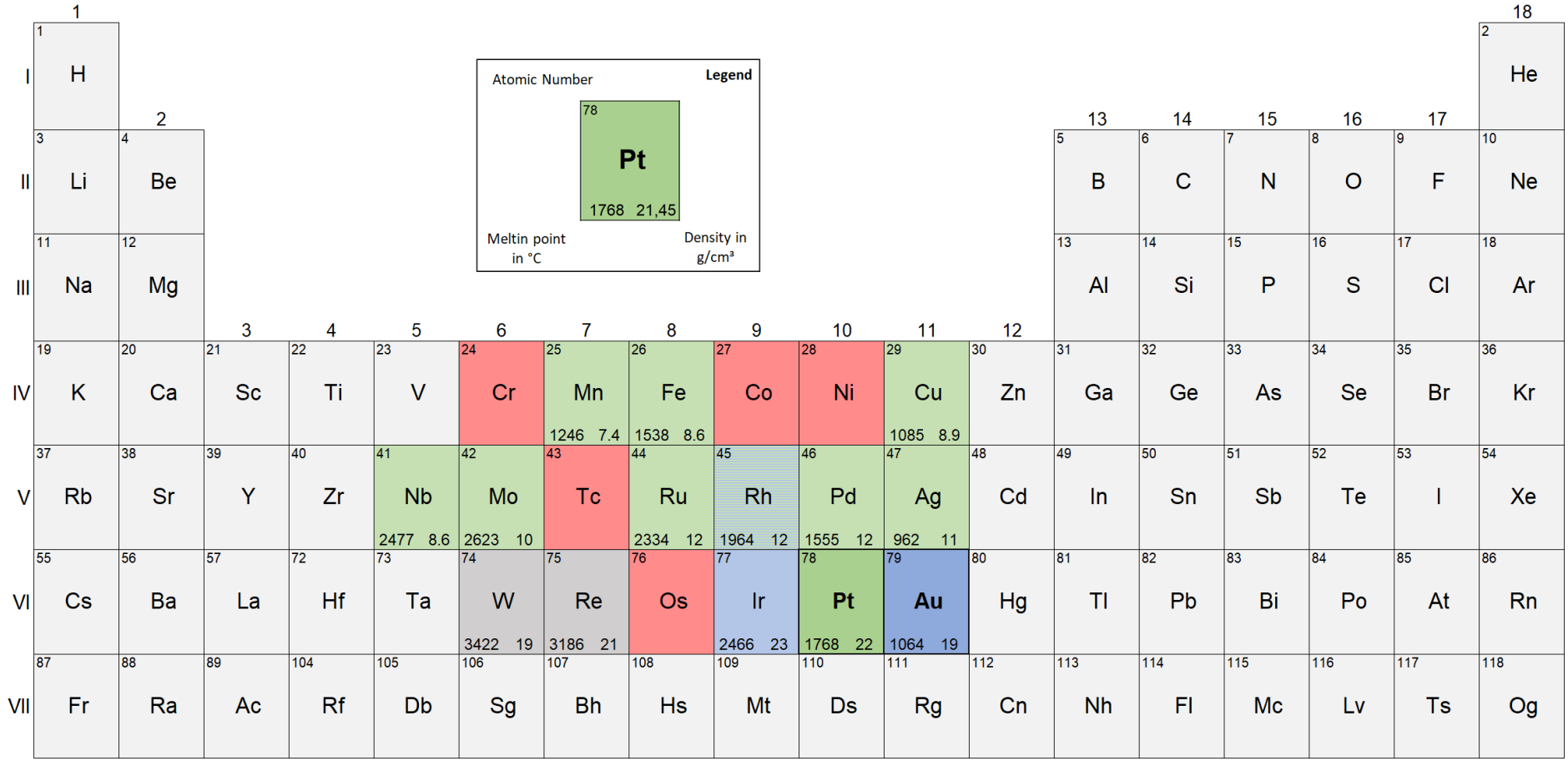

Figure 11 Periodic table of the elements. The elements used are marked. In green are all elements that were combined with platinum and in blue are all elements that were combined with gold. For all elements marked in red, there were explicit reasons for exclusion. The mixture palladium/copper is not marked separately. The production of the elements in dark grey proved to be particularly challenging during the course of the study, so only target production studies were carried out for them.

In summary, the following material compositions are selected for the study. Mixtures of *platinum with niobium, molybdenum, tungsten, ruthenium and rhenium* are investigated with a special focus on the ageing stability of the catalysts. Mixtures of *platinum with iron, copper and manganese* serve to optimise the economic efficiency of the catalyst. Mixtures of *platinum with silver, gold or rhodium* serve to improve the activity, while the mixture with *palladium* forms the comparative reference to the commercial system. Apart from this, mixtures of *gold with iridium or rhodium*, as well as *palladium with copper*, will be investigated. A detailed list of the selected alloying elements is given in Annex A1 and a quick overview can be found in Figure 11.

3.1.1 Choice of Compositions

Once the alloying elements are selected, the question of a sensible composition of the mixture arises. For this study, four different compositions will be investigated for each alloy. In the distribution of the mixture ratios, the field of expectation was divided into two groups. For all alloys where both elements are expected to be highly active in CO oxidation, compositions are determined that span a wide mixing range (typically 10-99 at%). The only exception here is the mixture of platinum with rhodium, where a maximum proportion of 50 at% rhodium has been specified due to cost considerations. This category includes blends of gold with iridium and rhodium, of palladium with copper and of platinum with ruthenium, gold, copper and silver.

For all compositions in which the aggregate element is refined by platinum or the alloy is examined for durability, the minimum platinum content is set at 50 at%. Only compositions in the range 50-99 at% are examined there. This category includes mixtures of platinum with niobium, molybdenum, manganese and iron.

In the final selection of the mixing ratios, the phase diagrams of the material mixtures are taken into account. For example, eutectic and dystectic mixing ratios are selected for niobium and manganese, or consideration is given to intermetallic phases for Pt-Mo and Pt-Fe. Apart from this deterministic composition definition, however, the unique opportunity is also taken to pursue explorative material development. Following this approach, macroscopically unknown compositions are chosen. Some of the chosen material mixtures (e.g., Au-Ir) show a wide miscibility gap with largely missing miscibility. Homogeneous mixtures of these compositions are actually not thermodynamically stable, but could persist in small nanoparticles due to the high contribution of the surface energy to the thermodynamic equilibrium [255]. These explorative mixtures include some from the gold-iridum or gold-rhodium system, but also some mixtures of platinum with silver, gold or rhodium. All mixtures also have in common at least one, often even two mixtures with a

high platinum content. These are included in the matrix due to the known high activity of platinum. A detailed breakdown of all alloy compositions sorted by mixing range with assignment of phase diagrams and detailed selection criteria can be found in Annex A2.

3.2 Target Manufacturing

Generally, laser synthesis in liquids is based upon a solid target. Many studies researching metallic nanoparticles employ a metal sheet as target, upon which the laser is focussed and from which the nanoparticles are created. Metal sheets help the ablation in several ways. Firstly, the material is robust against impacts and ductile which means that it can be mounted within the ablation chamber without special precautions and won't be damaged if it is dropped. Furthermore, it is easily dried, which allows for easy measurement of the ablated mass and thus precise determination of the ablation rate which is needed in long term ablation for planning purposes. Similarly, laser ablation and the shock wave occurring from the cavitation bubbles do not damage the surface nor does the target disintegrate into microparticles which need to be removed from the colloid and might distort the ablation mass measurement. If alloy nanoparticles are desired, process control considerations make pre-alloyed metal sheets favourable, as they possess the same properties as single metal sheets. While this approach is used in literature, for example for Pt-Pd [24], it is limited to alloys that are miscible in the bulk. Also, these targets may have to be purchased through a third party, as the infrastructure to produce metal sheets is not always easily available and this adds considerable extra cost and possible time delays. An easier method of

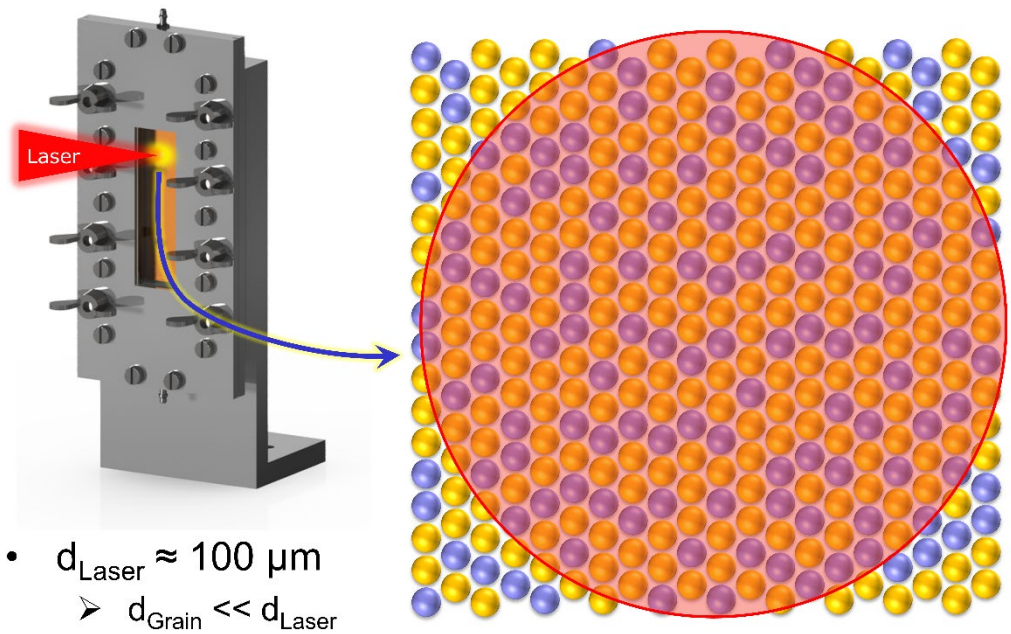

Figure 12 Schematic illustration of laser spot size and grain size within the powder target surface. The primary particle size of the metal educt powders should be much smaller than the laser spot diameter in order to allow for sufficient elemental mixing in the ablated zone.

producing targets for alloy nanoparticle synthesis takes advantage of the fact that the alloying does not need to be done “in advance” as in before the laser ablation. As illustrated in chapter 2.3.2, laser ablation can induce alloying which means that the target only needs to comprise of the desired elements in the appropriate proportions. This approach has also been reported in literature, for example for Ni-Mo [14]. Starting with metal powders, means that there are a few extra considerations that regard to the raw material and processing. Since alloy formation is supposed to happen after ablation, or within the formed melt pool [49], it is best, if the educt particle size of the metal powder is much smaller than the laser spot diameter. This follows from the simple geometrical consideration, that a good mixture will occur if the laser spot ablates as many individual particles as possible, which then can mix into the alloy (Figure 12). For this study, the spot diameter was estimated to be around 100 µm in diameter, so educt powders were purchased, that have a primary particle size of about 10 µm (cf. particle size specifications outlined in S1.1). To ensure intimate mixing, theses powders were mixed within a closable vessel with 5 mm YTZ (Yttria stabilized Zircon oxide) milling balls (by volume: 1/3 powder, 1/3 milling balls, 1/3 void). This assembly was then rotated for several hours to ensure intimate mixing after which the mixture was strained through a sieve and processed further. The hard milling balls ensure the purity of the material as they minimize the abrasion, that would occur in less hard balls like steel. For mixing, it is also important to have dry powders that hinder caking which would prohibit proper mixing. Also, during storage and mixing, less noble base metals were kept under nitrogen or argon to lessen oxide formation, which helps the sintering process.

Sintering is needed to solidify the targets, which gives them enough structural rigidity to prevent microparticle formation upon laser ablation and also allows the targets to be handled easily. To be able to sinter the powder into a usable target, the powder is filled into a die press and compacted by applying between 240 and 250 MPa of pressure. The two used dies are depicted in Figure 13. As some scanning systems profit from rectangular targets (i.e., if the scanning pattern is set by a polygonal scanner), producing rectangular targets allows a more efficient use of surface area, but this also comes with several challenges. First of all, it is very difficult to manufacture a die press with very tight tolerances without electrical discharge machining (EDM). Since the powders that need to be compacted have a particle diameter of around 10 µm the matching surfaces ideally need to have a gap smaller than this, so that the powders are not pushed between punch and sleeve, where they can jam the mechanism. Additionally, the rectangular press shape can induce stresses within the target that can break the target while extracting it from the die. While many targets were successfully produced with a rectangular press, ultimately a switch to a circular variant was made. This press was built from off-the-shelf and high tolerance parts typically

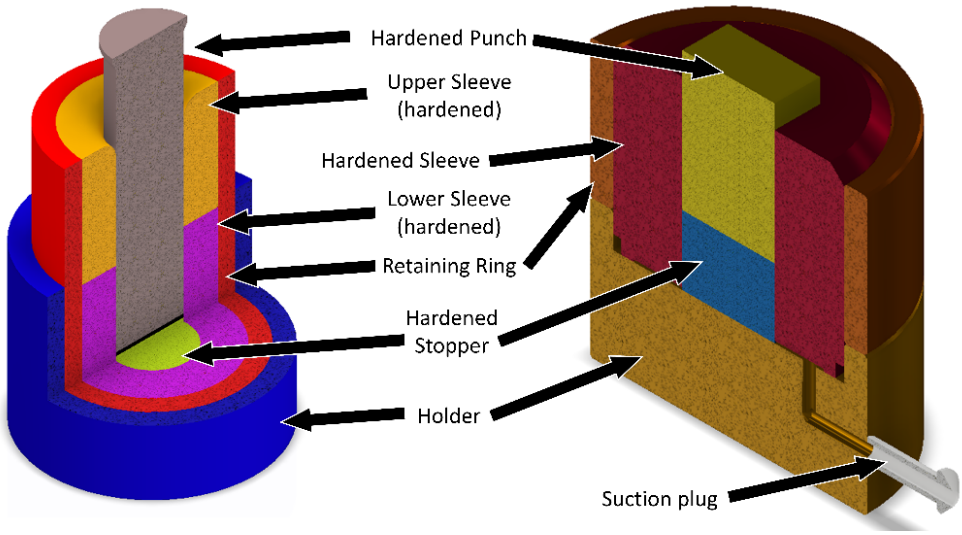

Figure 13 Cut view of the used die presses. On the left: Circular press tool designed by Alexander Schmitz-Wunderlich and Alexander Schug using industrial cutting bushes within their maser thesis. On the right: Rectangular press tools designed by Friedrich Waag.

employed in die pressing. Therefore, the surfaces not only met the high tolerance specifications that were needed, but they were also hardened, minimizing erosion during operation. This resulted in a more robust pressing process and less damaged pressed parts. After the powders have been pressed into shape, they were sintered in a furnace. Noble metal combinations were sintered in air in a Nabertherm LHT 01/17 D that allowed for a maximum temperature of 1650°C. Blends of noble and base metals were sintered in a tube furnace equipped with gas control, that was able to reach a maximum temperature of ~1000°C. In order to prevent oxidation, the pressed targets were loaded into the tube furnace and then the furnace was flushed with ARCAL F5 (a mixture of 5% H_2 in N_2 by Air Liquide). This mixture contains a high amount of hydrogen, without being an explosion risk, thus optimizing safety of operation while retaining sufficient reductive properties. After flushing the chamber, the sintering process is started. The temperatures are set, so that 2/3 of the solidus temperature of the final alloy, or of the lower melting element in case of immiscibility, is reached and held for many ours (typically overnight) (cf. S1.1 for details about all sintering temperatures and durations). During sintering the chamber is continuously flushed with the hydrogen gas mixture at 16 cm^3/s (= 2.3 cm/s flushed length). After sintering the gas mixture is exchanged for argon (@19 cm^3/s = 2.7 cm/s). This removes adsorbed hydrogen and marks the end of the target manufacturing process. The targets are then stored under argon or nitrogen until the ablation starts. The long sintering times not only allow for rigid targets, but also aid the elemental mixing, where possible, which helps the synthesis of alloy nanoparticles. Generally, this process turned out to be very robust and allowed for the manufacture of a large variety of targets, that also did not crack during handling. Notably, they were also mechanically stable when placed

onto a hotplate to expel liquid from the pores to allow correct differential mass measurements. Nevertheless, some limitations also applied, that should be mentioned here. First of all, sintering relies on the temperatures being high enough to allow for material transport. In fact, the temperature has an exponential influence on the time required for sintering. This means that if 2/3 of the solidus temperature is above what the provided ovens can provide, a sufficient sintering can hardly be achieved. This was observed for the mixture of Pd-Re. With Pd melting at 1828 K and Re at 3459 K, sintering temperatures should at least reach 1220 K, considering the phase diagram, 1270 K or above would be even better. As Rhenium is susceptible to oxidation, sintering needed to be carried out under the reducing atmosphere provided in the tube furnace. With sintering occurring at 1000 C, (i.e., right at 2/3 of the solidus temperature) only insufficient powder compaction and target stability could be achieved. Higher temperatures would be desirable but were only achievable in the Nabertherm oven with air atmosphere. Here the targets showed significant oxidation, which made the targets brittle and not usable. This means that some metal combinations are not achievable, e.g., of very high melting compositions like Pt-W.

3.3 Choice of Laser and Process Parameters

In chapter 2.3.2 it was already discussed that ns-pulsed lasers are more reliable in synthesizing alloy nanoparticles and are more robust regarding the target composition. Therefore, it is sensible to also chose ns-pulsed lasers for this study. In order to ensure a high catalytic activity of the synthesized nanoparticles, a small particle size is desirable. Most laser and process parameters are chosen with this goal in mind. Additionally, the purity of the particles and the productivity play an important role and also need to be considered (cf. chapter 3.4). Regarding the particle size, the first decision has to be made regarding the laser wavelength. While 1064 nm (IR) is common, it is also possible to use 532 nm (Green) irradiation. The green laser induces a larger amount of post-irradiation as more of the laser energy is absorbed by the colloid, when compared to IR irradiation. For this study the effect was compared using Pt colloids, synthesized at the point of maximum productivity. As shown in Figure 14, ablation with a green laser yields significantly smaller particles. This comes at the cost of reduced ablation rate though, as the available power at the green beam line is reduced to about 40% when compared to IR. When comparing the productivity for particles <10 nm, the IR beam still exceeds the productivity of the green beam, but extraction of the small particle fraction would need post-processing in the form of centrifugation. As centrifugation is a process that strongly relies on particle density, this route is not favourable in the case of alloys because centrifugation might also lead to segregation of unevenly mixed alloy nanoparticles, leading to concentration of the less dense

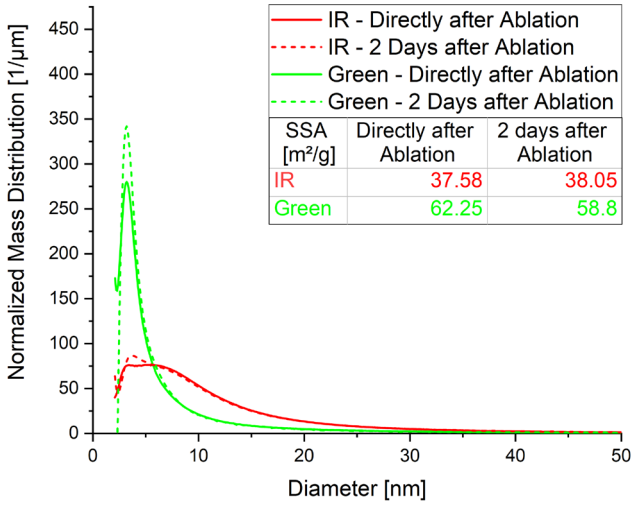

Figure 14 Comparison of particle size distribution of Pt colloids synthesized by 532 nm (green) and 1064 nm (IR) ablation on a ns-pulsed laser system in 0.1 mmol/l aqueous KOH.

material. Therefore, the green beamline is chosen, as it provides the smallest particles in a one-step synthesis, while the ablation rate is still high enough to provide the needed mass of nanoparticles in a reasonable amount of time (i.e., 200-500 mg/h for 1500 mg = 3-8 h ablation time). When it comes to reaching this productivity, some effort needs to be put into engineering a sufficient ablation chamber. Originally, simple glass beakers with the metal sheet at the bottom were employed as synthesis vessels [47,256]. While this approach is appealing because of its simplicity, the accumulation of nanoparticles, the rising gas bubbles and the batch nature of the process limits the maximum productivity. A similar argument also prohibits the use of the improved process, demonstrated with a "batch ablation chamber" [257]. An ideal process would allow for fresh solution being supplied to the ablation region, while simultaneously removing generated colloid. Ideally the liquid would be supplied from the bottom, aiding the removal of generated bubbles, that rise due to their lower density (cf. Figure 15). This approach has been developed in the Barcikowski group (demonstrated for example by Kohsakowski et al. [258]) and will also be employed in this study as it allows for semi-continuous ablation with high ablation rates in the order of several hundred mg per hour.

When it comes to synthesizing alloy nanoparticles composed of base metals, it was established in chapter 2.3.2 that an organic solvent is much better suited as liquid than water. This means that considerations regarding productivity also need to include ablations in organic solvents. Unfortunately, ns-pulsed ablation in organic solvents usually results in a severe loss of productivity, possibly due to strong gas generation from solvent evaporation and decomposition, which scatters the laser beam [160]. This problem is much less pronounced when

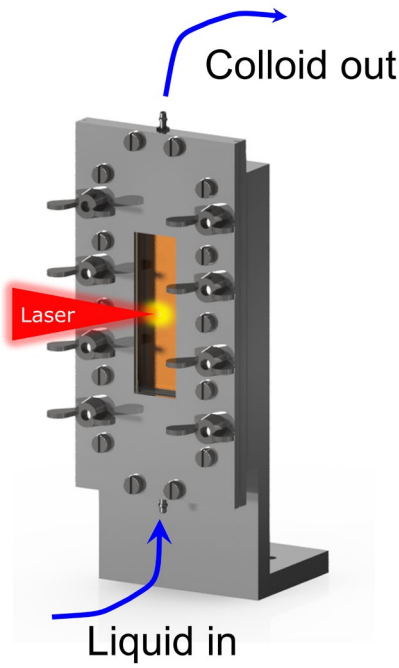

Figure 15 Ablation chamber and flow direction used in this work.

ps pulses are employed (cf. Figure 1 in A4, where a higher power specific productivity was measured for ps-pulsed laser ablation in propylene carbonate than for ns-pulsed laser ablation). For this reason, the ablation of base metal combinations is planned to be executed with a ps laser and since this is limited to 1064 nm, it also will be carried out with this wavelength.

As soon as ablations are carried out in solvents, it is sensible to consider impurities entering the colloid through leeching from seals, which are usually made from silicone rubber. Additionally, solvents may attack the seals in a way, that leads to the ablation chamber leaking, which in the case of flammable organic solvents is a safety concern. Both problems can be solved by employing fluorocarbon rubber (FFKM), to seal the mating surfaces. These materials have excellent stability against most solvents, acids and bases [259], which makes them ideally suited for the flexible application in research. Unfortunately, at the time of experimenting, flat stock material was prohibitively expensive at about 1000 € per 100x100x1mm sheet. A good alternative to this was found to be expanded PTFE (e-PTFE). With the good chemical stability of PTFE and the conforming ability of the foamy structure and lower price, at about 40€ per pre-cut set, this material was able to prevent leaks and made leaching of impurities unlikely. Regarding tubing, PTFE-tubing bent with the help of a hot air gun, was found to be sufficient, though better alternatives in the form of PTFE-lined tubing are available and might increase reliability.

3.4 Choice of Additives and Solvent

As water is the cheapest and most researched liquid, it is also used for noble metal combinations following the differentiation outlined in S1.2 of Annex A4. The water used is desalinated and further purified by filtration through a MiliQ-System. As pure water does not allow for the smallest particle size distributions, micromolar additives are employed. In the example in Figure 14, this was a 100 µM solution of KOH. However, the choice of additive is also closely related to colloidal purity. As the particles will be used as oxidation catalysts, any additive should be removable by oxidation at elevated temperatures, while at the same time helping to control size and stability in the colloidal phase. This means that an ideal additive will decompose into gaseous products when exposed to high temperatures and an oxidative environment. KOH does not meet this design criterion as it oxidises to give a solid product. A better choice would be ammonium hydroxide, which readily decomposes into nitrogen and hydrogen when combusted. A comparison between ammonium hydroxide and potassium hydroxide showed that this base is not suitable as it induces colloidal instability, particularly in the case of silver. A better alternative proved to be tetraethylammonium hydroxide (TEAOH), an organic base with properties superior to

ammonia and comparable to KOH, making it the ideal substitute. HNO_3 was chosen for titration purposes, as this acid will also decompose within a high temperature oxidative environment as will its reaction products with TEAOH. To further stabilize the colloids, a salt like NaCl can be used. This has a similar disadvantage to KOH though, as the chloride may tightly bind to the nanoparticle and the sodium cannot be removed upon oxidation. The chlorine can be replaced by citrate, which can be removed easily, and the sodium can be replaced by ammonia. Ablations carried out with ammonium citrate showed stable colloids and thus were used throughout the aqueous ablations.

The choice of an organic solvent for the ablation of materials that are sensitive to oxidation is much more difficult. Jendrzej et al. showed that a higher solvent viscosity can be beneficial for colloid stability when they synthesised particles in polyalphaolefins that were stable even when used as engine oil under engine operating conditions [260]. There is also evidence that a high dipole moment is beneficial for particle stability after synthesis [146]. A high polarity is also attributed to smaller particles, at least when comparing protic and aprotic solvents [220]. The search for a high polarity, high dipole moment solvent led to propylene carbonate. Not only does it have a very high dipole moment of about $17*10^{-30}$ Cm, it also has a high relative dielectric constant of about 67 [261]. Additionally, it has a high boiling point (249°C) with exceptionally low vapour pressure of about 3 Pa at room temperature [262]. It is reasonable to assume that this will result in small cavitation bubbles, as solvent evaporation is limited. Also, this will make working with the solvent rather safe because ignition of spills is not to be expected and if the solvent breaks down upon laser irradiation its decomposition products won't contain anything that can't be burned off of the nanoparticles. Finally, its viscosity is higher than that of water at 2.4 mPas [262]. On top of this, propylene carbonate is only mildly irritant and can be synthesized from CO_2, which makes it a green solvent that is already applied in a wide range of processes and products [263]. The only downside that it shares with many other solvents is, that it won't allow supporting the nanoparticles via a pH assisted route. One option would be to find suitable cross-linkers, where one side selectively binds to the nanoparticles and the other side to the support. But many times these cross-linkers may introduce impurities like sulphur [264], which this work aims to avoid. This means that supporting the nanoparticles from this solvent will be carried out using the concentration by distillation approach illustrated in chapter 2.3.3. In order to be able to distil the colloids gently, this entailed building a vacuum distillation in order to overcome the high boiling point and low vapour pressure. Another approach can be to use the ability of a propylene carbonate based colloid to solvate ions, selectively destabilizing the nanoparticles. Experiments in this regard led to a patent showcasing that only a colloid is able to solvate sodium-, potassium and ammonium

nitrate as well as potassium iodide. This leads to a destabilized colloid adsorbing on support particles that are stirred into the solution [265]. While this route allows omitting the vacuum distillation it currently lacks particle size control. Since the adsorption of particles is triggered by selectively destabilizing the colloids, adsorption is always accompanied by particle agglomeration. This could negatively impact the performance of the catalysts and therefore this route wasn't employed.

4 Results

4.1 Application of catalysts in an industrial test setting

Activity and Durability Patters of 45 Binary Noble Metal Alloy Nanoparticle Variants for Commercial Diesel Exhaust Aftertreatment

Published on 5th July 2023 in ChemCatChem (doi: 10.1002/cctc.202300563)

Simon Siebeneicher [1], Dr. Sven Reichenberger [1], Dr. Christoph Hengst [2], Dr. Franz Dornhaus [2], Bernd Wittek [2], Prof. Dr. Stephan Barcikowski [1*]

1 Technical Chemistry I and Center for Nanointegration Duisburg-Essen (CENIDE)
University of Duisburg-Essen
Universitaetsstr. 7, Essen 45141, Germany
simon.siebeneicher@uni-due.de (S. S.); sven.reichenberger@uni-due.de (S. R.); stephan.barcikowski@uni-due.de (S.B.)

1 Umicore AG & Co. KG
Rodenbacher Chaussee 4, 63457 Hanau, Germany
hengst1031@gmail.com (C. H.); franz.dornhaus@eu.umicore.com (F. D.); wittek.b@gmail.com (B. W.)

Highlights:

- Description of laser particle synthesis, catalyst preparation and testing
- Overview of particle characterization
- In-depth analysis of physical base parameters (e.g., adsorption enthalpy CO, NO, O and melting temperature) on catalyst performance
- Summary of design criteria for alloy nanoparticle catalysts
- Outlook towards multinary alloy catalysts

Appendix:

- Supporting information in A4

ChemCatChem

Research Article
doi.org/10.1002/cctc.202300563

Chemistry Europe
European Chemical Societies Publishing

www.chemcatchem.org

Activity and Durability Patterns of 45 Binary Noble Metal Alloy Nanoparticle Variants for Commercial Diesel Exhaust Aftertreatment

Simon Siebeneicher,[a] Sven Reichenberger,[a] Christoph Hengst,[b] Franz Dornhaus,[b] Bernd Wittek,[b] and Stephan Barcikowski*[a]

Commercial diesel oxidation catalysis mainly uses monometallic and bimetallic Pt–Pd-based catalysts, but alloying with different elements has rarely been done systematically under industrial testing conditions. 45 binary alloys made of platinum and a selected 1st and 2nd-row transition metal, platinum group element, or coin metal were synthesized via a scalable laser synthesis method. Then, catalytic performance and durability were evaluated for one diesel oxidation and two ammonia-slip environments. The results show the highest activity when the adsorption enthalpy of molecular oxygen of the alloy was similar to the value of Pt. Furthermore, the durability of the alloy catalysts was found to increase with the melting point of the 2nd element Pt was alloyed with, even at molar fractions. Our results further indicate beneficial synergies beyond the binary systems underlining the possibility of further improvements by considering ternary or multinary alloys, which are accessible via laser synthesis.

1. Introduction

To protect citizens and improve their quality of life, emission restrictions have been imposed and have become stricter over time.[1–4] Apart from other strategies, car manufacturers use catalytic abatement of waste gas to adhere to regulations.[5] For automotive use, active and durable catalysts are needed to cover a large temperature range (RT-~700 °C) and perform in changing engine conditions with varying gas feed compositions.[6] Commercial diesel oxidation catalysts historically used noble metal nanoparticles (Pt and/or Pd).[6,7] With increasing noble metal prices, there is interest in reducing Platinum Group Elements (PGEs) usage. This can be achieved by alloying with different PGEs or cheaper noble or base metals. This strategy also promises to improve catalytic activity. For example, considering Montemore et al.'s work, it can be estimated that alloying of Pt (or Pd) with Ag, Au or Cu might improve CO-Oxidation capabilities.[8] Looking further at the literature, a lot of work has been put into abatement of NO_x[9,10] and soot emissions,[11] but previous studies on alloy catalysts either only comprised a very limited set of alloys[12–16] or were set far apart from automotive applications (e.g., electrochemical studies or fuel cells[17–23]). Also, interesting work has been done in the field of three-way catalysts,[24,25] where multinary alloys have proven their good activity and durability. This points to the need for a systematic study, that focuses on alloyed nanoparticles in diesel oxidation catalysis. Since extrapolating from simple gas mixtures on the lab scale is difficult due to the complexity of exhaust gas catalysis, this study aims to evaluate catalysts close to real application. This is done by screening supported alloy nanoparticle catalysts while preparing them according to industry standards and testing in an industrial setting. Testing will be done in three reaction gas mixtures, one mixture representing a Diesel Oxidation Catalysis (DOC) environment (Feed=CO, C_3H_6, O_2, H_2O, CO_2 in N_2) and two mixtures representing an Ammonia Slip Catalysis (ASC) environment where either NO is present or not (ASC; Feed=NH_3, (NO), O_2, H_2O in N_2). Due to the high noble metal content of commercial catalysts for DOC and ASC, this is where alloying can show the most benefit.

With these environments in mind, the alloys are chosen. The main constituent of the alloys is chosen to be Pt as it is ubiquitous in exhaust gas catalysis, either as a pure metal or as a constituent of alloys.[26–28] Typically alloys from Pt and Pd are used,[28] in part because of the excellent activity and durability, that come from Pd inhibiting the Pt particle growth.[29] For this reason, also Pt–Pd is included in this study. Rh is chosen because it is typical for three-way catalysts[28] and has an activation energy similar to Pt for CO-oxidation,[30] making it a good candidate for high activity. Its high melting point should also aid in making the alloy durable. An alloy of Pt with either Ag or Au is expected to show improved tolerance for water in the wet gas stream.[31–34] Alloying Pt with base metals like Cu, Mn or Fe promises to show good performance in ammonia

[a] S. Siebeneicher, Dr. S. Reichenberger, Prof. S. Barcikowski
Technical Chemistry I and Center for Nanointegration Duisburg-Essen (CENIDE)
University of Duisburg-Essen
Universitaetsstr. 7, Essen 45141 (Germany)
E-mail: stephan.barcikowski@uni-due.de
Homepage: http://www.uni-due.de/barcikowski-group/
[b] Dr. C. Hengst, Dr. F. Dornhaus, B. Wittek
Umicore AG & Co. KG
Rodenbacher Chaussee 4, 63457 Hanau (Germany)

Supporting information for this article is available on the WWW under https://doi.org/10.1002/cctc.202300563

oxidation, as the oxides of the base metals belong to the active catalysts.[35] Especially Fe is expected to favour N_2 in the reaction (reducing NO_x emissions) as its high activation energy for N_2-dissociation[36] prevents N_2, once formed, from splitting and thus removes nitrogen from the oxidation reaction. Pt–Cu is also expected to show good CO-Oxidation properties due to the Sabatier principle.[8] Ruthenium is chosen as a promising candidate for CO-Oxidation and N_2-formation.[36] Generally, its high activity is attributed to a thin oxide layer, which is inactivated through oxide layer growth and water adsorption.[37,38] This layer growth and water adsorption are hypothesized to be inhibited by ennobling Ru with Pt. Ruthenium is also expected to improve durability due to its high melting point, as are alloys from Pt and Nb or Mo. In addition to binary Pt alloys, some other combinations will be studied. Pd–Cu alloys are chosen, as the Sabatier principle suggests an improvement in CO-oxidation.[34] Furthermore, Au–Ir and Au–Rh will be tested. Ir and Rh are expected to be moderated by the addition of gold, allowing for an increase in selectivity by an O-spillover from Rh or Ir to Au.[8,39]

The precise composition of the alloy is determined mainly by the underlying bulk phase diagram of the mixture with a distinction into two main categories. For all alloys that were expected to show a high CO-oxidation activity (Pt + Pd, Ru, Cu, Au, Ag, Rh and Pd + Cu), a large mixing interval is chosen (10–99 at% Pt) with Pt + Rh, Au + Ir and Au + Rh as exceptions. Due to cost reasons the maximum proportion of Rh and Ir was kept at 50 at% for these alloys. For all alloys where an ennobling by platinum was hypothesized and where durability was the main focus, the minimum proportion of Pt was kept to 50 at% (Pt + Nb, Mn, Mo, Fe). Detailed compositions can be found in S1.

In total this screening study comprises 13 alloy systems with overall 45 different compositions. For this highly diverse sample setup, a high-throughput alloy nanoparticle synthesis method is needed. Rather than develop a different wet-chemical synthesis strategy for every alloy system, synthesis by laser ablation in liquids was chosen. In this method, a high-power pulsed laser is employed to synthesise nanoparticles by ablating material immersed in a liquid.[40–45] This process has been shown to yield alloyed nanoparticles in a simple process with pre-alloyed metal sheets, thin metal bilayers or sintered/pressed powder mixtures.[12,17,46–50] Also, this method is able to provide high amounts of nanoparticles in the gram scale,[12,51,52] which is needed to fulfil the demands of industrial catalyst testing. For example, Au-Pt alloy nanoparticle productivity has been demonstrated to robustly yield 8.3 g/h,[52] equivalent to 830 g supported catalyst at 1 wt% loading.

It will be shown that laser ablation synthesis is able to provide sufficient amounts of the 45 different alloy nanoparticle compositional variants, as a basis for a demanding industrial screening study for waste gas abatement of diesel combustion engines.

2. Catalytic Measurements

2.1. Result evaluation

For an evaluation of the catalysts, various single-point analyses of the spectra are used, which will be briefly presented below and in Figure 1.

2.1.1. DOC – CO- and HC-Oxidation

Since the main task of the diesel oxidation catalyst is to completely oxidize carbonaceous exhaust gases, the DOC test first determines the light-up temperature, at which a turnover (of CO or propene) of 50% is achieved (LU_{50}) (cf. Figure 1 a) and b)). The lower the measured temperature, the better the catalyst is to be classified. In some samples, when temperatures rise, CO is formed due to the oxidation of propene. As a result, there is sometimes more than one crossing point at 50%

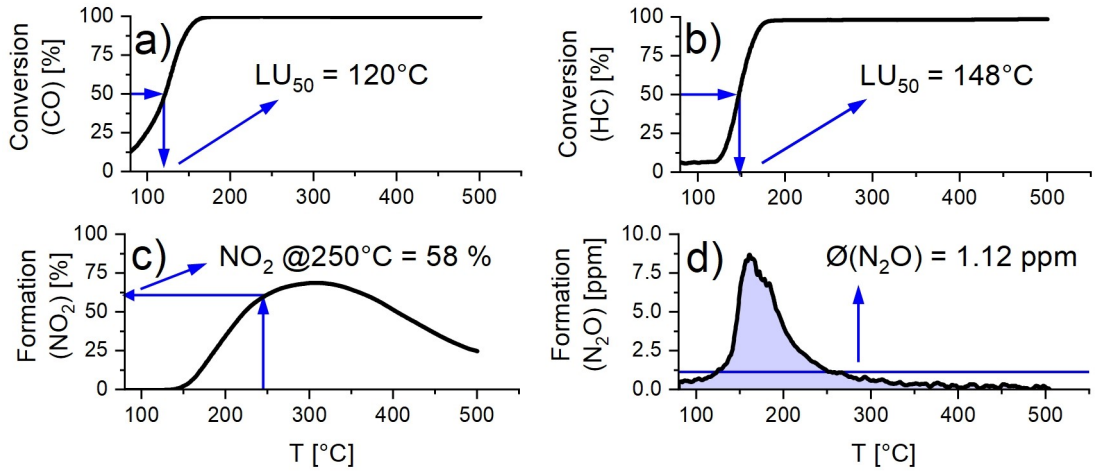

Figure 1. Exemplary results evaluation of a Pt–Pd sample. From the CO and HC conversion curves (a, b) the temperature of 50% conversion (LU_{50}) is read out. The NO_2formation (c) is evaluated at 250 °C and the N_2O formation (d) is evaluated as mean formation.

turnover. For samples where this is the case, the area is indicated by an error bar.

2.1.2. DOC – Nitric-oxide formation

In addition to the oxidation of the carbon-containing exhaust gas components, the diesel oxidation catalyst stage is intended to help provide NO and NO_2 in a 1:1 stoichiometric proportion to enable a fast-SCR reaction downstream in the motor vehicle. Since this cannot be guaranteed over the entire temperature range for thermodynamic reasons, the efficiency of the catalyst is mainly measured by how much NO_2 is formed at 250 °C. At this temperature, the equilibrium is still on the side of NO_2, so it can be expected that a lot is formed in the presence of a good catalyst. The measured NO_2 concentrations are normalized for application to the NO input concentration (eq.(1)). According to this equation, the percentage of NO_2 -content at 250 °C is evaluated (cf. Figure 1 c)).

$$NO_{2,frm} = \frac{NO_2(out)}{NO(in)} \tag{1}$$

As a side reaction, nitrous oxide can still form in the oxidation catalyst. As an undesirable greenhouse gas, the amount is also measured. The catalysts are then compared based on the average amount of N_2O formed. For this purpose, the amount of nitrous oxide formed is first integrated over the entire temperature range and finally weighted with the temperature interval (eq. (2)) (cf. Figure 1 d)).

$$\varnothing(N_2O) = \int_{T_1}^{T_2} c_{N_2O}\,dT \cdot {}^{1}/_{T_2 - T_1} \tag{2}$$

2.1.3. ASC

The ammonia slip catalyst needs to oxidize surplus ammonia to nitrogen and water. This needs to happen as fast as possible, with as few nitrous oxide by-products as possible. The result evaluation, therefore, centres around the ammonia conversion, which is quantified, just as with CO– and HC-conversion, as the LU_{50} temperature (cf. Figure 1 a and b)). In the measurement NO_2, NO, and N_2O are also quantified and evaluated as the mean quantity in the complete temperature interval, as demonstrated for N_2O in the DOC measurement (cf. Figure 1 d)). Additionally, the amount of formed nitrogen can be obtained. This is also evaluated as an average amount.

3. Results and Discussion

3.1. Particle characterisation

The particles were analysed as described in the methods section. To illustrate this process Figure 2 shows an exemplary analysis and summarizes particle size distribution and composition data.

The obtained particle size distributions (cf. Figure 2 (a)) show that all samples synthesized by the nanosecond laser at 532 nm wavelength have the peak particle diameter (distribu-

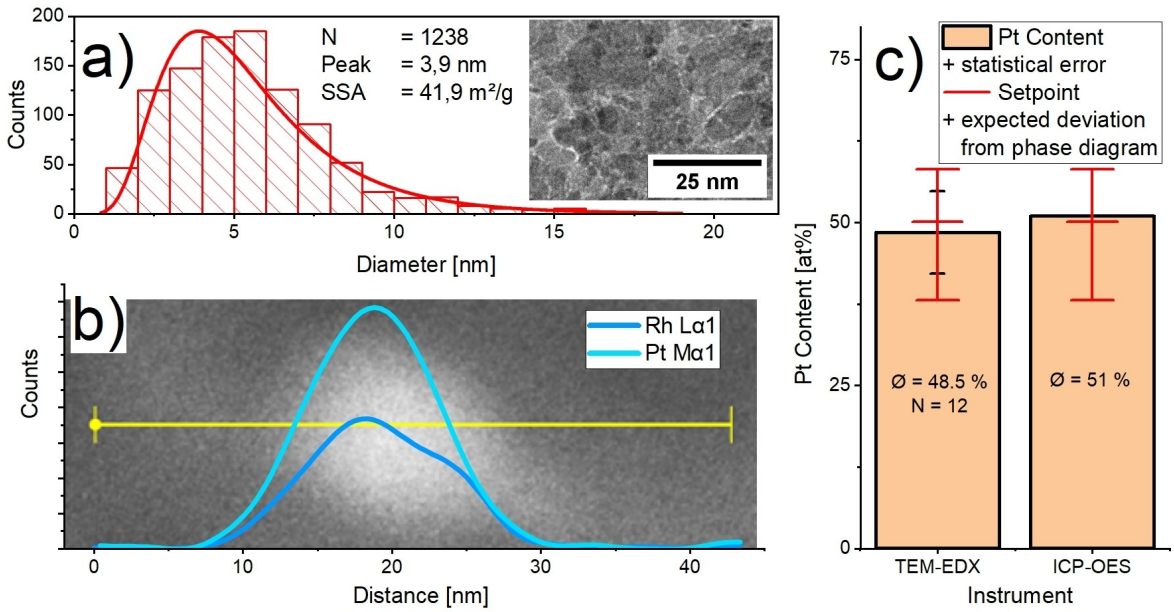

Figure 2. Exemplary sample analysis (on $Pt_{50}Rh_{50}$). Particles were counted via TEM (a), single particle composition was verified on several EDX line and area-scans (b) and bulk composition was checked with ICP-OES (c).

tion modus) between 3.4 and 5 nm and at 1064 nm wavelength at about 2 nm diameter, whereas the samples synthesized by the picosecond laser show a modus between 1.8 and 3.8 nm. Overall, the particle size distributions are comparable, with some outliers towards larger particle sizes. The overview of the particle distribution modi can be found in Figure 3 and exemplary STEM images as well as all detailed particle distribution plots with additional information are given in sections S2.1 and S2.2 of the supplementary information.

The sample composition was checked via digestion in ICP-OES and TEM-EDX (cf. Figure 2 (b, c)) and S2.3 of the SI. While the TEM-EDX line scans mostly confirm the alloying of materials, the overall compositions differ from the results of ICP-OES in many cases. This difference is attributed to the low sample size in TEM-EDX of mainly 12 scans. For this reason, the data from ICP-OES is used for evaluations where sample composition is relevant. Additionally, the catalyst loading could be obtained from ICP-OES measurements. The nominal loading of the samples could be achieved to within 0.1 wt.% except for four samples (Pt–Ru and Au–Ir). The large observed divergence, in this case, may be attributed to sedimentation issues that prevented accurate measurement of the catalyst loading.

3.2. Catalysis

The tested alloys have been chosen, to show two different properties. Firstly, the catalytic activity should be evaluated. Secondly, the metals were chosen to show a trend in catalyst ageing resistance. The catalyst stability was hypothesized to correlate to the melting point of the alloy-metal (i.e., refractory metals are better than non-refractory metals when only catalyst stability is considered).

3.2.1. DOC

Regarding the overall activity, the conventional Pt–Pd system outperforms all other catalyst alloys. This system is closely followed by Pt–Cu, which is especially good in the fresh state and shows remarkably little dependency on the amount of copper added. With alloys comprising 90% copper still performing as well as alloys containing only 10%. As a noble-metal combination, Pt_xRh_{100-x} also shows high activity for $x \geq 90$. Even though rhodium should show good oxidation activity on its own, alloys with high rhodium content drastically decrease in activity. Other noteworthy alloys are Pt–Mo and Pd–Cu. Both mainly because of their durability and for Pd–Cu also the low dependency on mixing ratio. As is to be expected in a screening study, some alloys did not show appreciable activity at all. These alloys mainly contain gold (Au–Ir, Au–Rh, Pt–Au) and the Pt–Ag system also shows signs of inactivity, though not as strong as the aforementioned three systems. The observed trends with the CO oxidation, continue, though less obvious, in the evaluation of HC oxidation and NO_2 and N_2O formation. The respective overviews are plotted in S5.2.

To give a better overview of the CO oxidation trends, the activity of the catalysts is evaluated regarding their affinity towards the reactants. The statistical significance of the obtained results is verified by using an ANOVA test. From DFT calculations it is known that the CO oxidation on metal nanoparticles will show a volcano like dependency when plotted over the CO adsorption enthalpy or the O adsorption enthalpy. The peak activity is calculated and found to occur for materials that have about −1 eV adsorption enthalpy for CO as well as for atomic oxygen.[34]

As obtaining the exact enthalpy for all alloys is beyond the scope of this study, the comparison is done based on alloy metal (i.e., Pt + **X**) and an extensive list of sources can be found in S4.

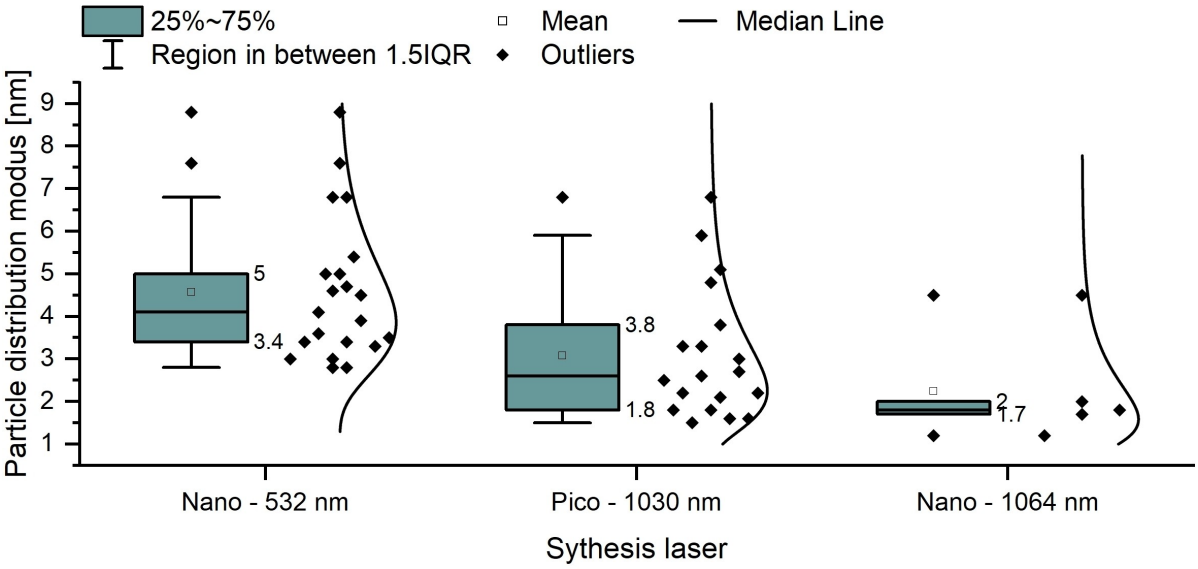

Figure 3. Summary of the particle size distribution modi of all samples sorted by synthesis laser.

Comparing our data to the literature we find that the dependence on CO adsorption enthalpy only shows a slight scaling relation and that also only for aged samples (cf. S5.3.1). This can be explained by observing the environmental conditions. Apart from other constituents, the catalyst is exposed to an abundance of oxygen. On Pt(111) and for $CO:O_2$ ratios $<10\%$ the CO mass transfer to the catalyst is the rate-limiting step.[53] This same rule applies also to platinum group metals.[54] Since the $CO:O_2$ ratio in this study equals 0.4%, the limited CO mass transfer should explain the minor observed scaling relation.

When plotting the activity over the O adsorption enthalpy a volcano-like dependency can be found for the fresh samples (Figure 4). The plot using this adsorption enthalpy as the x-axis has several benefits because the activated oxygen is important for all occurring reactions in the DOC environment (i.e., CO oxidation, propene oxidation and NO oxidation[28,55]). It may therefore show the effect of the combined gas mixture. Therefore, the LU_{50} of the CO oxidation is analysed with respect to the adsorption enthalpy of atomic oxygen.

The observed volcano shape suggests an optimum close to the adsorption enthalpy of platinum This dependence disappears for aged samples that contain metals with an absolute affinity to oxygen higher than platinum. The optimum lies 1 eV lower than what would be expected for the CO oxidation from the literature.[34] As this study is working with a complex gas mixture this behaviour can be explained. Our gas mixture also contains NO, water, and propene. Propene, for example, is known to inhibit oxygen adsorption on Pt[28] and also the other gasses can be expected to compete with oxygen for surface occupancy. Since the availability of activated oxygen is important for all oxidation reactions,[28] the optimum should shift in the direction of higher oxygen affinity as observed here.

The high oxygen affinity could also explain, why the scaling relation for the aged samples and materials of a high affinity disappears. A strong bond to oxygen might lead to surface segregation of the base metal. Subsequent oxidation might then lead to slight deactivation of the catalysts. Counter-intuitively, the opposite may also happen. It was recently shown, that PdO segregates from Pt–Pd particles upon ageing under oxidative conditions. The formed janus-partices then enable a self-healing property, explaining the high durability of this alloy.[56] The role of phase-segregation upon oxidation and the formation of mobile oxide species is difficult to quantify but may play a significant role in the correlation to the heats of adsorption. Further in-depth study of the segregation and reconstruction behaviour and possibly measurement of the adsorption enthalpy of these platinum-nanoalloys and quantification of oxide formation especially after aging will help pinpoint the cause of the observed behaviour.

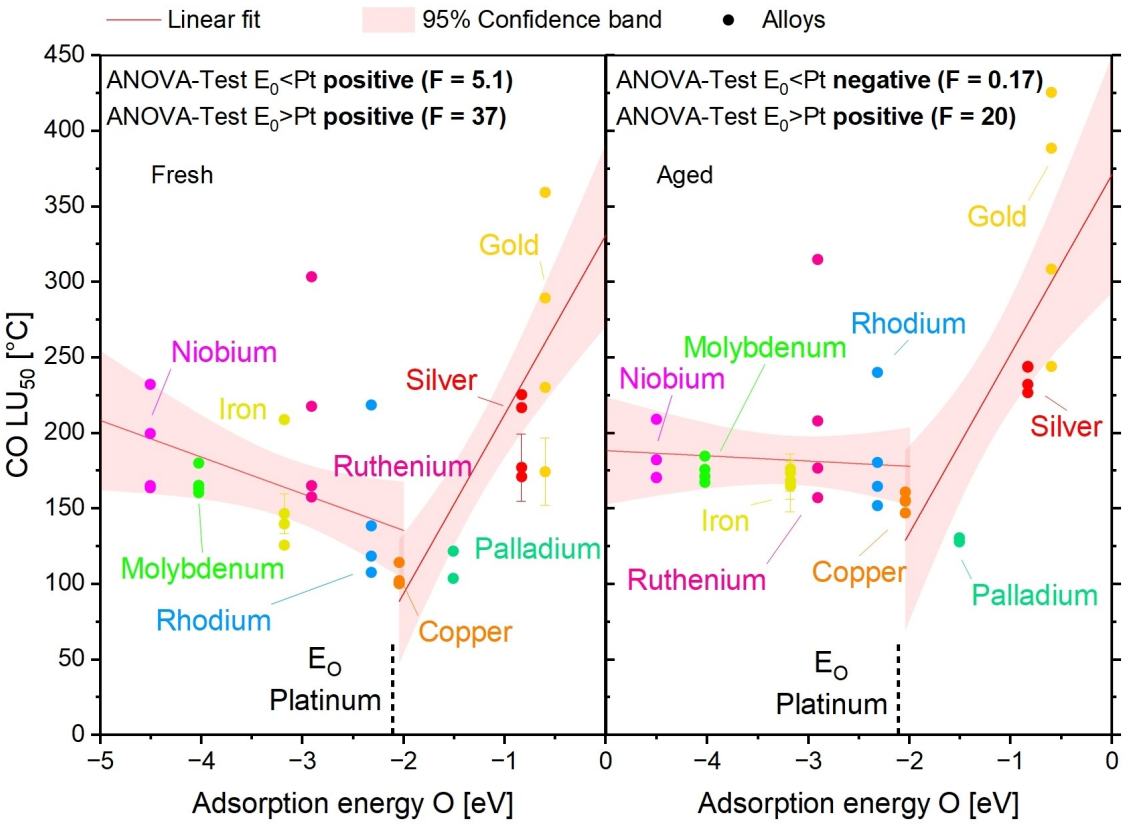

Figure 4. LU_{50} of laser-generated alloy catalyst (Pt + X) in the CO oxidation reaction. In fresh state (a) a volcano-like dependence from the adsorption energy of atomic oxygen is visible. The dependence in the left arc disappears for aged samples (b).

Looking at the other sub-reactions (propene-oxidation, NO_2 and N_2O formation, cf. S5.3), the correlation for metals with a lower affinity towards oxygen than platinum holds strong. Generally, it is obvious in those reactions that silver and gold make the catalyst performance worse. Also, no strong correlation between oxygen affinity and light-up/formation can be found for alloys with a higher oxygen affinity. This suggests, that with those alloys the reaction pathway is not strongly influenced by the adsorption enthalpy of molecular oxygen.

With respect to the durability of the catalysts, another overview plot is generated. In this, the difference in light-up temperature between the fresh and the aged samples (650 °C) is plotted. When alloying platinum with different metals a change in ageing behaviour is suspected. Alloying with metals of lower melting point lowers the overall alloy melting point and should allow for less inhibited material movement on the support surface during catalysis. If platinum is alloyed with metals of higher melting point this behaviour is expected to inhibit the material movement and thus the ageing due to particle growth and subsequent loss of active surface area. When plotting the difference in LU_{50} in the CO-Oxidation reaction in dependence on the melting point of the alloy a clear trend is visible (cf. Figure 5). Figure 5 a) shows that the correlation is strongest when the melting point of the metal (Pt +**X**) with which the alloy is formed is used as the x-axis. If the melting point of the alloy is taken from the bulk phase diagram (Figure 5 b)), the correlation is smaller. This is to be expected, as many alloys in this study contain a high amount of platinum and thus the alloy melting point is situated close to that of platinum. As is in line with the hypothesis, alloys of low melting point (e.g., containing gold, silver or copper) belong to the catalysts that age the strongest, while catalysts with alloy metals of high melting point (e.g., niobium, molybdenum or ruthenium) show the highest durability. The analysis was repeated for the reactions of propene-oxidation and nitric-oxide formations and the same correlations were found. A correlation towards the alloy metal melting point can be found for all reactions except N_2O-Formation (cf. S5.4). Variations in the durability within the alloy compositions might also correlate to oxidation and the formation of volatile oxides that increase the durability of some combinations (like for Pt–Pd reported by Porter et al.[56]) or decrease the durability for others, where no synergistic behaviour exists.

In summary, it may be concluded that when designing a catalyst for durability, the type of element used for alloying can be more important than the amount used. Even small amounts of a high melting point metal can improve resistance against aging.

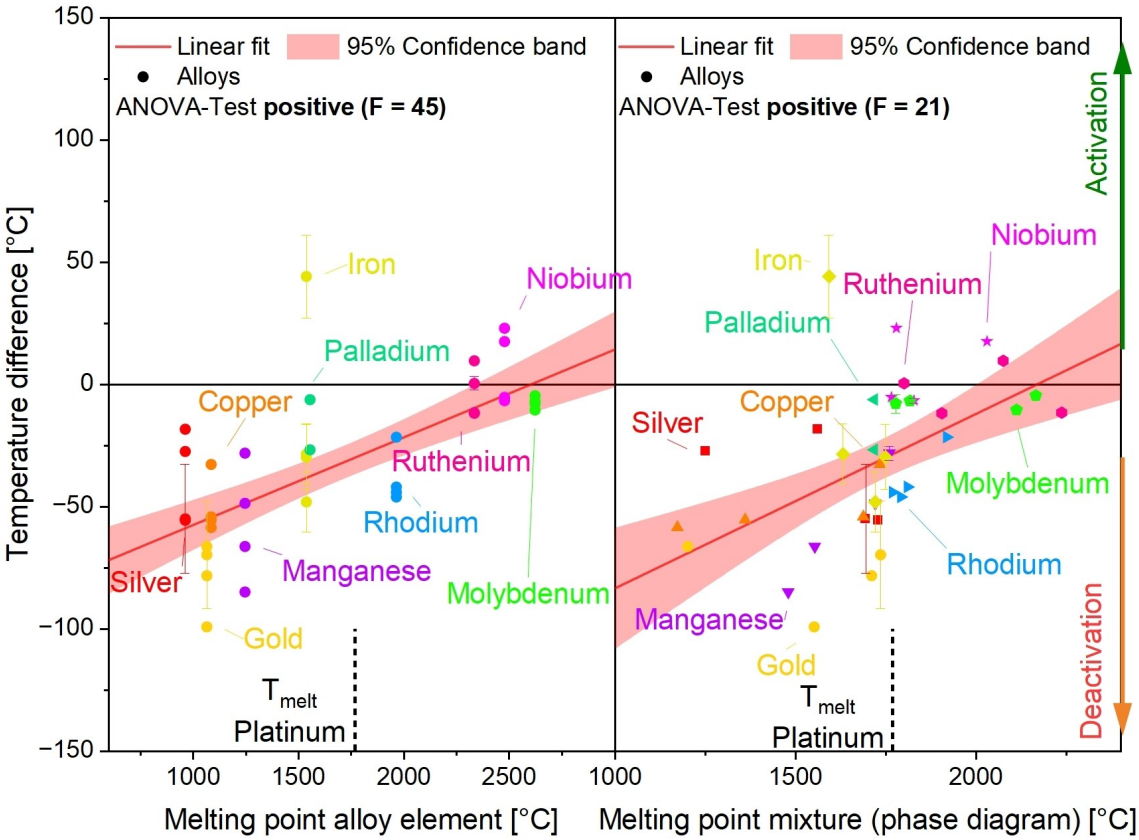

Figure 5. Difference between LU_{50} (fresh minus aged) of laser-generated alloy catalyst in the CO oxidation reaction. Comparison to melting point of alloy element (a) and to melting point of the mixture taken from the underlying bulk phase diagrams (b).

3.2.2. ASC

In the ammonia oxidation catalysis, well-performing alloy catalysts are mixtures of Pt with Pd, Nb, Ru, Fe, and Mn containing a medium to high proportion of Pt. Pt–Cu and Pt–Mo show good activity over the whole tested mixing range. Those two systems also show exceptionally good ageing behaviour. Well-performing systems show NH_3-LU_{50} temperatures of ca. 150–180 °C (with NO present) and 190–205 °C (without NO present). The alloys Pt–Ru, Pt–Rh, and Pt–Ag containing a low amount of platinum are less active, while the systems Au–Rh, Au–Ir, Au–Pt and Pd–Cu are inactive and durable. (Cf. S6.2 and S6.5).

In order to extract patterns, it seems worthwhile to also plot the ASC data depending on an adsorption enthalpy. From literature, it is known that the oxidation of ammonia begins with the adsorption of ammonia and oxygen on acidic and redox sites respectively. This is followed by the abstraction of hydrogen by active O species or OH groups formed either by O_2 activation on redox sites or O vacancies on metal oxides. Generally, the reaction pathway is divided into three distinct mechanisms, the imide-, hydrazine- and i-SCR-mechanism.[57] From these three, the imide-mechanism is the most prevalent for Pt nanoparticles supported on alumina and needs the O_2 activation as an important step for NH_3 dissociation.[58] It is however notable, that on one catalyst surface, more than one mechanism can occur. Which reaction pathway takes place is dependent, for example, on catalyst support material and reaction temperature.[57]

Considering Pt(100), the rate of ammonia oxidation is mainly dependent on NO desorption.[59] As this study focuses on alloys comprising mainly Pt alloyed with different metals, this would make it prudent, to plot the obtained data over the NO adsorption enthalpy of the respective metal.

When evaluating the LU_{50} of the NH_3 oxidation with and without NO present in the feed gas stream, it quickly becomes obvious that no clear correlation towards the NO adsorption enthalpy can be drawn (cf. S6). Just as with the DOC reaction, the common rate-limiting step was not obvious in our study. The complex gas mixtures and the industrial test setting apparently change the common mode of operation, underlining the importance of testing the catalysts in these real-world environments.

Our test regime showed that in the case of ammonia oxidation also the adsorption enthalpy of oxygen plays an important role. Especially, when considering side reactions towards nitric oxides, two major patterns emerge. All systems produce nitric oxides in varying amounts, but either the reaction towards NO or towards NO_2 and N_2 is favoured.

This correlation can be seen best in Figure 6. The negative ANOVA test of the linear fit towards oxygen adsorptions shows that there are two big groups. Pt-alloys with Mo, Ru, Nb, Fe, and Mn form little NO when compared to Cu, Rh, and Ag with the Pt–Pd alloy being an exception. The positive correlation in the right arch of the aged samples is mainly attributable to the inactiveness of the Pt–Au alloys and disappears when the worst catalysts are excluded. This leads to the hypothesis that when the adsorption enthalpy for molecular oxygen is equal to or higher than that of rhodium, NO is a favoured reaction product when considering the alloys with Pt.

This analysis has been performed for all reaction pathways, similar to the DOC section. All data is plotted in S6.3 and S6.6. The grouping shows up whether NO is present in the feed gas or not and is also visible when considering the other reaction products like NO_2, N_2O, and N, with N_2O being the least obvious due to a large signal-to-noise ratio in the data. First, this allows the conclusion that the tested catalysts are all robust towards the NO concentration and can be expected to catalyse the ammonia oxidation selectively and independently from NO concentration.

Looking at the literature the grouping behaviour may be loosely attributed to the underlying reaction mechanisms. From Lan et al. we can conclude that the hydrazine mechanism is not relevant to our experiments since it requires low oxygen partial pressures that don't reflect our experiment.[57] The remaining three mechanisms are the imide-, i-SCR-, and N_2-mechanism.

The i-SCR and N_2-mechanism explain the observed intermediates for reactions over silver-based catalysts, so for catalysts that have a low adsorption enthalpy for oxygen. Since in the N_2 mechanism no NO is detected, but our catalysts produce it, this mechanism may also be excluded. The observed by-products of the i-SCR mechanism are the same as for the imide mechanism: N_2, NO, and N_2O. Considering that NO is mainly found as an intermediate in the imide mechanism, catalysts with a high affinity for oxygen and thus high surface coverage may have a high possibility to over-oxidise the NO to NO_2. Catalysts with a low affinity toward oxygen would have a lower probability for this and thus mainly yield NO. Summarizing, this means that catalysts with a low oxygen affinity will favour NO as a by-product, while catalysts with a higher affinity will favour NO_2. This fits the picture we observe, where the border appears to be the adsorption enthalpy of rhodium (cf. eq. (3)):

$$\begin{aligned} &E_{O-Ads} \lesssim E_{O-Ads}(Rh) \rightarrow N_2, NO_2 \\ &E_{O-Ads} \geq E_{O-Ads}(Rh) \rightarrow NO, (N_2O) \end{aligned} \tag{3}$$

It is therefore possible that a platinum alloy may exhibit two different ammonia oxidation mechanisms dependent on the alloy material.

Finally, the durability of the alloy catalysts was also evaluated. While the correlation between ageing and melting point is higher when only the melting point of the alloy element is considered, no significant correlation could be found for either the melting point of the alloy element or of the alloy (cf. also to S6.4 and S6.7). In contrast to the DOC measurement, the ASC ageing of the catalysts does not seem to correlate strongly to the alloy element or composition. This may be due to the influence of particle oxidation and the formation of volatile oxide species, which may, for the ASC environment, equalize the durability shown by the catalysts.

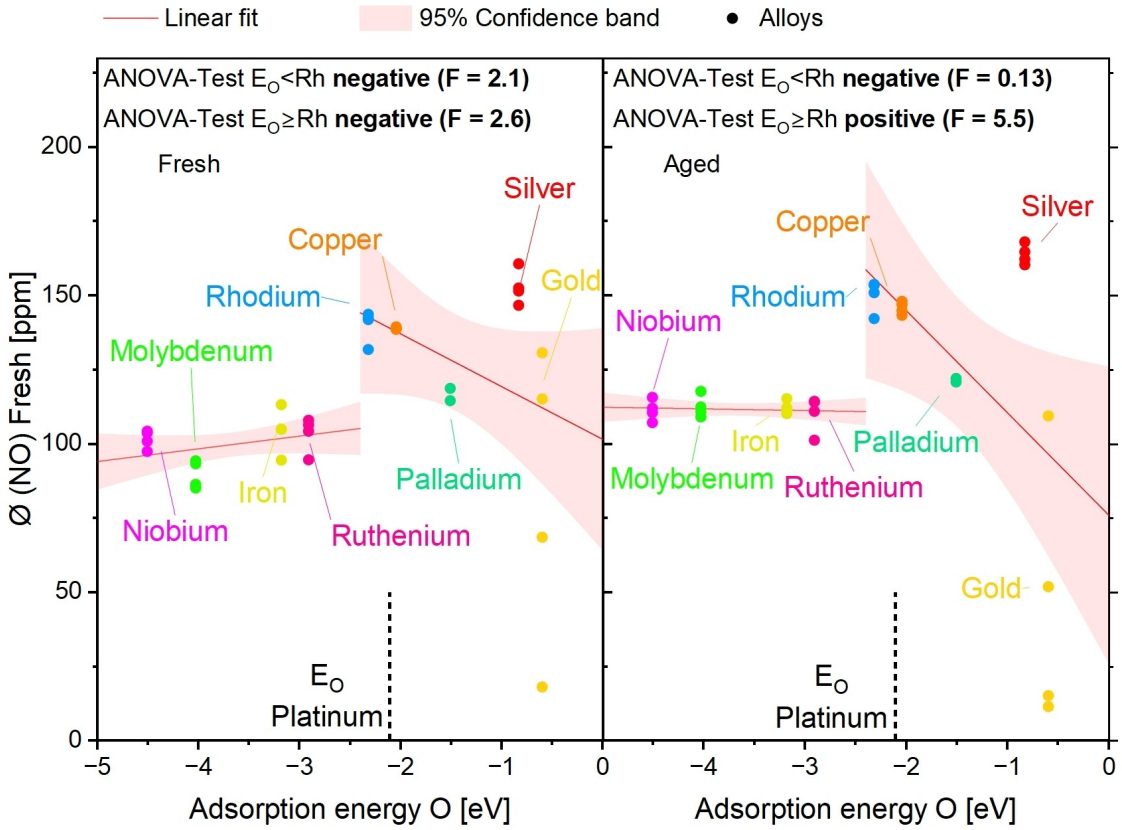

Figure 6. Average NO concentration of laser-generated catalyst in the ammonia oxidation reaction. In fresh (a) and aged state (b) a volcano-like dependence from the adsorption energy of atomic oxygen is visible for $E_O < E_{O,Rh}$.

4. Conclusions

This study aims to broaden the composition-related knowledge regarding waste gas abatement by synthesizing 45 binary alloys of platinum with other metals. The screening is enabled by a scalable laser synthesis method, since today, fully enclosed, automated benchtop laser synthesis machines are available.[60–62] The catalysts were tested in an industrial environment with one DOC and two ASC gas mixtures, and two aging regimes. This allowed for identification of composition-activity and composition-durability correlations.

When comparing the tested material systems individually our results show that alloys of Pt with Cu, Mo, or Pd show particularly promising activity correlations in DOC. Despite them being not the most active (especially in aged states), the alloy systems Pt–Cu and Pt–Mo are also very notable, as they show a hardly any dependence between activity and alloy composition. They share this behaviour with Pd–Cu.

In the case of ASC, the most favourable compositions are alloys of Pt with Nb, Ru, Fe, or Mn. All these compositions show a high selectivity for N_2 and have high activity. One very promising alloy constituent was shown to be Cu. This metal showed a high activity whereby the activity of Pt–Cu exceeds that of Pd–Cu. Furthermore, alloys from Pd or Pt with Cu show particularly low dependence of the activity and selectivity on composition, making copper a very cost-effective catalyst additive. Pt-Mn and Pt–Fe alloys showed good activities in the DOC- and the ASC environment with Fe also exhibiting a high selectivity for N_2. Alloys of Pt and Ru exhibited a high selectivity for N_2, although high amounts of Pt are required to also provide a good activity (DOC: >80 at%; ASC: >50 at%). The ennobling of Ru by Pt seems to work over the whole tested mixing range, with the Pt–Ru-catalysts exhibiting very good durability in DOC as well as ASC.

Apart from the individual comparison, the data was used to develop composition-activity- and composition-durability-correlations for DOC and ASC. When correlating the catalytic activity with the adsorption enthalpy of molecular oxygen, a volcano trend appears for DOC. Compared to DFT studies, the observed oxygen adsorption enthalpy at maximum activity is shifted by 1 eV towards stronger oxygen binding. This behaviour could be attributed to the more complex gas mixtures present in this study. For the aged alloy catalysts, there is no statistically significant correlation between activity and oxygen adsorption enthalpy when $|E_{O,ads}| > |E_{O,ads}(Pt)|$. This observation may be linked to element segregation and/or passivation due to oxidation of the catalyst surface, but formation of volatile oxides may also play a role.

Regarding the durability in the DOC environment, the catalysts show a statistically significant positive correlation

between the change in activity and melting temperature for both the alloy and the element platinum was mixed with. Hereby, the highest durability is observed for elements and alloys with the highest melting point. The data allowed for the conclusion, that the type of element used for alloying can be more important than the amount. For ASC reactions, no correlation was found between ammonia oxidation and NO adsorption enthalpy, contradicting literature, and highlighting the importance of testing catalysts in environments similar to waste gas abatement. In turn, a strong link was found between oxygen adsorption enthalpy and reaction products. Alloy catalysts with oxygen adsorption enthalpy below Rhodium favoured N_2 and NO_2, while Pt alloys with lower oxygen adsorption enthalpy favoured NO and N_2O. This was attributed to the imide-mechanism and i-SCR-mechanism. Pt–Pd was the only exception, favouring N_2 and NO_2.

In summary, this study shows that the industrial testing conditions are important to the catalyst screening, as some of the observed performance trends were not expected from literature (especially for ASC). It was shown that alloy catalysts have a high potential to reduce the need for noble metals (i.e., Pd–Cu, Pt–Cu) but the durability needs to be further optimized. In this regard, improved durability was observed when alloying platinum with refractory metals where particularly low contents were already beneficial. With this in mind, ternary alloys (e.g., Pt–Cu–Mo or Pt–Cu–Nb) appear as a sensible next step for further studies. With laser synthesis being a mature and well-established synthesis method, multinary alloy catalysts can be obtained similar to this study.[50,63,64] Multinary alloys consisting of Pt and (a combination of) Cu, Mo, Nb, or Mn to tune activity and durability appear possible. Such complex high-entropy alloys have found recent attention in three-way catalysis[24,25] ($\lambda = 1$) and multinary alloy catalysts designed with the knowledge from this study may be interesting to apply for $\lambda > 1$ environments.

5. Materials and Methods

5.1. Colloid synthesis

The tested catalysts were synthesised from independently produced mixed-metal targets. These targets were pressed from base metal powder and subsequently sintered. Additional detail on the target production process can be found in the supplementary information (cf. S1.1).

The mixed-metal targets were used to synthesise colloids via pulsed laser ablation. Noble metal nanoparticles were synthesised with water as the medium, and base metal combinations were ablated using propylene carbonate as the medium. The latter was selected as it is a technical liquid that has a very low vapour pressure allowing safe handling and is thermostable which would allow recycling via vapour condensation. The ablation was done using two different laser systems. Generally, a nanosecond pulsed laser system (Edgewave IS160-1-T) with 532 nm wavelength and 5 kHz repetition frequency and 50 W of power was used to ablate the water-based samples (Max. ablation rate: ~488 mg/h, i.e., ~11 mg/Wh). Ablation in water was assisted with adding micromolar amounts of additives (KOH, Sodium citrate or Ammonium citrate). The

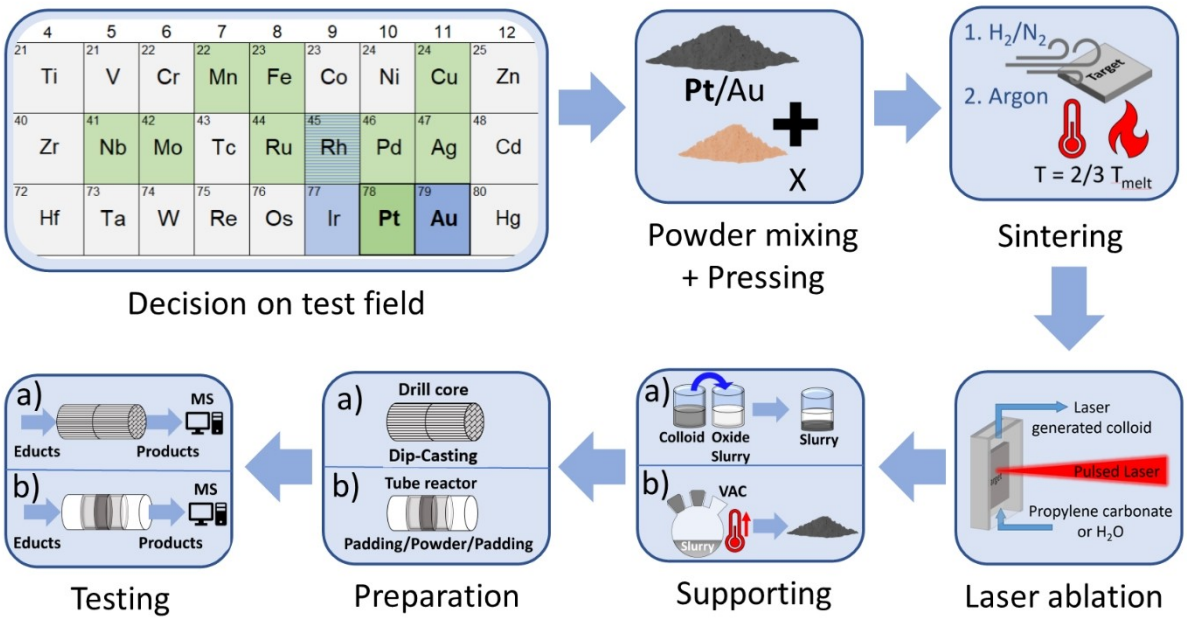

Figure 7. Experimental design of this study. After the decision on the systems (Pt + X, green; Au + X, blue), the elemental powders were mixed, pressed, and sintered under appropriate atmosphere to obtain alloyed targets. Targets were ablated in a liquid with a pulsed laser. The colloids were supported on alumina powder and prepared for catalysis measurement. The exact procedure differs for samples produced in water (a) and propylene carbonate (b). Performance testing was done with automotive gas mixture and test equipment.

organic solvent-based samples were synthesised using a picosecond pulsed laser system (Amphos Poly 500). This system was used at 1030 nm wavelength, 5 MHz repetition frequency and 467 W of laser power before duty cycling (Max. ablation rate: ~1100 mg/h, i.e., ~14 mg/Wh). More details are described in the supplementary information, section S1.2.

5.2. Colloid immobilization

After obtaining the colloids the nanoparticles needed to be immobilized on a support material. For this purpose, pure aluminium oxide was chosen, so that no promoters would interfere with the catalytic reaction. The aluminium oxide powder was either wet-milled in an acid environment (pH 4, for water-based samples) or jet-milled to attain a highly disperse powder.

The water-based alumina was pH-adjusted and mixed with the dispersed colloids by pumping the colloid slowly into the alumina slurry and a pH-driven adsorption strategy was employed to adsorb the nanoparticles on the support surface. Sedimentation was then used to concentrate the samples to approx. 150 g/l for use in dip casting.

For the propylene carbonate-based samples a pH-driven adsorption strategy could not be used. Therefore, the colloids were mixed with the support powder, which was dispersed by strong ultrasonication. While stirring vigorously under a vacuum, the propylene carbonate was gently distilled off. This causes diffusion-driven supporting, resulting in dry catalyst powder (Figure 7). A more in-depth description of the supporting routes can be found in the supplementary information (cf. S1.3).

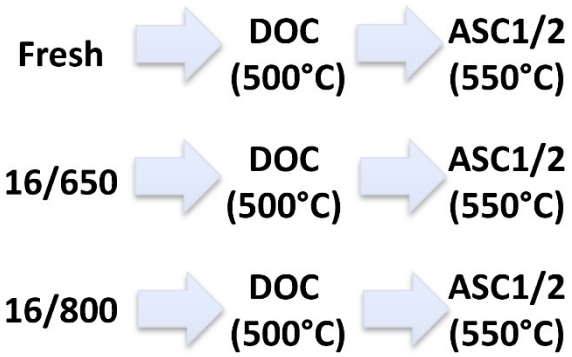

Figure 8. Catalyst testing procedure.

5.3. Particle analysis

Prior to catalytic testing, all samples were characterized in detail for particle size (STEM, JEOL JEM-2200 FS), composition (EDX (JEOL JEM-2200 FS), ICP-OES (Varian 725ES, microwave pressure digestion)) and loading (ICP-OES). Information on the composition was used to correct the measured data for deviations from the nominal composition values.

Particle size measurements were carried out using STEM images of diluted and dried washcoat. After being supported, further growth of the particles is inhibited, while the colloids might undergo ripening. As there will be a time delay between supporting and measuring the colloids, measuring the particle distribution via TEM should represent the samples best. With little exception, for all samples, at least 500 particles were manually counted, and the distribution was fitted. From this, the specific surface area and peak particle diameter were calculated.

Alloying of the particles was verified using the same device, measuring EDX line scans and EDX mappings. For most samples, about 12 EDX measurements were performed. Compositions found this way don't always match the compositions found by digesting the samples and measuring ICP-OES, but generally show homogeneous alloying. The discrepancy in the composition is attributed to the small sample size and high difficulty in analysing sub-10-nm particles. Data presented in this study, which contains the composition data, always shows the data obtained by ICP-OES. Both size- and elemental composition data can be found in the supplementary information S2.

5.4. Preparation of catalytic measurements

All water-based samples weighed in at 150 g of washcoat each. Due to limitations in the solvent process, samples produced this way were limited in mass and comprised 10 g. This in turn means that two different approaches need to be utilized to study the catalytic properties. All water-based samples were processed as slurry, that was dip-coated on cordierite drill cores. These coated drill cores were dried and calcined. After this

Table 1. Measured gases and evaluated values for the performed analyses.

DOC			ASC		
Gas	Evaluated		Gas	Evaluated	
CO	Conversion	$X_{CO} = 1 - \frac{CO(out)}{CO(in)}$	NH_3	Conversion + Concentration	$X_{NH_3} = 1 - \frac{NH_3(out)}{NH_3(in)}$
C_3H_6	Conversion	$X_{HC} = 1 - \frac{C_3H_6(out)}{C_3H_6(in)}$	NO	Evaluated as concentration	
NO_2	Formation	$NO_{2,frm} = \frac{NO_2(out)}{NO(in)}$	NO_2	Evaluated as concentration	
N_2O	Evaluated as concentration		N_2O	Evaluated as concentration	

preparation, all samples were catalytically tested in one DOC and two ASC-gas mixtures. Testing was carried out with fresh samples and samples that were aged to two different extents. All catalysts were subjected to ageing by exposing the samples to a water-saturated atmosphere (10 vol% H_2O, 10 vol% O_2 in N_2 balance) for 16 hours at 650 °C (16/650). A smaller set of catalysts was also subjected to ageing in the same atmosphere at 800 °C (16/800). Since the observed activity trends are similar for both ageing protocols and most catalysts, all data presented the discussion relates to the more complete set of aged samples at 650 °C. In addition, all catalytic data can be found in the supplementary information.

All solvent-based samples underwent the same thermal cycling as the water-based samples. After being thoroughly mixed they were pressed into a pill, which was subsequently broken and sieved to obtain catalyst particles of about 500 μm diameter. 150 mg of these particles were then packed into a tube furnace where they were aged and tested with an identical procedure as the water-based samples.

5.5. Catalyst testing procedures

The gas mixtures were chosen according to automotive industry standards. The DOC-gas mixture was comprised of CO, C_3H_6, NO, O_2, and H_2O in an N_2 carrier gas flow. One ASC gas mixture was comprised of NH_3, O_2 and H_2O in an N_2 carrier gas flow, while a second mixture additionally contained NO. The detailed composition can be found in S5.1 and S6.1.

After the preparation of the samples, catalytic testing was carried out according to the schematic illustrated in Figure 8. All samples were first characterized in the DOC gas stream and after that, the ASC testing ensued, first without NO and then with NO present in the gas stream. A slight deviation from this plan was made for the Pt-Pd and Pt–Cu systems (for details confer S1.4.).

The acquisition of measurement data was carried out using an FTIR (FT-IR MKS Multigas 2030). Zero-point calibration was carried out once a day. Before the measurements, the concentrations of the gas mixtures are verified using the same system by a bypass flow setup. The analysed gases are summarized in Table 1. Information on the concentration of the product gases is then used to calculate the extent of conversion or formation.

As the water-based samples were tested as cordierite cores and the solvent-based samples as powder, a crossover measurement was carried out. Select water-based samples were characterized in the powder reactor after being prepared like the solvent-based samples. The results showed, that while the absolute values sometimes differ from the measurement of the cordierite cores, the order in which they are classified, does not (for details confer S3). Therefore, the measurements are comparable between water-based and solvent-based samples.

Supporting Information

The authors have cited additional references within the Supporting Information.[34,40,70–79,47,80–87,50,51,65–69]

Acknowledgements

We gratefully acknowledge the financial support of this research from Umicore AG & CO. KG. Furthermore, the authors appreciate the support of Dr. Markus Heidelmann (Interdisciplinary Center for Analytics on the Nanoscale – ICAN, University of Duisburg-Essen) and Jurij Jakobi (Technical Chemistry I – University of Duisburg-Essen) for their HR-TEM and EDX measurements. Open Access funding enabled and organized by Projekt DEAL. The University of Duisburg-Essen is acknowledged for funding of open access fees.

Conflict of Interests

The study has been financially supported by the company Umicore.

Data Availability Statement

The data that support the findings of this study are available from the corresponding author upon reasonable request.

Keywords: waste gas abatement · supported catalysts · Heterogeneous Catalysis · alloys · alloy nanoparticles

[1] Umweltbundesamt, "Grenzwerte für Schadstoffemissionen von PKW," can be found under http://www.umweltbundesamt.de/sites/default/files/medien/376/bilder/dateien/tabelle_grenzwerte_fuer_schadstoffe-missionen_von_pkw.pdf, **2018**, (accessed March 21, 2023).
[2] Environmental Protection Agency, **2018**, *79*, 23414–23886.
[3] P. Granger, *Catal. Sci. Technol.* **2017**, *7*, 5195–5211, 10.1039/C7CY00983F.
[4] I. Lebrusán, J. Toutouh, *Air Qual. Atmos. Heal.* **2021**, *14*, 333–342, 10.1007/s11869-020-00938-z.
[5] C. Descorme, P. Gallezot, C. Geantet, C. George, *ChemCatChem* **2012**, *4*, 1897–1906, 10.1002/cctc.201200483.
[6] G. Koltsakis, *Prog. Energy Combust. Sci.* **1997**, *23*, 1–39, 10.1016/S0360-1285(97)00003-8.
[7] D. Bosteels, R. A. Searles, *Platinum Met. Rev.* **2002**, *46*, 27–36.
[8] M. M. Montemore, M. A. van Spronsen, R. J. Madix, C. M. Friend, *Chem. Rev.* **2018**, *118*, 2816–2862, 10.1021/acs.chemrev.7b00217.
[9] R. Zhang, N. Liu, Z. Luo, W. Yang, X. Liang, R. Xu, B. Chen, D. Duprez, S. Royer, *ChemCatChem* **2014**, *6*, 2263–2269, 10.1002/cctc.201402172.
[10] A. H. Clark, R. J. G. Nuguid, P. Steiger, A. Marberger, A. W. Petrov, D. Ferri, M. Nachtegaal, O. Kröcher, *ChemCatChem* **2020**, *12*, 1429–1435, 10.1002/cctc.201901916.
[11] A. Rinkenburger, T. Toriyama, K. Yasuda, R. Niessner, *ChemCatChem* **2017**, *9*, 3513–3525, 10.1002/cctc.201700338.
[12] S. Dittrich, S. Kohsakowski, B. Wittek, C. Hengst, B. Gökce, S. Barcikowski, S. Reichenberger, *Nanomaterials* **2020**, *10*, 1582, 10.3390/nano10081582.
[13] Y. Wei, Z. Zhao, B. Jin, X. Yu, J. Jiao, K. Li, J. Liu, *Catal. Today* **2015**, *251*, 103–113, 10.1016/j.cattod.2014.08.034.
[14] M.-J. Kim, H. J. Kim, S.-J. Lee, I.-S. Ryu, H. C. Yoon, K. B. Lee, S. G. Jeon, *Catal. Commun.* **2019**, *130*, 105764, 10.1016/j.catcom.2019.105764.

[15] F. Dong, K. Yamazaki, *Catal. Today* **2021**, *376*, 47–54, 10.1016/j.cattod.2020.08.019.
[16] S. Swislocki, K. Stöwe, W. F. Maier, *ChemCatChem* **2015**, *7*, 261–270, 10.1002/cctc.201402769.
[17] G. Marzun, A. Levish, V. Mackert, T. Kallio, S. Barcikowski, P. Wagener, *J. Colloid Interface Sci.* **2017**, *489*, 57–67, 10.1016/j.jcis.2016.09.014.
[18] V. Stamenković, T. J. Schmidt, P. N. Ross, N. M. Marković, *J. Phys. Chem. B* **2002**, *106*, 11970–11979, 10.1021/jp021182h.
[19] J. Greeley, I. E. L. Stephens, A. S. Bondarenko, T. P. Johansson, H. A. Hansen, T. F. Jaramillo, J. Rossmeisl, I. Chorkendorff, J. K. Nørskov, *Nat. Chem.* **2009**, *1*, 552–556, 10.1038/nchem.367.
[20] Y. Bing, H. Liu, L. Zhang, D. Ghosh, J. Zhang, *Chem. Soc. Rev.* **2010**, *39*, 2184, 10.1039/b912552c.
[21] H. A. Gasteiger, S. S. Kocha, B. Sompalli, F. T. Wagner, *Appl. Catal. B* **2005**, *56*, 9–35, 10.1016/j.apcatb.2004.06.021.
[22] A. K. Singh, Q. Xu, *ChemCatChem* **2013**, *5*, 652–676, 10.1002/cctc.201200591.
[23] B. J. Plowman, B. Sidhureddy, S. V. Sokolov, N. P. Young, A. Chen, R. G. Compton, *ChemElectroChem* **2016**, *3*, 1039–1043, 10.1002/celc.201600212.
[24] T. Hirakawa, Y. Shimokawa, W. Tokuzumi, T. Sato, M. Tsushida, H. Yoshida, J. Ohyama, M. Machida, *ACS Appl. Nano Mater.* **2020**, *3*, 9097–9107, 10.1021/acsanm.0c01769.
[25] K. Kusada, D. Wu, Y. Nanba, M. Koyama, T. Yamamoto, X. Q. Tran, T. Toriyama, S. Matsumura, A. Ito, K. Sato, K. Nagaoka, O. Seo, C. Song, Y. Chen, N. Palina, L. S. R. Kumara, S. Hiroi, O. Sakata, S. Kawaguchi, Y. Kubota, H. Kitagawa, *Adv. Mater.* **2021**, *33*, 2005206, 10.1002/adma.202005206.
[26] A. Gremminger, J. Pihl, M. Casapu, J.-D. Grunwaldt, T. J. Toops, O. Deutschmann, *Appl. Catal. B* **2020**, *265*, 118571, 10.1016/j.apcatb.2019.118571.
[27] D. Kunwar, S. Zhou, A. DeLaRiva, E. J. Peterson, H. Xiong, X. I. Pereira-Hernández, S. C. Purdy, R. ter Veen, H. H. Brongersma, J. T. Miller, H. Hashiguchi, L. Kovarik, S. Lin, H. Guo, Y. Wang, A. K. Datye, *ACS Catal.* **2019**, *9*, 3978–3990, 10.1021/acscatal.8b04885.
[28] A. Russell, W. S. Epling, *Catal. Rev.* **2011**, *53*, 337–423, 10.1080/01614940.2011.596429.
[29] C. Carrillo, T. R. Johns, H. Xiong, A. DeLaRiva, S. R. Challa, R. S. Goeke, K. Artyushkova, W. Li, C. H. Kim, A. K. Datye, *J. Phys. Chem. Lett.* **2014**, *5*, 2089–2093, 10.1021/jz5009483.
[30] Z. P. Liu, P. Hu, *J. Chem. Phys.* **2001**, *115*, 4977–4980, 10.1063/1.1403006.
[31] W. Huang, G. Sun, T. Cao, *Chem. Soc. Rev.* **2017**, *46*, 1977–2000, 10.1039/C6CS00828C.
[32] F. B. de Mongeot, U. Valbusa, M. Rocca, *Surf. Sci.* **1995**, *339*, 291–296, 10.1016/0039-6028&DELETE;TRzwj;(95)00594-3.
[33] A. . Carley, P. . Davies, M. . Roberts, K. . Thomas, *Surf. Sci.* **1990**, *238*, L467–L472, 10.1016/0039-6028&DELETE;TRzwj;(90)&DELETE;TRzwj;90056-E.
[34] T. Jiang, D. J. Mowbray, S. Dobrin, H. Falsig, B. Hvolbæk, T. Bligaard, J. K. Nørskov, *J. Phys. Chem. C* **2009**, *113*, 10548–10553, 10.1021/jp811185g.
[35] V. Sadykov, L. Isupova, I. Zolotarskii, L. Bobrova, A. Noskov, V. Parmon, E. Brushtein, T. Telyatnikova, V. Chernyshev, V. Lunin, *Appl. Catal. A* **2000**, *204*, 59–87, 10.1016/S0926-860X&DELETE;TRzwj;(00)00506-8.
[36] S. Dahl, A. Logadottir, C. J. H. Jacobsen, J. K. Nørskov, *Appl. Catal. A* **2001**, *222*, 19–29, 10.1016/S0926-860X(01)00826-2.
[37] H. Over, *Chem. Rev.* **2012**, *112*, 3356–3426, 10.1021/cr200247n.
[38] X. Cui, J. Zhou, Z. Ye, H. Chen, L. Li, M. Ruan, J. Shi, *J. Catal.* **2010**, *270*, 310–317, 10.1016/j.jcat.2010.01.005.
[39] T. Zhang, S. M. Driver, S. J. Pratt, D. A. King, *Surf. Sci.* **2013**, *615*, 1–5, 10.1016/j.susc.2013.04.004.
[40] D. Zhang, B. Gökce, S. Barcikowski, *Chem. Rev.* **2017**, *117*, 3990–4103, 10.1021/acs.chemrev.6b00468.
[41] A. FOJTIK, A. HENGLEIN, *Ber. Bunsen-Ges.* **1993**, *97*, 252–254.
[42] V. Amendola, M. Meneghetti, *Phys. Chem. Chem. Phys.* **2009**, *11*, 3805, 10.1039/b900654k.
[43] V. Amendola, R. Pilot, M. Frasconi, O. M. Maragò, M. A. Iatì, *J. Phys. Condens. Matter* **2017**, *29*, 203002, 10.1088/1361-648X/aa60f3.
[44] C.-Y. Shih, R. Streubel, J. Heberle, A. Letzel, M. V. Shugaev, C. Wu, M. Schmidt, B. Gökce, S. Barcikowski, L. V. Zhigilei, *Nanoscale* **2018**, *10*, 6900–6910, 10.1039/C7NR08614H.
[45] C.-Y. Shih, C. Wu, M. V. Shugaev, L. V. Zhigilei, *J. Colloid Interface Sci.* **2017**, *489*, 3–17, 10.1016/j.jcis.2016.10.029.
[46] F. Waag, W. I. M. A. Fares, Y. Li, C. Andronescu, B. Gökce, S. Barcikowski, *J. Mater. Sci.* **2022**, *57*, 3041–3056, 10.1007/s10853-021-06731-2.
[47] G. Marzun, H. Bönnemann, C. Lehmann, B. Spliethoff, C. Weidenthaler, S. Barcikowski, *ChemPhysChem* **2017**, *18*, 1175–1184, 10.1002/cphc.201601315.
[48] C.-Y. Shih, C. Chen, C. Rehbock, A. Tymoczko, U. Wiedwald, M. Kamp, U. Schuermann, L. Kienle, S. Barcikowski, L. V. Zhigilei, *J. Phys. Chem. C* **2021**, *125*, 2132–2155, 10.1021/acs.jpcc.0c09970.
[49] R. G. Nikov, N. N. Nedyalkov, R. G. Nikov, D. B. Karashanova, *Appl. Phys. A* **2018**, *124*, 847, 10.1007/s00339-018-2272-3.
[50] F. Waag, Y. Li, A. R. Ziefuß, E. Bertin, M. Kamp, V. Duppel, G. Marzun, L. Kienle, S. Barcikowski, B. Gökce, *RSC Adv.* **2019**, *9*, 18547–18558, 10.1039/C9RA03254A.
[51] R. Streubel, G. Bendt, B. Gökce, *Nanotechnology* **2016**, *27*, 205602, 10.1088/0957-4484/27/20/205602.
[52] F. Waag, R. Streubel, B. Gökce, S. Barcikowski, *Appl. Nanosci.* **2021**, 10.1007/s13204-021-01693-y.
[53] J. Liu, M. Xu, F. Zaera, *Catal. Lett.* **1996**, *37*, 9–13, 10.1007/BF00813512.
[54] M. Chen, Y. Zheng, H. Wan, *Top. Catal.* **2013**, *56*, 1299–1313, 10.1007/s11244-013-0140-0.
[55] G. J. Lauth, J. Kowalczyk, *Einführung in Die Physik Und Chemie Der Grenzflächen Und Kolloide*, Springer Spektrum Berlin, Heidelberg, Berlin, Heidelberg, **2016**,, 10.1007/978-3-662-47018-3.
[56] S. Porter, A. Ghosh, C. H. Liu, D. Kunwar, C. Thompson, R. Alcala, D. P. Dean, J. T. Miller, A. DeLaRiva, H. Pham, E. Peterson, A. Brearley, J. Watt, E. A. Kyriakidou, A. K. Datye, *ACS Catal.* **2023**, *13*, 5456–5471, 10.1021/acscatal.3c00360.
[57] T. Lan, Y. Zhao, J. Deng, J. Zhang, L. Shi, D. Zhang, *Catal. Sci. Technol.* **2020**, *10*, 5792–5810, 10.1039/D0CY01137A.
[58] M. Sun, J. Liu, C. Song, Y. Ogata, H. Rao, X. Zhao, H. Xu, Y. Chen, *ACS Appl. Mater. Interfaces* **2019**, *11*, 23102–23111, 10.1021/acsami.9b02128.
[59] G. Novell-Leruth, J. M. Ricart, J. Pérez-Ramírez, *J. Phys. Chem. C* **2008**, *112*, 13554–13562, 10.1021/jp802489y.
[60] F. Waag, "Autopronano synthesis machine," can be found under http://www.autopronano.eu/, **2022**, (accessed March 30, 2023).
[61] T. Bessel, S. Dittrich, B. Gökce, S. Barcikowski, F. Waag, in *Lasers Manuf. Conf.*, Bayerisches Laserzentrum GmbH, **2021**.
[62] T. BESSEL, S. BARCIKOWSKI, F. WAAG, in *NANOCON Conf. Proc. - Int. Conf. Nanomater.*, **2021**, pp. 405–410,, 10.37904/nanocon.2021.4317.
[63] J. Johny, Y. Li, M. Kamp, O. Prymak, S. Liang, T. Krekeler, M. Ritter, L. Kienle, C. Rehbock, S. Barcikowski, S. Reichenberger, *Nano Res.* **2022**, *15*, 4807–4819, 10.1007/s12274-021-3804-2.
[64] T. Löffler, F. Waag, B. Gökce, A. Ludwig, S. Barcikowski, W. Schuhmann, *ACS Catal.* **2021**, *11*, 1014–1023, 10.1021/acscatal.0c03313.
[65] P. Wagener, J. Jakobi, C. Rehbock, V. S. K. Chakravadhanula, C. Thede, U. Wiedwald, M. Bartsch, L. Kienle, S. Barcikowski, *Sci. Rep.* **2016**, *6*, 23352, 10.1038/srep23352.
[66] RÖMPP-Redaktion, "Spannungsreihe," can be found under https://roempp.thieme.de/lexicon/RD-19-03139, **2002**, (accessed March 1, 2021).
[67] W. M. Haynes, D. R. Lide, T. J. Bruno, Eds., *CRC Handbook of Chemistry and Physics*, CRC Press, London, New York, **2012**.
[68] M. Kosmulski, *Adv. Colloid Interface Sci.* **2016**, *238*, 1–61, 10.1016/j.cis.2016.10.005.
[69] V. Pokorný, V. Štejfa, M. Fulem, C. Červinka, K. Růžička, *J. Chem. Eng. Data* **2017**, *62*, 4174–4186, 10.1021/acs.jced.7b00578.
[70] Y. Y. Yeo, L. Vattuone, D. A. King, *J. Chem. Phys.* **1996**, *104*, 3810–3821, 10.1063/1.471034.
[71] P. CHOU, *J. Catal.* **1987**, *104*, 17–30, 10.1016/0021-9517(87)90332-0.
[72] R. A. Beebe, E. L. Wildner, *J. Am. Chem. Soc.* **1934**, *56*, 642–645, 10.1021/ja01318a030.
[73] M. Smedh, A. Beutler, M. Borg, R. Nyholm, J. N. Andersen, *Surf. Sci.* **2001**, *491*, 115–123, 10.1016/S0039-6028(01)01375-9.
[74] T. Ward, L. Delannoy, R. Hahn, S. Kendell, C. J. Pursell, C. Louis, B. D. Chandler, *ACS Catal.* **2013**, *3*, 2644–2653, 10.1021/cs400569v.
[75] S. Derrouiche, P. Gravejat, D. Bianchi, *J. Am. Chem. Soc.* **2004**, *126*, 13010–13015, 10.1021/ja0470719.
[76] I. Ganzmann, D. Borgmann, G. Wedler, *Mol. Phys.* **1992**, *76*, 823–831, 10.1080/00268979200101711.
[77] F. J. E. Scheijen, D. C. Ferré, J. W. (Hans) Niemantsverdriet, *J. Phys. Chem. C* **2009**, *113*, 11041–11049, 10.1021/jp811130k.
[78] S. H. Payne, J.-S. McEwen, H. J. Kreuzer, D. Menzel, *Surf. Sci.* **2005**, *594*, 240–262, 10.1016/j.susc.2005.07.031.
[79] W. A. Brown, in *Adsorbed Layers on Surfaces*, Springer-Verlag, Berlin/Heidelberg, **n.d.**, pp. 302–340,, 10.1007/10857873_18.

[80] D. W. Johnson, M. H. Matloob, M. W. Roberts, *J. Chem. Soc. Faraday Trans. 1 Phys. Chem. Condens. Phases* **1979**, *75*, 2143–2159, 10.1039/F19797502143.
[81] P. J. Godowski, J. Onsgaard, *Vacuum* **2013**, *94*, 6–13, 10.1016/j.vacuum.2013.01.011.
[82] M. Yamaguchi, F. Mafuné, *J. Phys. Chem. C* **2019**, *123*, 15575–15581, 10.1021/acs.jpcc.9b02629.
[83] M. E. Bartram, B. E. Koel, *Surf. Sci.* **1989**, *213*, 137–156, 10.1016/0039-6028(89)90255-0.
[84] K. Kishi, M. W. Roberts, *Proc. R. Soc. London. A. Math. Phys. Sci.* **1976**, *352*, 289–302, 10.1098/rspa.1976.0175.
[85] H. Ning, J.-Q. Cai, X.-M. Tao, M.-Q. Tan, *Appl. Surf. Sci.* **2012**, *258*, 4428–4435, 10.1016/j.apsusc.2012.01.001.
[86] J. K. Nørskov, F. Studt, F. Abild-Pedersen, T. Bligaard, *Fundamental Concepts in Heterogeneous Catalysis*, John Wiley & Sons, Inc, Hoboken, NJ, USA, **2014**,, 10.1002/9781118892114.
[87] P. Błoński, A. Kiejna, J. Hafner, *J. Phys. Condens. Matter* **2007**, *19*, 096011, 10.1088/0953-8984/19/9/096011.

Manuscript received: April 21, 2023
Revised manuscript received: June 14, 2023
Accepted manuscript online: July 5, 2023
Version of record online: ■■, ■■

4.2 In depth Discussion of Selected Alloys

The catalysts were synthesized via laser ablation of sintered-metal targets. The targets were composed of a mixture of two metals, typically Pt+X, and ablated in a liquid flow. Noble metal combinations were synthesized using water as a medium, while combinations of Pt with a non-noble metal utilized propylene carbonate to hinder particle oxidation during ablation. After colloid synthesis the particles were supported on alumina particles, concentrated and deposited onto cordierite cores for all water-based samples, or tested as catalyst grains for propylene carbonate based samples. Characterization of the catalyst was carried out using HR-TEM, EDX, ICP-OES to verify composition and quantify the particle size distribution. Details on synthesis and characterization can be found in Section 5 of the publication, with further details provided in section 3 of this work. After synthesis of the catalysts, they were subjected to an industry standard ageing protocol by exposing the catalysts to an atmosphere of 10 vol% H_2O and 10 vol% O_2 in a N_2-balance at two different temperatures – 650°C and 800°C for 16 hours (cf. [63]). This results in the ability to test the catalysts in fresh state and evaluate durability from the two additional aged samples (cf. Figure 16).

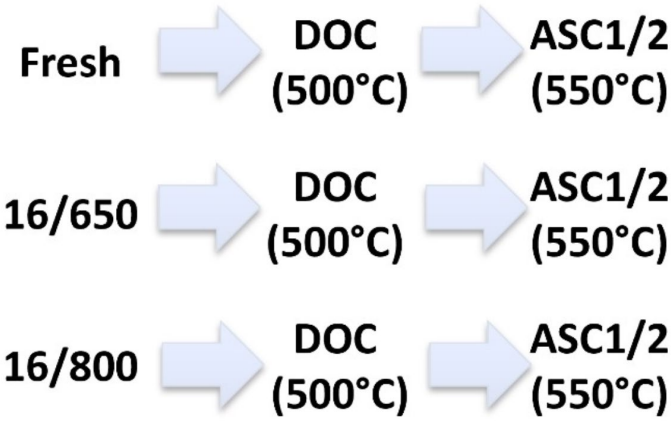

Figure 16 Catalytic testing procedure. Reprinted with permission from S. Siebeneicher, S. Reichenberger, C. Hengst, F. Dornhaus, B. Wittek, S. Barcikowski, ChemCatChem 2023, DOI: 10.1002/cctc.202300563.

The catalytic testing was conducted in three different gas mixtures, DOC, ASC1 and ASC2 (cf. Figure 16). As discussed in section 2.1 and 2.2, the diesel oxidation catalyst is directly exposed to products of fuel combustion. These are mainly H_2O (7.5 vol%) and CO_2 (7 vol%) with a lot of O_2 (10 vol%) still being present after lean combustion as well. Apart from this, there are also unburnt components of the fuel in the waste gas stream. In this study the unburnt components are represented by C_3H_6 (180 ppm) and CO (250 ppm). Furthermore, also NO (750 ppm) is mixed into the gas stream, which occurs in an engine from hot spots during combustion. The remainder of the gas stream is made up of N_2, as would be during engine operation. Tabulated values of the used composition can be found in section S5.1 of A4.

The ammonia slip catalyst is exposed to an environment reflecting the one present after DOC mainly aimed at evaluating the selective ammonia oxidation as discussed in section 2.2. The gas mixtures utilized for the ASC tests are as follows. One test, ASC1, is performed without NO, representing the case of full reduction in the SCR catalyst. This gas mixture then only contains "remaining" NH_3 (300 ppm) with mainly H_2O (5 vol%) as reaction product in a stream of O_2 (5 vol%) and carried by N_2. An additional test, ASC2, is performed to replicate the situation of incomplete reduction of NO by adding NO (200 ppm) to the gas stream. The tabulated concentrations of all ASC gas mixtures are available in section S6.1 of A4.
From the DOC experiments CO and C_3H_6 light up temperatures were evaluated and the NO_2 formation as well as N_2O formation calculated. The data obtained from the ASC experiments was used to measure the NH_3 light up temperature and evaluate the formation of NO, NO_2 and N_2O. Analyses of the data were done in accordance with the methodology presented in section 2.1 of the publication. Comprehensive overview plots are available in Figures S5.2 (for DOC) and Figures S6.2 and S6.5 (for ASC).

The most important results of this study have been published and can be found in the prior chapter. The presented results include the finding that for the CO-Oxidation in DOC a volcano-like dependence can be found with maximum activity being achieved when the oxygen binding enthalpy for the metal platinum is alloyed with is close to that of platinum (e.g. for Pt-Pd, Pt-Cu, Pt-Rh (only Pt-rich alloys)). Also, a relationship between the durability and the melting point of the element Pt is alloyed with could be found with alloys comprised from platinum and refractory metals showing significantly higher durability (e.g., Pt-Mo, Pt-Nb, Pt-Ru). A similar dependence could not be found for ASC, where the activities are also rather similar. Most importantly for ASC, a dependence of byproduct and the oxygen binding enthalpy could be found with elements that have a stronger affinity to oxygen than Rh favouring NO and N_2O and elements with a weaker affinity favouring NO_2 and N_2. Generally, some materials followed initial hypothesis, while others did not. For example, Pt-Cu, Pt-Ag and Pt-Au were chosen because a mixture of them may improve activity due to the CO oxidation activity following a volcano relationship with the maximum of the activity assumed between the elements (cf. Figure 17 (d)). Activity enhancements above Pt-Pd (the industrial reference) could nevertheless not be found. Pt-Cu shows hardly any dependence on mixing ratio, which is notable, but Pt-Ag and Pt-Au don't show the initially hypothesized activity improvements. Similarly alloys with Au did not allow for conclusions regarding selectivity. It was initially hypothesized that Au is able to moderate the activity of an alloy, but the observed activities were too low to conclude meaningful results regarding selectivity. Pt-Rh in itself is also notable. Its application in TWC [9] made

it appear possible, that it should show high activities in an oxygen-rich environment as well. It is known from literature that Rh, while initially active quickly deactivates in oxygen-rich environments [12]. An ennobling with Pt was therefore hypothesized to prevent this deactivation. This however is something that could not be observed. In fact, the lower the Pt-content of the alloy, the less active the catalyst turned out to be, making an ennobling of Rh by Pt unlikely. A similar argument is true for Pt-Ru, where also an ennobling by Pt was hypothesized to prevent inactive surface-oxides from forming. This, however, is not reflected in the data, as Pt-Ru just as Pt-Rh shows lower activities the lower the Pt-content is (cf. S5.2.1 in A4.). Regarding ASC measurements promising alloys could also be identified. Apart from Pt-Pd, which showed good activity, Pt-Nb, Pt-Ru, Pt-Fe and Pt-Mn were found to be notably active and selective for N_2, which is a characteristic that is known for the oxides of Fe and Mn [38,39] and seems to be carried over to the alloys with Pt. Ru could also be expected to exhibit a high selectivity to molecular nitrogen as it is known to have a high activation energy for the dissociation of N_2 making it rather unlikely that once formed molecular nitrogen gets split again [39].

Since this study is mainly focused on the exploration of new material combinations a detailed discussion of each alloy seems unnecessary. Therefore, this section will primarily emphasize the evaluation of the most active and durable catalysts within the DOC domain with one "negative" example being discussed as well. As CO-Oxidation is a well-studied reaction, performance data will be discussed on the basis of this fundamental reaction. Additionally, juxtapositions will be made with an example of the least durable and active catalysts. The ASC evaluations revealed a distinct trend, categorizing the materials into catalysts exhibiting selectivity either for NO_2 and N_2 or NO and N_2O. This observed categorization also warrants further discussion.
From all tested catalysts and using the CO-Oxidation as benchmark, the most active were Pt-Pd, Pt-Rh (for high Pt-contents), Pt-Cu and Pt-Mo. As Pt-Pd and Pt-Rh are well known elements and used broadly in waste gas abatement this in-depth discussion will focus on the more exotic alloys of Pt-Mo and Pt-Cu. Incidentally, Pt-Mo is also one of the alloys showing the highest durability in CO-Oxidation. On the other end of the spectrum, Pt-Ag is one of the least active and durable catalysts. Of these catalysts, Pt-Mo is selective to NO_2 and N_2, whereas Pt-Cu and Pt-Ag are selective to NO and N_2O.

4.2.1 Pt-Cu

As discussed in section 3.1 the alloy of Pt and Cu was chosen because Jiang et al showed data on the high temperature activity of Pt and Cu [37]. The volcano-like dependence of the activity in CO-Oxidation on CO- and O-binding enthalpy of the metals means, that a

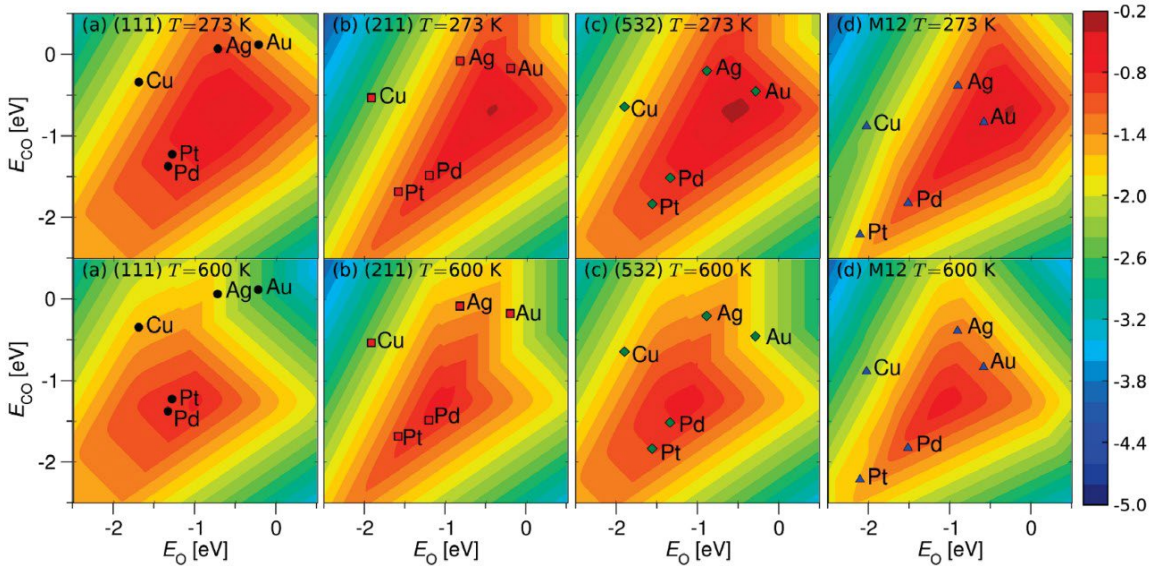

Figure 17 Reaction rate of CO oxidation (logarithmic colour scale) as a function of the adsorption energies of CO and O calculated using microkinetic models. Red indicates high rate, blue low. Upper row at low pressure (0.22 bar) and low temperature, lower row at high pressure (1 bar) and high temperature. Reprinted with permission from T. Jiang, D. J. Mowbray, S. Dobrin, H. Falsig, B. Hvolbæk, T. Bligaard, and J. K. Nørskov, The Journal of Physical Chemistry C 2009 113 (24), 10548-10553, DOI: 10.1021/jp811185g. Copyright © 2009 American Chemical Society.

combination of Pt and Cu may be a good idea (cf. Figure 17). While Pt in many cases is close to the maximum, an improvement of activity may be possible for the {532} crystal facet. The M12-clusters, which could be seen as geometrically closer to a nanoparticle (as opposed single crystal facets), would possibly exhibit similar activities for an alloy of Pt-Cu (Figure 17 (d)). From this graph, the activity of a copper-rich alloy should be lower than a 50:50 mixture with a platinum-rich combination being a little higher. Should this be the case, a substitution of Pt with Cu would be economically interesting due to the negligible price of copper when compared to platinum.

In Figure 18 a) the light-up temperature of all studied Pt-Cu alloys is plotted. With about 100°C the fresh catalysts belong to the most active ones studied in this work (cf. Fig. 24 in section A4). Also, the activity of the catalysts hardly depends on the mixing ratio of the two elements in the studied range between 10 and 90 at.% of Pt. This stays true for the aged samples at 650 and 800°C. The hypothesis from Figure 17, that a copper-rich alloy would be slightly less active than a platinum-rich one, cannot be seen here. If anything, there is an improvement towards the extremes (Cu-rich, Pt-rich), with less activity of the alloy in the middle of the mixing ratio. When comparing this to the phase-diagram of bulk Pt-Cu in Figure 18 b), it may be assumed, that the most stable alloy should be the catalyst with 30 at.% Pt, whereas all other compositions should undergo a local compositional change. This should be especially true for the samples that were aged at 800°C. Evidently, this trend cannot be observed in the activity or durability data in Figure 18 a). Therefore,

either the alloys don't change their composition, or a compositional change has no effect on the overall activity.

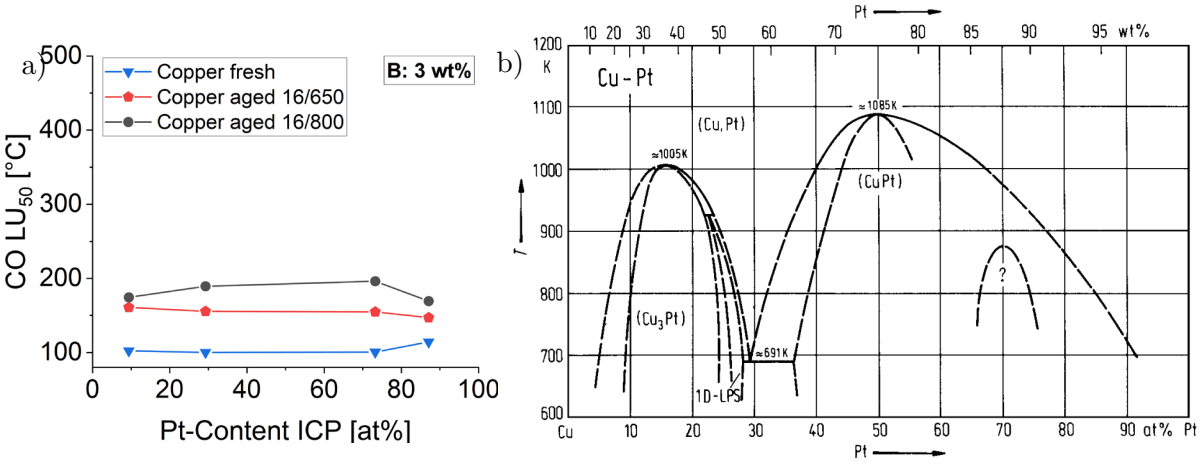

Figure 18 LU_{50} temperatures of the CO turnover of all Pt-Cu alloys (a) and phase diagram of Pt-Cu (b) (a) Reprinted with permission from S. Siebeneicher, S. Reichenberger, C. Hengst, F. Dornhaus, B. Wittek, S. Barcikowski, ChemCatChem 2023, DOI: 10.1002/cctc.202300563. Copyright © 2023 Wiley-VCH GmbH. (b) Reprinted with permission from B. Predel, in Landolt-Börnstein - Gr. IV Phys. Chem. - 5d -Cr-Cs – Cu-Zr (Ed.: O. Madelung), Springer-Verlag, Berlin/Heidelberg, 1994, pp. 1–6, DOI: 10.1007/10086090_1106. Copyright © 1994 Springer.

The similarities between the catalysts are mirrored in their particle size distributions (Figure 19). All Pt-Cu alloys have their size distribution peak around 3 nm with $Pt_{90}Cu_{10}$ having a slightly stronger pronounced peak. This could lead to a slightly improved activity, as for this sample the active surface area is larger than for the other three. Looking at the activity data, this trend is not visible. $Pt_{90}Cu_{10}$ is even slightly less active than the rest. Ultimately, the most probable explanation for the missing correlation is based in statistics. The size distributions are based upon measured particles from HR-TEM and due to the limited sample number at best qualitatively comparable. The number of particles counted for $Pt_{90}Cu_{10}$ is double that of the other samples and these may also exhibit a larger peak, if sufficient numbers of particles are measured. In a nutshell this means, that the HR-TEM findings support the finding of similar activity, while the expected dealloying from the phase diagram warrants further discussion on why the alloys of Pt-Cu show such an unpronounced dependency on mixing ratio.

From literature it is known, that Cu_2O is the most active copper species in CO-Oxidation. Cu as well as CuO show a lesser degree of activity [266]. Through a combination of HR-TEM, FTIR spectroscopy and electrochemical studies, Sadykov et al. showed that Cu^+ cations at edge sites on extended grain boundaries are the most active sites for CO-Oxidation [267]. Oxygen that is removed from these sites through oxidation would need to

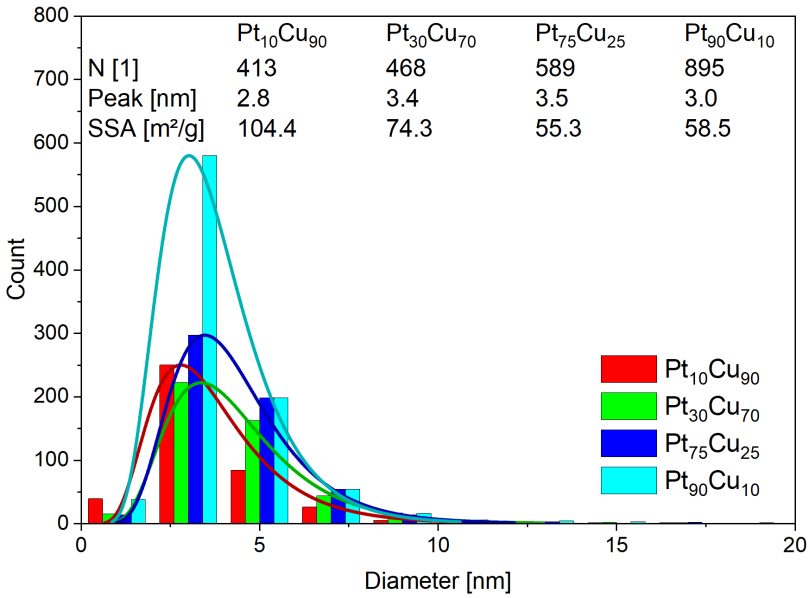

Figure 19 Particle size distributions of all Pt-Cu alloys from HR-TEM. Reprinted with permission from S. Siebeneicher, S. Reichenberger, C. Hengst, F. Dornhaus, B. Wittek, S. Barcikowski, ChemCatChem 2023, DOI: 10.1002/cctc.202300563. Copyright © 2023 Wiley-VCH GmbH.

be replenished. And while first assumed to diffuse through the lattice, Sadykov et al. pointed out, that this diffusion pathway is too slow. Grain boundary diffusion on the other hand can allow much faster, sufficient diffusion. [268,269] As on nanoparticles, especially on laser-generated ones, defects are very prominent [270], it can be assumed, that the Pt-Cu particles expose Cu edge sites. If the high oxygen content of the lean waste gas stream is able to oxidise these copper atoms to Cu^{+}, a high activity of copper-rich alloys could be explained by this species. The Pt-content of the alloys may also prevent the Cu(I) from oxidizing to the less active Cu(II), analogous to the ennobling properties exhibited in other alloys [251]. Also, Pt could provide oxygen species to these edge sites because it is able to bind to physisorbed (O_2^{0-}), superoxo (O_2^{-}), peroxo (O_2^{2-}) and atomic (O) species of oxygen as evidenced by Montemore et al [13].

The observed durability trends would fit this hypothesis. Wang et al. reported that Pt is able to oxidise to form PtO_2, which due to its low vapour pressure is a mobile species [271]. If there is no capture mechanism, this leads to loss of active surface are through Ostwald ripening. In fact, Carillo et al. reported PdO capturing mobile PtO_2 [32]. If Cu is not able to provide a similar capturing effect the catalysts would suffer particle growth and loss of active surface. The removal of Pt from the alloy may result in particles enriched in Cu. Without the protective influence of Pt against oxidation, these particles might transform into CuO and display reduced activity. Even without platinum evaporation from the particles this would be a reasonable explanation for the observed durability. Oxidation of Pt and in turn of Cu(I) to Cu(II) may successively deactivate the catalyst.

This work shows that their negligible dependence on mixing ratio, makes alloys from Pt-Cu interesting candidates for oxidation catalysis. Further research on similar alloys should

investigate ageing in greater depth and with focus on the oxidation of surface sites as well as particle composition upon thermal cycling and catalysis operation.

4.2.2 Pt-Ag

Like copper, silver has been chosen due to the fact that it promises enhanced activity due to the volcano-like activity relationships Jiang et al. observed [37] (cf. Figure 17). In contrast to copper, for almost all cases silver lies exactly opposite platinum, with the peak activity between both metals. This means that a combination of Pt and Ag may result in increased CO-Oxidation activity. At the same time, silver is also a much cheaper metal than platinum, promising to offer economic benefits, albeit a little smaller than non-noble metals would. Silver is also very well known in literature for its high activity towards CO-Oxidation [265,272,273] Propene-Oxidation [274,275] and is used in selective-oxidation reactions like methanol oxidation, ethylene oxidation and coupling reactions as well [276]. Aside from this uses, silver has been shown to exhibit good activity due to its optical properties in photocatalysis [274,277,278] and is also been tested in oxygen reduction reactions for aluminium-air-batteries [274,279] and sodium borohydride electrooxidation [280,281]. Despite these plenty uses and possible benefits of an alloy of Pt and Ag, the studied alloys did not exhibit any exceeding activities, when compared to other tested alloys. Figure 20 shows, that the light-up temperatures are around 200°C for fresh samples and exceed 250°C for aged samples. It can be seen that the platinum-rich alloys are among the more active ones, and the least activity can be observed in the middle of the mixing range with silver-rich alloys again improving a little. This means that the best activities of Pt-Ag are still worse than the worst of Pt-Cu, despite Figure 17 suggesting that the alloy of Pt-Ag should show higher activities. This discrepancy may be loosely attributed to the different size distributions observed for Pt-Ag. Figure 21 shows an overview of all Pt-Ag samples. This shows that all samples are of a similar distribution with peak particle sizes around 5 nm. More active samples generally showed a little smaller particle size of around 3 nm, like Pt-Cu, Pt-Mo, Pt-Pd, Pt-Rh and others. Though this difference in particle size would not be expected to have such strong

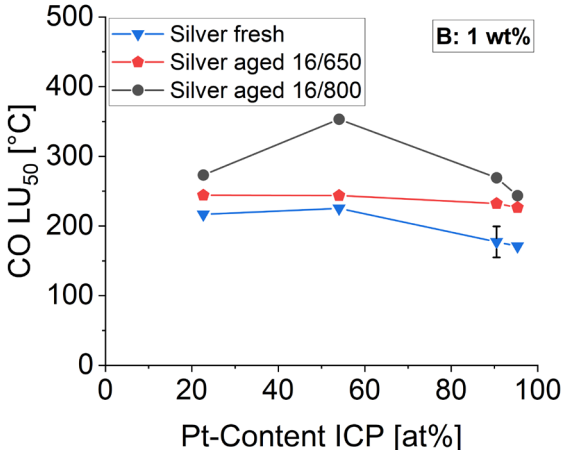

Figure 20 LU_{50} temperatures of the CO turnover of all Pt-Ag alloys. Reprinted with permission from S. Siebeneicher, S. Reichenberger, C. Hengst, F. Dornhaus, B. Wittek, S. Barcikowski, ChemCatChem 2023, DOI: 10.1002/cctc.202300563. Copyright © 2023 Wiley-VCH GmbH.

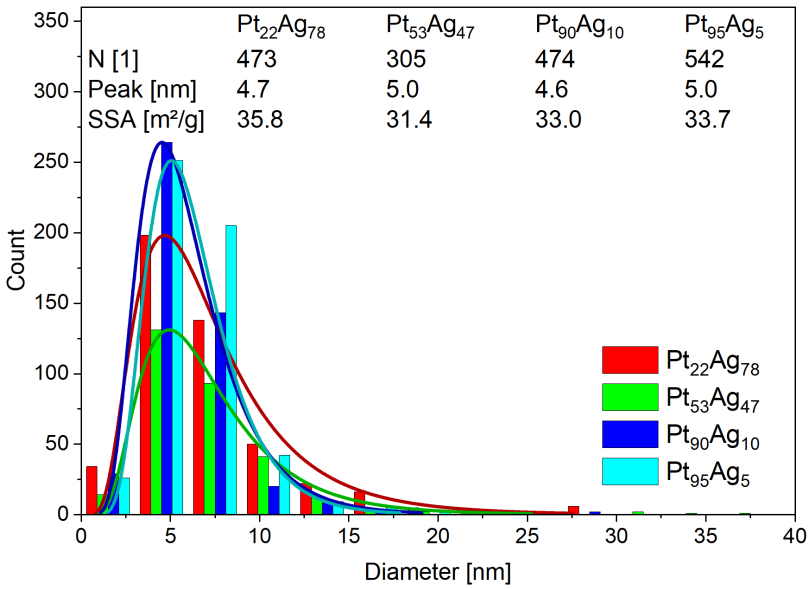

Figure 21 Particle size distributions of all Pt-Ag alloys from HR-TEM. Reprinted with permission from S. Siebeneicher, S. Reichenberger, C. Hengst, F. Dornhaus, B. Wittek, S. Barcikowski, ChemCatChem 2023, DOI: 10.1002/cctc.202300563. Copyright © 2023 Wiley-VCH GmbH.

effects on activity, other alloys with larger particle sizes, like Pt-Au and Pd-Cu also exhibit low CO-Oxidation activity. The slightly larger particle size can therefore not be excluded as a reason for lower observed activity in comparison to the test field. Nevertheless, a dedicated literature review points to another different reason for lower-than-expected activity. All studies that focus on the activity of Ag in oxidation catalysis, aiming for full combustion, mention the use of oxygen-donating support materials, like CeO_2 or ZrO_2. For example, Mamontov et al. showed that it is the addition of CeO_2 to a Ag/SiO_2 catalyst, that significantly increases the observed activity [272]. Older studies looking at silver under oxidative conditions also report its unique ability to form subsurface oxygen [282]. Remarkably, Qu et al. was able to demonstrate that this subsurface oxygen is able to directly react with CO in an atmosphere with an excess of H_2 to selectively form CO_2 [273]. Later on, Skaf et al. showed that it is the oxidized silver species Ag^{2+} that is responsible for silver's high activity in CO- and C_3H_6-Oxidation [275]. Notably, many studies reporting high activities for silver also mention the use of the oxygen donating CeO_2 [265,272–275,277–281]. This allows the hypothesis, that silver will only exhibit high activities, when there is a possibility for it to oxidizes and a lean atmosphere as well as an oxygen donating support should aid in this. In comparison, experiments in this study were carried out with only Al_2O_3 as support material, albeit with a lean atmosphere. Analogous to the hypothesis for Pt-Cu, Ag may be ennobled in Pt-Ag based upon the mechanism shown by Potgieter et al. [251]. While for copper this meant that a more active, less oxidized species may have been

stabilized, Ag^{2+} is most likely not being stabilized via an ennobling. In contrast, the alloying with Pt would rather be expected to result in more metallic silver exposed on the surface and therefore possibly even reduce the activity compared to pristine silver. The observed activity decrease upon ageing, which happens especially for the 50:50 mixture, fits this hypothesis. The Pt-Ag phase diagram shown in Figure 22 shows that all Pt-rich alloys should undergo some kind of restructuring, resulting in particles that are particularly Pt- or Ag-rich (98 at% and ~10 at% respectively), while there are stable phases expected around 50 and 75 at% Ag. Still, the 50:50 mixture shows the lowest durability, indicating that possibly a loss of active surface area occurred. An in-depth study carried out on this alloy in section 4.3.2 indeed shows limited particle growth but could not find convincing evidence related to dealloying. This leaves the hypothesis that silver upon alloying with Pt does not retain the ability to form oxidized surface species. Strong ageing should promote this formation as it is done under elevated temperatures and a 10 vol% oxygen and water atmosphere, well capable of oxidizing the surface. It would be of interest to study an alloy of Pt-Ag, where this effect is taken into account and tested for. If it is possible to combine Pt with Ag in a way that retains silver's ability to oxidize, the catalysts could be expected to exhibit better activity than demonstrated here.

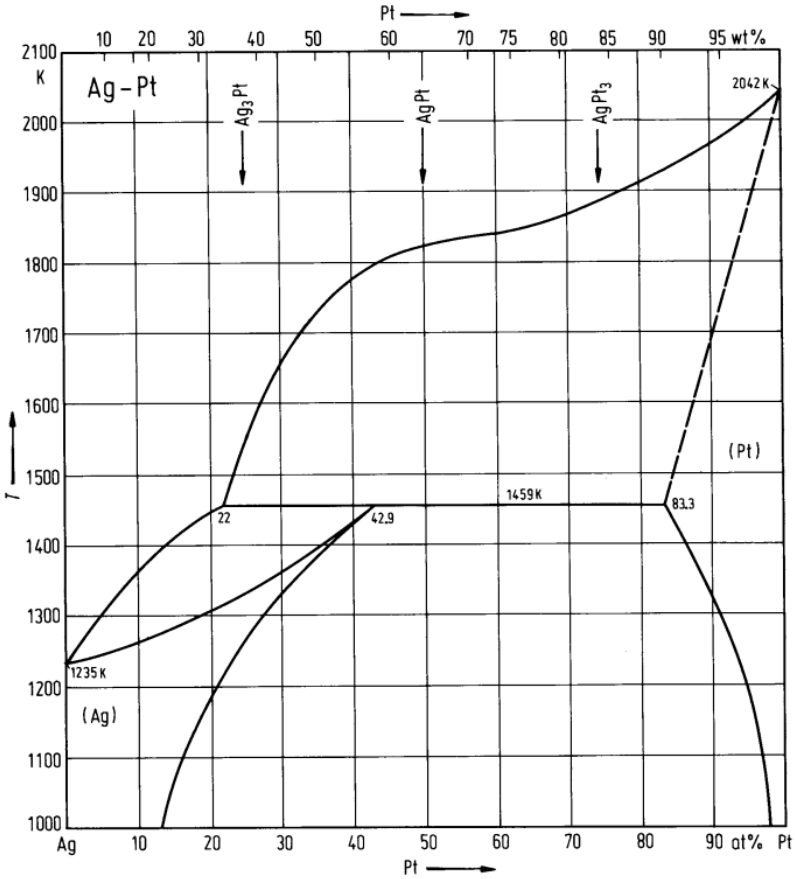

Figure 22 Phase diagram of Pt-Ag. Reprinted with permission from B. Predel, in Landolt-Börnstein - Gr. IV Phys. Chem. 5A, Ac-Au – Au-Zr, Springer-Verlag, Berlin/Heidelberg, 1991, pp. 1–3, DOI: 10.1007/10000866_58. Copyright © 1991 Springer.

4.2.3 Pt-Mo

The alloy Pt-Mo was mainly chosen because of its high melting point, inspiring the possibility of enhanced durability. Like many other alloys in this study, Mo would also be an attractive substitute for Pt for economic reasons in case of acceptable activity. Notably, Mo is rarely discussed in publications discussing waste gas catalysis or CO-Oxidation. Prominent publications revolve around the use of $MoO(O_2)_{2-}$ in oxygen transfer reactions used in epoxidation of alkenes or oxidation of alcohols to aldehydes [283] and its beneficial application in fuels cells when alloyed with Ni [284]. An exception from that rule is the study of CO-Dehydrogenase in bacteria by Hänzelmann and Meyer. In their studies they found the Mo-site to be the active site for Co-Oxidation [285,286]. With CO-Oxidation being an important part of exhaust gas catalysis, an alloy of Pt-Mo could therefore be expected to exhibit relevant activities.

Looking at the light-up temperatures of CO-Oxidation in Figure 23, the tested alloys of Pt-Mo exhibit notable activity. The most active alloy with 99 at.% Pt has a light up at 163°C in the fresh state and the least active alloy with 50 at.% Pt still shows a light up temperature of 180°C. Compared to the rest of the alloys tested in this study, this classifies the alloy system Pt-Mo to be among the more active ones (cf. section 5.2.1 in A4). Additionally, over the covered composition range of 50-99%, the dependence on mixing ratio is hardly visible. The light-up temperature increases from fresh to 16/850 only between 9 and 15°C; a temperature difference hardly achieved by any other tested alloy.

While the alloys with the least amount of Pt were chosen to form a stable phase (PtMo and Pt_2Mo), the alloys with a higher amount of Pt may tend to segregate Pt following the bulk phase-diagram shown in Figure 24. From the results in may be concluded, that a segregation of Pt, should it have happened, did not influence the activity in any major way.

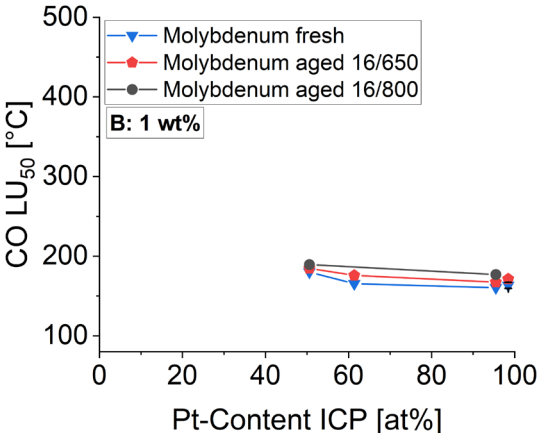

Figure 23 LU_{50} temperatures of the CO turnover of all Pt-Mo alloys. Reprinted with permission from S. Siebeneicher, S. Reichenberger, C. Hengst, F. Dornhaus, B. Wittek, S. Barcikowski, ChemCatChem 2023, DOI: 10.1002/cctc.202300563. Copyright © 2023 Wiley-VCH GmbH.

The measured size distributions of the alloys also helps in clarifying that differing particle sizes don't influence the activity strongly. If anything, the most active alloys are composed of slightly larger particle sizes, when compared to the other Pt-Mo alloys (cf. Figure 25). But it has to be considered, that in the measured peak particle size of

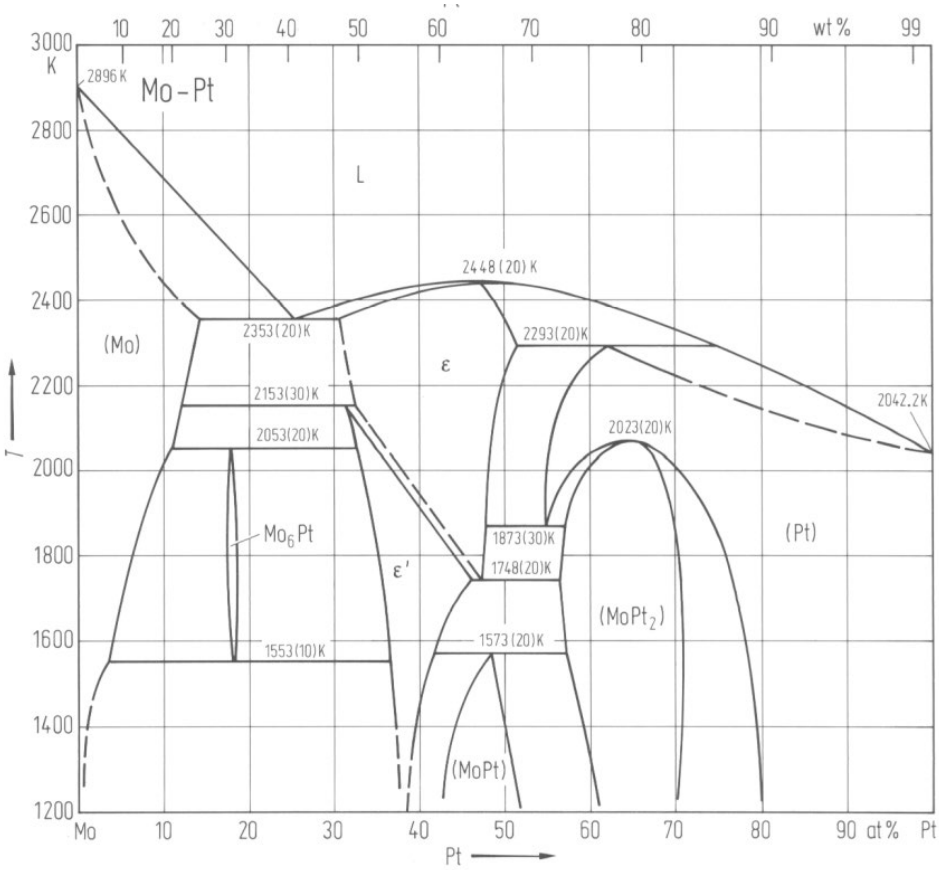

Figure 24 Phase diagram of Pt-Mo. Reprinted with permission from B. Predel, in Landolt-Börnstein - Gr. IV Phys. Chem. (Numerical Data Funct. Relationships Sci. Technol. Li-Mg – Nd-Zr, Springer-Verlag, Berlin/Heidelberg, 1997, pp. 1–2, DOI: 10.1007/10522884_2085. Copyright © 1997 Springer.

around 2 nm, even HR-TEM measurements exhibit a relevant uncertainty, making differences at this scale not a good basis for discussion. Therefore, the particle size distributions need to be assumed as very similar to each other.

An explanation for the beneficial combination of Pt-Mo in CO-Oxidation can be found in a review by Yeetsorn et al.. This review deals with molybdenum-based nanocatalysts in the context of direct alcohol fuel cells. In these fuel cells, the oxidation of an alcohol means that at some point also CO needs to be oxidized by the catalyst because not doing so may result in the surfaces getting poisoned by this reactant. The proposed mechanism follows a Langmuir-Hinshelwood mechanism, as first proposed by Gilman [287]. The reaction begins with the adsorption of CO on Pt. If water is present, as it is in our experimental setup, it can be split into H^+ and OH^- on the surface of the catalyst particle, with OH^- primarily binding to Mo-surface sites. The adsorbed CO on Pt can then subsequently react with the OH bound to Mo to form CO_2 and another H^+. [288] While any H^+ in the fuel cell may be solubilized, it is more likely in our setup that any hydrogen will stay bound to the catalytic particle and oxidized to more water during the course of the reaction. Yeetsorn at al. point

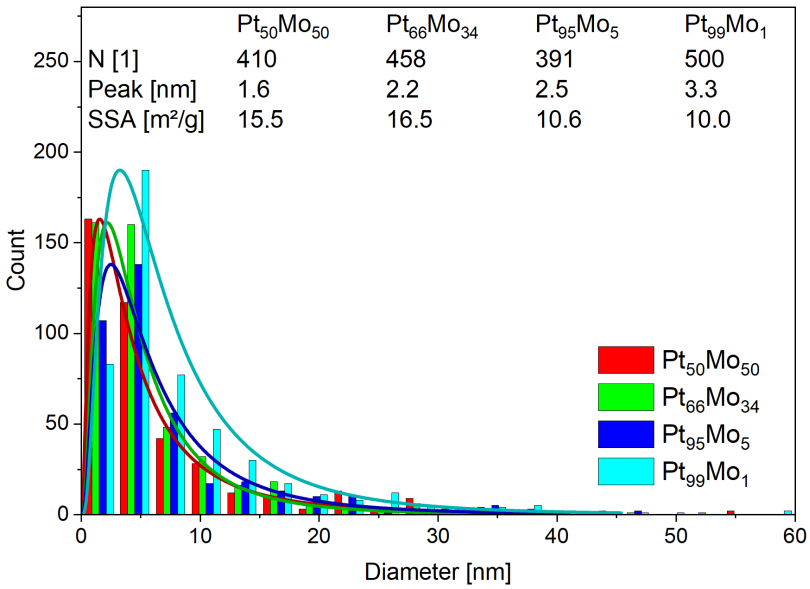

Figure 25 Particle size distributions of all Pt-Mo alloys from HR-TEM. Reprinted with permission from S. Siebeneicher, S. Reichenberger, C. Hengst, F. Dornhaus, B. Wittek, S. Barcikowski, ChemCatChem 2023, DOI: 10.1002/cctc.202300563. Copyright © 2023 Wiley-VCH GmbH.

out that the combination of Pt with Mo leads to a few different effects that make the alloy particularly active. First of all, it is molybdenum's ability to dissociatively adsorb water molecules, that makes it well suited for applications requiring CO-Oxidation in a water-containing environment. Any adsorbed OH on Mo can act as ligand for CO and thereby weaken the binding between CO and Pt, which ultimately helps the CO-oxidation on Pt. Second of all, Mo is able to electronically interact with Pt. Its d-orbital is able to donate delocalized electrons to Pt, enhancing its activity for CO-oxidation. Lastly, the migration of hydrogen atoms from Pt to Mo weakens the bond between Mo and CO, which leads to an easier oxidation of CO. [288]

Similar to a combination of Pt and Cu, the combination of Pt with Mo is shown to exhibit beneficial properties for waste gas catalysis. The small dependence on mixing ratio combined with the high durability makes Pt-Mo well suited as catalyst. Albeit it would be interesting to study how alloys formed with grater percentages of Mo would behave in the tested reactions. The small observed dependence on mixing ratio may persist, making Pt-Mo an even better substitute in an economical sense.

4.2.4 Comparing ASC trends - Pt-Cu, Pt-Ag and Pt-Mo

The catalysts were tested in two different atmospheres. One test was carried out with 300 ppm NH_3 in an atmosphere of 5 vol% O_2 and 5 vol% H_2O in an N_2 balance. A second test was carried out, that had an additional 200 ppm NO present. The results of both tests were generally comparable, with light-up temperatures decreasing with NO present, as would be expected from the addition of this oxidizer. The test performed without NO in the feed is very similar to the literature standard of NH_3-SCO (selective catalytic oxidation) with the difference of the added H_2O. Depending on the catalyst material this selective oxidation occurs via several different pathways. Lan et al. provided a comprehensible

overview of the reaction mechanisms that is reproduced in Figure 26. The Imide mechanism depicted in a) is the one mostly observed for Pt surfaces. It starts out by the activation of O_2, with atomic O being bound to the catalyst surface. The abstraction of two hydrogen atoms from the surface-bound ammonia then leads to the formation of NH and H_2O. The NH can subsequently form HNO with further surface bound atomic oxygen. By further oxygen uptake this can react to HNO_2, which reacts to form NO and H_2O. Alternatively, HNO can react with another HNO bound to the surface to form N_2O and H_2O. Therefore, N_2O is one of the possible by-products of this reaction mechanism. The desired reaction pathway is selective for N_2 formation via the HNO + NH → N_2 + H_2O pathway. The hydrazine mechanism illustrated in Figure 26 b) is another possible mechanism, but generally only occurs for low oxygen partial pressures demonstrated by Bagnasco et al for CuO on TiO_2 [289]. The i-SCR and N^{2-}-mechanism are both mechanisms mainly found on silver based catalysts [290–292] whereby the N^{2-}-mechanism was only observed by Wang et al. on a catalyst comprised of silver on nano Al_2O_3 [291]. Since the latter mechanism cannot explain the byproducts observed in this study it can also be excluded. The i-SCR-mechanism is somewhat similar to the Imide-mechanism as it starts out with adsorbed atomic oxygen abstracting H from the ammonia and subsequently forming NH that can then react to NO

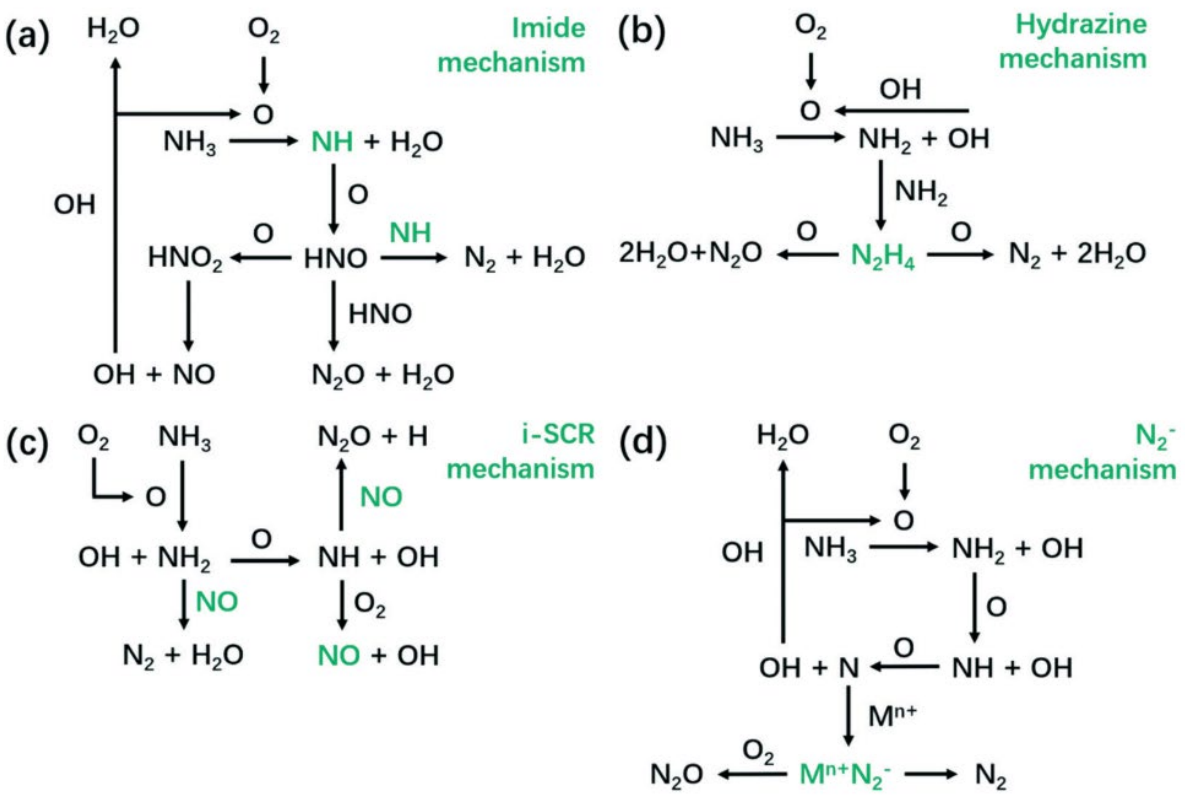

Figure 26 Reaction mechanisms for NH_3-SCO. a) Imide mechanism, b) Hydrazine mechanism, c) i-SCR-mechanism, d) N^{2-}-mechanism. Reprinted with permission from T. Lan, Y. Zhao, J. Deng, J. Zhang, L. Shi, D. Zhang, Catal. Sci. Technol. 2020, 10, 5792–5810, DOI: 10.1039/D0CY01137A.

or N_2O. The pathway is different in so far as the hydrogen abstraction happens stepwise and N_2 is the product of the reaction of NH_2 with NO and no HNO is observed. Regarding reaction by-products the imide- as well as the i-SCR-mechanism can explain NO, but not the NO_2 that is observed in this study.

The relevant mechanisms for the following discussion therefore are the imide and i-SCR-mechanism. An overview of the results of all catalysts tested can be found for the test without NO in section 6.2 and for the test with NO in section 6.5 of A4. Since the catalysts that were discussed prior exhibit interesting characteristics in the ammonia slip test as well, they will be discussed in more detail here. Figure 27 shows the light-up temperatures of all Pt-Cu, Pt-Ag and Pt-Mo catalysts. Pt-Cu belongs to the most active tested catalysts in the test field with light-up temperatures around 200°C a high durability and only minor dependence of catalytic activity on mixing ratio. Especially the high durability appears interesting, as Pt-Cu did exhibit strong ageing in the DOC test. Pt-Ag on the other hand exhibits comparably low activity in the ammonia oxidation just like it was less active in DOC. Figure 27 b) shows a strong dependence on mixing ratio, with Ag-rich alloys generally performing worse than Pt-rich ones. Figure 27 c) shows all Pt-Mo alloys. In DOC these alloys were amongst the most durable, a trend that isn't as obvious in this ASC test, albeit the minor dependence on mixing ratio is comparable to that observed for DOC.
In literature Cu is applied in many different studies to the selective oxidation of ammonia. Generally it is found that the underlying reaction mechanism follows the i-SCR route [293–296]. Wang et al. reported that the activity of a CuO based catalyst benefits from the CeO_2 support material, because it helps to replenish the lattice oxygen [294]. Similarly, Wang et al. reported for CuO-Fe_2O_3 catalyst, that active surface oxygen aids the ammonia oxidation [295]. These findings then culminated in Zhang et al and Guo et al. identifying Cu^{2+} as the active species, both for a copper-exchanged zeolite [293,296]. Generally, this fits what is observed in this study. For DOC it was observed that the Pt-Cu catalysts did not show good durability. This was attributed to a possible loss of Pt. The most active species in CO oxidation is Cu_2O, a species that may only be stable under strong oxidizing conditions if ennobled by Pt. The possible loss of Pt due to hydrothermal treatment leads to a subsequent oxidizing of copper to the less active CuO. This can explain why Pt-Cu suffers from great activity loss upon ageing in DOC. In ASC on the other hand, CuO turns out to be the most active copper species. The possible oxidation of copper would lead to the formation of the most active species CuO and explain why the durability of the Pt-Cu alloys is as good as observed in Figure 27 a).

As described earlier Pt-Ag shows very comparable results to what is observed in DOC. Generally, the activity as well as durability is comparably low. In addition, in the ASC environment Pt-Ag exhibits a strong dependence on mixing ratio (cf. Figure 27 b)). From literature it is known that silver mainly follows the i-SCR mechanism in selective ammonia oxidation. For example Wang et al. presented evidence for this mechanism for a catalyst of Ag on Al_2O_3 [290,291]. Similarly Qu et al. found evidence for the i-SCR mechanism for a silver catalyst supported on SiO_2, NaY, Al_2O_3 or TiO_2 [297]. All these papers report that Ag^+ is the active species for ammonia oxidation. Zhang et al. detailed this and found that Ag^+ is the active species above a temperature of 140°C and that smaller particles are less selective to N_2 [298]. When comparing these findings with those for CO oxidation the picture is not as clear as for Pt-Cu. For CO oxidation Ag^{2+} is found to be the active centre. It may be possible, that Pt ennobles Ag more effectively than Cu because the only way that oxidation state influences the activity in a negative way for CO and NH_3 oxidation is that silver stays reduced. It is also possible that the higher proportion of reduced silver results in the reduced activity of Ag-rich alloys, explaining the observed strong dependence of activity for ammonia oxidation. But in that case this dependence should show up under CO oxidation conditions as well, which it does not. Ultimately this leads to the conclusion that further investigation regarding surface states of the used alloy catalysts need to be done in order to identify reasons for the differing dependence on mixing ratio between DOC and ASC.

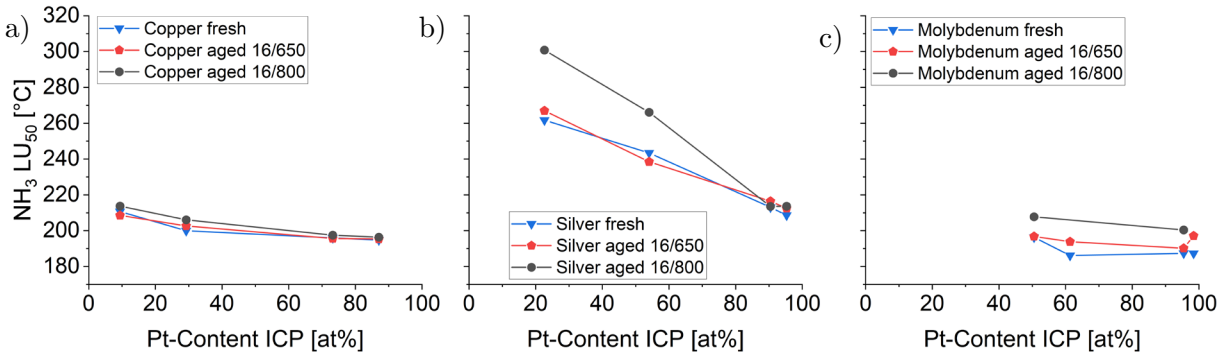

Figure 27 Light up temperatures of NH_3 for Pt-Cu (a), Pt-Ag (b) and Pt-Mo (c) in ASCI atmosphere (without NO in feed). Reprinted with permission from S. Siebeneicher, S. Reichenberger, C. Hengst, F. Dornhaus, B. Wittek, S. Barcikowski, ChemCatChem 2023, DOI: 10.1002/cctc.202300563.

Regarding Pt-Mo, all alloys show comparable performance to DOC. The activity is similar to Pt-Cu, the dependence on mixing ratio similar to what is observed in DOC, only the durability is not as pronounced for Pt-Mo in ASC as it is in DOC (cf. Figure 27 c)). Literature regarding molybdenum in ammonia oxidation catalysis is sparse. There are some studies reporting activities for MoO_3 on several different supports like SiO_2 [299], SiO_2 and Al_2O_3 [300] and TiO_2 [301]. Neither of the found studies allow conclusions for the underlying

reaction mechanism, although notably MoO_3 on TiO_2 does form very little NO as reported by Duan et al. [301]. Védrine, Hutchins and Kiely report, that molybdenum, like many other transition metal oxides, reacts with alkanes via a Mars-van-Krevelen mechanism [302]. This means that the lattice oxygen bound to molybdenum could play a relevant role in the oxidation of hydrocarbons in DOC and possibly also be the underlying mechanism for ammonia oxidation. Since MoO_3 is reported as active species in literature it remains unclear, if molybdenum, should it stay reduced via an ennobling effect of platinum, would exhibit similar activities. The oxygen spillover that may happen from platinum may lead to the formation of active surface oxides, but it does not make much sense to assume that during ageing the surface oxide gets very prominent, albeit literature shows that this should lead to notable activity still. Generally, it would be a worthy topic for further studies to shed light on the surface chemistry of the studied alloys and to try and pinpoint the active site.

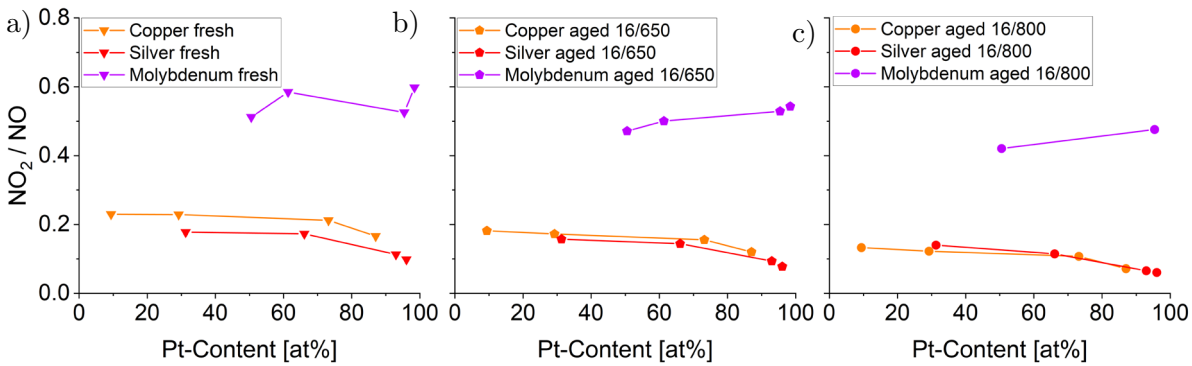

Figure 28 NO_2/NO relationship for Pt-Cu, Pt-Ag and Pt-Mo in fresh (a), slightly aged(b) and strongly aged state (c) in ASCI atmosphere (without NO in feed).

In Figure 28 the relationship between NO_2 and NO has been plotted for all three different ageing states and alloys of Pt-Cu, Pt-Ag and Pt-Mo. From this it can be seen that the alloys of Pt with Ag and Cu tend to form less NO_2 than the alloys of Pt with Mo. This categorization stays constant independent of ageing state. Interestingly this relationship appears to hardly depend on the mixing ratio between the elements. In section 4.1 it was found that the dependence whether an alloy tends to form more NO_2 than NO relates to the binding enthalpy of molecular oxygen to the metal that Pt is mixed with. It was also discussed that both, the i-SCR and imide-mechanism could explain the observed byproducts of ammonia oxidation N_2O and NO. But neither mechanism gives a good reason for why NO_2 is a prevalent byproduct, especially for elements with a high affinity for oxygen. Overall literature also does not provide many helpful insights into why NO_2 is formed during ammonia oxidation. At least for molybdenum it was reported that it will form nitrate surface groups if exposed to NO and O_2 and subsequently heated [303]. This NO_3 groups may react with further NH_3 to form NO_2, explaining the observed NO_2. This is in contrast to the rest of the literature though, where NO_2 has not been observed. One important difference

between literature and this study is the inclusion of water into the gas mixture though. If there is excess water present this may influence the imide-mechanism and change the equilibrium of the reaction from HNO_2 to NO and H_2O. Excess water could adsorb onto the surface, form OH species that react directly with HNO_2 to form H_2O and NO_2, which subsequently desorbs. This mechanism would be most prominent on materials that have a high binding enthalpy for atomic oxygen and therefore may favour the binding of OH as well. Nevertheless, this is a mechanism that has not been demonstrated and should be studied in depth with the catalysts presented in this study and the used the feed-gas composition. As both, the presence of an alloy and water, seem to play an important role in the formation of NO_2. If water should be a deciding factor here, this should mean that alloys tending to form NO_2 would follow the imide-mechanism, whereas NO favouring alloys should follow the i-SCR mechanism which would not be as susceptible for byproducts formed from adsorbed H_2O. There is, however, still the possibility, that materials with high oxygen affinity tend to bind to more oxygen which increases the chances of NO oxidizing to NO_2 before desorbing – this remains to be tested as well.

4.3 Ageing of Alloys on the Example of $Pt_{50}Au_{50}$ and $Pt_{47}Au_{53}$

Prior to receiving any catalytical results two samples had to be chosen to be evaluated in more depth. Pt-Au and Pt-Ag were chosen to be compared because both were expected to be active and show different durability. Pt-Au was expected to be less durable due to a large mixing gap in the bulk phase diagram, whereas Pt-Ag was chosen because the 50:50 alloy should be stable according to the bulk phase diagram and was therefore expected to be more durable. In hindsight, it would have been intriguing to study Pt-Cu as this alloy exhibited high activity and pronounced ageing, but time constraints meant, that no samples could be obtained from this alloy. Hence the following sections will focus on the data obtained from Pt-Au and Pt-Ag.

4.3.1 $Pt_{50}Au_{50}$ in different Ageing Stages

The alloy of 50 at% platinum and gold was examined in detail for its ageing behaviour. This alloy is an example of a material mixture in which increased ageing is expected due to the low melting point of gold and the fact that the bulk phase diagram shows a large miscibility gap for the solid phase indicating possible material segregation [157]. In fact, the alloy exhibits poor activity in comparison to the rest of the test field; in fresh state as well as in all aged states. Figure 29 shows the measured CO-Conversion curves. From this it can be seen that the fresh catalyst is the most active, but counterintuitively the strongest aged sample shows slightly better activity than the less severely aged sample. This poses the questions, if the unexpected activity gain can be attributed to particle size or morphology changes happening to the samples. In order to investigate this, the samples were subjected to detailed HR-TEM measurements including EDX to check the elemental distribution. The

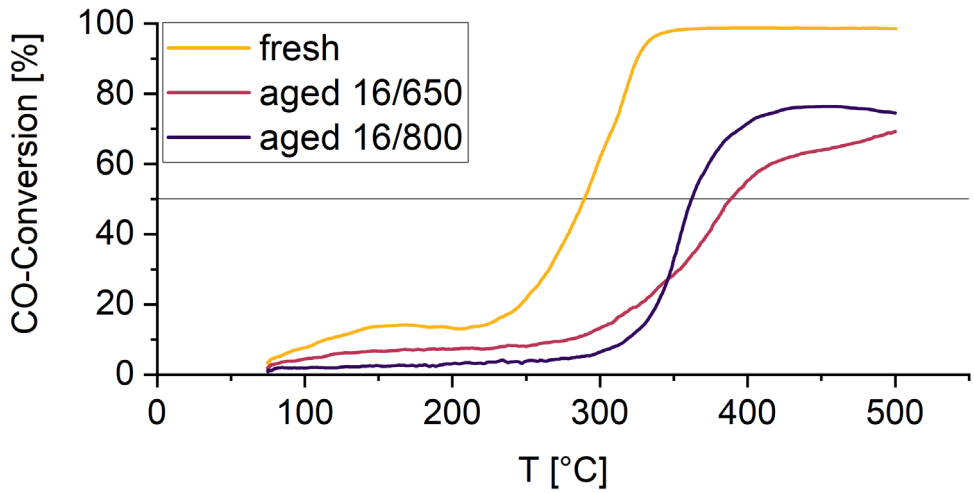

Figure 29 CO-conversion curves of Pt_{50}-Au_{50} in all ageing states.

following sections will first focus on morphological changes before pivoting to a focus on the elemental distribution within the particles.

Morphology and particle growth

Investigation of the particle size distributions obtained by HR-TEM in Figure 30 first shows that the fresh sample consists of the smallest particles which is in line with the observation that this is the most active sample. A fact that it most likely linked to the larger surface area of this sample. Surprisingly and in contrast to other samples, the fresh Pt-Au alloy does not only comprise of spherical particles, but in many cases chain-like structures with spherical subunits can be found. This observation was unexpected and prompted detailed analysis regarding the supporting mechanism. It was observed that during the supporting of this sample, larger doses of 1 M base were used in order to adjust the pH of the solution. This may have led to pockets of caustic solution, at least for a brief amount of time, despite the vigorous stirring. Under strongly basic conditions the Al_2O_3 may have released aluminate ions into the solution, which because of their strong charge are very able to destabilize colloids. This may have led to the colloid agglomerating during adsorption, prompting the chain-like morphology. This hypothesis was tested thoroughly in a bachelor thesis, but no experiment could find significant amounts of dissolved alumina, even after extended amounts of exposure time. Therefore, dissolution of the support material, could be concluded to not have a significant impact on the formation of the chain-like agglomerates. After the first reaction and upon further ageing, the observed agglomerates disappear (cf. Figure 30). This can be most likely be attributed to sintering of the chain-like particles. Close

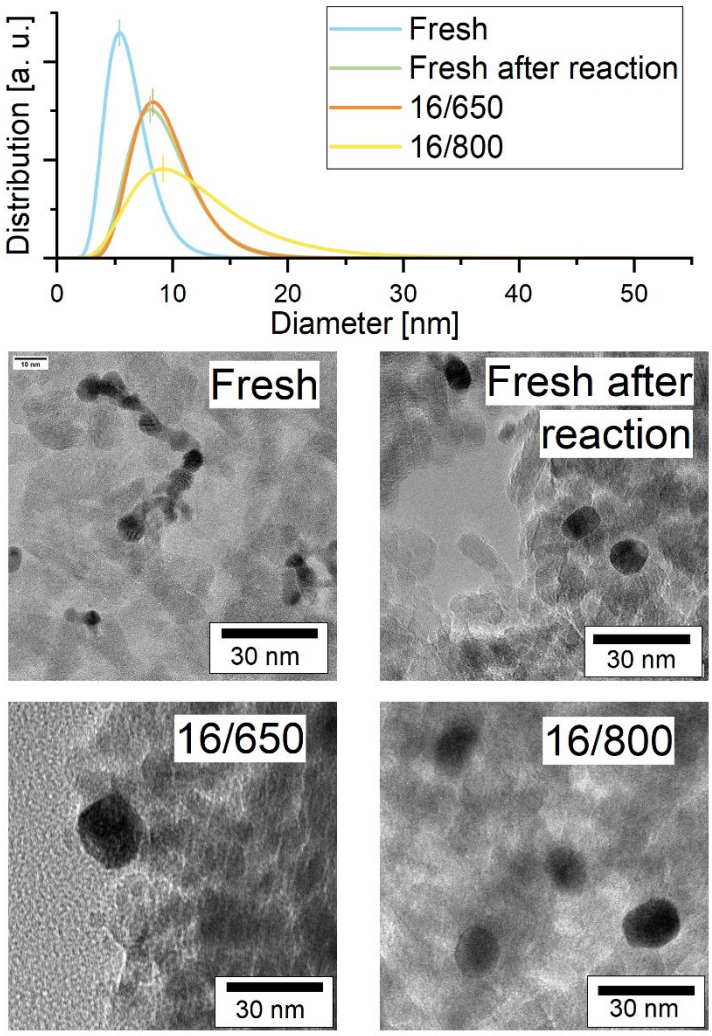

Figure 30 Ageing of the $Pt_{50}Au_{50}$ alloy. Shown are both the normalized size distribution and exemplary TEM images.

investigation of the particles also reveals that the aged samples reveal more pronounced crystal facets when compared to the initial spherical particles. Overall, the size distribution changes in a way that would be expected. The stronger the ageing conditions, the larger and wider the particle size distribution is. It can also be observed that the size distribution after reaction mostly matches the distribution found for the sample that was aged at 650°C. Since the sample is subjected to a similar reaction temperature (550°C), this would be somewhat expected, since the temperature difference is not too pronounced. Only the sample aged at 800°C shows significant particle growth again. This is not surprising from an ageing perspective, but it is surprising that this sample does not loose activity when compared to its lesser aged counterpart. From the obvious loss of active surface, it would be expected that the stronger aged sample exhibits less activity. This may be the result of a kind of elemental restructuring, exposing a more active surface on the same particles, which overcompensates the loss of particle surface area. A detailed look at TEM-EDX may reveal, if this hypothesis is valid.

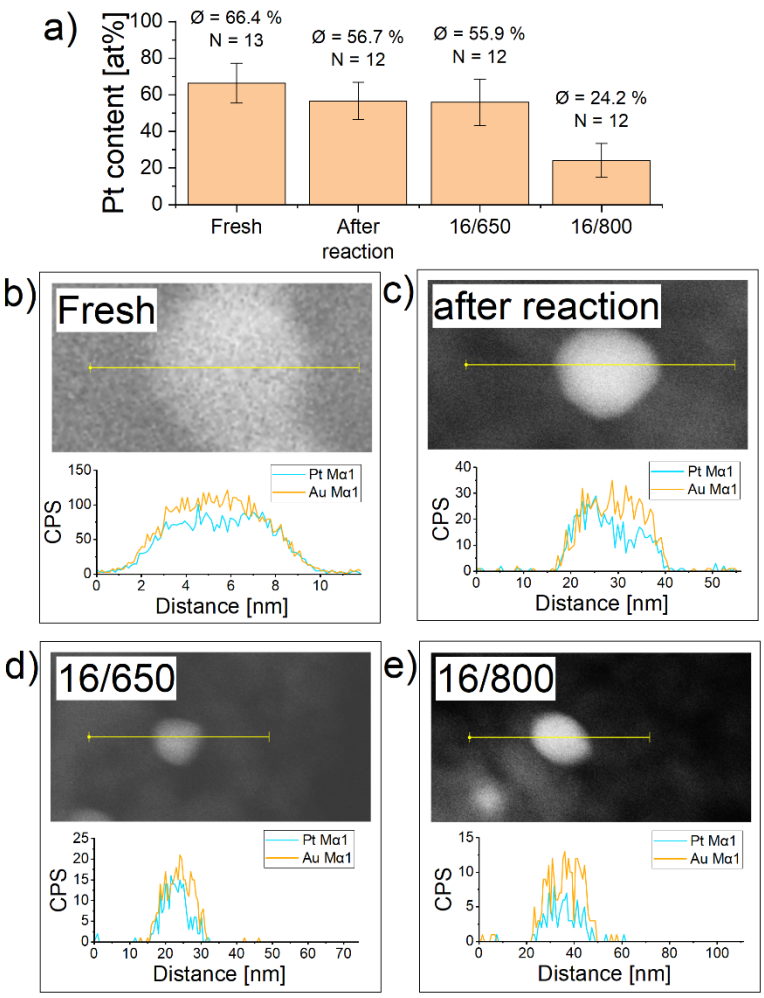

Figure 31 Ageing of the $Pt_{50}Au_{50}$ alloy. In a) the development of the mean platinum quantity (in at% via TEM-EDX) is plotted over the ageing steps. b), c), d), e) each shows a representative line scan TEM-EDX line scan of the alloyed particles.

Material distribution

Figure 31 shows the collected data regarding elemental distribution from HR-TEM-EDX. In a) the mean of the Pt-content of all measured particles is displayed. This shows that the particles of the fresh sample contain slightly elevated amounts of Pt, while the content slightly decreases for the sample already subjected to the first DOC reaction. The Pt content then stays constant for the sample aged at 650°C before ultimately decreasing to only 25% for the sample aged at 800°C. This does not match the observed activity trends. A reduced amount of Pt could explain, why the

sample aged at 650°C exhibits lower activity, but a further loss of Pt should lead to a decrease in activity upon stronger ageing. From studying the dependence on mixing ratio, it can be concluded, that higher Pt-contents correlate with higher catalyst activity (cf. S5.2.1 in A4). Interestingly, the elemental composition of each particle appears to be homogeneous overall. All throughout the samples only homogeneously alloyed particles can be found. This is especially notable, given the large mixing gap bulk Pt-Au exhibits in this region [157]. What is also surprising, is the lack of Pt-particles found. Assuming that elemental segregation takes place, Pt-rich particles should be found on the sample, yet none could be located. This may be attributed to the small sample size, but is notable, nonetheless. It could on the other hand also be possible, that the ageing protocol leads to a loss of Pt from the particles. This could happen, as Pt is known to form volatile oxides upon high-temperature oxidative treatment [32]. These volatile oxides may be carried away from the sample and lead to an overall loss of platinum from the catalyst. ICP-OES could be used to test for this loss, but it needs to be considered, that the amount of sample required for such an analysis is difficult to obtain. Finally, it needs to be considered that EDX is not ideally suited to differentiate between Pt and Au. Both, M and Lα emission lines are very near each other (M_{Pt} = 9.441 eV, M_{Au} = 9.712 eV; $L\alpha_{1\ Pt}$ = 2.048 eV, $L\alpha_{1\ Au}$ = 2.120 eV) [304]. This means that differentiating between these two elements is difficult and due to overlapping peaks the error for identification is particularly pronounced. Therefore, the findings of reduced Pt-content for the strongest aged sample and the overall surprising homogenous elemental distribution may be a result of this difficulty. It would be necessary to employ different methods to measure the elemental distribution within the nanoparticles. One option could be the use of an atom probe. Future studies working with Pt-Au should keep this in mind.

4.3.2 $Pt_{53}Ag_{47}$ in different Ageing Stages

From the bulk phase diagram, it was expected that Pt-Ag would not show segregating behaviour. An alloy of around 50 at% Ag is expected to form a stable bulk phase with Pt as shown in the phase diagram by Predel and as was revisited in detail by Hart et al. [305,306] (cf. Figure 22 in section 4.2.2). The obtained catalytical data in Figure 32 show that this alloy nevertheless does not exhibit high durability. Generally, the fresh sample is the most active sample with a light-up temperature around 225°C. The ageing at 650°C leads to a slight loss in durability with a light-up temperature for this sample around 245°C. The strongest ageing at 800°C, however, strongly deactivates the catalyst, which then achieves 50 % CO conversion only at 350°C. The “minima” observed at 200°C for the fresh and 210°C for the aged samples can most likely be attributed to the onset of hydrocarbon

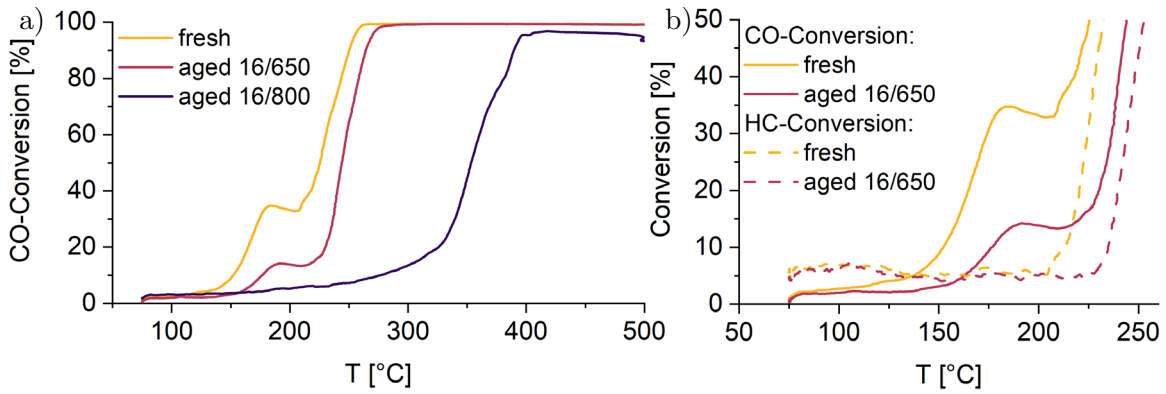

Figure 32 CO-conversion curves of Pt_{53}-Ag_{47} in all ageing states.

oxidation (cf. Figure 32 b)). This onset is slightly obscured by a baseline noise in the data but corresponds roughly with the minimum in CO-Oxidation. From literature it is known that some catalysts tend to incompletely combust hydrocarbons, resulting in the release of CO in a certain temperature range [307]. This results in the detector measuring the CO from hydrocarbon combustion in addition to the concentration that is already present, resulting in the observed curve progression.

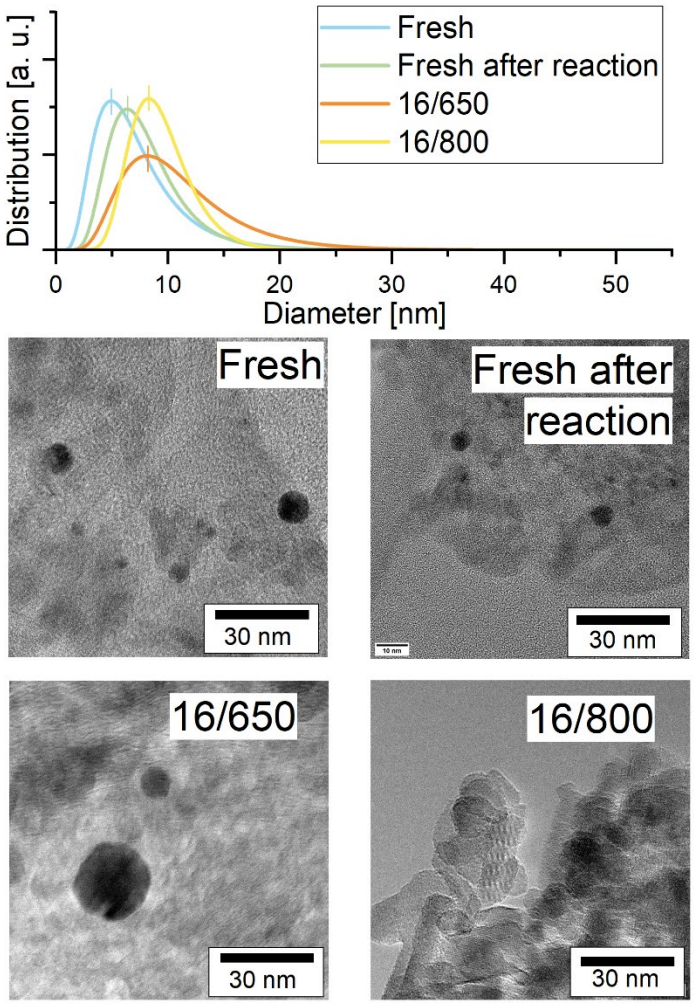

Figure 33 Ageing of the $Pt_{53}Ag_{47}$ alloy. Shown are both the normalized size distribution and exemplary TEM images.

The data presented in Figure 32 shows that the strongest aged samples should undergo a drastic reduction in active surface area. This could either be a result from particle growth or stem from elemental segregation as well as a loss of active substance.

Morphology and particle growth

Assessment of the particle morphology of the fresh sample shows a homogeneous loading of the alumina particles. Unlike Pt-Au no chain-like deposition is visible. Comparing the size distribution upon ageing indeed also reveals a particle growth. In contrast to Pt-Au, where the distributions from

the sample after DOC reaction and the one aged at 650°C were comparable, Pt-Ag shows a more gradual particle growth (cf. Figure 33). The peak of the distribution shifts from 5 nm for the fresh sample to 6.4 nm for the sample after DOC reaction. After this the size distribution shifts to 8 nm for the sample aged at 650°C. Unintuitively, this distribution is also the widest observed. It would be expected that the sample aged at 800°C has the widest distribution with the peak being shifted even further than the 8 nm. This it not something that can be observed here. In fact, the distribution of the strongest aged sample is a little narrower and the peak is virtually identical with the sample aged at 650°C. The significant loss of activity of the sample aged at 800°C therefore cannot be attributed to a loss of surface area, as this stays almost constant and appears mostly independent of pretreatment. A close inspection of the images nevertheless reveals, that subjecting the sample to reaction and thermal cycling produces more facetted particles. This morphology change is exceptionally well visible in the sample aged at 650°C. Part of the activity loss can possibly be attributed to loss of surface area, but the TEM data can only account for the activity decrease between fresh and slightly aged sample. This leaves material segregation or loss of active material as a possible reason for the loss of activity.

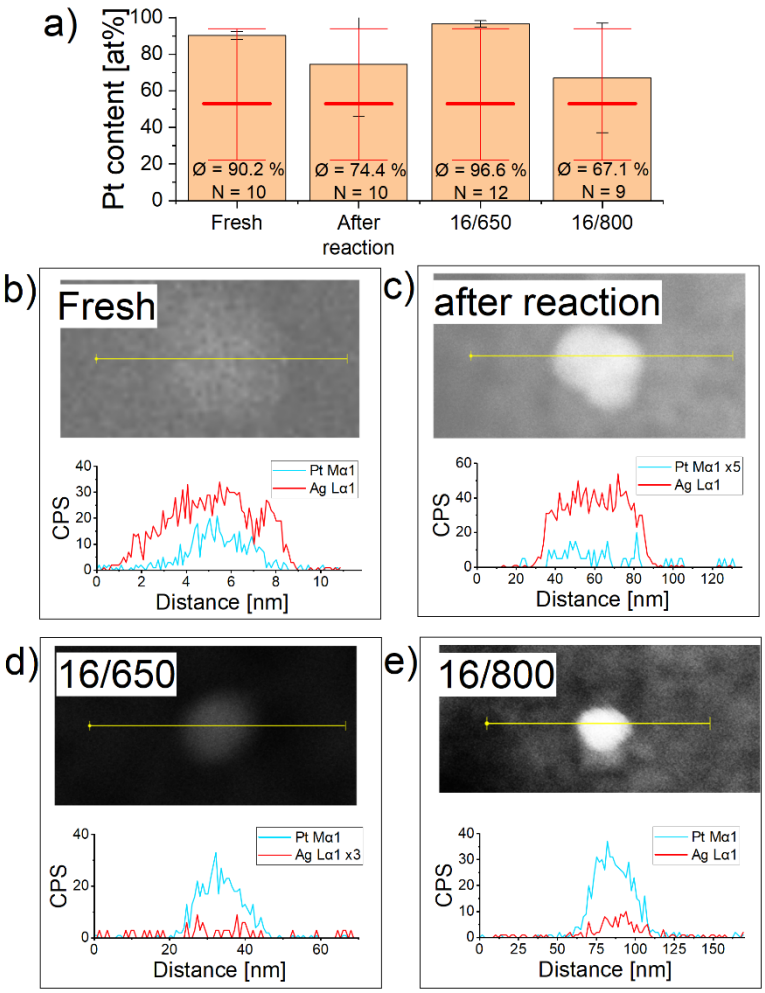

Figure 34 Ageing of the $Pt_{53}Ag_{47}$ alloy. In a) the development of the mean platinum quantity (in at% via TEM-EDX) is plotted over the ageing steps. b), c), d), e) each shows a representative line scan TEM-EDX line scan of the alloyed particles. Note that for improved visibility some line scans have been multiplied.

Material mixture

TEM-EDX evaluation of elemental composition and distribution in Figure 34 gives results that are very different from the expected values. Firstly, the elemental composition of almost all the particles measured deviates drastically from the target of 53 at.% Pt. The fresh sample appears to contain 90 at% of

Pt, with an apparent loss of platinum upon testing in DOC atmosphere resulting in a content of 74 at% Pt. The sample aged at 650°C then again appears to contain 96 at% Pt, while the sample that was aged most strongly shows less Pt at 67 at%, but still more than the mean concentration of 53 at%. Overall, the data gives an erratic image of elemental content. The particles, that were found, showed homogenous alloying, but the mixtures don't reflect what would be expected from ICP-OES (54 at% Pt). This could be the result of a sampling error during the TEM-EDX measurements. The tested samples are already supported on Al_2O_3, since that is what the catalyst tests were performed with. This means that particles for EDX evaluation need to be differentiated from the support material prior to measurement. Since this is mainly done by contrast, there is bound to be a bias towards Pt-rich particles. These particles show up much more clearly in the images because of platinum's high atomic weight in comparison to silver or alumina. It is well possible, that silver-rich particles are also present in the sample but were impossible to distinguish from the alumina background. Additionally, selection of particles is made increasingly difficult because smaller particles are hardly visible. This again reduces the likelihood of finding small particles as evidenced by comparison of the exemplary pictures Figure 34 b), c), d), e). the smallest shown and measured particle measures 6 nm in diameter and hardly stands out from the background, while particles, that are clearly visible are much larger and possibly don't reflect the majority of particles in the sample. Ultimately, a discussion based on these samples cannot be very reliable. Further measurements should be performed to clarify the composition of nanoparticles in the aged samples. This could be done via atom probe measurements for example. Results from chapter 4.2.2 also warrant a study focussing on the chemical surface composition of the nanoparticles. This could be achieved by subjecting the samples to x-ray photoelectron spectroscopy.

4.4 In depth Discussion of Ageing Trends

When selecting the alloying elements for platinum, some of the alloying elements were specifically chosen to slow down the ageing of the catalysts. It was assumed that the high melting point of an alloying element results in a reduced diffusion rate of the atoms. This property could be transferred to the alloy through the intermetallic bond and slow down nanoparticle growth by slowing surface diffusion. It is conceivable that both the movement of the nanoparticles on the support and the sintering of the particles are slowed down by surface, lattice and grain boundary diffusion. In addition, a reduced vapour pressure of the alloy with a refractory metal would slow down the vapour transport of the constituents, which would also be conducive to increased durability.

As the effect of ageing is particularly evident in CO oxidation, this reaction is used as a benchmark to test the hypothesis that high melting metals are beneficial for ageing. This is done by calculating the difference in LU_{50} temperatures between a fresh sample and one aged at 650 °C and plotting this against the melting point of the alloying element. This application avoids a strong overlap of the common high platinum alloys. It also eliminates difficulties of interpretation arising from the phase diagram based theoretical melting point of the alloy. The effect of the alloying element becomes more apparent.

As briefly discussed in chapter 4.1, alloying elements with a low melting point, such as silver, gold, copper and manganese, show a large temperature difference between fresh and aged samples - a strong ageing. An alloy of Pt with Pd shows reasonable durability and, with the exception of rhodium, all the alloying elements with a higher melting point, such as ruthenium, niobium, molybdenum, show small temperature differences and therefore high durability. Overall, there is also a strong scatter within the selected compositions, which on the one hand is due to the large mixing interval (e.g. silver). On the other hand, synergetic effects are also visible. For example, the Pt-Fe alloy at 50 at% shows an activation that is also present in other reactions tested (cf. S5.2.1 in A4). The dependence of the durabilty on the melting point suggests that the ageing of the catalysts is a diffusion driven process, which is at least partly related to the melting temperature. The reorganisation of the particles, i.e., both the restructuring of the particle surface and potential particle growth, is only possible through the movement of atoms. The slower this movement, the less restructuring takes place, which is reflected in increased durability.

A simplified representation of the possible atomic motions is shown in Figure 35. In a particle containing a thermodynamically unstable mixture of elements, there is a directed volume diffusion D_V within the particle. This volume diffusion leads to a restructuring of the particle surface due to the locally changing material mixture. Two different diffusion processes can take place on the surface of the particle. On the one hand, the atoms can diffuse along the particle surface (surface diffusion D_O), on the other hand, evaporation with subsequent vapour diffusion D_D is conceivable. As a result of surface diffusion, diffusion

along the support particle surface D_{Tr} can also occur. In principle, it is also possible for whole nanoparticles to diffuse on the support (D_P).

In order to estimate which of these diffusion processes mainly influence the aggregation of the particles, a rough estimate of the relevance of the material transport channels can be made.

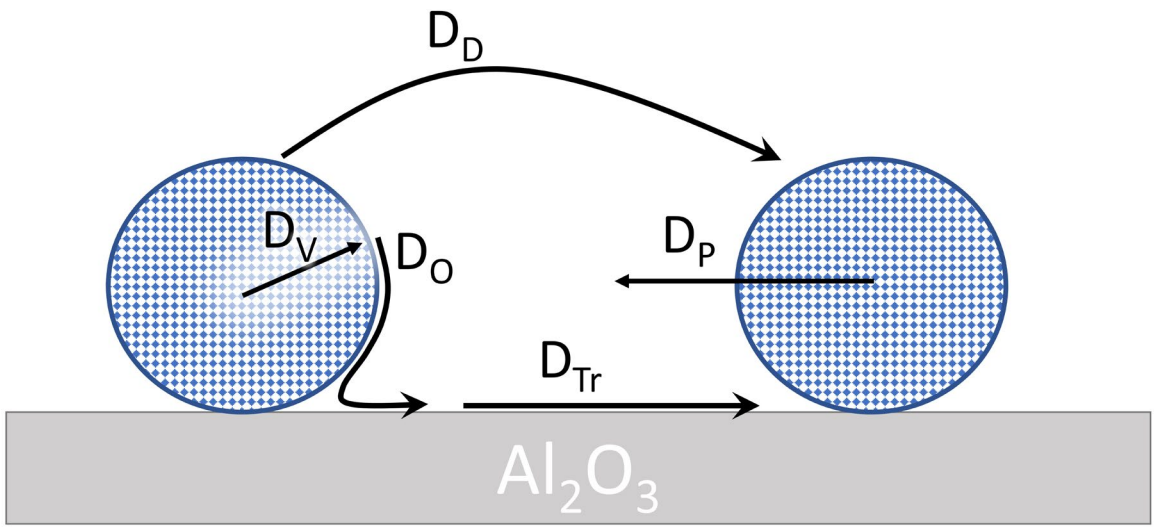

Figure 35 Sketch of the possible diffusion processes that can lead to reorganisation of the particles on the support.

Insert: Vapour pressure deviation in the nanoscale

The Gibbs-Thomson effect describes the increase in vapour pressure due to the strong surface curvature of nanoparticles. The saturation vapour pressure p_{sat} increases exponentially as the particle radius r decreases. This relationship is described by the following equation (cf. e.g., [308]):

$$p = p_{sat} \exp\left(\frac{r_{crit}}{r}\right) \tag{4.1}$$

Here, r_{crit} denotes a critical material-dependent radius that strongly influences the increase in vapour pressure. This radius depends on the surface tension of the material γ, the volume of a molecule in the particle V and the temperature T, as well as the Boltzmann constant k_B:

$$r_{crit} = \frac{2\gamma V_{molecule}}{k_B T} \tag{4.2}$$

To estimate the critical radius, the molecular volume is estimated via the covalent radius r_{cov} of the metals:

$$V_{molecule} = \frac{4}{3}\pi r_{cov}^{\ 3} \tag{4.3}$$

Table 1 summarises the relevant material values and resulting findings.

Table 1 Vapour pressure increase due to Gibbs-Thomson effect.

Alloying Metal	Gold	Molybdenum
Durability	Strong aging	Weak aging
Vapour pressure (@ 600°C) [bar] [69]	6.3E-16	3.5E-32
Surface tension [J/cm²] [309]	1,5	3
Covalent radius [pm] [310]	124	138
Critical radius [nm]	2	5,5
Assumed particle radius [nm]	3	3
Vapour pressure increase (factor)	**1.9**	**6.2**

By means of the Hertz-Knudsen equation (4.4), the expected evaporation rate can be estimated for the case of a surrounding vacuum. [311]

$$\frac{dN}{dt} = \frac{C}{\sqrt{2\pi MRT}}\left(p^* - p\right) \tag{4.4}$$

Here, C is a constant that depends on the number of rotational degrees of freedom in the liquid and gas, M is the molar mass of the evaporating species, R is the universal gas constant and T is the ambient temperature. p^* and p are the vapour pressure of the evaporating material and the pressure at the surface respectively. To estimate the maximum evaporation rate, the number of degrees of freedom assumed to be maximum (i.e., C=1) and that of the surface pressure is assumed to be 0 Pa. The final result for gold is an evaporation rate of about 255 pg/(m²s) (molybdenum: 31E-15 pg/(m²s)). Even under ideal conditions (vacuum), evaporation is therefore not significantly fast (i.e., evaporation of 10% of the particle mass would need between 87 days (gold) and 106E12 days (molybdenum)).

The lower the bonding of the elements to each other, the higher the diffusion speed generally turns out to be. This means that the highest diffusion coefficients should be assumed for vapour diffusion. However, this presumes that the metals of the nanoparticles enter the gas phase at all. As an example, gold is therefore considered as a strongly ageing metal with

low melting temperature and molybdenum as a hardly ageing metal with high melting temperature (both representing Pt-Au and Pt-Mo respectively). With 6E-16 bar (gold) and 3E-32 bar (molybdenum) the vapour pressures show the extremely low tendency of the metals to vaporise at reaction conditions (600°C) [312]. Even the presence of the metals as nanoparticles has no significant effect on the increase in vapour pressure. The Gibbs-Thomson effect does cause a two- to six-fold increase in vapour pressure, but this is not nearly enough to raise the low vapour pressure to a relevant level. As was demonstrated in the previous insert, a rough estimate of the evaporation rate using the Hertz-Knudsen equation also shows negligibly small values. Therefore, pure vapour diffusion probably does not play a significant role.

Table 2 Reaction conditions for the formation of metal carbonyls.

Metal	Mn [313]	Fe [314]	Rh [313]	Ru [313]	Mo [313]
Necessary intermediate	Mn(II)-salt	Metal	Chloride[1]	Chloride	Chloride
Typical reaction temperature [°C]	100	150-200	60	145	100
Typical CO-pressure [bar]	300	100	40	120	150

Apart from vapour diffusion, another gas-based pathway for material transport is conceivable. A reaction of the metals with CO in the gas stream could lead to carbonyl formation. Many carbonyls would be volatile at the reaction temperature of 600°C and could therefore drive material transport.

Table 2 shows typical reaction conditions for the formation of the relevant metal carbonyls. It can be seen that the formation of the carbonyls can only take place under high CO partial pressure and in all cases, apart from iron, chlorine compounds of the metals are required. A formation of volatile metal carbonyls can therefore very probably also be excluded. Material transport via the carbonyl-route thus generally seems to play a minor role. In addition to that, gold does not form carbonyls under reaction conditions [315], but Pt-Au still exhibits low durability.

Particle diffusion D_P can probably also be placed in the same category. Just by taking into account the orders of magnitude higher mass compared to atoms, only a very low diffusion is to be expected. Surface diffusion of particles on the other hand would result in characteristic agglomerates on the surface. Woehl et al demonstrated for 30 nm gold

[1] Or much more complex via $[RhCl(CO)_2]_2$ or $Rh_2(CH_3CO_2)_4$.

particles that adsorption to each other initially leads to the formation of elongated and subsequently star-shaped agglomerates [316]. Once this has occurred, sintering of the particles at elevated temperatures would lead to larger, more rounded particles. As examples, Pt-Au und Pt-Ag particles were examined in different ageing stages. A characteristic particle shape could not be found in the aged samples (cf. chapter 4.3). In fact, the examination of the particles most likely indicates volume or surface diffusion. This also manifests itself in the formation of clear crystal facets. To form these facets, there must be diffusion in the particle and on its surface.

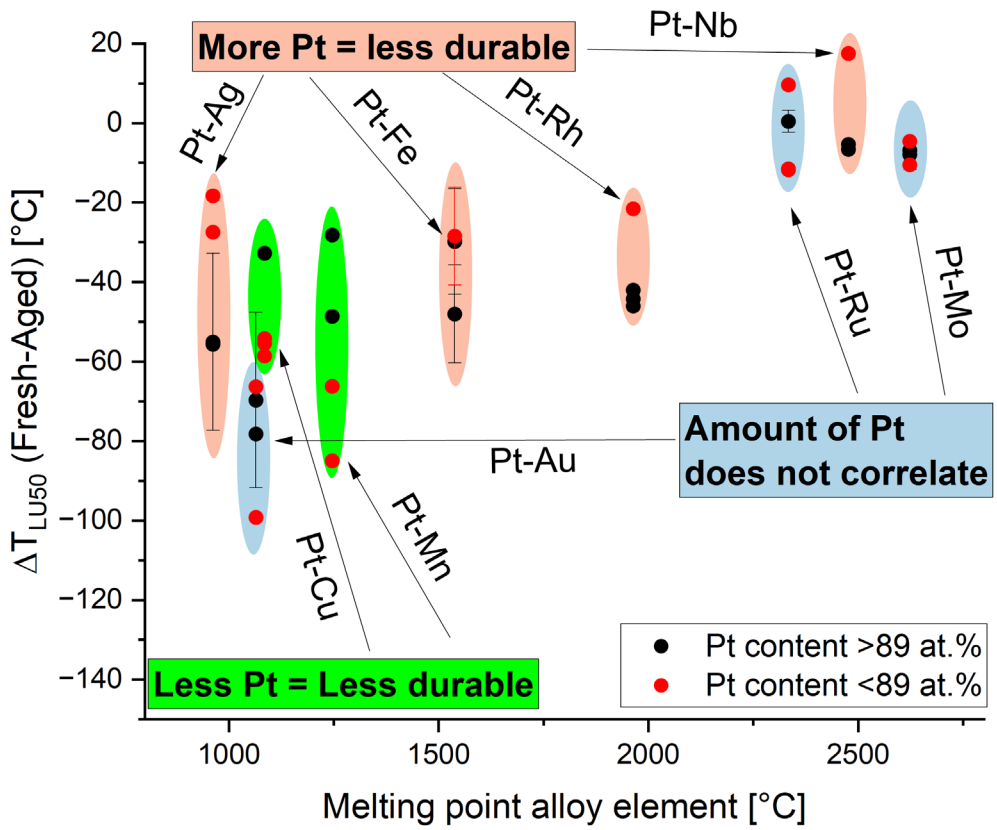

Figure 36 Durability of Pt-containing alloys in CO oxidation, plotted against the melting point of the alloying element (Pt+**X**) and distinguishing the Pt-content.

Since particle growth via the surface D_O and subsequent support diffusion D_{Tr} seems rather exotic, Ostwald ripening via the gas phase is still the most likely process by which the samples age. This is particularly likely, when considering, that most tested catalysts have a significant platinum content. It is known from literature that Pt can oxidise to form PtO_2, which is known to have a low vapour pressure and is therefore a mobile species [271]. In certain alloy combinations this diffusion path is hindered by the species formed from the alloy particle. For example, Rappe et al. reported segregation of PdO from Pt-Pd particles under high temperature and oxidative conditions [63]. A similar mechanism was reported by Carrillo et al., who showed capturing of mobile PtO_2 species on PdO particles which could explain the observed excellent durability of a Pt-Pd catalyst [32].

In order to disseminate the influence of Pt-content in this screening study, the durability within the CO-oxidation was plotted in Figure 36, while highlighting, if the alloys have a high (>89 at%) or low (<89 at%) Pt-content. When evaluating the durability patterns, three groups emerge. In the first group, a high Pt-content seems to correlate with reduced durability. This trend is evident for alloys of Pt with Ag, Fe, Rh and Nb. In the second group a low Pt-content seems to correlate with reduced durability (Pt-Cu, Pt-Mn). While in the third group there is no clear correlation (Pt-Au, Pt-Ru, Pt-Mo). On the basis, that Pt oxidises to a mobile species under reaction conditions, alloys with a high Pt content should be particularly susceptible to material loss and ageing unless the Pt is stabilized by a second species (as shown for Pt-Pd). This appears to be a cause of activity loss in the Pt-Ag, Pt-Fe, Pt-Rh and Pt-Nb alloys, as these alloys are possibly not able to resist the migration of PtO_2 once formed. The other two groups seem to have the ability to stabilize the platinum, either because there is no correlation to the content (Pt-Au, Pt-Ru, Pt-Mo) or because a higher durability is correlated with a high Pt-content (Pt-Cu, Pt-Mn). As 50:50 mixtures of Pt-Au (possible stabilizing influence) and Pt-Ag (possibly no stabilizing influence) were evaluated in more detail, the results can be considered here. Unfortunately, the quality of data obtained for Pt-Ag and Pt-Au does not allow for a founded discussion here. The data for Pt-Ag shows mostly Pt-rich particles, even upon ageing, which is not consistent with the hypothesis formulated here. Since this is most likely an artifact of the measurement method, the measurement of elemental composition needs to be revisited. From this hypothesis the samples should show a loss of Pt upon ageing. The same is true for Pt-Au. While the TEM-EDX measurements indicate a loss of Pt with stronger ageing, this loss may be a measurement artifact. This artifact stems from the fact that Pt and Au have very similar EDX peaks, making discrimination between the two extremely difficult. Ultimately, this highlights the need for further investigation into the ageing behaviour of alloys that can now be selected on the basis of the patterns found in this study.

5 Summary and Outlook

There is a need for high performance exhaust treatment catalysts to meet increasingly stringent emission regulations. While elemental noble metals and some binary alloys have been tested and used in oxygen-rich catalytic environments ($\lambda > 1$) relevant to commercial diesel oxidation catalysis, pure or alloyed Pt and Pd remain the main catalysts for diesel emission control. This study aims to extend the compositional knowledge base by synthesising 45 binary alloys of platinum and selected first-row transition, platinum group and coin metal elements. The compositions have been selected from literature studies, which have mostly considered monometallic catalysts for exhaust gas treatment. The screening is made possible by a scalable laser synthesis method that allows rapid and robust compositional screening of alloy nanoparticles. This method is becoming increasingly available through commercial synthesis machines, which are fully enclosed, automated and benchtop sized [317–319]. The prepared catalysts were tested in an industrial test environment consisting of one DOC and two ASC gas mixtures. In addition, two ageing regimes were measured, providing activity data for three ageing states of each catalyst, allowing the identification of associated composition-activity and composition-durability correlations of each test environment.

An individual comparison of all systems shows that for DOC the most promising activities are demonstrated by alloys of Pt-Cu, Pt-Mo and Pt-Pd. Although lacking the best activity after aging, Pt-Cu and Pt-Mo as well as Pd-Cu have a very low dependency of the activity on the composition, which makes them economically interesting. A similar comparison for ASC shows that promising compositions are Pt-Nb, Pt-Ru, Pt-Fe and Pt-Mn. This is due to their high selectivity for N_2 and their high activity over most of their mixing range. Comparing the results with the initial hypotheses gives a mixed picture. While Pt-Rh alloys were expected to show high activity based on the literature on $\lambda = 1$ environments [9], this could not be verified. This may be due to rhodium oxidation deactivating the catalyst as reported in the literature [12] and is consistent with the observation that only Pt-rich

catalysts were active. Pt-Ag and Pt-Au alloys were selected for their expected ability to withstand the wet exhaust gas stream. However, the measured activities for these alloys did not reflect a particularly good resistance to water or ageing in general. Similar to the observation in DOC, alloys of Pt-Cu and Pd-Cu showed good activity, with Pt-Cu exceeding Pd-Cu. In addition, the activity of both alloys is hardly correlated with the composition, making them an ideal choice from an economic point of view. Both Pt-Mn and Pt-Fe were chosen for their high ammonia oxidation activity, which they also showed in the experiments. Both performed well in DOC and ASC, and alloys with Fe were selective for N_2 in ASC, as proposed. Pt-Ru was chosen because Ru has a high selectivity for N_2. This selectivity was observed albeit high activity needed high Pt-contents. This is consistent with the hypothesis that Pt ennobles Ru and limits the formation of ruthenium oxides, which are inactive. Manufacturing constraints prevented the use of low Au content targets for the Au-Ir and Au-Rh systems (due to a large difference in melting and hence sintering temperature). The initial hypothesis was that with increasing gold content in the Au-Ir and Au-Rh catalysts, the rate of formation of nitrogen oxides would decrease due to the activity moderating effect of gold. However, the latter proved to significantly deactivate the catalysts at the high gold contents of this study. Nevertheless, similar Au-Ir and Au-Rh catalysts with gold contents below 50 at% may still be promising material systems.

Part of the work for this thesis focused on optimising the supporting of nanoparticles from a solvent. One route tested was by destabilizing the colloids through the addition of salts. Although the salts used were not soluble, they were found to be able to destabilise the nanoparticles which, under the right conditions, resulted in the nanoparticles being supported on the support particles. The novelty of this finding led to a patent application supported by Umicore.

The catalytic results were also published in a peer-reviewed journal [320]. These results include the finding that the catalyst activity in DOC does not correlate with the heat of adsorption of CO, but rather with the heat of adsorption of molecular oxygen. The latter showed a volcano-like dependence with the maximum activity being shifted by 1 eV towards higher oxygen binding, when compared to DFT studies. In the publication this was attributed to the complex gas mixtures compared to the literature. The disappearance of this correlation with ageing was attributed to elemental segregation, which is likely to occur by oxidation as well as passivation and formation of volatile oxides for the same reason. Within this publication the durability of catalysts was also analysed. It was shown that there is a significant positive correlation between the melting point of the alloying metal (Pt+**X**) and the difference in activity between fresh and aged samples in DOC, and that the type of element is more important for the durability than the amount used. The

dependence on the platinum content was then further investigated in this thesis, showing that there are alloys which appear to stabilize the Pt in a manner similar to literature (i.e., Pt-Au, Pt-Ru, Pt-Mo, Pt-Cu and Pt-Mn), while others do not possess this ability (i.e., Pt-Ag, Pt-Fe, Pt-Rh and Pt-Nb).

In evaluating the ASC results, it was evident, that no scaling relationships were found with respect to the heat of adsorption of NO. While this contradicts the literature which shows (for simpler gas mixtures and Pt) that NO desorption is the rate-limiting step, it also highlights the importance of testing the catalysts in a test environment that most closely mimics the one found in exhaust gas abatement. The study also allowed the catalysts to be grouped into alloys favouring N_2/NO_2 and alloys favouring NO/N_2O. The deciding factor appeared to be the heat of adsorption of oxygen, with alloys with a higher heat of adsorption than rhodium favouring the former and the others favouring the latter. The underlying factor may be attributed to the reaction mechanism, with the i-SCR-mechanism favouring NO and the imide-mechanism favouring NO_2.

In summary this screening study illustrates the importance of testing catalysts close to their intended application, as this allows for better identification of the correct influencing factors, that could not be interpolated from the literature (as seen in particular for ASC). The possibility of replacing large proportions of precious metals with base metals has been demonstrated (e.g., Pt-Cu, Pd-Cu), while durability limitations require further development. However, important conclusions have also been drawn with regard to durability. In particular, DOC catalysts benefit from a certain amount of refractory metal as an alloying component. A reasonable research approach would be the synthesis of ternary alloys (e.g., Pt-Cu-Mo or Pt-Cu-Nb) and the extension to multinary alloys consisting of Pt and combinations of Cu, Mo, Nb and Mn. Laser synthesis has already been shown to be capable of providing complex high-entropy alloys [45,154,321]. In addition, this approach would follow research efforts in tree-way catalysis, where high-entropy alloys are already being studied [21,22].

References

[1] Umweltbundesamt, Grenzwerte für Schadstoffemissionen von PKW, (2018). https://www.umweltbundesamt.de/sites/default/files/medien/376/bilder/dateien/tabelle_grenzwerte_fuer_schadstoffemissionen_von_pkw.pdf (accessed March 21, 2023).

[2] Environmental Protection Agency, Control of Air Pollution From Motor Vehicles : Tier 3 Motor Vehicle ACTION, 79 (2018) 23414–23886. https://www.govinfo.gov/content/pkg/FR-2014-04-28/pdf/2014-06954.pdf.

[3] P. Granger, Challenges and breakthroughs in post-combustion catalysis: how to match future stringent regulations, Catal. Sci. Technol. 7 (2017) 5195–5211. doi:10.1039/C7CY00983F.

[4] I. Lebrusán, J. Toutouh, Car restriction policies for better urban health: a low emission zone in Madrid, Spain, Air Qual. Atmos. Heal. 14 (2021) 333–342. doi:10.1007/s11869-020-00938-z.

[5] C. Descorme, P. Gallezot, C. Geantet, C. George, Heterogeneous Catalysis: A Key Tool toward Sustainability, ChemCatChem. 4 (2012) 1897–1906. doi:10.1002/cctc.201200483.

[6] K. Reif, Dieselmotor-Management, Vieweg+Teubner Verlag, Wiesbaden, 2012. doi:10.1007/978-3-8348-2179-9.

[7] B. Giechaskiel, A.A. Zardini, M. Clairotte, Exhaust Gas Condensation during Engine Cold Start and Application of the Dry-Wet Correction Factor, Appl. Sci. 9 (2019) 2263. doi:10.3390/app9112263.

[8] R. Sun, E. Jack Sweet, J.R. Zurlo, W.C. Pfefferle, Diesel Engine Cold Starting with Catalytically Ignited Recirculated Exhaust Gas, in: SAE Tech. Pap., 1994: pp. 18–31. doi:10.4271/940086.

[9] A. Russell, W.S. Epling, Diesel Oxidation Catalysts, Catal. Rev. 53 (2011) 337–423. doi:10.1080/01614940.2011.596429.

[10] G. Koltsakis, Catalytic automotive exhaust aftertreatment, Prog. Energy Combust. Sci. 23 (1997) 1–39. doi:10.1016/S0360-1285(97)00003-8.

[11] D. Bosteels, R.A. Searles, Exhaust emission catalyst technology, Platin. Met. Rev. 46 (2002) 27–36.

[12] C. Hagelüken, Autoabgaskatalysatoren, 3., expert-verlag, Rennigen, 2016.

[13] M.M. Montemore, M.A. van Spronsen, R.J. Madix, C.M. Friend, O 2 Activation by Metal Surfaces: Implications for Bonding and Reactivity on Heterogeneous Catalysts, Chem. Rev. 118 (2018) 2816–2862. doi:10.1021/acs.chemrev.7b00217.

[14] G. Marzun, A. Levish, V. Mackert, T. Kallio, S. Barcikowski, P. Wagener, Laser synthesis, structure and chemical properties of colloidal nickel-molybdenum nanoparticles for the substitution of noble metals in heterogeneous catalysis, J. Colloid Interface Sci. 489 (2017) 57–67. doi:10.1016/j.jcis.2016.09.014.

[15] V. Stamenković, T.J. Schmidt, P.N. Ross, N.M. Marković, Surface Composition Effects in Electrocatalysis: Kinetics of Oxygen Reduction on Well-Defined Pt 3 Ni and Pt 3 Co Alloy Surfaces, J. Phys. Chem. B. 106 (2002) 11970–11979. doi:10.1021/jp021182h.

[16] J. Greeley, I.E.L. Stephens, A.S. Bondarenko, T.P. Johansson, H.A. Hansen, T.F. Jaramillo, J. Rossmeisl, I. Chorkendorff, J.K. Nørskov, Alloys of platinum and early transition metals as oxygen reduction electrocatalysts, Nat. Chem. 1 (2009) 552–556. doi:10.1038/nchem.367.

[17] Y. Bing, H. Liu, L. Zhang, D. Ghosh, J. Zhang, Nanostructured Pt-alloy electrocatalysts for PEM fuel cell oxygen reduction reaction, Chem. Soc. Rev. 39 (2010) 2184. doi:10.1039/b912552c.

[18] H.A. Gasteiger, S.S. Kocha, B. Sompalli, F.T. Wagner, Activity benchmarks and requirements for Pt, Pt-alloy, and non-Pt oxygen reduction catalysts for PEMFCs, Appl. Catal. B Environ. 56 (2005) 9–35. doi:10.1016/j.apcatb.2004.06.021.

[19] A.K. Singh, Q. Xu, Synergistic Catalysis over Bimetallic Alloy Nanoparticles, ChemCatChem. 5 (2013) 652–676. doi:10.1002/cctc.201200591.

[20] B.J. Plowman, B. Sidhureddy, S. V. Sokolov, N.P. Young, A. Chen, R.G. Compton, Electrochemical Behavior of

Gold-Silver Alloy Nanoparticles, ChemElectroChem. 3 (2016) 1039–1043. doi:10.1002/celc.201600212.

[21] T. Hirakawa, Y. Shimokawa, W. Tokuzumi, T. Sato, M. Tsushida, H. Yoshida, J. Ohyama, M. Machida, Multicomponent 3d Transition-Metal Nanoparticles as Catalysts Free of Pd, Pt, or Rh for Automotive Three-Way Catalytic Converters, ACS Appl. Nano Mater. 3 (2020) 9097–9107. doi:10.1021/acsanm.0c01769.

[22] K. Kusada, D. Wu, Y. Nanba, M. Koyama, T. Yamamoto, X.Q. Tran, T. Toriyama, S. Matsumura, A. Ito, K. Sato, K. Nagaoka, O. Seo, C. Song, Y. Chen, N. Palina, L.S.R. Kumara, S. Hiroi, O. Sakata, S. Kawaguchi, Y. Kubota, H. Kitagawa, Highly Stable and Active Solid-Solution-Alloy Three-Way Catalyst by Utilizing Configurational-Entropy Effect, Adv. Mater. 33 (2021) 2005206. doi:10.1002/adma.202005206.

[23] Z. Guo, B. Liu, Q. Zhang, W. Deng, Y. Wang, Y. Yang, Recent advances in heterogeneous selective oxidation catalysis for sustainable chemistry, Chem. Soc. Rev. 43 (2014) 3480. doi:10.1039/c3cs60282f.

[24] S. Dittrich, S. Kohsakowski, B. Wittek, C. Hengst, B. Gökce, S. Barcikowski, S. Reichenberger, Increasing the Size-Selectivity in Laser-Based g/h Liquid Flow Synthesis of Pt and PtPd Nanoparticles for CO and NO Oxidation in Industrial Automotive Exhaust Gas Treatment Benchmarking, Nanomaterials. 10 (2020) 1582. doi:10.3390/nano10081582.

[25] Y. Wei, Z. Zhao, B. Jin, X. Yu, J. Jiao, K. Li, J. Liu, Synthesis of AuPt alloy nanoparticles supported on 3D ordered macroporous oxide with enhanced catalytic performance for soot combustion, Catal. Today. 251 (2015) 103–113. doi:10.1016/j.cattod.2014.08.034.

[26] M.-J. Kim, H.J. Kim, S.-J. Lee, I.-S. Ryu, H.C. Yoon, K.B. Lee, S.G. Jeon, Promotion of N2O decomposition by Zr4+-doped CeO2 used as support of Rh catalyst, Catal. Commun. 130 (2019) 105764. doi:10.1016/j.catcom.2019.105764.

[27] F. Dong, K. Yamazaki, The Pt-Pd alloy catalyst and enhanced catalytic activity for diesel oxidation, Catal. Today. 376 (2021) 47–54. doi:10.1016/j.cattod.2020.08.019.

[28] S. Swislocki, K. Stöwe, W.F. Maier, Chromia on Anatase: A Catalyst for Selective Hydrocarbon Combustion in the Presence of CO, ChemCatChem. 7 (2015) 261–270. doi:10.1002/cctc.201402769.

[29] G. Marzun, C. Streich, S. Jendrzej, S. Barcikowski, P. Wagener, Adsorption of Colloidal Platinum Nanoparticles to Supports: Charge Transfer and Effects of Electrostatic and Steric Interactions, Langmuir. 30 (2014) 11928–11936. doi:10.1021/la502588g.

[30] A. Gremminger, J. Pihl, M. Casapu, J.-D. Grunwaldt, T.J. Toops, O. Deutschmann, PGM based catalysts for exhaust-gas after-treatment under typical diesel, gasoline and gas engine conditions with focus on methane and formaldehyde oxidation, Appl. Catal. B Environ. 265 (2020) 118571. doi:10.1016/j.apcatb.2019.118571.

[31] D. Kunwar, S. Zhou, A. DeLaRiva, E.J. Peterson, H. Xiong, X.I. Pereira-Hernández, S.C. Purdy, R. ter Veen, H.H. Brongersma, J.T. Miller, H. Hashiguchi, L. Kovarik, S. Lin, H. Guo, Y. Wang, A.K. Datye, Stabilizing High Metal Loadings of Thermally Stable Platinum Single Atoms on an Industrial Catalyst Support, ACS Catal. 9 (2019) 3978–3990. doi:10.1021/acscatal.8b04885.

[32] C. Carrillo, T.R. Johns, H. Xiong, A. DeLaRiva, S.R. Challa, R.S. Goeke, K. Artyushkova, W. Li, C.H. Kim, A.K. Datye, Trapping of Mobile Pt Species by PdO Nanoparticles under Oxidizing Conditions, J. Phys. Chem. Lett. 5 (2014) 2089–2093. doi:10.1021/jz5009483.

[33] Z.P. Liu, P. Hu, General trends in the barriers of catalytic reactions on transition metal surfaces, J. Chem. Phys. 115 (2001) 4977–4980. doi:10.1063/1.1403006.

[34] W. Huang, G. Sun, T. Cao, Surface chemistry of group IB metals and related oxides, Chem. Soc. Rev. 46 (2017) 1977–2000. doi:10.1039/C6CS00828C.

[35] F.B. de Mongeot, U. Valbusa, M. Rocca, Oxygen adsorption on Ag(111), Surf. Sci. 339 (1995) 291–296. doi:10.1016/0039-6028(95)00594-3.

[36] A.. Carley, P.. Davies, M.. Roberts, K.. Thomas, Hydroxylation of molecularly adsorbed water at Ag(111) and Cu(100) surfaces by dioxygen: photoelectron and vibrational spectroscopic studies, Surf. Sci. 238 (1990) L467–L472. doi:10.1016/0039-6028(90)90056-E.

[37] T. Jiang, D.J. Mowbray, S. Dobrin, H. Falsig, B. Hvolbæk, T. Bligaard, J.K. Nørskov, Trends in CO Oxidation Rates for Metal Nanoparticles and Close-Packed, Stepped, and Kinked Surfaces, J. Phys. Chem. C. 113 (2009) 10548–10553. doi:10.1021/jp811185g.

[38] V.. Sadykov, L.. Isupova, I.. Zolotarskii, L.. Bobrova, A.. Noskov, V.. Parmon, E.. Brushtein, T.. Telyatnikova, V.. Chernyshev, V.. Lunin, Oxide catalysts for ammonia oxidation in nitric acid production: properties and perspectives, Appl. Catal. A Gen. 204 (2000) 59–87. doi:10.1016/S0926-860X(00)00506-8.

[39] S. Dahl, A. Logadottir, C.J.H. Jacobsen, J.K. Nørskov, Electronic factors in catalysis: the volcano curve and the effect of promotion in catalytic ammonia synthesis, Appl. Catal. A Gen. 222 (2001) 19–29. doi:10.1016/S0926-860X(01)00826-2.

[40] H. Over, Surface Chemistry of Ruthenium Dioxide in Heterogeneous Catalysis and Electrocatalysis: From Fundamental to Applied Research, Chem. Rev. 112 (2012) 3356–3426. doi:10.1021/cr200247n.

[41] X. Cui, J. Zhou, Z. Ye, H. Chen, L. Li, M. Ruan, J. Shi, Selective catalytic oxidation of ammonia to nitrogen over mesoporous CuO/RuO2 synthesized by co-nanocasting-replication method, J. Catal. 270 (2010) 310–317. doi:10.1016/j.jcat.2010.01.005.

[42] T. Zhang, S.M. Driver, S.J. Pratt, D.A. King, Spillover of oxygen adatoms from Ir to Au on an Ir/Au{111} bimetallic surface, Surf. Sci. 615 (2013) 1–5. doi:10.1016/j.susc.2013.04.004.

[43] C.-Y. Shih, C. Chen, C. Rehbock, A. Tymoczko, U. Wiedwald, M. Kamp, U. Schuermann, L. Kienle, S. Barcikowski, L. V. Zhigilei, Limited Elemental Mixing in Nanoparticles Generated by Ultrashort Pulse Laser Ablation of AgCu Bilayer Thin Films in a Liquid Environment: Atomistic Modeling and Experiments, J. Phys. Chem. C. 125 (2021) 2132–2155. doi:10.1021/acs.jpcc.0c09970.

[44] R.G. Nikov, N.N. Nedyalkov, R.G. Nikov, D.B. Karashanova, Nanosecond laser ablation of Ag–Au films in water for fabrication of nanostructures with tunable optical properties, Appl. Phys. A. 124 (2018) 847. doi:10.1007/s00339-018-2272-3.

[45] F. Waag, Y. Li, A.R. Ziefuß, E. Bertin, M. Kamp, V. Duppel, G. Marzun, L. Kienle, S. Barcikowski, B. Gökce, Kinetically-controlled laser-synthesis of colloidal high-entropy alloy nanoparticles, RSC Adv. 9 (2019) 18547–18558. doi:10.1039/C9RA03254A.

[46] D. Zhang, B. Gökce, S. Barcikowski, Laser Synthesis and Processing of Colloids: Fundamentals and Applications, Chem. Rev. 117 (2017) 3990–4103. doi:10.1021/acs.chemrev.6b00468.

[47] A. FOJTIK, A. HENGLEIN, Laser ablation of films and suspended particles in a solvent : formation of cluster and colloid solutions, Berichte Der Bunsen-Gesellschaft. 97 (1993) 252–254. http://cat.inist.fr/?aModele=afficheN&cpsidt=4681816 (accessed January 16, 2016).

[48] V. Amendola, M. Meneghetti, Laser ablation synthesis in solution and size manipulation of noble metal nanoparticles, Phys. Chem. Chem. Phys. 11 (2009) 3805. doi:10.1039/b900654k.

[49] V. Amendola, R. Pilot, M. Frasconi, O.M. Maragò, M.A. Iatì, Surface plasmon resonance in gold nanoparticles: a review, J. Phys. Condens. Matter. 29 (2017) 203002. doi:10.1088/1361-648X/aa60f3.

[50] C.-Y. Shih, R. Streubel, J. Heberle, A. Letzel, M. V. Shugaev, C. Wu, M. Schmidt, B. Gökce, S. Barcikowski, L. V. Zhigilei, Two mechanisms of nanoparticle generation in picosecond laser ablation in liquids: the origin of the bimodal size distribution, Nanoscale. 10 (2018) 6900–6910. doi:10.1039/C7NR08614H.

[51] C.-Y. Shih, C. Wu, M. V. Shugaev, L. V. Zhigilei, Atomistic modeling of nanoparticle generation in short pulse laser ablation of thin metal films in water, J. Colloid Interface Sci. 489 (2017) 3–17. doi:10.1016/j.jcis.2016.10.029.

[52] F. Waag, W.I.M.A. Fares, Y. Li, C. Andronescu, B. Gökce, S. Barcikowski, Identification of the main mixing process in the synthesis of alloy nanoparticles by laser ablation of compacted micropowder mixtures, J. Mater. Sci. 57 (2022) 3041–3056. doi:10.1007/s10853-021-06731-2.

[53] G. Marzun, H. Bönnemann, C. Lehmann, B. Spliethoff, C. Weidenthaler, S. Barcikowski, Role of Dissolved and Molecular Oxygen on Cu and PtCu Alloy Particle Structure during Laser Ablation Synthesis in Liquids, ChemPhysChem. 18 (2017) 1175–1184. doi:10.1002/cphc.201601315.

[54] R. Streubel, G. Bendt, B. Gökce, Pilot-scale synthesis of metal nanoparticles by high-speed pulsed laser ablation in liquids, Nanotechnology. 27 (2016) 205602. doi:10.1088/0957-4484/27/20/205602.

[55] F. Waag, R. Streubel, B. Gökce, S. Barcikowski, Synthesis of gold, platinum, and gold-platinum alloy nanoparticle colloids with high-power megahertz-repetition-rate lasers: the importance of the beam guidance method, Appl. Nanosci. (2021). doi:10.1007/s13204-021-01693-y.

[56] H. Braess, U. Seiffert, Vieweg Handbuch Kraftfahrzeugtechnik, Vieweg+Teubner Verlag, Wiesbaden, 2012. doi:10.1007/978-3-8348-8298-1.

[57] R. Pischinger, M. Klell, T. Sams, Thermodynamik der Verbrennungskraftmaschine, Springer Vienna, Vienna, 2010. doi:10.1007/978-3-211-99277-7.

[58] P.A. Lakshminarayanan, Y. V. Aghav, Modelling Diesel Combustion, Springer Netherlands, Dordrecht, 2010. doi:10.1007/978-90-481-3885-2.

[59] G.A. LAVOIE, J.B. HEYWOOD, J.C. KECK, Experimental and Theoretical Study of Nitric Oxide Formation in Internal Combustion Engines, Combust. Sci. Technol. 1 (1970) 313–326. doi:10.1080/00102206908952211.

[60] European Commission, Euro 7 Proposal, Com(2022). 586 (2022).

[61] C. Trapp, R. Böwing, Handbuch Dieselmotoren, Springer Fachmedien Wiesbaden, Wiesbaden, 2018. doi:10.1007/978-3-658-07697-9.

[62] T.V.W. Janssens, H. Falsig, L.F. Lundegaard, P.N.R. Vennestrøm, S.B. Rasmussen, P.G. Moses, F. Giordanino, E. Borfecchia, K.A. Lomachenko, C. Lamberti, S. Bordiga, A. Godiksen, S. Mossin, P. Beato, A Consistent Reaction Scheme for the Selective Catalytic Reduction of Nitrogen Oxides with Ammonia, ACS Catal. 5 (2015) 2832–2845. doi:10.1021/cs501673g.

[63] K.G. Rappé, C. DiMaggio, J.A. Pihl, J.R. Theis, S.H. Oh, G.B. Fisher, J. Parks, V.G. Easterling, M. Yang, M.L. Stewart, K.C. Howden, Aftertreatment Protocols for Catalyst Characterization and Performance Evaluation: Low-Temperature Oxidation, Storage, Three-Way, and NH3-SCR Catalyst Test Protocols, Emiss. Control Sci. Technol. 5 (2019) 183–214. doi:10.1007/s40825-019-00120-7.

[64] A.S. Ayodhya, K.G. Narayanappa, An overview of after-treatment systems for diesel engines, Environ. Sci. Pollut. Res. 25 (2018) 35034–35047. doi:10.1007/s11356-018-3487-8.

[65] T. Lan, Y. Zhao, J. Deng, J. Zhang, L. Shi, D. Zhang, Selective catalytic oxidation of NH 3 over noble metal-based catalysts: state of the art and future prospects, Catal. Sci. Technol. 10 (2020) 5792–5810. doi:10.1039/D0CY01137A.

[66] C.P. Cho, Y.D. Pyo, J.Y. Jang, G.C. Kim, Y.J. Shin, NO x reduction and N 2 O emissions in a diesel engine exhaust using Fe-zeolite and vanadium based SCR catalysts, Appl. Therm. Eng. 110 (2017) 18–24. doi:10.1016/j.applthermaleng.2016.08.118.

[67] K. Kamasamudram, C. Henry, N. Currier, A. Yezerets, N 2 O Formation and Mitigation in Diesel Aftertreatment Systems, SAE Int. J. Engines. 5 (2012) 2012-01–1085. doi:10.4271/2012-01-1085.

[68] European Commission, Annexes to Euro 7 Proposal, Com(2022). 586 (2022).

[69] D.R. Lide, ed., CRC - Handbook of Chemistry and Physics, 84th ed., CRC Press, 2003.

[70] A. Heintz, Thermodynamik der Mischungen, Springer Berlin Heidelberg, Berlin, Heidelberg, 2017. doi:10.1007/978-3-662-49924-5.

[71] European Commission, Regulation (EC) No 595/2009 of the European Parliament and of the Council of 18 June 2009 on type-approval of motor vehicles and engines with respect to emissions from heavy duty vehicles (Euro VI) and on access to vehicle repair and maintenance informati, (2009) 1–20. https://eur-lex.europa.eu/legal-content/en/ALL/?uri=CELEX%3A32009R0595.

[72] A. Scheuer, W. Hauptmann, A. Drochner, J. Gieshoff, H. Vogel, M. Votsmeier, Dual layer automotive ammonia oxidation catalysts: Experiments and computer simulation, Appl. Catal. B Environ. 111–112 (2012) 445–455. doi:10.1016/j.apcatb.2011.10.032.

[73] A. Grossale, I. Nova, E. Tronconi, Study of a Fe-zeolite-based system as NH3-SCR catalyst for diesel exhaust aftertreatment, Catal. Today. 136 (2008) 18–27. doi:10.1016/j.cattod.2007.10.117.

[74] M. Jabłońska, Progress on Noble Metal-Based Catalysts Dedicated to the Selective Catalytic Ammonia Oxidation into Nitrogen and Water Vapor (NH3-SCO), Molecules. 26 (2021) 6461. doi:10.3390/molecules26216461.

[75] M. Jabłońska, R. Palkovits, Copper based catalysts for the selective ammonia oxidation into nitrogen and water vapour—Recent trends and open challenges, Appl. Catal. B Environ. 181 (2016) 332–351. doi:10.1016/j.apcatb.2015.07.017.

[76] C.-M. Hung, Fabrication, characterization, and evaluation of the cytotoxicity of platinum–rhodium nanocomposite materials for use in ammonia treatment, Powder Technol. 209 (2011) 29–34. doi:10.1016/j.powtec.2011.01.023.

[77] J. Liu, M. Sun, Q. Lin, S. Liu, H. Xu, Y. Chen, Promotional effects of ethylenediamine on the low-temperature catalytic activity of selective catalytic oxidation of ammonia over Pt/SiAlOx: States and particle sizes of Pt, Appl. Surf. Sci. 481 (2019) 1344–1351. doi:10.1016/j.apsusc.2019.03.199.

[78] S. Shrestha, M.P. Harold, K. Kamasamudram, A. Yezerets, Ammonia Oxidation on Structured Composite Catalysts, Top. Catal. 56 (2013) 182–186. doi:10.1007/s11244-013-9949-9.

[79] D.A. Svintsitskiy, E.M. Slavinskaya, O.A. Stonkus, A. V. Romanenko, A.I. Stadnichenko, L.S. Kibis, E.A. Derevyannikova, A.A. Evtushkova, A.I. Boronin, The State of Platinum and Structural Features of Pt/Al2O3 Catalysts in the Reaction of NH3 Oxidation, J. Struct. Chem. 60 (2019) 919–931. doi:10.1134/S0022476619060064.

[80] S. Chang, G. Harle, J. Ma, J. Yi, The effect of textural properties of CeO2-SiO2 mixed oxides on NH3-SCO activity of Pt/CeO2-SiO2 catalyst, Appl. Catal. A Gen. 604 (2020) 117775. doi:10.1016/j.apcata.2020.117775.

[81] M. Jabłońska, TPR study and catalytic performance of noble metals modified Al2O3, TiO2 and ZrO2 for low-temperature NH3-SCO, Catal. Commun. 70 (2015) 66–71. doi:10.1016/j.catcom.2015.07.012.

[82] M.-S. Kim, D.-W. Lee, S.-H. Chung, Y.-K. Hong, S.H. Lee, S.-H. Oh, I.-H. Cho, K.-Y. Lee, Oxidation of ammonia to nitrogen over Pt/Fe/ZSM5 catalyst: Influence of catalyst support on the low temperature activity, J. Hazard. Mater. 237–238 (2012) 153–160. doi:10.1016/j.jhazmat.2012.08.026.

[83] M. Sun, S. Wang, Y. Li, H. Xu, Y. Chen, Promotion of catalytic performance by adding W into Pt/ZrO2 catalyst for selective catalytic oxidation of ammonia, Appl. Surf. Sci. 402 (2017) 323–329. doi:10.1016/j.apsusc.2016.12.241.

[84] L. Gang, B.. Anderson, J. van Grondelle, R.. van Santen, NH3 oxidation to nitrogen and water at low temperatures using supported transition metal catalysts, Catal. Today. 61 (2000) 179–185. doi:10.1016/S0920-5861(00)00375-8.

[85] R.Q. Long, R.T. Yang, Noble metal (Pt, Rh, Pd) promoted Fe-ZSM-5 for selective catalytic oxidation of ammonia to N2 at low temperatures, Catal. Letters. 78 (2002) 353–357. doi:10.1023/A:1014929222854.

[86] C.-M. Hung, W.-L. Lai, J.-L. Lin, Removal of Gaseous Ammonia in Pt-Rh Binary Catalytic Oxidation, Aerosol Air Qual. Res. 12 (2012) 583–591. doi:10.4209/aaqr.2012.01.0015.

[87] E.M. Slavinskaya, L.S. Kibis, O.A. Stonkus, D.A. Svintsitskiy, A.I. Stadnichenko, E.A. Fedorova, A. V. Romanenko, V. Marchuk, D.E. Doronkin, A.I. Boronin, The Effects of Platinum Dispersion and Pt State on Catalytic Properties of Pt/Al 2 O 3 in NH 3 Oxidation, ChemCatChem. 13 (2021) 313–327. doi:10.1002/cctc.202001320.

[88] M. Zhou, Z. Wang, Q. Sun, J. Wang, C. Zhang, D. Chen, X. Li, High-Performance Ag–Cu Nanoalloy Catalyst for the Selective Catalytic Oxidation of Ammonia, ACS Appl. Mater. Interfaces. 11 (2019) 46875–46885. doi:10.1021/acsami.9b16349.

[89] G. OLOFSSON, L. REINEWALLENBERG, A. ANDERSSON, Selective catalytic oxidation of ammonia to nitrogen at low temperature on Pt/CuO/Al2O3, J. Catal. 230 (2005) 1–13. doi:10.1016/j.jcat.2004.11.023.

[90] R. Burch, B.W.L. Southward, Low-temperature, clean catalytic combustion of N-bearing gasified biomass using a novel NH3 trapping catalyst, Chem. Commun. 2 (2000) 1115–1116. doi:10.1039/b002594l.

[91] H.M.J. Kušar, A.G. Ersson, M. Vosecký, S.G. Järås, Selective catalytic oxidation of NH3 to N2 for catalytic combustion of low heating value gas under lean/rich conditions, Appl. Catal. B Environ. 58 (2005) 25–32.

doi:10.1016/j.apcatb.2004.02.020.

[92] R. Abbas-Ghaleb, D. Chlala, Selective catalytic oxidation of NH3 into N2 during biogas combustion over 2 wt%PdO/5 wt%CuO/γ-Al2O3, SN Appl. Sci. 2 (2020) 592. doi:10.1007/s42452-020-2397-9.

[93] R. Ferrando, J. Jellinek, R.L. Johnston, Nanoalloys: From Theory to Applications of Alloy Clusters and Nanoparticles, Chem. Rev. 108 (2008) 845–910. doi:10.1021/cr040090g.

[94] M. Faraday, The Bakerian Lecture : Experimental Relations of Gold (and Other Metals) to Light, Philos. Trans. R. Soc. London. 147 (1857) 145–181.

[95] J. Turkevich, P.C. Stevenson, J. Hillier, A study of the nucleation and growth processes in the synthesis of colloidal gold, Discuss. Faraday Soc. 11 (1951) 55. doi:10.1039/df9511100055.

[96] H. Bönnemann, R.M. Richards, Nanoscopic Metal Particles − Synthetic Methods and Potential Applications, Eur. J. Inorg. Chem. 2001 (2001) 2455–2480. doi:10.1002/1099-0682(200109)2001:10<2455::AID-EJIC2455>3.0.CO;2-Z.

[97] C. Burda, X. Chen, R. Narayanan, M.A. El-Sayed, Chemistry and Properties of Nanocrystals of Different Shapes, Chem. Rev. 105 (2005) 1025–1102. doi:10.1021/cr030063a.

[98] R.. Richards, Metal Clusters in Chemistry, Wiley, 1999. doi:10.1002/9783527618316.

[99] D. V. Goia, E. Matijević, Preparation of monodispersed metal particles, New J. Chem. 22 (1998) 1203–1215. doi:10.1039/a709236i.

[100] C.N.R. Rao, G.U. Kulkarni, P.J. Thomas, P.P. Edwards, Metal nanoparticles and their assemblies, Chem. Soc. Rev. 29 (2000) 27–35. doi:10.1039/a904518j.

[101] S.K. Krishnan, E. Prokhorov, D. Bahena, R. Esparza, M. Meyyappan, Chitosan-Covered Pd@Pt Core–Shell Nanocubes for Direct Electron Transfer in Electrochemical Enzymatic Glucose Biosensor, ACS Omega. 2 (2017) 1896–1904. doi:10.1021/acsomega.7b00060.

[102] A. Henglein, M. Giersig, Radiolytic Formation of Colloidal Tin and Tin-Gold Particles in Aqueous Solution, J. Phys. Chem. 98 (1994) 6931–6935. doi:10.1021/j100079a008.

[103] A. Holewinski, J. Idrobo, S. Linic, High-performance Ag–Co alloy catalysts for electrochemical oxygen reduction, Nat. Chem. 6 (2014) 828–834. doi:10.1038/nchem.2032.

[104] I. ul Haq, Egon Matijević*, K. Akhtar, Preparation and Properties of Uniform Coated Inorganic Colloidal Particles. 11. Nickel and Its Compounds on Manganese Compounds, Chem. Mater. 9 (1997) 2659–2665. doi:10.1021/cm970230l.

[105] I. ul Haq, E. Matijević, Preparation and properties of uniform coated inorganic colloidal particles. 12. Tin and its compounds on hematite, in: Horizons 2000 – Asp. Colloid Interface Sci. Turn Millenium, Steinkopff, Darmstadt, 1997: pp. 185–191. doi:10.1007/BFb0118170.

[106] G. Schmid, Clusters and Colloids, Wiley, 1994. doi:10.1002/9783527616077.

[107] G. Schmid, A. Lehnert, J.-O. Malm, J.-O. Bovin, Ligand-Stabilized Bimetallic Colloids Identified by HRTEM and EDX, Angew. Chemie Int. Ed. English. 30 (1991) 874–876. doi:10.1002/anie.199108741.

[108] M.A. Watzky, R.G. Finke, Nanocluster Size-Control and "Magic Number" Investigations. Experimental Tests of the "Living-Metal Polymer" Concept and of Mechanism-Based Size-Control Predictions Leading to the Syntheses of Iridium (0) Nanoclusters Centering about Four Sequential Magic, Chem. Mater. 9 (1997) 3083–3095. doi:10.1021/cm9704387.

[109] N. Toshima, T. Yonezawa, Bimetallic nanoparticles—novel materials for chemical and physical applications, New J. Chem. 22 (1998) 1179–1201. doi:10.1039/a805753b.

[110] K. Torigoe, K. Esumi, Preparation of bimetallic silver-palladium colloids from silver(I) bis(oxalato)palladate(II), Langmuir. 9 (1993) 1664–1667. doi:10.1021/la00031a011.

[111] P. Braunstein, L.A. Oro, P.R. Raithby, eds., Metal Clusters in Chemistry, Wiley, 1999. doi:10.1002/9783527618316.

[112] R. Raja, J.M. Thomas, M.D. Jones, B.F.G. Johnson, D.E.W. Vaughan, Constraining Asymmetric Organometallic Catalysts within Mesoporous Supports Boosts Their Enantioselectivity, J. Am. Chem. Soc. 125 (2003) 14982–14983. doi:10.1021/ja030381r.

[113] K. Esumi, T. Tano, K. Torigoe, K. Meguro, Preparation and characterization of bimetallic palladium-copper colloids by thermal decomposition of their acetate compounds in organic solvents, Chem. Mater. 2 (1990) 564–567. doi:10.1021/cm00011a019.

[114] J.S. Bradley, G.H. Via, L. Bonneviot, E.W. Hill, Infrared and EXAFS Study of Compositional Effects in Nanoscale Colloidal Palladium−Copper Alloys, Chem. Mater. 8 (1996) 1895–1903. doi:10.1021/cm960093c.

[115] K. Bhunia, S. Khilari, D. Pradhan, Trimetallic PtAuNi alloy nanoparticles as an efficient electrocatalyst for the methanol electrooxidation reaction, Dalt. Trans. 46 (2017) 15558–15566. doi:10.1039/C7DT02608K.

[116] J. Li, Q. Wu, J. Wu, T.S. Division, O. Ridge, O. Ridge, C. Sciences, E. Division, Handbook of Nanoparticles, Springer International Publishing, Cham, 2015. doi:10.1007/978-3-319-13188-7.

[117] K.D. Gilroy, A. Ruditskiy, H.-C. Peng, D. Qin, Y. Xia, Bimetallic Nanocrystals: Syntheses, Properties, and Applications, Chem. Rev. 116 (2016) 10414–10472. doi:10.1021/acs.chemrev.6b00211.

[118] G. Sharma, D. Kumar, A. Kumar, A.H. Al-Muhtaseb, D. Pathania, M. Naushad, G.T. Mola, Revolution from monometallic to trimetallic nanoparticle composites, various synthesis methods and their applications: A review, Mater. Sci. Eng. C. 71 (2017) 1216–1230. doi:10.1016/j.msec.2016.11.002.

[119] C. Elschenbroich, A. Salzer, Active Metals, Wiley-VCH Verlag GmbH, Weinheim, Germany, 1995.

doi:10.1002/9783527615179.

[120] M.T. Reetz, W. Helbig, S.A. Quaiser, Electrochemical Preparation of Nanostructural Bimetallic Clusters, Chem. Mater. 7 (1995) 2227–2228. doi:10.1021/cm00060a004.

[121] U. Kolb, S.A. Quaiser, M. Winter, M.T. Reetz, Investigation of Tetraalkylammonium Bromide Stabilized Palladium/Platinum Bimetallic Clusters Using Extended X-ray Absorption Fine Structure Spectroscopy, Chem. Mater. 8 (1996) 1889–1894. doi:10.1021/cm960062h.

[122] E.E. Elemike, D.C. Onwudiwe, O.E. Fayemi, T.L. Botha, Green synthesis and electrochemistry of Ag, Au, and Ag–Au bimetallic nanoparticles using golden rod (Solidago canadensis) leaf extract, Appl. Phys. A. 125 (2019) 42. doi:10.1007/s00339-018-2348-0.

[123] A.L. Querejeta, M.C. del Barrio, S.G. García, Electrochemical synthesis of Rh-Pd bimetallic nanoparticles onto a glassy carbon surface, J. Electroanal. Chem. 778 (2016) 98–102. doi:10.1016/j.jelechem.2016.07.035.

[124] Y. Mizukoshi, T. Fujimoto, Y. Nagata, R. Oshima, Y. Maeda, Characterization and Catalytic Activity of Core−Shell Structured Gold/Palladium Bimetallic Nanoparticles Synthesized by the Sonochemical Method, J. Phys. Chem. B. 104 (2000) 6028–6032. doi:10.1021/jp994255e.

[125] C. Kan, W. Cai, C. Li, L. Zhang, H. Hofmeister, Ultrasonic synthesis and optical properties of Au/Pd bimetallic nanoparticles in ethylene glycol, J. Phys. D. Appl. Phys. 36 (2003) 1609–1614. doi:10.1088/0022-3727/36/13/328.

[126] S. Remita, M. Mostafavi, M.O. Delcourt, Bimetallic Ag-Pt and Au-Pt aggregates synthesized by radiolysis, Radiat. Phys. Chem. 47 (1996) 275–279. doi:10.1016/0969-806X(94)00172-G.

[127] J. Belloni, M. Mostafavi, H. Remita, J.-L. Marignier, and M.-O. Delcourt, Radiation-induced synthesis of mono- and multi-metallic clusters and nanocolloids, New J. Chem. 22 (1998) 1239–1255. doi:10.1039/a801445k.

[128] M. Treguer, C. de Cointet, H. Remita, J. Khatouri, M. Mostafavi, J. Amblard, J. Belloni, R. de Keyzer, Dose Rate Effects on Radiolytic Synthesis of Gold−Silver Bimetallic Clusters in Solution, J. Phys. Chem. B. 102 (1998) 4310–4321. doi:10.1021/jp981467n.

[129] C.M. Doudna, M.F. Bertino, A.T. Tokuhiro, Structural Investigation of Ag−Pd Clusters Synthesized with the Radiolysis Method, Langmuir. 18 (2002) 2434–2435. doi:10.1021/la0155404.

[130] C.M. Doudna, M.F. Bertino, S. Pillalamarri, F.D. Blum, A.T. Tokuhiro, S. Chattopadhyay, J. Terry, Radiolytic Synthesis of Bimetallic Nanoparticles with High Aspect Ratio, MRS Proc. 740 (2002) I11.2. doi:10.1557/PROC-740-I11.2.

[131] I. Călinescu, D. Martin, D. Ighigeanu, A. Gavrila, A. Trifan, M. Patrascu, C. Munteanu, A. Diacon, E. Manaila, G. Craciun, Nanoparticles synthesis by electron beam radiolysis, Open Chem. 12 (2014) 774–781. doi:10.2478/s11532-014-0502-x.

[132] J. Kugai, T. Moriya, S. Seino, T. Nakagawa, Y. Ohkubo, H. Nitani, H. Daimon, T.A. Yamamoto, CeO2-supported Pt–Cu alloy nanoparticles synthesized by radiolytic process for highly selective CO oxidation, Int. J. Hydrogen Energy. 37 (2012) 4787–4797. doi:10.1016/j.ijhydene.2011.12.070.

[133] J. Bhagwan, S.K. Hussain, J.S. Yu, Facile Hydrothermal Synthesis and Electrochemical Properties of CaMoO 4 Nanoparticles for Aqueous Asymmetric Supercapacitors, ACS Sustain. Chem. Eng. (2019) acssuschemeng.9b01708. doi:10.1021/acssuschemeng.9b01708.

[134] P. Thakur, R. Sharma, M. Kumar, S.C. Katyal, N.S. Negi, N. Thakur, V. Sharma, P. Sharma, Superparamagnetic La doped Mn–Zn nano ferrites: dependence on dopant content and crystallite size, Mater. Res. Express. 3 (2016) 075001. doi:10.1088/2053-1591/3/7/075001.

[135] N. Baig, I. Kammakakam, W. Falath, Nanomaterials: a review of synthesis methods, properties, recent progress, and challenges, Mater. Adv. 2 (2021) 1821–1871. doi:10.1039/D0MA00807A.

[136] Y.S. Park, S. Kodama, H. Sekiguchi, Preparation of Metal Nitride Particles Using Arc Discharge in Liquid Nitrogen, Nanomaterials. 11 (2021) 2214. doi:10.3390/nano11092214.

[137] Y. Liao, Y. Li, R. Zhao, J. Zhang, L. Zhao, L. Ji, Z. Zhang, X. Liu, G. Qin, X. Zhang, High-entropy-alloy nanoparticles with 21 ultra-mixed elements for efficient photothermal conversion, Natl. Sci. Rev. 9 (2022). doi:10.1093/nsr/nwac041.

[138] S. Gao, S. Hao, Z. Huang, Y. Yuan, S. Han, L. Lei, X. Zhang, R. Shahbazian-Yassar, J. Lu, Synthesis of high-entropy alloy nanoparticles on supports by the fast moving bed pyrolysis, Nat. Commun. 11 (2020) 2016. doi:10.1038/s41467-020-15934-1.

[139] Y. Yang, B. Song, X. Ke, F. Xu, K.N. Bozhilov, L. Hu, R. Shahbazian-Yassar, M.R. Zachariah, Aerosol Synthesis of High Entropy Alloy Nanoparticles, Langmuir. 36 (2020) 1985–1992. doi:10.1021/acs.langmuir.9b03392.

[140] Y. Yao, Q. Dong, L. Hu, Overcoming Immiscibility via a Milliseconds-Long "Shock" Synthesis toward Alloyed Nanoparticles, Matter. 1 (2019) 1451–1453. doi:10.1016/j.matt.2019.11.006.

[141] X. Wang, Q. Dong, H. Qiao, Z. Huang, M.T. Saray, G. Zhong, Z. Lin, M. Cui, A. Brozena, M. Hong, Q. Xia, J. Gao, G. Chen, R. Shahbazian-Yassar, D. Wang, L. Hu, Continuous Synthesis of Hollow High-Entropy Nanoparticles for Energy and Catalysis Applications, Adv. Mater. 32 (2020) 2002853. doi:10.1002/adma.202002853.

[142] J. Feng, D. Chen, P. V. Pikhitsa, Y. Jung, J. Yang, M. Choi, Unconventional Alloys Confined in Nanoparticles: Building Blocks for New Matter, Matter. 3 (2020) 1646–1663. doi:10.1016/j.matt.2020.07.027.

[143] K.-H. Huynh, X.-H. Pham, J. Kim, S.H. Lee, H. Chang, W.-Y. Rho, B.-H. Jun, Synthesis, Properties, and Biological

Applications of Metallic Alloy Nanoparticles, Int. J. Mol. Sci. 21 (2020) 5174. doi:10.3390/ijms21145174.

[144] V.E. Bondybey, G.P. Schwartz, J.H. English, Laser vaporization of alloys: Laser induced fluorescence of heteronuclear metal clusters, J. Chem. Phys. 78 (1983) 11–15. doi:10.1063/1.444532.

[145] V.E. Bondybey, M. Heaven, T.A. Miller, Laser vaporization of tin: Spectra and ground state molecular parameters of Sn2, J. Chem. Phys. 78 (1983) 3593–3598. doi:10.1063/1.445187.

[146] D. Zhang, Z. Li, K. Sugioka, Laser ablation in liquids for nanomaterial synthesis: Diversities of targets and liquids, JPhys Photonics. 3 (2021). doi:10.1088/2515-7647/ac0bfd.

[147] E. Fazio, B. Gökce, A. De Giacomo, M. Meneghetti, G. Compagnini, M. Tommasini, F. Waag, A. Lucotti, C.G. Zanchi, P.M. Ossi, M. Dell'Aglio, L. D'Urso, M. Condorelli, V. Scardaci, F. Biscaglia, L. Litti, M. Gobbo, G. Gallo, M. Santoro, S. Trusso, F. Neri, Nanoparticles Engineering by Pulsed Laser Ablation in Liquids: Concepts and Applications, Nanomaterials. 10 (2020) 2317. doi:10.3390/nano10112317.

[148] T.L. Anisimov, Sergei I. Kepeliovich B. L., Perel'man, Electron emission from metal surfaces exposed to ultrashort laser pulses, Sov. Phys. JETP. 39 (1974) 375–377. http://www.jetp.ras.ru/cgi-bin/dn/e_039_02_0375.pdf.

[149] L. Jiang, H.-L. Tsai, Improved Two-Temperature Model and Its Application in Ultrashort Laser Heating of Metal Films, J. Heat Transfer. 127 (2005) 1167–1173. doi:10.1115/1.2035113.

[150] D. Werner, S. Hashimoto, Improved Working Model for Interpreting the Excitation Wavelength- and Fluence-Dependent Response in Pulsed Laser-Induced Size Reduction of Aqueous Gold Nanoparticles, J. Phys. Chem. C. 115 (2011) 5063–5072. doi:10.1021/jp109255g.

[151] D. Burgess, P.C. Stair, E. Weitz, Calculations of the surface temperature rise and desorption temperature in laser-induced thermal desorption, J. Vac. Sci. Technol. A Vacuum, Surfaces, Film. 4 (1986) 1362–1366. doi:10.1116/1.573571.

[152] R.H.M. Groeneveld, R. Sprik, A. Lagendijk, Effect of a nonthermal electron distribution on the electron-phonon energy relaxation process in noble metals, Phys. Rev. B. 45 (1992) 5079–5082. doi:10.1103/PhysRevB.45.5079.

[153] C. Chen, L. V. Zhigilei, Atomistic modeling of pulsed laser ablation in liquid: spatially and time-resolved maps of transient nonequilibrium states and channels of nanoparticle formation, Appl. Phys. A. 129 (2023) 288. doi:10.1007/s00339-023-06525-0.

[154] J. Johny, Y. Li, M. Kamp, O. Prymak, S. Liang, T. Krekeler, M. Ritter, L. Kienle, C. Rehbock, S. Barcikowski, S. Reichenberger, Laser-generated high entropy metallic glass nanoparticles as bifunctional electrocatalysts, Nano Res. 15 (2022) 4807–4819. doi:10.1007/s12274-021-3804-2.

[155] K.A. Kane, A.C. Reber, S.N. Khanna, M.F. Bertino, Laser synthesized nanoparticle alloys of metals with bulk miscibility gaps, Prog. Nat. Sci. Mater. Int. 28 (2018) 456–463. doi:10.1016/j.pnsc.2018.05.001.

[156] J. Zhang, D.N. Oko, S. Garbarino, R. Imbeault, M. Chaker, A.C. Tavares, D. Guay, D. Ma, Preparation of PtAu Alloy Colloids by Laser Ablation in Solution and Their Characterization, J. Phys. Chem. C. 116 (2012) 13413–13420. doi:10.1021/jp302485g.

[157] B. Predel, Au-Pt (Gold-Platinum), in: O. Madelung (Ed.), Landolt-Börnstein - Gr. IV Phys. Chem. - 5A- Ac-Au – Au-Zr, Springer-Verlag, Berlin/Heidelberg, 1991: pp. 1–3. doi:10.1007/10000866_308.

[158] S. Ibrahimkutty, P. Wagener, A. Menzel, A. Plech, S. Barcikowski, Nanoparticle formation in a cavitation bubble after pulsed laser ablation in liquid studied with high time resolution small angle x-ray scattering, Appl. Phys. Lett. 101 (2012) 103104. doi:10.1063/1.4750250.

[159] M.-R. Kalus, N. Bärsch, R. Streubel, E. Gökce, S. Barcikowski, B. Gökce, How persistent microbubbles shield nanoparticle productivity in laser synthesis of colloids – quantification of their volume, dwell dynamics, and gas composition, Phys. Chem. Chem. Phys. 19 (2017) 7112–7123. doi:10.1039/C6CP07011F.

[160] M.-R. Kalus, R. Lanyumba, N. Lorenzo-Parodi, M.A. Jochmann, K. Kerpen, U. Hagemann, T.C. Schmidt, S. Barcikowski, B. Gökce, Determining the role of redox-active materials during laser-induced water decomposition, Phys. Chem. Chem. Phys. 21 (2019) 18636–18651. doi:10.1039/C9CP02663K.

[161] A.A. Nastulyavichus, S.I. Kudryashov, N.A. Smirnov, A.A. Rudenko, A.Y. Kharin, N.I. Busleev, D.A. Zayarny, A.A. Ionin, D.A. Kirilenko, P.N. Brunkov, Novel approach of controllable stoichiometric fabrication of alloyed Au/Ag nanoparticles by nanosecond laser ablation of thin bi-layered films in water, Laser Phys. Lett. 16 (2019) 096002. doi:10.1088/1612-202X/ab35cf.

[162] S. Grade, J. Eberhard, J. Jakobi, A. Winkel, M. Stiesch, S. Barcikowski, Alloying colloidal silver nanoparticles with gold disproportionally controls antibacterial and toxic effects, Gold Bull. 47 (2014) 83–93. doi:10.1007/s13404-013-0125-6.

[163] M. Censabella, V. Torrisi, S. Boninelli, C. Bongiorno, M.G. Grimaldi, F. Ruffino, Laser ablation synthesis of mono- and bimetallic Pt and Pd nanoparticles and fabrication of Pt-Pd/Graphene nanocomposites, Appl. Surf. Sci. 475 (2019) 494–503. doi:10.1016/j.apsusc.2019.01.029.

[164] D.N. Oko, S. Garbarino, J. Zhang, Z. Xu, M. Chaker, D. Ma, D. Guay, A.C. Tavares, Dopamine and ascorbic acid electro-oxidation on Au, AuPt and Pt nanoparticles prepared by pulse laser ablation in water, Electrochim. Acta. 159 (2015) 174–183. doi:10.1016/j.electacta.2015.01.192.

[165] S. Aksoy, Synthesis and characterization of NiMnIn nanoparticles, J. Magn. Magn. Mater. 373 (2015) 236–239. doi:10.1016/j.jmmm.2014.04.003.

[166] P. Liu, H. Wang, J. Chen, X. Li, H. Zeng, Rapid and High-Efficiency Laser-Alloying Formation of ZnMgO Nanocrystals, Sci. Rep. 6 (2016) 28131. doi:10.1038/srep28131.

[167] L. Torrisi, A. Torrisi, Ni, Ti, and NiTi laser ablation in vacuum and in water to deposit thin films or to generate nanoparticles in solution, Contrib. to Plasma Phys. 61 (2021) 1–11. doi:10.1002/ctpp.202000070.

[168] N. Mintcheva, A.A. Aljulaih, S. Bito, M. Honda, T. Kondo, S. Iwamori, S.A. Kulinich, Nanomaterials produced by laser beam ablating Sn-Zn alloy in water, J. Alloys Compd. 747 (2018) 166–175. doi:10.1016/j.jallcom.2018.02.350.

[169] Y. Feng, Z. Li, H. Liu, C. Dong, J. Wang, S.A. Kulinich, X. Du, Laser-Prepared CuZn Alloy Catalyst for Selective Electrochemical Reduction of CO 2 to Ethylene, Langmuir. 34 (2018) 13544–13549. doi:10.1021/acs.langmuir.8b02837.

[170] O.R. Musaev, E. Sutter, J.M. Wrobel, M.B. Kruger, Structures of BiInSn nanoparticles formed through laser ablation, Appl. Phys. A. 110 (2013) 329–333. doi:10.1007/s00339-012-7244-4.

[171] W.-J. Qin, J. Sun, J. Yang, X.-W. Du, Control of Cu-doping and optical properties of ZnO quantum dots by laser ablation of composite targets, Mater. Chem. Phys. 130 (2011) 425–430. doi:10.1016/j.matchemphys.2011.07.001.

[172] J. Jakobi, S. Petersen, A. Menéndez-Manjón, P. Wagener, S. Barcikowski, Magnetic Alloy Nanoparticles from Laser Ablation in Cyclopentanone and Their Embedding into a Photoresist, Langmuir. 26 (2010) 6892–6897. doi:10.1021/la101014g.

[173] V. Torresan, D. Forrer, A. Guadagnini, D. Badocco, P. Pastore, M. Casarin, A. Selloni, D. Coral, M. Ceolin, M.B. Fernández van Raap, A. Busato, P. Marzola, A.E. Spinelli, V. Amendola, 4D Multimodal Nanomedicines Made of Nonequilibrium Au–Fe Alloy Nanoparticles, ACS Nano. 14 (2020) 12840–12853. doi:10.1021/acsnano.0c03614.

[174] V. Amendola, M. Meneghetti, O.M. Bakr, P. Riello, S. Polizzi, D.H. Anjum, S. Fiameni, P. Arosio, T. Orlando, C. de Julian Fernandez, F. Pineider, C. Sangregorio, A. Lascialfari, Coexistence of plasmonic and magnetic properties in Au89Fe11 nanoalloys, Nanoscale. 5 (2013) 5611. doi:10.1039/c3nr01119d.

[175] S. Scaramuzza, D. Badocco, P. Pastore, D.F. Coral, M.B. Fernández van Raap, V. Amendola, Magnetically Assembled SERS Substrates Composed of Iron-Silver Nanoparticles Obtained by Laser Ablation in Liquid, ChemPhysChem. 18 (2017) 1026–1034. doi:10.1002/cphc.201600651.

[176] V. Amendola, S. Scaramuzza, S. Agnoli, G. Granozzi, M. Meneghetti, G. Campo, V. Bonanni, F. Pineider, C. Sangregorio, P. Ghigna, S. Polizzi, P. Riello, S. Fiameni, L. Nodari, Laser generation of iron-doped silver nanotruffles with magnetic and plasmonic properties, Nano Res. 8 (2015) 4007–4023. doi:10.1007/s12274-015-0903-y.

[177] R. Brandiele, V. Amendola, A. Guadagnini, G.A. Rizzi, D. Badocco, P. Pastore, A.A. Isse, C. Durante, A. Gennaro, Facile synthesis of Pd3Y alloy nanoparticles for electrocatalysis of the oxygen reduction reaction, Electrochim. Acta. 320 (2019) 134563. doi:10.1016/j.electacta.2019.134563.

[178] Y.S. Tveryanovich, G.O. Abdrashitov, L.G. Menchikov, Effect of the magnetic field on the size of nanoparticles obtained by ablation of a cobalt – copper target in a liquid, Quantum Electron. 50 (2020) 861–865. doi:10.1070/QEL17301.

[179] W. Guo, B. Liu, Liquid-Phase Pulsed Laser Ablation and Electrophoretic Deposition for Chalcopyrite Thin-Film Solar Cell Application, ACS Appl. Mater. Interfaces. 4 (2012) 7036–7042. doi:10.1021/am3022976.

[180] T. Yamamoto, Y. Shimotsuma, M. Sakakura, M. Nishi, K. Miura, K. Hirao, Intermetallic Magnetic Nanoparticle Precipitation by Femtosecond Laser Fragmentation in Liquid, Langmuir. 27 (2011) 8359–8364. doi:10.1021/la201211e.

[181] P. Wagener, J. Jakobi, C. Rehbock, V.S.K. Chakravadhanula, C. Thede, U. Wiedwald, M. Bartsch, L. Kienle, S. Barcikowski, Solvent-surface interactions control the phase structure in laser-generated iron-gold core-shell nanoparticles, Sci. Rep. 6 (2016) 23352. doi:10.1038/srep23352.

[182] N. Lasemi, C. Rentenberger, R. Pospichal, A.S. Cherevan, M. Pfaffeneder-Kmen, G. Liedl, D. Eder, Femtosecond laser-assisted synthesis of Ni/Au BONs in various alcoholic solvents, Appl. Phys. A. 125 (2019) 544. doi:10.1007/s00339-019-2826-z.

[183] F. Davodi, E. Mühlhausen, D. Settipani, E.-L. Rautama, A.-P. Honkanen, S. Huotari, G. Marzun, P. Taskinen, T. Kallio, Comprehensive study to design advanced metal-carbide@garaphene and metal-carbide@iron oxide nanoparticles with tunable structure by the laser ablation in liquid, J. Colloid Interface Sci. 556 (2019) 180–192. doi:10.1016/j.jcis.2019.08.056.

[184] F. Davodi, E. Mühlhausen, M. Tavakkoli, J. Sainio, H. Jiang, B. Gökce, G. Marzun, T. Kallio, Catalyst Support Effect on the Activity and Durability of Magnetic Nanoparticles: toward Design of Advanced Electrocatalyst for Full Water Splitting, ACS Appl. Mater. Interfaces. 10 (2018) 31300–31311. doi:10.1021/acsami.8b08830.

[185] B. Stephan, A. Vincenzo, L. Marcus, M. Galina, R. Christoph, R. Sven, Z. Dongshi, Bilal Gökce, Handbook of Laser synthesis & Processing of colloids, Second Edi, 2019. doi:10.17185/duepublico/70584.

[186] D. Zhang, Z. Ma, M. Spasova, A.E. Yelsukova, S. Lu, M. Farle, U. Wiedwald, B. Gökce, Formation Mechanism of Laser-Synthesized Iron-Manganese Alloy Nanoparticles, Manganese Oxide Nanosheets and Nanofibers, Part. Part. Syst. Charact. 34 (2017) 1600225. doi:10.1002/ppsc.201600225.

[187] Y. Ishikawa, K. Kawaguchi, Y. Shimizu, T. Sasaki, N. Koshizaki, Preparation of Fe–Pt alloy particles by pulsed laser ablation in liquid medium, Chem. Phys. Lett. 428 (2006) 426–429. doi:10.1016/j.cplett.2006.07.076.

[188] K. Kawaguchi, R. Wu, Y. Ishikawa, T. Sasaki, N. Koshizaki, FePt Nanoparticles Fabricated by Pulsed Laser

Ablation, J. Nanosci. Nanotechnol. 9 (2009) 1454–1457. doi:10.1166/jnn.2009.C177.

[189] A. Hamad, L. Li, Z. Liu, A comparison of the characteristics of nanosecond, picosecond and femtosecond lasers generated Ag, TiO2 and Au nanoparticles in deionised water, Appl. Phys. A. 120 (2015) 1247–1260. doi:10.1007/s00339-015-9326-6.

[190] C. Rehbock, J. Jakobi, L. Gamrad, S. van der Meer, D. Tiedemann, U. Taylor, W. Kues, D. Rath, S. Barcikowski, Current state of laser synthesis of metal and alloy nanoparticles as ligand-free reference materials for nano-toxicological assays, Beilstein J. Nanotechnol. 5 (2014) 1523–1541. doi:10.3762/bjnano.5.165.

[191] A. V. Kabashin, M. Meunier, Synthesis of colloidal nanoparticles during femtosecond laser ablation of gold in water, J. Appl. Phys. 94 (2003) 7941. doi:10.1063/1.1626793.

[192] S. Besner, A. V. Kabashin, F.M. Winnik, M. Meunier, Ultrafast laser based "green" synthesis of non-toxic nanoparticles in aqueous solutions, Appl. Phys. A. 93 (2008) 955–959. doi:10.1007/s00339-008-4773-y.

[193] M.H. Mahdieh, B. Fattahi, Size properties of colloidal nanoparticles produced by nanosecond pulsed laser ablation and studying the effects of liquid medium and laser fluence, Appl. Surf. Sci. 329 (2015) 47–57. doi:10.1016/j.apsusc.2014.12.069.

[194] Y.-H. Chen, C.-S. Yeh, Laser ablation method: use of surfactants to form the dispersed Ag nanoparticles, Colloids Surfaces A Physicochem. Eng. Asp. 197 (2002) 133–139. doi:10.1016/S0927-7757(01)00854-8.

[195] R. Intartaglia, K. Bagga, F. Brandi, G. Das, A. Genovese, E. Di Fabrizio, A. Diaspro, Optical properties of femtosecond laser-synthesized silicon nanoparticles in deionized water, J. Phys. Chem. C. 115 (2011) 5102–5107. doi:10.1021/jp109351t.

[196] R. Intartaglia, K. Bagga, F. Brandi, Study on the productivity of silicon nanoparticles by picosecond laser ablation in water: towards gram per hour yield, Opt. Express. 22 (2014) 3117. doi:10.1364/OE.22.003117.

[197] E. Solati, L. Dejam, D. Dorranian, Effect of laser pulse energy and wavelength on the structure, morphology and optical properties of ZnO nanoparticles, Opt. Laser Technol. 58 (2014) 26–32. doi:10.1016/j.optlastec.2013.10.031.

[198] P. Chewchinda, O. Odawara, H. Wada, The effect of energy density on yield of silicon nanoparticles prepared by pulsed laser ablation in liquid, Appl. Phys. A. 117 (2014) 131–135. doi:10.1007/s00339-014-8293-7.

[199] H. Kwon, K.K. Kim, J.K. Song, S.M. Park, The Effects of Ambient Ions on the Growth of Gold Nanoparticles by Laser Ablation in Liquid, Bull. Korean Chem. Soc. 35 (2014) 865–870. doi:10.5012/bkcs.2014.35.3.865.

[200] J.P. Sylvestre, S. Poulin, A. V. Kabashin, E. Sacher, M. Meunier, J.H.T. Luong, Surface chemistry of gold nanoparticles produced by laser ablation in aqueous media, J. Phys. Chem. B. 108 (2004) 16864–16869. doi:10.1021/jp047134+.

[201] V. Merk, C. Rehbock, F. Becker, U. Hagemann, H. Nienhaus, S. Barcikowski, In Situ Non-DLVO Stabilization of Surfactant-Free, Plasmonic Gold Nanoparticles: Effect of Hofmeister's Anions, Langmuir. 30 (2014) 4213–4222. doi:10.1021/la404556a.

[202] M.G. John, K.M. Tibbetts, Controlling the morphology of copper-silica nanocomposites from laser ablation in liquid, Appl. Surf. Sci. 510 (2020) 145037. doi:10.1016/j.apsusc.2019.145037.

[203] M.G. John, K.M. Tibbetts, Mechanism of Nickel Phyllosilicate Formation by Laser Ablation in Liquid, J. Phys. Chem. C. 124 (2020) 13273–13282. doi:10.1021/acs.jpcc.0c03732.

[204] D.M. Arboleda, J.M.J. Santillán, V.B. Arce, M.B. Fernández van Raap, D. Muraca, M.A. Fernández, R.M. Torres Sanchez, D.C. Schinca, L.B. Scaffardi, A simple and "green" technique to synthesize long-term stability colloidal Ag nanoparticles: Fs laser ablation in a biocompatible aqueous medium, Mater. Charact. 140 (2018) 320–332. doi:10.1016/j.matchar.2018.04.021.

[205] J. Lin, C. Xi, Z. Li, Y. Feng, D. Wu, C. Dong, P. Yao, H. Liu, X. Du, Lattice-strained palladium nanoparticles as active catalysts for the oxygen reduction reaction - Supporting Material, Chem. Commun. 55 (2019) 3121–3123. doi:10.1039/C9CC00447E.

[206] C.H. Bae, S.H. Nam, S.M. Park, Formation of silver nanoparticles by laser ablation of a silver target in NaCl solution, Appl. Surf. Sci. 197–198 (2002) 628–634. doi:10.1016/S0169-4332(02)00430-0.

[207] G. Palazzo, G. Valenza, M. Dell'Aglio, A. De Giacomo, On the stability of gold nanoparticles synthesized by laser ablation in liquids, J. Colloid Interface Sci. 489 (2017) 47–56. doi:10.1016/j.jcis.2016.09.017.

[208] D.A. Goncharova, T.S. Kharlamova, I.N. Lapin, V.A. Svetlichnyi, Chemical and Morphological Evolution of Copper Nanoparticles Obtained by Pulsed Laser Ablation in Liquid, J. Phys. Chem. C. 123 (2019) 21731–21742. doi:10.1021/acs.jpcc.9b03958.

[209] T. Del Rosso, N.A. Rey, T. Rosado, S. Landi, D.G. Larrude, E.C. Romani, F.L.F. Junior, S.M. Quinteiro, M. Cremona, R.Q. Aucelio, G. Margheri, O. Pandoli, Synthesis of oxocarbon-encapsulated gold nanoparticles with blue-shifted localized surface plasmon resonance by pulsed laser ablation in water with CO 2 absorbers, Nanotechnology. 27 (2016) 255602. doi:10.1088/0957-4484/27/25/255602.

[210] D. Katsuki, T. Sato, R. Suzuki, Y. Nanai, S. Kimura, T. Okuno, Red luminescence of Eu3+ doped ZnO nanoparticles fabricated by laser ablation in aqueous solution, Appl. Phys. A. 108 (2012) 321–327. doi:10.1007/s00339-012-6962-y.

[211] C. He, T. Sasaki, H. Usui, Y. Shimizu, N. Koshizaki, Fabrication of ZnO nanoparticles by pulsed laser ablation in aqueous media and pH-dependent particle size: An approach to study the mechanism of enhanced green photoluminescence, J. Photochem. Photobiol. A Chem. 191 (2007) 66–73. doi:10.1016/j.jphotochem.2007.04.006.

[212] R. Singh, R.K. Soni, Laser synthesis of aluminium nanoparticles in biocompatible polymer solutions, Appl. Phys. A. 116 (2014) 689–701. doi:10.1007/s00339-014-8487-z.

[213] R. Zamiri, B.Z. Azmi, M. Darroudi, A.R. Sadrolhosseini, M.S. Husin, A.W. Zaidan, M.A. Mahdi, Preparation of starch stabilized silver nanoparticles with spatial self-phase modulation properties by laser ablation technique, Appl. Phys. A. 102 (2011) 189–194. doi:10.1007/s00339-010-6129-7.

[214] C. Rehbock, V. Merk, L. Gamrad, R. Streubel, S. Barcikowski, Size control of laser-fabricated surfactant-free gold nanoparticles with highly diluted electrolytes and their subsequent bioconjugation, Phys. Chem. Chem. Phys. 15 (2013) 3057–3067. doi:10.1039/C2CP42641B.

[215] M. Darroudi, M.B. Ahmad, R. Zamiri, A.H. Abdullah, N.A. Ibrahim, K. Shameli, M. Shahril Husin, Preparation and characterization of gelatin mediated silver nanoparticles by laser ablation, J. Alloys Compd. 509 (2011) 1301–1304. doi:10.1016/j.jallcom.2010.10.018.

[216] R. Zamiri, B.Z. Azmi, M.G. Naseri, H.A. Ahangar, M. Darroudi, F.K. Nazarpour, Laser based fabrication of chitosan mediated silver nanoparticles, Appl. Phys. A. 105 (2011) 255–259. doi:10.1007/s00339-011-6525-7.

[217] F. Mafuné, J. Kohno, Y. Takeda, T. Kondow, H. Sawabe, Formation and Size Control of Silver Nanoparticles by Laser Ablation in Aqueous Solution, J. Phys. Chem. B. 104 (2000) 9111–9117. doi:10.1021/jp001336y.

[218] M.A. Sobhan, M.J. Withford, E.M. Goldys, Enhanced Stability of Gold Colloids Produced by Femtosecond Laser Synthesis in Aqueous Solution of CTAB, Langmuir. 26 (2010) 3156–3159. doi:10.1021/la903088e.

[219] P.C. Van Der Hoeven, J. Lyklema, Electrostatic stabilization in non-aqueous media, Adv. Colloid Interface Sci. 42 (1992) 205–277. doi:10.1016/0001-8686(92)80024-R.

[220] S. Dadashi, R. Poursalehi, H. Delavari, Optical and structural properties of Bi-based nanoparticles prepared via pulsed Nd:YAG laser ablation in organic liquids, Appl. Phys. A. 124 (2018) 406. doi:10.1007/s00339-018-1817-9.

[221] E. Giorgetti, M. Muniz-Miranda, P. Marsili, D. Scarpellini, F. Giammanco, Stable gold nanoparticles obtained in pure acetone by laser ablation with different wavelengths, J. Nanoparticle Res. 14 (2012) 648. doi:10.1007/s11051-011-0648-9.

[222] R.M. Tilaki, A. Iraji zad, S.M. Mahdavi, Stability, size and optical properties of silver nanoparticles prepared by laser ablation in different carrier media, Appl. Phys. A. 84 (2006) 215–219. doi:10.1007/s00339-006-3604-2.

[223] M. Labusch, S. Puthenkalam, E. Cleve, S. Barcikowski, S. Reichenberger, Pore penetration of porous catalyst supports by in-situ-adsorbed, agglomeration-quenched nanoparticles from pulsed laser ablation in supercritical CO2, J. Supercrit. Fluids. 169 (2021) 105100. doi:10.1016/j.supflu.2020.105100.

[224] P.C. Hiemenz, R. Rajagopalan, Principles of colloid and surface chemistry, 3rd ed., 1997.

[225] G.J. Lauth, J. Kowalczyk, Einführung in die Physik und Chemie der Grenzflächen und Kolloide, Springer Spektrum Berlin, Heidelberg, Berlin, Heidelberg, 2016. doi:10.1007/978-3-662-47018-3.

[226] H.-D. Dörfler, Grenzflächen und kolloid-disperse Systeme, 1st ed., Springer Berlin, Heidelberg, Heidelberg, 2002.

[227] R. Hogg, T.W. Healy, D.W. Fuerstenau, Mutual coagulation of colloidal dispersions, Trans. Faraday Soc. 62 (1966) 1638. doi:10.1039/tf9666201638.

[228] P. Wagener, A. Schwenke, S. Barcikowski, How Citrate Ligands Affect Nanoparticle Adsorption to Microparticle Supports, Langmuir. 28 (2012) 6132–6140. doi:10.1021/la204839m.

[229] S. Barcikowski;, P. Wagener;, A. Schwenke, Method for producing micro-nano combined active systems, EP2651593A1; WO2012080458A1, 2018.

[230] G. Marzun, J. Nakamura, X. Zhang, S. Barcikowski, P. Wagener, Size control and supporting of palladium nanoparticles made by laser ablation in saline solution as a facile route to heterogeneous catalysts, Appl. Surf. Sci. 348 (2015) 75–84. doi:10.1016/j.apsusc.2015.01.108.

[231] S. Reichenberger, G. Marzun, M. Muhler, S. Barcikowski, Perspective of Surfactant-Free Colloidal Nanoparticles in Heterogeneous Catalysis, ChemCatChem. 11 (2019) 4489–4518. doi:10.1002/cctc.201900666.

[232] P. Sabatier, Hydrogénations et déshydrogénations par catalyse, Berichte Der Dtsch. Chem. Gesellschaft. 44 (1911) 1984–2001. doi:10.1002/cber.19110440303.

[233] A.A. Balandin, Modern State of the Multiplet Theor of Heterogeneous Catalysis, in: Adv. Catal., 1969: pp. 1–210. doi:10.1016/S0360-0564(08)60029-2.

[234] J.K. Nørskov, T. Bligaard, B. Hvolbæk, F. Abild-Pedersen, I. Chorkendorff, C.H. Christensen, The nature of the active site in heterogeneous metal catalysis, Chem. Soc. Rev. 37 (2008) 2163. doi:10.1039/b800260f.

[235] S. Xie, S.-I. Choi, X. Xia, Y. Xia, Catalysis on faceted noble-metal nanocrystals: both shape and size matter, Curr. Opin. Chem. Eng. 2 (2013) 142–150. doi:10.1016/j.coche.2013.02.003.

[236] T. Bligaard, J.K. Nørskov, Ligand effects in heterogeneous catalysis and electrochemistry, Electrochim. Acta. 52 (2007) 5512–5516. doi:10.1016/j.electacta.2007.02.041.

[237] M. Laskar, S.E. Skrabalak, A balancing act: manipulating reactivity of shape-controlled metal nanocatalysts through bimetallic architecture, J. Mater. Chem. A. 4 (2016) 6911–6918. doi:10.1039/C5TA09368F.

[238] P. Strasser, S. Koh, T. Anniyev, J. Greeley, K. More, C. Yu, Z. Liu, S. Kaya, D. Nordlund, H. Ogasawara, M.F. Toney, A. Nilsson, Lattice-strain control of the activity in dealloyed core–shell fuel cell catalysts, Nat. Chem. 2 (2010) 454–460. doi:10.1038/nchem.623.

[239] D. Xu, S. Bliznakov, Z. Liu, J. Fang, N. Dimitrov, Composition-dependent electrocatalytic activity of Pt-Cu nanocube

catalysts for formic acid oxidation, Angew. Chemie - Int. Ed. 49 (2010) 1282–1285. doi:10.1002/anie.200905248.

[240] L.E. Marbella, D.M. Chevrier, P.D. Tancini, O. Shobayo, A.M. Smith, K.A. Johnston, C.M. Andolina, P. Zhang, G. Mpourmpakis, J.E. Millstone, Description and Role of Bimetallic Prenucleation Species in the Formation of Small Nanoparticle Alloys, J. Am. Chem. Soc. 137 (2015) 15852–15858. doi:10.1021/jacs.5b10124.

[241] V.R. Stamenkovic, B. Fowler, B.S. Mun, G. Wang, P.N. Ross, C.A. Lucas, N.M. Marković, Improved Oxygen Reduction Activity on Pt 3 Ni(111) via Increased Surface Site Availability, Science (80-.). 315 (2007) 493–497. doi:10.1126/science.1135941.

[242] Y. Gu, G. Wu, X.F. Hu, D.A. Chen, T. Hansen, H.-C. zur Loye, H.J. Ploehn, PAMAM-stabilized Pt–Ru nanoparticles for methanol electro-oxidation, J. Power Sources. 195 (2010) 425–434. doi:10.1016/j.jpowsour.2009.07.044.

[243] Y. Hu, P. Wu, Y. Yin, H. Zhang, C. Cai, Effects of structure, composition, and carbon support properties on the electrocatalytic activity of Pt-Ni-graphene nanocatalysts for the methanol oxidation, Appl. Catal. B Environ. 111–112 (2012) 208–217. doi:10.1016/j.apcatb.2011.10.001.

[244] A.-Q. Wang, J.-H. Liu, S.D. Lin, T.-S. Lin, C.-Y. Mou, A novel efficient Au–Ag alloy catalyst system: preparation, activity, and characterization, J. Catal. 233 (2005) 186–197. doi:10.1016/j.jcat.2005.04.028.

[245] J.-H. Liu, A.-Q. Wang, Y.-S. Chi, H.-P. Lin, C.-Y. Mou, Synergistic Effect in an Au−Ag Alloy Nanocatalyst: CO Oxidation, J. Phys. Chem. B. 109 (2005) 40–43. doi:10.1021/jp044938g.

[246] A.-Q. Wang, C.-M. Chang, C.-Y. Mou, Evolution of Catalytic Activity of Au−Ag Bimetallic Nanoparticles on Mesoporous Support for CO Oxidation, J. Phys. Chem. B. 109 (2005) 18860–18867. doi:10.1021/jp051530q.

[247] V. Abdelsayed, A. Aljarash, M.S. El-Shall, Z.A. Al Othman, A.H. Alghamdi, Microwave Synthesis of Bimetallic Nanoalloys and CO Oxidation on Ceria-Supported Nanoalloys, Chem. Mater. 21 (2009) 2825–2834. doi:10.1021/cm9004486.

[248] S. Hu, M. Tian, E.L. Ribeiro, G. Duscher, D. Mukherjee, Tandem laser ablation synthesis in solution-galvanic replacement reaction (LASiS-GRR) for the production of PtCo nanoalloys as oxygen reduction electrocatalysts, J. Power Sources. 306 (2016) 413–423. doi:10.1016/j.jpowsour.2015.11.078.

[249] G. Ertl, H. Knözinger, J. Weitkamp, eds., Handbook of Heterogeneous Catalysis, Wiley, 1997. doi:10.1002/9783527619474.

[250] S. Royer, D. Duprez, Catalytic Oxidation of Carbon Monoxide over Transition Metal Oxides, ChemCatChem. 3 (2011) 24–65. doi:10.1002/cctc.201000378.

[251] J.H. Potgieter, E. Van Der Lingen, Noble Metal Additions to Passive Alloys: Effect on Corrosion Resistance, in: Ref. Modul. Mater. Sci. Mater. Eng., Elsevier, 2016: pp. 1–39. doi:10.1016/B978-0-12-803581-8.01649-0.

[252] C.G. Susanne Preuss, Henning Peitsmeier, An Kongo führt kein Weg vorbei, Frankfurter Allg. Zeitung. (2020). https://www.faz.net/aktuell/wirtschaft/auto-verkehr/die-nachhaltige-produktion-von-kobalt-fuer-elektroautos-17051536.html.

[253] K. Witsch, Die schwierige Suche nach der kobaltfreien Batterie, Handelsblatt. (2020). https://www.handelsblatt.com/unternehmen/energie/elektromobilitaet-die-schwierige-suche-nach-der-kobaltfreien-batterie/25566142.html?ticket=ST-4169307-qRuKhd0BwIrs90wa9Yac-ap2.

[254] K. Witsch, Lithium-Ionen-Batterien sind ein Milliardengeschäft – mit Schattenseite, Handelsblatt. (2020). https://www.handelsblatt.com/unternehmen/energie/elektromobilitaet-mit-dem-hype-kommen-probleme/25440402-2.html?ticket=ST-4169315-3SfueYfcWhGMDBmdpIDM-ap2.

[255] A. Tymoczko, M. Kamp, O. Prymak, C. Rehbock, J. Jakobi, U. Schürmann, L. Kienle, S. Barcikowski, How the crystal structure and phase segregation of Au–Fe alloy nanoparticles are ruled by the molar fraction and size, Nanoscale. 10 (2018) 16434–16437. doi:10.1039/C8NR03962C.

[256] T. Tsuji, D.-H. Thang, Y. Okazaki, M. Nakanishi, Y. Tsuboi, M. Tsuji, Preparation of silver nanoparticles by laser ablation in polyvinylpyrrolidone solutions, Appl. Surf. Sci. 254 (2008) 5224–5230. doi:10.1016/j.apsusc.2008.02.048.

[257] S. Barcikowski, A. Menéndez-Manjón, B. Chichkov, M. Brikas, G. Račiukaitis, Generation of nanoparticle colloids by picosecond and femtosecond laser ablations in liquid flow, Appl. Phys. Lett. 91 (2007) 083113. doi:10.1063/1.2773937.

[258] S. Kohsakowski, F. Seiser, J.-P. Wiederrecht, S. Reichenberger, T. Vinnay, S. Barcikowski, G. Marzun, Effective size separation of laser-generated, surfactant-free nanoparticles by continuous centrifugation, Nanotechnology. 31 (2020) 095603. doi:10.1088/1361-6528/ab55bd.

[259] CKD-Dichtungstechnik, Elastomere Medienbeständigkeit, 2018 (n.d.) 15. http://www.ckd-dichtungstechnik.de/produkte/medienbestaendigkeit.

[260] S. Jendrzej, B. Gökce, S. Barcikowski, Colloidal Stability of Metal Nanoparticles in Engine Oil under Thermal and Mechanical Load, Chem. Eng. Technol. 40 (2017) 1569–1576. doi:10.1002/ceat.201600541.

[261] Y. Chernyak, Dielectric Constant, Dipole Moment, and Solubility Parameters of Some Cyclic Acid Esters, J. Chem. Eng. Data. 51 (2006) 416–418. doi:10.1021/je050341y.

[262] E.W. Flick, Industrial Solvents Handbook, 5th ed., Noyes Data Corporation, 1998.

[263] B. Schäffner, S.P. Verevkin, A. Börner, Organische Carbonate. Grüne Lösungsmittel für Synthese und Katalyse, Chemie Unserer Zeit. 43 (2009) 12–21. doi:10.1002/ciuz.200900468.

[264] T. Mizutaru, G. Marzun, S. Kohsakowski, S. Barcikowski, D. Hong, H. Kotani, T. Kojima, T. Kondo, J. Nakamura,

Y. Yamamoto, Peptide Cross-linkers: Immobilization of Platinum Nanoparticles Highly Dispersed on Graphene Oxide Nanosheets with Enhanced Photocatalytic Activities, ACS Appl. Mater. Interfaces. 9 (2017) 9996–10002. doi:10.1021/acsami.6b16765.

[265] C. Wen, A. Yin, W.-L. Dai, Recent advances in silver-based heterogeneous catalysts for green chemistry processes, Appl. Catal. B Environ. 160–161 (2014) 730–741. doi:10.1016/j.apcatb.2014.06.016.

[266] T.J. Huang, D.H. Tsai, CO oxidation behavior of copper and copper oxides, Catal. Letters. 87 (2003) 173–178. doi:10.1023/A:1023495223738.

[267] V.A. Sadykov, S.F. Tikhov, N.N. Bulgakov, A.P. Gerasev, Catalytic oxidation of CO on CuOx revisited: Impact of the surface state on the apparent kinetic parameters, Catal. Today. 144 (2009) 324–333. doi:10.1016/j.cattod.2008.12.018.

[268] S. ROYER, D. DUPREZ, S. KALIAGUINE, Role of bulk and grain boundary oxygen mobility in the catalytic oxidation activity of LaCo1–xFexO3, J. Catal. 234 (2005) 364–375. doi:10.1016/j.jcat.2004.11.041.

[269] D. Wolf, High-temperature structure and properties of grain boundaries: long-range vs. short-range structural effects, Curr. Opin. Solid State Mater. Sci. 5 (2001) 435–443. doi:10.1016/S1359-0286(01)00024-9.

[270] D. Zhang, J. Liu, P. Li, Z. Tian, C. Liang, Recent Advances in Surfactant-Free, Surface-Charged, and Defect-Rich Catalysts Developed by Laser Ablation and Processing in Liquids, ChemNanoMat. 3 (2017) 512–533. doi:10.1002/cnma.201700079.

[271] X. Wang, J.A. van Bokhoven, D. Palagin, Ostwald ripening versus single atom trapping: towards understanding platinum particle sintering, Phys. Chem. Chem. Phys. 19 (2017) 30513–30519. doi:10.1039/C7CP05887J.

[272] G. V. Mamontov, V. V. Dutov, V.I. Sobolev, O. V. Vodyankina, Effect of transition metal oxide additives on the activity of an Ag/SiO2 catalyst in carbon monoxide oxidation, Kinet. Catal. 54 (2013) 487–491. doi:10.1134/S0023158413040137.

[273] Z. QU, M. CHENG, W. HUANG, X. BAO, Formation of subsurface oxygen species and its high activity toward CO oxidation over silver catalysts, J. Catal. 229 (2005) 446–458. doi:10.1016/j.jcat.2004.11.043.

[274] M. Grabchenko, N. Mikheeva, G. Mamontov, M. Salaev, L. Liotta, O. Vodyankina, Ag/CeO2 Composites for Catalytic Abatement of CO, Soot and VOCs, Catalysts. 8 (2018) 285. doi:10.3390/catal8070285.

[275] M. Skaf, S. Aouad, S. Hany, R. Cousin, E. Abi-Aad, A. Aboukaïs, Physicochemical characterization and catalytic performance of 10% Ag/CeO 2 catalysts prepared by impregnation and deposition–precipitation, J. Catal. 320 (2014) 137–146. doi:10.1016/j.jcat.2014.10.006.

[276] C.G. Freyschlag, R.J. Madix, Precious metal magic: catalytic wizardry, Mater. Today. 14 (2011) 134–142. doi:10.1016/S1369-7021(11)70085-2.

[277] X.-J. Wen, C.-G. Niu, L. Zhang, C. Liang, G.-M. Zeng, A novel Ag2O/CeO2 heterojunction photocatalysts for photocatalytic degradation of enrofloxacin: possible degradation pathways, mineralization activity and an in depth mechanism insight, Appl. Catal. B Environ. 221 (2018) 701–714. doi:10.1016/j.apcatb.2017.09.060.

[278] I.-T. Liu, M.-H. Hon, C.-Y. Kuan, L.-G. Teoh, Structure and optical properties of Ag/CeO2 nanocomposites, Appl. Phys. A. 111 (2013) 1181–1186. doi:10.1007/s00339-012-7339-y.

[279] S. Sun, Y. Xue, Q. Wang, S. Li, H. Huang, H. Miao, Z. Liu, Electrocatalytic activity of silver decorated ceria microspheres for the oxygen reduction reaction and their application in aluminium–air batteries, Chem. Commun. 53 (2017) 7921–7924. doi:10.1039/C7CC03691D.

[280] X. Zhang, G. Li, X. Song, S. Yang, Z. Sun, Three-dimensional architecture of Ag/CeO 2 nanorod composites prepared by dealloying and their electrocatalytic performance, RSC Adv. 7 (2017) 32442–32451. doi:10.1039/C7RA04651K.

[281] G. Li, F. Lu, X. Wei, X. Song, Z. Sun, Z. Yang, S. Yang, Nanoporous Ag–CeO2 ribbons prepared by chemical dealloying and their electrocatalytic properties, J. Mater. Chem. A. 1 (2013) 4974. doi:10.1039/c3ta01506h.

[282] D.S. Su, T. Jacob, T.W. Hansen, D. Wang, R. Schlögl, B. Freitag, S. Kujawa, Surface Chemistry of Ag Particles: Identification of Oxide Species by Aberration-Corrected TEM and by DFT Calculations, Angew. Chemie. 120 (2008) 5083–5086. doi:10.1002/ange.200800406.

[283] M.H. Dickman, M.T. Pope, Peroxo and Superoxo Complexes of Chromium, Molybdenum, and Tungsten, Chem. Rev. 94 (1994) 569–584. doi:10.1021/cr00027a002.

[284] G. Marzun, H. Bönnemann, C. Lehmann, B. Spliethoff, C. Weidenthaler, S. Barcikowski, Role of Dissolved and Molecular Oxygen on Cu and PtCu Alloy Particle Structure during Laser Ablation Synthesis in Liquids, ChemPhysChem. 18 (2017) 1175–1184. doi:10.1002/cphc.201601315.

[285] P. Hänzelmann, O. Meyer, Effect of molybdate and tungstate on the biosynthesis of CO dehydrogenase and the molybdopterin cytosine-dinucleotide-type of molybdenum cofactor in Hydrogenophaga pseudoflava, Eur. J. Biochem. 255 (1998) 755–765. doi:10.1046/j.1432-1327.1998.2550755.x.

[286] P. Hänzelmann, H. Dobbek, L. Gremer, R. Huber, O. Meyer, The effect of intracellular molybdenum in Hydrogenophaga pseudoflava on the crystallographic structure of the seleno-molybdo-iron-sulfur flavoenzyme carbon monoxide dehydrogenase, J. Mol. Biol. 301 (2000) 1221–1235. doi:10.1006/jmbi.2000.4023.

[287] S. Gilman, THE MECHANISM OF ELECTROCHEMICAL OXIDATION OF CARBON MONOXIDE AND METHANOL ON PLATINUM. I. CARBON MONOXIDE ADSORPTION AND DESORPTION AND SIMULTANEOUS OXIDATION OF THE PLATINUM SURFACE AT CONSTANT POTENTIAL 1, J. Phys.

Chem. 67 (1963) 1898–1905. doi:10.1021/j100803a041.

[288] R. Yeetsorn, G. Kumar Yogesh, W. Wanchan, P. Koinkar, K. Yadav, Molybdenum-based Nanocatalysts for CO Oxidation Reactions in Direct Alcohol Fuel Cells: A Critical Review, ChemCatChem. 15 (2023). doi:10.1002/cctc.202301040.

[289] G. Bagnasco, G. Peluso, G. Russo, M. Turco, G. Busca, G. Ramis, Ammonia oxidation over CuO/TiO2 catalyst: Selectivity and mechanistic study, in: 1997: pp. 643–652. doi:10.1016/S0167-2991(97)81026-9.

[290] F. Wang, G. He, B. Zhang, M. Chen, X. Chen, C. Zhang, H. He, Insights into the Activation Effect of H 2 Pretreatment on Ag/Al 2 O 3 Catalyst for the Selective Oxidation of Ammonia, ACS Catal. 9 (2019) 1437–1445. doi:10.1021/acscatal.8b03744.

[291] F. Wang, J. Ma, G. He, M. Chen, C. Zhang, H. He, Nanosize Effect of Al2O3 in Ag/Al2O3 Catalyst for the Selective Catalytic Oxidation of Ammonia, ACS Catal. 8 (2018) 2670–2682. doi:10.1021/acscatal.7b03799.

[292] Z. Qu, H. Wang, S. Wang, H. Cheng, Y. Qin, Z. Wang, Role of the support on the behavior of Ag-based catalysts for NH 3 selective catalytic oxidation (NH 3 -SCO), Appl. Surf. Sci. 316 (2014) 373–379. doi:10.1016/j.apsusc.2014.08.023.

[293] J. Guo, W. Yang, Y. Zhang, L. Gan, C. Fan, J. Chen, Y. Peng, J. Li, A multiple-active-site Cu/SSZ-13 for NH3-SCO: Influence of Si/Al ratio on the catalytic performance, Catal. Commun. 135 (2020) 105751. doi:10.1016/j.catcom.2019.105751.

[294] Z. Wang, Z. Qu, X. Quan, Z. Li, H. Wang, R. Fan, Selective catalytic oxidation of ammonia to nitrogen over CuO-CeO2 mixed oxides prepared by surfactant-templated method, Appl. Catal. B Environ. 134–135 (2013) 153–166. doi:10.1016/j.apcatb.2013.01.029.

[295] H. Wang, Q. Zhang, T. Zhang, J. Wang, G. Wei, M. Liu, P. Ning, Structural tuning and NH3-SCO performance optimization of CuO-Fe2O3 catalysts by impact of thermal treatment, Appl. Surf. Sci. 485 (2019) 81–91. doi:10.1016/j.apsusc.2019.04.196.

[296] T. Zhang, H. Chang, Y. You, C. Shi, J. Li, Excellent Activity and Selectivity of One-Pot Synthesized Cu–SSZ-13 Catalyst in the Selective Catalytic Oxidation of Ammonia to Nitrogen, Environ. Sci. Technol. 52 (2018) 4802–4808. doi:10.1021/acs.est.8b00267.

[297] K. Góra-Marek, K.A. Tarach, Z. Piwowarska, M. Łaniecki, L. Chmielarz, Ag-loaded zeolites Y and USY as catalysts for selective ammonia oxidation, Catal. Sci. Technol. 6 (2016) 1651–1660. doi:10.1039/C5CY01446H.

[298] L. ZHANG, C. ZHANG, H. HE, The role of silver species on Ag/Al2O3 catalysts for the selective catalytic oxidation of ammonia to nitrogen, J. Catal. 261 (2009) 101–109. doi:10.1016/j.jcat.2008.11.004.

[299] J.J.P. Biermann, F.J.J.G. Janssen, M. De Boer, A.J. Van Dillen, J.W. Geus, E.T.C. Vogt, Molybdena on silica catalysts: selective catalytic oxidation of ammonia to nitrogen over MoO3 on siO2 catalysts, J. Mol. Catal. 60 (1990) 229–238. doi:10.1016/0304-5102(90)85272-J.

[300] M. de Boer, H.M. Huisman, R.J.M. Mos, R.G. Leliveld, A.J. van Dillen, J.W. Geus, Selective oxidation of ammonia to nitrogen over SiO2-supported MoO3 catalysts, Catal. Today. 17 (1993) 189–200. doi:10.1016/0920-5861(93)80023-T.

[301] K. Duan, X. Tang, H. Yi, Y. Zhang, P. Ning, Comparative Study on Low Temperature Selective Catalytic Oxidation of Ammonia over Transition Metals Supported on TiO2, in: 2010 Int. Conf. Manag. Serv. Sci., IEEE, 2010: pp. 1–4. doi:10.1109/ICMSS.2010.5576789.

[302] J.C. Védrine, G.J. Hutchings, C.J. Kiely, Molybdenum oxide model catalysts and vanadium phosphates as actual catalysts for understanding heterogeneous catalytic partial oxidation reactions: A contribution by Jean-Claude Volta, Catal. Today. 217 (2013) 57–64. doi:10.1016/j.cattod.2013.01.004.

[303] G. Ghiotti, F. Prinetto, FT-IR study of the nature and stability of NOx surface species on ZrO2, VOx/ZrO2 and MoOx/ZrO2 catalysts, Res. Chem. Intermed. 25 (1999) 131–156. doi:10.1163/156856799X00266.

[304] NIST, X-ray Transition Energies Database, (n.d.). doi:10.18434/T4859Z.

[305] B. Predel, Ag-Pt (Silver-Platinum), in: O. Madelung (Ed.), Ac-Au – Au-Zr, Springer-Verlag, Berlin/Heidelberg, 1991: pp. 1–3. doi:10.1007/10000866_58.

[306] G.L.W. Hart, L.J. Nelson, R.R. Vanfleet, B.J. Campbell, M.H.F. Sluiter, J.H. Neethling, E.J. Olivier, S. Allies, C.I. Lang, B. Meredig, C. Wolverton, Revisiting the revised Ag-Pt phase diagram, Acta Mater. 124 (2017) 325–332. doi:10.1016/j.actamat.2016.10.053.

[307] A. Buzková Arvajová, J. Březina, R. Pečinka, P. Kočí, Modeling of two-step CO oxidation light-off on Pt/γ-Al2O3 in the presence of C3H6 and NO, Appl. Catal. B Environ. 233 (2018) 167–174. doi:10.1016/j.apcatb.2018.03.081.

[308] R.T. Sataloff, M.M. Johns, K.M. Kost, VDI-Wärmeatlas, 11th ed., Springer Berlin Heidelberg, Berlin, Heidelberg, 2013. doi:10.1007/978-3-642-19981-3.

[309] L. Vitos, A.V. Ruban, H.L. Skriver, J. Kollár, The surface energy of metals, Surf. Sci. 411 (1998) 186–202. doi:10.1016/S0039-6028(98)00363-X.

[310] P. Pyykkö, M. Atsumi, Molecular Single-Bond Covalent Radii for Elements 1-118, Chem. - A Eur. J. 15 (2009) 186–197. doi:10.1002/chem.200800987.

[311] E. Guides, Handbook of Physical Vapor Deposition (PVD) Processing, Elsevier, 2010. doi:10.1016/C2009-0-18800-1.

[312] D.R. Lide, ed., CRC - Handbook of Chemistry and Physics, 84th ed., CRC Press, Boca Raton, 2003.

[313] G. Brauer, Handbuch der präparativen anorganischen Chemie in drei Bänden, Ferdinand Enke, 1981.

[314] E. Riedel, C. Janiak, Anorganische Chemie, DE GRUYTER, 2010. doi:10.1515/9783110225679.

[315] D. McIntosh, G.A. Ozin, Synthesis of binary gold carbonyls, Au(CO)n (n = 1 or 2). Spectroscopic evidence for isocarbonyl(carbonyl)gold, a linkage isomer of bis(carbonyl)gold, Inorg. Chem. 16 (1977) 51–59. doi:10.1021/ic50167a013.

[316] T.J. Woehl, T. Prozorov, The Mechanisms for Nanoparticle Surface Diffusion and Chain Self-Assembly Determined from Real-Time Nanoscale Kinetics in Liquid, J. Phys. Chem. C. 119 (2015) 21261–21269. doi:10.1021/acs.jpcc.5b07164.

[317] F. Waag, Autopronano synthesis machine, (2022). https://www.autopronano.eu/ (accessed March 30, 2023).

[318] T. Bessel, S. Dittrich, B. Gökce, S. Barcikowski, F. Waag, Automated synthesis of colloidal nanoparticles powered by microchip lasers, in: Lasers Manuf. Conf., Bayerisches Laserzentrum GmbH, 2021.

[319] T. BESSEL, S. BARCIKOWSKI, F. WAAG, Fully-Automatic Benchtop Machine for the Production of Nanoparticle Suspensions, in: NANOCON Conf. Proc. - Int. Conf. Nanomater., 2021: pp. 405–410. doi:10.37904/nanocon.2021.4317.

[320] S. Siebeneicher, S. Reichenberger, C. Hengst, F. Dornhaus, B. Wittek, S. Barcikowski, Activity and Durability Patterns of 45 Binary Noble Metal Alloy Nanoparticle Variants for Commercial Diesel Exhaust Aftertreatment, ChemCatChem. (2023). doi:10.1002/cctc.202300563.

[321] T. Löffler, F. Waag, B. Gökce, A. Ludwig, S. Barcikowski, W. Schuhmann, Comparing the Activity of Complex Solid Solution Electrocatalysts Using Inflection Points of Voltammetric Activity Curves as Activity Descriptors, ACS Catal. 11 (2021) 1014–1023. doi:10.1021/acscatal.0c03313.

[322] H. Okamoto, T.B. Massalski, The Au-Rh (Gold-Rhodium) system, Bull. Alloy Phase Diagrams. 5 (1984) 384–387. doi:10.1007/BF02872960.

[323] B. Predel, Au-Ir (Gold-Iridium), in: Landolt-Börnstein - Gr. IV Phys. Chem. (Numerical Data Funct. Relationships Sci. Technol. Ac-Au – Au-Zr, Springer-Verlag, Berlin/Heidelberg, 1991: pp. 1–1. doi:10.1007/10000866_286.

[324] B. Predel, Pt-Ru (Platinum-Ruthenium), in: Phase Equilibria, Crystallogr. Thermodyn. Data Bin. Alloy. · Ni-Np – Pt-Zr, Springer-Verlag, Berlin/Heidelberg, 1998: pp. 1–1. doi:10.1007/10542753_2519.

[325] B. Predel, Cu-Pt (Copper-Platinum), in: O. Madelung (Ed.), Landolt-Börnstein - Gr. IV Phys. Chem. - 5d -Cr-Cs – Cu-Zr, Springer-Verlag, Berlin/Heidelberg, 1994: pp. 1–6. doi:10.1007/10086090_1106.

[326] P.. Subramanian, D.. Laughlin, Cu-Pd (Copper-Palladium), J. Phase Equilibria. 12 (1991) 231–243. doi:10.1007/BF02645723.

[327] B. Predel, Pt-Rh (Platinum-Rhodium), in: O. Madelung (Ed.), Landolt-Börnstein - Gr. IV Phys. Chem. - 5l - Ni-Np – Pt-Zr, Springer-Verlag, Berlin/Heidelberg, 1998: pp. 1–2. doi:10.1007/10542753_2518.

[328] B. Predel, Nb-Pt (Niobium-Platinum), in: O. Madelung (Ed.), Li-Mg – Nd-Zr, Springer-Verlag, Berlin/Heidelberg, 1997: pp. 1–2. doi:10.1007/10522884_2185.

[329] S.N. Tripathi, S.R. Bharadwaj, S.R. Dharwadkar, The Nb-Pt (Niobium-Platinum) system, J. Phase Equilibria. 16 (1995) 465–470. doi:10.1007/BF02645357.

[330] B. Predel, Mn-Pt (Manganese-Platinum), in: Part Landolt-Börnstein - Gr. IV Phys. Chem. 5H Li-Mg – Nd-Zr, Springer-Verlag, Berlin/Heidelberg, 1997: pp. 1–5. doi:10.1007/10522884_2040.

[331] P. Franke, D. Neuschütz, Fe-Pt, in: Landolt-Börnstein - Gr. IV/5 - Bin. Syst. from Cs-K to Mg-Zr, Springer-Verlag, Berlin/Heidelberg, 2005. doi:10.1007/10757413_41.

[332] B. Predel, Mo-Pt (Molybdenum-Platinum), in: Landolt-Börnstein - Gr. IV Phys. Chem. (Numerical Data Funct. Relationships Sci. Technol. Li-Mg – Nd-Zr, Springer-Verlag, Berlin/Heidelberg, 1997: pp. 1–2. doi:10.1007/10522884_2085.

[333] H. MASUDA, K. IINOYA, THEORETICAL STUDY OF THE SCATTER OF EXPERIMENTAL DATA DUE TO PARTICLE-SIZE-DISTRIBUTION, J. Chem. Eng. JAPAN. 4 (1971) 60–66. doi:10.1252/jcej.4.60.

[334] H. Okamoto, Pd-Pt (Palladium-Platinum), J. Phase Equilibria. 12 (1991) 617–618. doi:10.1007/BF02645087.

[335] B. Predel, Pd-Pt (Palladium-Platinum), in: O. Madelung (Ed.), Landolt-Börnstein - Gr. IV Phys. Chem. - 5l Ni-Np – Pt-Zr, Springer-Verlag, Berlin/Heidelberg, 1998: pp. 1–2. doi:10.1007/10542753_2435.

[336] E. Raub, Metals and alloys of the platinum group, J. Less Common Met. 1 (1959) 3–18. doi:10.1016/0022-5088(59)90014-1.

[337] I. Karakaya, W.T. Thompson, The Ag-Pt (Silver-Platinum) system, Bull. Alloy Phase Diagrams. 8 (1987) 334–340. doi:10.1007/BF02869269.

Appendix

A1 Alloying elements with anticipated effect and outcome

Element/ Mixture	Anticipated effect	Background/Hypothesis
Platin	Base element	
Pt-**Pd**	High activity in oxidation reactions (DOC, ASC), moderate NO_x formation	Typical in waste gas abatement [9], alloy limits particle growth [32]
Pt-**Rh**	High activity in oxidation reactions (DOC, ASC), low NO_x formation, high durability	Typical in three way catalysts (for NO_x reduction), increased durability [9] Similar activation energy for CO oxidation as Pt [33]
Pt-**Ag**	Should perform similar to Pt-Pd in DOC	With H_2O present, O_2 dissociation is enhanced ([35,36])→ well suited for wet waste gas stream Sabatier-principle suggests improvements in CO oxidation when compared to Pt [37]
Pt-**Au**		With H_2O present, CO oxidation is enhanced [34] → well suited for wet waste gas stream Sabatier-principle suggests improvements in CO oxidation when compared to Pt [37]; preservation of high selectivity possible [13]
Pt-**Mn**	Should perform similar to Pt-Pd (ASC)	Oxides are amongst the most active for NH_3 oxidation [38] Ennobling via Pt

Element/ Mixture	Anticipated effect	Background/Hypothesis
Pt-**Cu**	Should perform similar to Pt-Pd (DOC, ASC)	Sabatier-principle suggests improvements in CO oxidation when compared to Pt [37] Oxides are amongst the most active for NH_3 oxidation [38] Ennobling via Pt
Pt-**Fe**	Should perform similar to Pt-Pd (ASC); high selectivity fo N_2 (ASC)	High activation energy for N_2 dissociation → N_2 (desired product) should be favoured [39] Oxides are amongst the most active for NH_3 oxidation [38] Ennobling via Pt
Pt-**Ru**	Should perform similar to Pt-Pd (DOC, ASC), high selectivity for N_2 (ASC) High durability	RuO_2 shows high activity in CO oxidation. Restructuring of the crystal and the presence of water lead to inactivity [40] → Ennobling via Pt should help prevent this High activation energy for N_2 dissociation → N_2 (desired product) should be favoured [39] High selectivity for NH_3 reduction to N_2 [40,41] High melting point
Pt-**Nb**	Should perform similar to Pt-Pd (DOC), High durability	High melting point Ennobling via Pt
Pt-**Mo**		
Additional alloys		
Pd-Cu	Should perform similar to Pt-Pd (DOC)	Sabatier-principle suggests improvements in CO oxidation when compared to Pd [37]
Au-Ir	Improved selectivity towards desired products (N_2, H_2O, CO_2)	Activity moderation of Ir by alloying with Au, O-Spillover from Ir to Au [13,42]
Au-Rh		Activity moderation of Rh by alloying with Au
Excluded due to target preparation challenges		
Rhenium		High melting point, interesting for target synthesis studies (Does not form stable targets without additional synthesis steps)
Wolfram		
Zinn		Low melting point interesting for target synthesis studies (melting of element before alloying)
Bismuth		

A2 Mixing ratios of the alloys

Alloy	Nominal share of first element [at%]				Reasons for selection
Pt-Pd	66	Twice (alloyed and mixed)			Little segregation to be expected during solidification.[2]
Au-Ir	(1)	(25)	50	99	Broad miscibility gap in solid (Au-Rh [322]) respectively in liquid and solid (Au-Ir [323]). Definition of a broad mix and orientation towards the dystectic at Au-Rh.
Au-Rh	(1)	(10)	(43)	90	
Pt-Ru	5	20	80	95	Broad solubility of both elements. Only narrow miscibility gap. [324] Gap is circumvented by blending at the extremes.
Pt-Cu	10	30	75	90	Selection of one precious metal-rich and one copper-rich mixture and two mixtures around the equimolar range. Some consideration of crystal transformation-related segregation after solidification.[325,326]
Pd-Cu	15	45	70	90	
Pt-Au	10	50	90	95	Explorative mixtures, as broad segregation is to be expected during solidification (Ag, Au) and through crystallisation (Au). For Au, one mixture with less (10 %) and one with greater (50 %) segregation tendency. [157]
Pt-Ag	22	53	90	95	For Ag: Orientation toward known intermetallic phases (22 %, 53 %*[3]). [305,306] In addition, two Pt-rich mixtures each.
Pt-Rh	50	90	95	99	Mainly alloys with a high platinum content, to reduce the price impact of rhodium and because miscibility in the solid state can be expected. In addition, an exploratory mixture in the middle of the miscibility gap (50 %) [327]

[2] In the solid state, a miscibility gap is predicted, although no specific details of the affected composition are given. [334–336]

[3] The phase diagram of the Pt-Ag system was recently re-examined. No evidence of a phase at 53 at% platinum was found and instead an equimolar intermetallic phase is suspected [306]. Prior to this work, the phase diagram of Karakaya et al. was the most widely accepted. In it, however, there remains some room for variation around the equimolar mixture [337]. A target of a 53 at% mixture therefore seems intriguing for this work.

Alloy	Nominal share of first element [at%]				Reasons for selection
Pt-Nb	43	75	95	99	Consideration of eutectic and dystectic in the low mixing range. [328–330] In addition, two mixtures with a high Pt content.
Pt-Mn	49	75	95	99	
Pt-Mo	50	66	95	99	Orientation towards various intermetallic phases in the Pt-poor region of both mixtures. [331,332] In addition, two mixtures with a high Pt content.
Pt-Fe	50	66	95	99	

The preceding table shows all mixtures with the assigned nominal share of the base element in the binary mixture. The base element is always the first element in the mixture column (Pt, Au or Pd). The mixtures marked in blue are those in which, among other things, a high CO oxidation activity is expected. Marked in orange are mixtures for which other reasons for selection were in the foreground (mainly ennobling and thus activation by platinum). Pt-Pd and Au-Ir are marked separately due to their special position. All bracketed mixture ratios were planned as targets but could not be successfully produced or ablated.

A3 Determination of the specific surface area by means of TEM

Application of a lognormal fit

The particle size distributions were created manually using TEM images. Sufficient images were taken to count and measure at least 500 particles. For a number-weighted particle distribution, assuming a standard deviation of the distribution of 0.47 as a measure of the distribution width, at least 490 particles must be measured for a particle size distribution with approx. 10 % error. For a similar accuracy of a mass-weighted distribution, however, 2800 particles per sample must be measured [333]. Since this number is not practicable, it cannot be avoided that large particles are measured whose occurrence is not statistically significant. In order to obtain a reliable determination of the specific surface area, the obtained histogram is fitted using a lognormal distribution function. Based on this fit, the specific surface area of the sample is then determined. The advantage of this method is that no number of large particles has a significant, falsifying influence on the determined specific surface area.

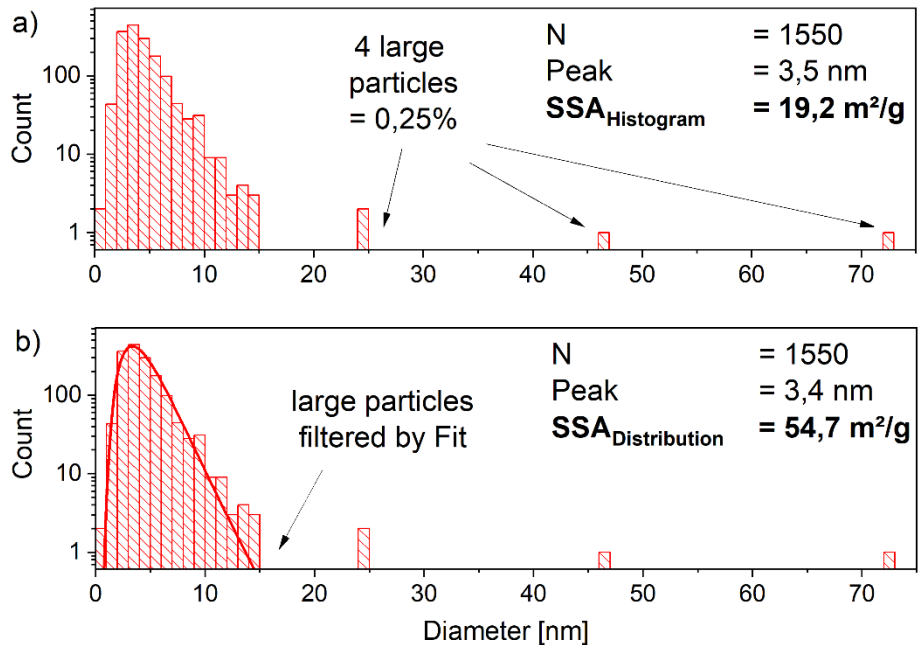

Figure 37 Exemplary size distribution. In a) only the histogram and the parameters determined from it are shown. In b) the lognormal fit is also shown and used as the basis for the calculations. The y axis is logarithmic for better recognition of the small number of "larger" particles.

By way of example, the usefulness and necessity of this procedure is illustrated using a sample. In Figure 37 the peak position and the specific surface area are calculated. In one case, the raw data of the histogram is used directly for the calculation (a), in another case, the data is first fitted and this fit is used as the basis for the calculation (b). A total of 1550

nanoparticles were counted in this sample. The specific surface area of the nanoparticles calculated directly from the histogram is 19.3 m^2/g. If the lognormal fit is now used as a basis, a specific surface area of 54.7 m^2/g results. A similar result is obtained when the four largest particles are filtered out of the histogram (52 m^2/g). These four particles only account for 0.25 % of the total number and, due to their size, cause the specific surface area to be reduced to less than half. Since the determined particle numbers are regularly well below 2800, and the mass-weighted distributions are therefore unreliable, the most sensible approach is to use the lognormal fit to determine the specific surface area.

Data for the calculation of the mean density

To determine a specific surface area, the density of the material under investigation is always required. The choice of the correct density is not as trivial as it seems at first sight. Apart from the fact that it is unknown whether the density of the alloys corresponds to an arithmetic mean of the constituents, there are several possibilities to determine the quantity proportions. The first attempt may be assuming of the nominal composition; however, slight deviations already result from the possible precision when weighing the single metals. Furthermore, these data points initially only correspond to the expectation. It is not guaranteed that the nominally set composition is also found in the target material. The main reason for this is a potentially inhomogeneous mixture in the target and the resulting shift in composition in the ablated spot. Furthermore, it is conceivable that an inhomogeneous mixture leads to preferential ablation of a constituent due to different threshold fluences of the individual materials. Thus, a target-based density determination is not target-oriented. TEM-EDX measurements would be most direct on the final material. However, these are out of the question because of their poor statistical significance due to their principle. The most suitable method for determining the average density therefore appears to be one that measures both a large proportion of the sample and the nanoparticles directly. The ICP-OES measurement fulfils these criteria.

Based on the composition determined by ICP-OES measurements, the average density of the alloy is finally determined. A simple arithmetic averaging of the constituent densities is assumed.

A4 Supporting information: Activity and Durability Patters of 45 Binary Noble Metal Alloy Nanoparticle Variants for Commercial Diesel Exhaust Aftertreatment

Published on 5th July 2023 in ChemCatChem (doi: 10.1002/cctc.202300563)

ChemCatChem

Supporting Information

Activity and Durability Patterns of 45 Binary Noble Metal Alloy Nanoparticle Variants for Commercial Diesel Exhaust Aftertreatment

Simon Siebeneicher, Sven Reichenberger, Christoph Hengst, Franz Dornhaus, Bernd Wittek, and Stephan Barcikowski*

Table of Contents

S1. Synthesis Details

S1.1. Target production

In addition to the presented samples in the main study, also mixtures of iridium and gold, as well as rhodium and gold and palladium and copper were tested. These samples will also be shown in the supplementary information.

To produce a mixed-metal target two metal powders are combined in the appropriate amounts. The mixture is then mixed with 5 mm ZrO_2-Balls in a rotary tumbler, mixtures with base metals are kept under an inert atmosphere (Argon). The mixed powder is filled into a die and pressed with 200 MPa for 30 seconds. The resulting green target is transferred into an oven and sintered at 2/3 of the solidus temperature of the mixture. The duration of sintering, and if necessary, the temperature is adjusted so that the resulting target will have sufficient mechanical stability. The gas mixture is chosen to prohibit oxidation of the powder. The origin of the raw materials is listed in Table 1 and the detailed sintering parameters can be found in Table 2.

Table 1 Origin of metal raw materials.

Metal	Manufacturer	Purity	d_{50}[µm]	Notice
$Pt_{66}Pd_{34}$	ACI Alloys, Inc.	99.95%	//	Alloyed target
Platinum	Ferro	99%	2-4	
Palladium	Umicore	99%	<32	Sieved from <53 µm
Rhodium	Ferro	>97%	2-5	
Copper	Alfa Aesar	99.9%	4	Stored under argon
Gold	Evochem	99.9%	1.5-4	
Silver	Evochem	99.9%	1.5-4	
Ruthenium	Evochem	99.9%	50	Stored under argon
Molybdenum	Alfa Aesar	99.9%	2-4	Stored under argon
Tungsten	H.C. Starck	99.95%	1.7	Stored under argon
Niobium	Alfa Aesar	99.8%	1-5	Stored under argon
Iridium	Evochem	99.9%	<10	
Iron	Alfa Aesar	>98%	1-3	Stored under argon
Manganese	Alfa Aesar	99.6	<10	Stored under argon

Table 2 Sintering parameters for all targets.

Sample system	Nominal content of first metal (Pt/Pd/Au) [at%]	Route	Sintering temperature [°C]	Sintering duration [hh:mm]
Pt-Pd	66	The pre-made target from melt	//	//
Pt-Pd	66		//	//
Pt-Rh	50	Sintering - Air	1200	03:00
Pt-Rh	90		1200	03:00
Pt-Rh	95		1200	03:00
Pt-Rh	99		1200	03:00

Sample system	Nominal content of first metal (Pt/Pd/Au) [at%]	Route	Sintering temperature [°C]	Sintering duration [hh:mm]
Pt-Au	10		900	03:00
Pt-Au	50		900	03:00
Pt-Au	90		900	03:00
Pt-Au	95		900	03:00
Pt-Ag	22		650	03:00
Pt-Ag	53		650	03:00
Pt-Ag	90		650 + 900[1]	3:00 + 9:00[1]
Pt-Ag	95		650 + 900[1]	3:00 + 9:00[1]
Au-Rh	90		900	3:00
Au-Ir	99		900	3:00
Au-Ir	50		900	3:00
Pd-Cu	15	Sintering - Shielding gas [2]	700	18:00
Pd-Cu	45		700	18:00
Pd-Cu	70		700	18:00
Pd-Cu	90		700	18:00
Pt-Cu	10	Sintering - Shielding gas	700 / 850[3]	27:00 / 3:00[3]
Pt-Cu	30		700 / 850[3]	27:00 / 3:00[3]
Pt-Cu	75		850	03:00
Pt-Cu	90		850	03:00
Pt-Fe	50		1100	12:00
Pt-Fe	66		1100	12:00
Pt-Fe	95		1100	12:00
Pt-Fe	99		1100	12:00
Pt-Mo	50		1100	12:00
Pt-Mo	66		1100	12:00
Pt-Mo	95		1100	12:00
Pt-Mo	99		1100	12:00
Pt-Mn	49		1100	18:00
Pt-Mn	75		1100	18:00

[1] After the first sintering the targets were still brittle. A second sintering at elevated temperatures and for a longer duration consolidated those targets and allowed ablation.

[2] During the sintering process with shielding gas, the atmosphere in the pipe furnace was ARCAL F5 (Air-Liquide, 5 %H_2 in N_2). During the cooling phase, the oven was flushed with argon.

[3] Two targets were produced to yield enough colloid. The first target was sintered for a long time at a lower temperature and the second one shorter and at elevated temperature.

Sample system	Nominal content of first metal (Pt/Pd/Au) [at%]	Route	Sintering temperature [°C]	Sintering duration [hh:mm]
Pt-Mn	95		1100	18:00
Pt-Mn	99		1100	18:00
Pt-Ru	5		1100	2x 21:00
Pt-Ru	20		1100	2x 21:00
Pt-Ru	80		1100	2x 21:00
Pt-Ru	95		1100	21:00
Pt-Nb	43		1100	2x 21:00
Pt-Nb	75		1100	2x 21:00
Pt-Nb	95		1100	21:00
Pt-Nb	99		1100	21:00

S1.2. Colloid Synthesis

To allow the formation of alloyed nanoparticles the conditions of ablation must be chosen to prevent oxidation of the metals, as alloying of the oxides is considered to be unlikely. While noble metals generally tend to stay reduced during ablation in water [40], base metals tend to form oxides [65], sometimes even when carbon-rich solvents are used [47]. To prevent oxidation in this study, propylene carbonate was used as the solvent. Its high polarity readily stabilizes the colloids, and its low vapour pressure means, that there is no flame risk while ablating. The last point is especially important if large amounts of colloid are synthesized, like in this study. Although the molecule contains a significant amount of oxygen, this did not seem to influence the alloy formation negatively.

The classification of metals into noble and base metal was chosen according to Table 3. As it is known that the ablation of copper in water leads to largely oxidized nanoparticles [47], and the ablation of silver in water leads to metallic nanoparticles [51], silver was classified as noble and everything with a lower standard potential as base metal.

Table 3 Standard potentials for used elements and grouping in noble (grey) and base metal (orange).

Element	oxidized species		reduced species	*Standard potential E°*
Gold (Au)	Au^+	$+ e^- \rightleftharpoons$	Au	+1,50 V [66]
Platinum (Pt)	Pt^{2+}	$+ 2 e^- \rightleftharpoons$	Pt	+1,20 V [66]
Iridium (Ir)	Ir^{3+}	$+ 3 e^- \rightleftharpoons$	Ir	+1,156 V [67]
Palladium (Pd)	Pd^{2+}	$+ 2 e^- \rightleftharpoons$	Pd	+0,951 V [67]
Silver (Ag)	Ag^+	$+ e^- \rightleftharpoons$	Ag	+0,80 V [66]

Element	oxidized species		reduced species	*Standard potential E°*
Ruthenium (Ru)	Ru^{2+}	$+ 2 e^- \rightleftharpoons$	Ru	+0,455 V [67]
Copper (Cu)	Cu^{+}	$+ e^- \rightleftharpoons$	Cu	+0,52 V [66]
Copper (Cu)	Cu^{2+}	$+ 2 e^- \rightleftharpoons$	Cu	+0,337 V [66]
Molybdenum (Mo)	Mo^{3+}	$+ 3 e^- \rightleftharpoons$	Mo	−0,20 V [67]
Iron (Fe)	Fe^{2+}	$+ 2 e^- \rightleftharpoons$	Fe	−0,44 V [66]
Niobium (Nb)	Nb^{3+}	$+ 3 e^- \rightleftharpoons$	Nb	−1,099 V [67]
Manganese (Mn)	Mn^{2+}	$+ 2 e^- \rightleftharpoons$	Mn	−1,185 V [67]

While the ablation in propylene carbonate was performed without the addition of additives, the ablation in water required additives to yield stable colloids with the desired particle size distribution.

The additives for water were chosen to stabilize the colloids but were also required to dissipate upon pyrolysis. This would ensure that no residue from stabilizers is present on the catalysts when measuring the catalytic performance. Upon the start of the project KOH (500 µM) and Sodium citrate (100 µM) were used, but as soon as it became available ammonium citrate (100 µM) was utilized. This way even minute amounts of stabilizer containing potassium or sodium could be avoided. Titration of the colloids for supporting was carried out using nitric acid and tetraethylammonium hydroxide (TEAOH), both with a 1M concentration. With the final choice of ammonium citrate, TEAOH and nitric acid a complete pyrolysis of the additives could be expected. Details, on which samples were synthesized with which additives, can be found in Table 4.

After deciding on a stabilizer and preparing a dispersant solution with which to perform the laser ablation a choice had to be made with which laser system to synthesize the colloids. For all water-based samples, the choice was made to use a nanosecond pulsed laser system, as this would aid in the alloying of the mixed and/or pre-alloyed metals upon laser ablation [50]. A wavelength of 532 nm was chosen to allow for maximized in situ fragmentation of the colloids after ablation which would help to attain as small colloid particles as possible. To maximize productivity overall, the laser was used at its maximum power of approx. 50 W and 5 kHz repetition rate to avoid reirradiation of the cavitation bubble.

All solvent-based samples were used with a picosecond-pulsed system. From prior experience, many solvents yield very low ablation rates compared to water in nanosecond pulsed systems. To allow the production of the large nanoparticle amounts a picosecond system was employed, even though the alloying abilities were expected to be not as well suited as with the other system. This problem was addressed within the preparation of the targets – it was made sure to prepare as well

alloyed targets as possible. The picosecond laser system works with a 1030 nm wavelength and 5 MHz repetition rate at approx. 94 µJ of pulse energy[4].
Due to a failure of the system, some samples had to be synthesized on the nanosecond system. In this case, the wavelength was kept as constant as possible (1064 nm) and the power as high as possible (120 W @5 kHz) to allow for sufficient productivity. Surprisingly propylene carbonate allowed a much higher ablation rate than expected, even comparable to water (around 400 mg/h, where 40 mg/h was expected). All detail on the used laser system and parameters, as well as the used additives can be found in Table 4. A comparison of the power-specific productivity (mg/Wh) can be found in Figure 1.

Table 4 Colloid synthesis parameters.

Sample system	Nominal content of first metal (Pt/Pd/Au) [at%]	Sample amount and loading	Laser pulse length [sec]	Laser wave-length [nm]	Laser frequency [kHz]	Medium	Additive with Ablation	the pH of the dispersant solution
Pt-Pd	66	50g, 3wt.%, dispersed	nano	532[5]	5	Water	KOH[6]	approx. 9.5
Pt-Pd	66							approx. 9.5
Pt-Cu	10	50g, 3wt.%, dispersed	nano	532	5	Water	Sodium citrate[7]	6.8-7.2
Pt-Cu	30							6.8-7.2
Pt-Cu	75							6.72-6.9
Pt-Cu	90							6.88
Pt-Rh	50	150g, 1wt.%, dispersed	nano	532	5	Water	Ammonium citrate[8]	6.82-7.1
Pt-Rh	90							6.99
Pt-Rh	95							7.0-7.1
Pt-Rh	99							6.96-7.1
Pt-Au	10	150g, 1wt.%, dispersed	nano	532	5	Water	Ammonium citrate + TEAOH	9.35
Pt-Au	50							9.36-9.5
Pt-Au	90							9.46-9.5
Pt-Au	95							9.45
Pt-Ag	22	150g, 1wt.%, dispersed	nano	532	5	Water	Ammonium citrate + TEAOH	9.33-9.42
Pt-Ag	53							9.33
Pt-Ag	90							9.2-9.32
Pt-Ag	95							9.2-9.27

[4] This translates to 467 W of Power. Due to temporary limitations of the scanning system only a duty cycle of approx. 20% could be attained. While the pulse energy stays the same (94 µJ), the laser power reaching the ablation chamber is limited to the mean power of 93 W.

[5] All samples on ns-Laser at 532 nm were synthesized with a pulse energy of about 10 mJ.

[6] KOH was used in a concentration of 500 µM.

[7] Sodium citrate was used in a concentration of 100 µM.

[8] Ammonium citrate was used at a concentration of 100 µM.

Sample system	Nominal content of first metal (Pt/Pd/Au) [at%]	Sample amount and loading	Laser pulse length [sec]	Laser wave-length [nm]	Laser frequency [kHz]	Medium	Additive with Ablation	the pH of the dispersant solution
Au-Rh	90	150g, 1wt.%, dispersed	nano	532	5	Water	Ammonium citrate + TEAOH	9.2
Au-Ir	50							9.34
Au-Ir	99							9.35
Pd-Cu	15	10g, 1wt.%, powder	pico	1030	5000	Propylene carbonate	/	/
Pd-Cu	45							
Pd-Cu	70							
Pd-Cu	90							
Pt-Fe	50	10g, 1wt.%, powder	pico	1030	5000	Propylene carbonate	/	/
Pt-Fe	66							
Pt-Fe	95							
Pt-Fe	99							
Pt-Mo	50	10g, 1wt.%, powder	pico	1030	5000	Propylene carbonate	/	/
Pt-Mo	66							
Pt-Mo	95							
Pt-Mo	99							
Pt-Mn	49	10g, 1wt.%, powder	nano[9]	1064	5	Propylene carbonate	/	/
Pt-Mn	75							
Pt-Mn	95							
Pt-Mn	99							
Pt-Ru	05	10g, 1wt.%, powder	nano	1064	5	Propylene carbonate	/	/
Pt-Ru	20		pico	1030	5000		/	/
Pt-Ru	80							
Pt-Ru	95							
Pt-Nb	43	10g, 1wt.%, powder	pico	1030	5000	Propylene carbonate	/	/
Pt-Nb	75							
Pt-Nb	95							
Pt-Nb	99							

[9] All samples synthesized with the ns-Laser at 1064 nm were obtained with a pulse energy of 24 mJ.

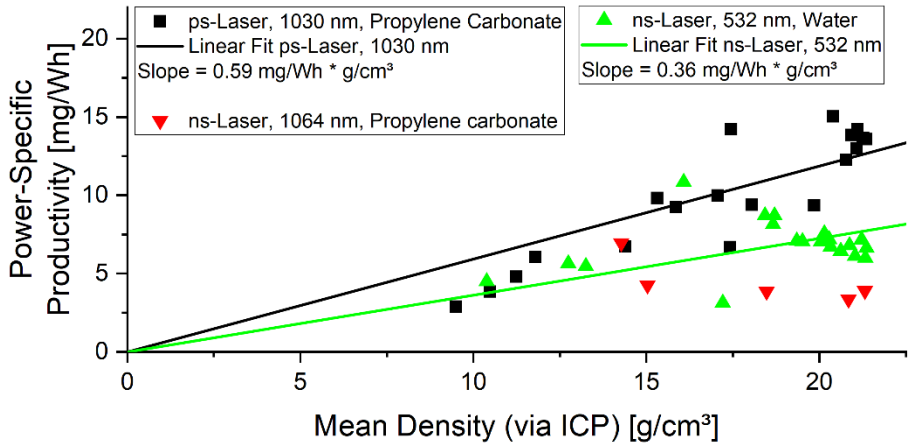

Figure 1 Power-specific productivity in comparison to the alloy density.

S1.3. Supporting Route

Supporting of the nanoparticles was done using two different mechanisms. The water-based samples were synthesized using an electrostatically driven supporting strategy. The propylene carbonate samples were synthesised using a diffusion-driven supporting mechanism.

To understand the adsorption of nanoparticles on a support, it is helpful to look at the surface charge of the nanoparticle and support. Generally, metallic nanoparticles are assumed to have an isoelectric point (IEP) at low pH (below 7). This was verified in this study for palladium, platinum and $Pt_{66}Pd_{34}$ colloids. A low IEP leads to a negative zeta potential for a large pH interval. Oxidic particles, with some exceptions, tend to have an IEP above pH 7, leading to a negative zeta potential at higher pH and a positive zeta potential at lower pH [68]. The IEP of the used alumina was verified to have an IEP at around 8.4. An example of this situation is shown in Figure 2. If both particle dispersions are mixed while having a high pH (ca. 9.5), electrostatic repulsion leads to a high energy barrier for adsorption. This means that the colloid and support can be mixed thoroughly, without premature adsorption. As this might

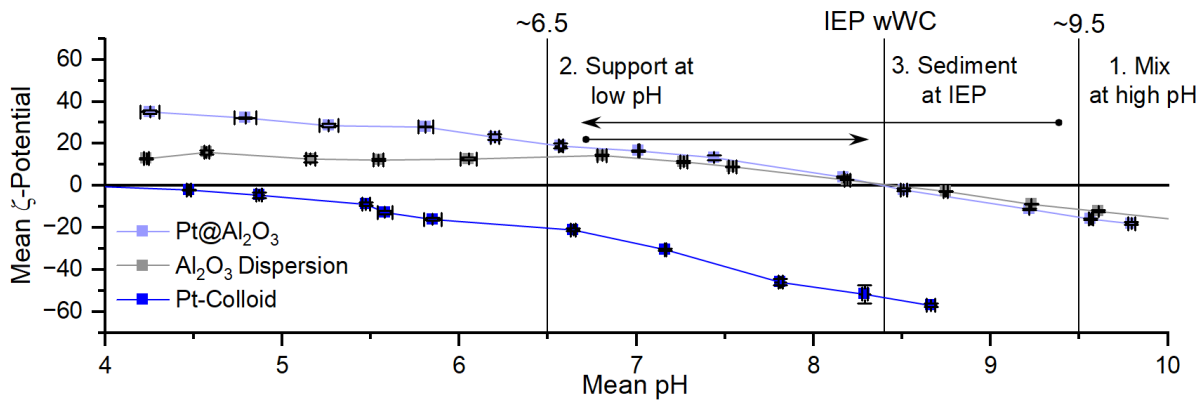

Figure 2 Exemplary zeta-potential curves for metallic (platinum) and oxidic (Al_2O_3) particles and illustration of the supporting strategy.

lead to inhomogeneous distribution of nanoparticles on the support material. After sufficient mixing, the pH can be adjusted, so that the support particles have a positive zeta-potential, while the nanoparticles still attain a negative surface charge. In this environment, the electrostatic attraction lowers the energy barrier for adsorption and the nanoparticles adsorb onto the support material.

This strategy is very robust: If the isoelectric point of the metallic nanoparticles is not too close to or higher than that of the support this strategy will work. That is because, during titration, the mixture will move twice through a region where the support is already positively charged, while the nanoparticles are still negatively charged.

In this study, the mass loading was between 1 and 3 wt.%. At this loading, the isoelectric point of the resulting catalyst is not very different from the support material (cf. Figure 2). This fact can be used to concentrate the solution. By adjusting the pH towards the IEP of the support material, agglomeration of the catalyst powder is induced. The sedimentation of the agglomerates leaves a clear liquid in case of successful adsorption. The adsorption efficiency can be probed at this point by measuring the supernatant in UV-VIS and comparing it to the colloid. In this study adsorption always worked and left a clear supernatant, meaning a near 100 % adsorption efficiency.

The synthesis of colloids and subsequent supporting leaves much potential for optimization. Synthesis of the colloid generally takes many hours, after which the titration of the colloid and support dispersion can start. All titration steps require sufficient waiting time to equilibrate surface charges to stay as close to the support theory as possible. If the colloid would exit the ablation chamber already at high pH, an addition to the caustic support dispersion could follow immediately. This removes the need for separate titration and mixing of the dispersions. After the conclusion of the laser synthesis process, the mixing of colloid and support is already complete and titration to support the particles can follow immediately. Table 5 details which route was used for which samples. Subsequent in this case means the colloid synthesis was concluded before the supporting started (mostly within 1 day). Downstream means the colloid was synthesised at caustic pH and directly mixed with the support as described before. In this table, it can also be found which acid and base were used for titration. Both substances should leave as little residue after titration as possible. The titration of KOH with HNO_3 leaves very soluble KNO_3 and the magnitude of this is removed during concentration via sedimentation. Even though, a switch was made to the organic base tetraethylammonium hydroxide (TEAOH). This ensures that as little residue is left on the samples as possible.

Table 5 Details on the supporting of the samples.

Sample system	Nominal content of first metal (Pt/Pd/Au) [at%]	Supporting route	Additives	Min / Max pH	Loading determined by ICP-OES [wt.%]	Maximum temperature [°C]
Pt-Pd	66	Subsequent – water-based	HNO_3, KOH	6.8 / 10.15	2.97	RT
Pt-Pd	66			6.8 / 10.15	3.04	
Pt-Cu	10	Subsequent – water-based	HNO_3, KOH	5.9 / 9.5	3.09	RT
Pt-Cu	30			6.0 / 9.7	2.98	
Pt-Cu	75			6.6 / 9.5	2.88	
Pt-Cu	90			6.6 / 9.5	3.1	
Pt-Rh	50	Subsequent – water-based	HNO_3, TEAOH	6.0 / 10.3	1.07	RT
Pt-Rh	90			6.3 / 9.8	1.05	
Pt-Rh	95			6.7 / 9.7	1.04	
Pt-Rh	99			6.7 / 9.7	1.07	
Pt-Au	10	Downstream	HNO_3, TEAOH	6.8 / 9.6	1.02	RT
Pt-Au	50			6.8 / 9.6	0.97	
Pt-Au	90			6.8 / 9.5	1.02	
Pt-Au	95			6.8 / 9.5	0.97	
Pt-Ag	22	Downstream	HNO_3, TEAOH	6.8 / 9.5	0.94	RT
Pt-Ag	53			6.8 / 9.5	0.97	
Pt-Ag	90			6.8 / 9.5	1.03	
Pt-Ag	95			6.8 / 9.5	1.03	
Au-Rh	90	Downstream	HNO_3, TEAOH	6.1 / 9.6	1.02	RT
Au-Ir	50			6.4 / 9.5	0.72	
Au-Ir	99			6.8 / 9.6	1.01	
Pd-Cu	15	Subsequent - Vacuum distillation	/	/	1.06	214
Pd-Cu	45				1.02	246
Pd-Cu	70				1.08	239
Pd-Cu	90				1.03	240
Pt-Fe	50	Subsequent - Vacuum distillation	/	/	1.07	249
Pt-Fe	66				1.14	235
Pt-Fe	95				1.06	227
Pt-Fe	99				1.09	133
Pt-Mo	50	Subsequent - Vacuum distillation	/	/	1.0	230
Pt-Mo	66				1.0	219
Pt-Mo	95				1.05	240
Pt-Mo	99				1.05	234

Sample system	Nominal content of first metal (Pt/Pd/Au) [at%]	Supporting route	Additives	Min / Max pH	Loading determined by ICP-OES [wt.%]	Maximum temperature [°C]
Pt-Mn	49	Subsequent - Vacuum distillation	/	/	0.9	215
Pt-Mn	75				0.99	215
Pt-Mn	95				1.03	228
Pt-Mn	99				1.04	204
Pt-Ru	05	Subsequent - Vacuum distillation	/	/	0.02	203
Pt-Ru	20				0.12	218
Pt-Ru	80				0.75	220
Pt-Ru	95				1.01	200
Pt-Nb	43	Subsequent - Vacuum distillation	/	/	0.89	229
Pt-Nb	75				0.95	205
Pt-Nb	95				1.06	225
Pt-Nb	99				1.04	199

In the case of the synthesis in propylene carbonate, an electrostatically driven adsorption cannot be used. Alteration of the surface charge as is possible in water fails in propylene carbonate. Therefore, diffusion-driven adsorption is chosen. For diffusion to drive the adsorption the concentration of the colloid must be steadily increased with the support present. This can be done by evaporating the solvent. It is important to prevent particle growth in this process as this can negatively impact the catalyst performance. This means that high temperatures of the colloid need to be prevented. To estimate which temperature is too high, gold colloids were synthesized in propylene carbonate. The zeta-potential of these colloids was measured using a solvent cell on a Malvern Zetasizer nano device. It was found to be around -45 meV. Translating this into thermal energy leads to 250°C. Thermodynamically the colloid would thus become unstable at and above 250°C. With propylene carbonate's boiling point at 242°C and very low vapour pressure [69], it may be reasonable to take extra precautions. Therefore, a vacuum distillation was built, that allowed the distillation of the mixture at 70°C head temperature. To fully dry the mixture for bottling, the powder was subsequently heated to <250°C. The maximum powder temperature is shown in Table 5. As the temperature was kept well below 250°C for most of the time, particle growth could be kept to a minimum.

S1.4. Catalytic testing procedures

For selected samples, a third stronger ageing procedure was additionally employed, where the samples were exposed to the water atmosphere at 800°C, for also 16 hours (16/800).

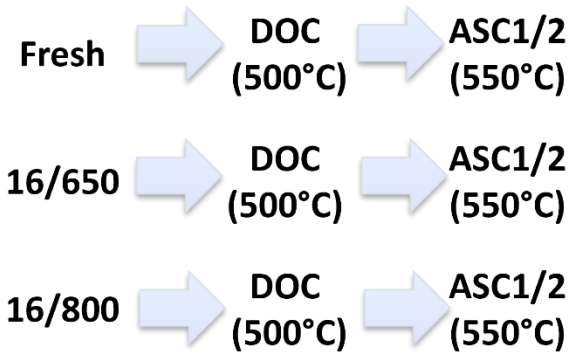

Figure 3 Catalyst testing procedure.

Due to a difference in mass loading for the Pt-Pd- and Pt-Cu-Systems (3 wt.% instead of 1 wt.% for the rest of the sample matrix), the catalytic testing procedure had to be adjusted.

Instead of having a cordierite core for every age state, the fresh core was reused after catalytic testing. This was subsequently aged to 16H650 and tested again (cf. Figure 4).

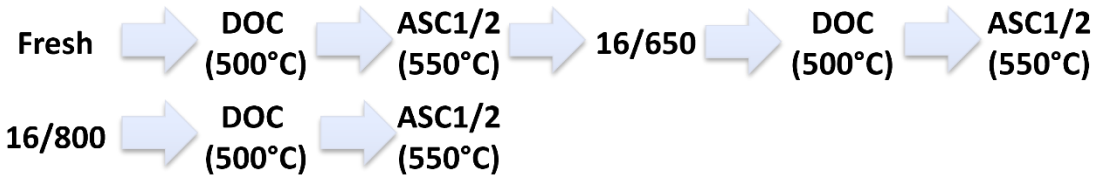

Figure 4 Catalyst testing procedure for Pt-Pd- and Pt-Cu-systems.

S2. Sample Details

S2.1. Exemplary TEM Images

S2.1.1. Pt-Pd, Au-Ir, Pt-Cu, Au-Rh

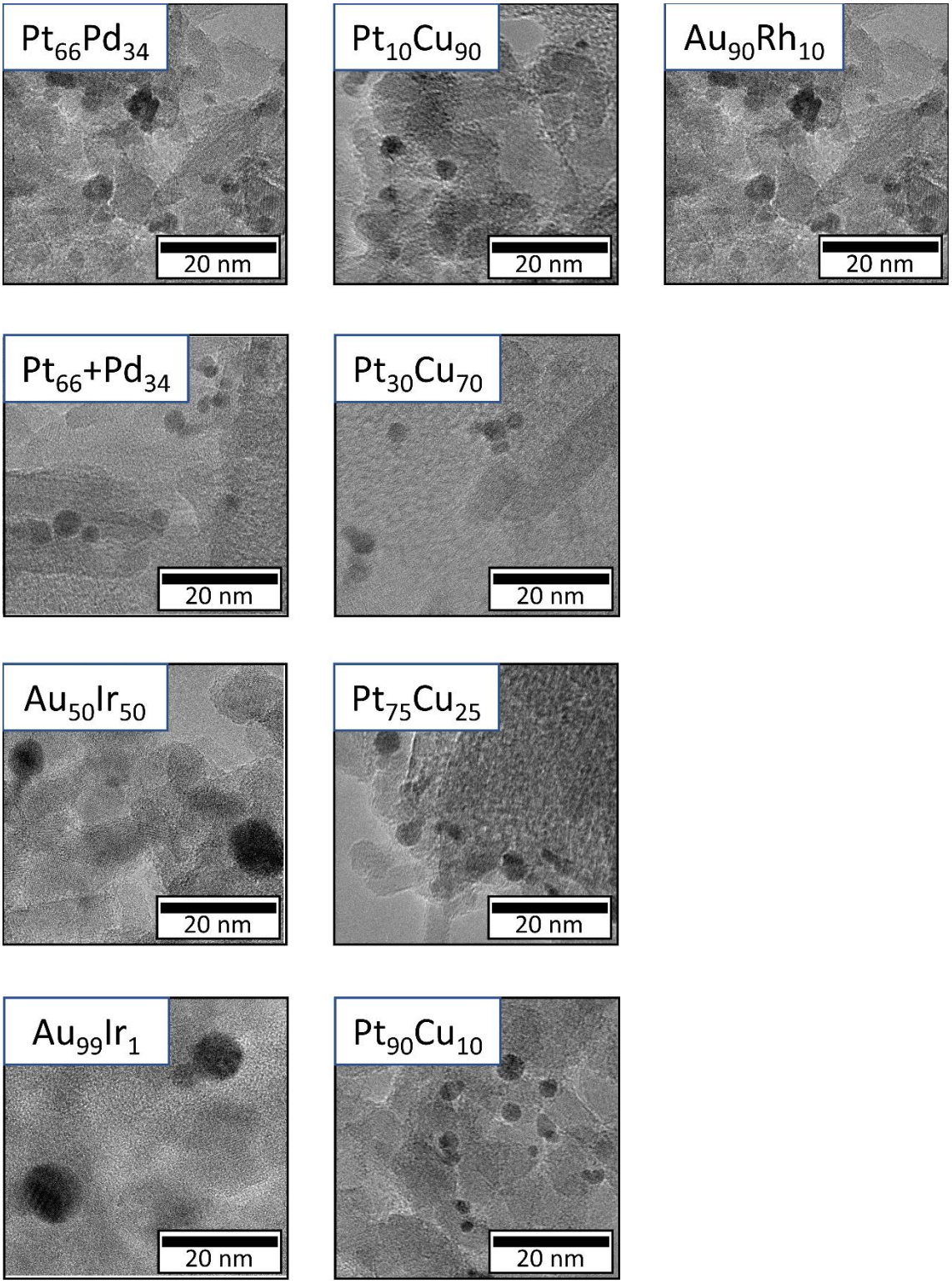

Figure 5 Exemplary STEM-Images of Pt-Pd, Au-Ir, Pt-Cu and Au-Rh. Mixture ratios are given as nominal values.

S2.1.2. Pt-Rh, Pt-Au, Pt-Ag

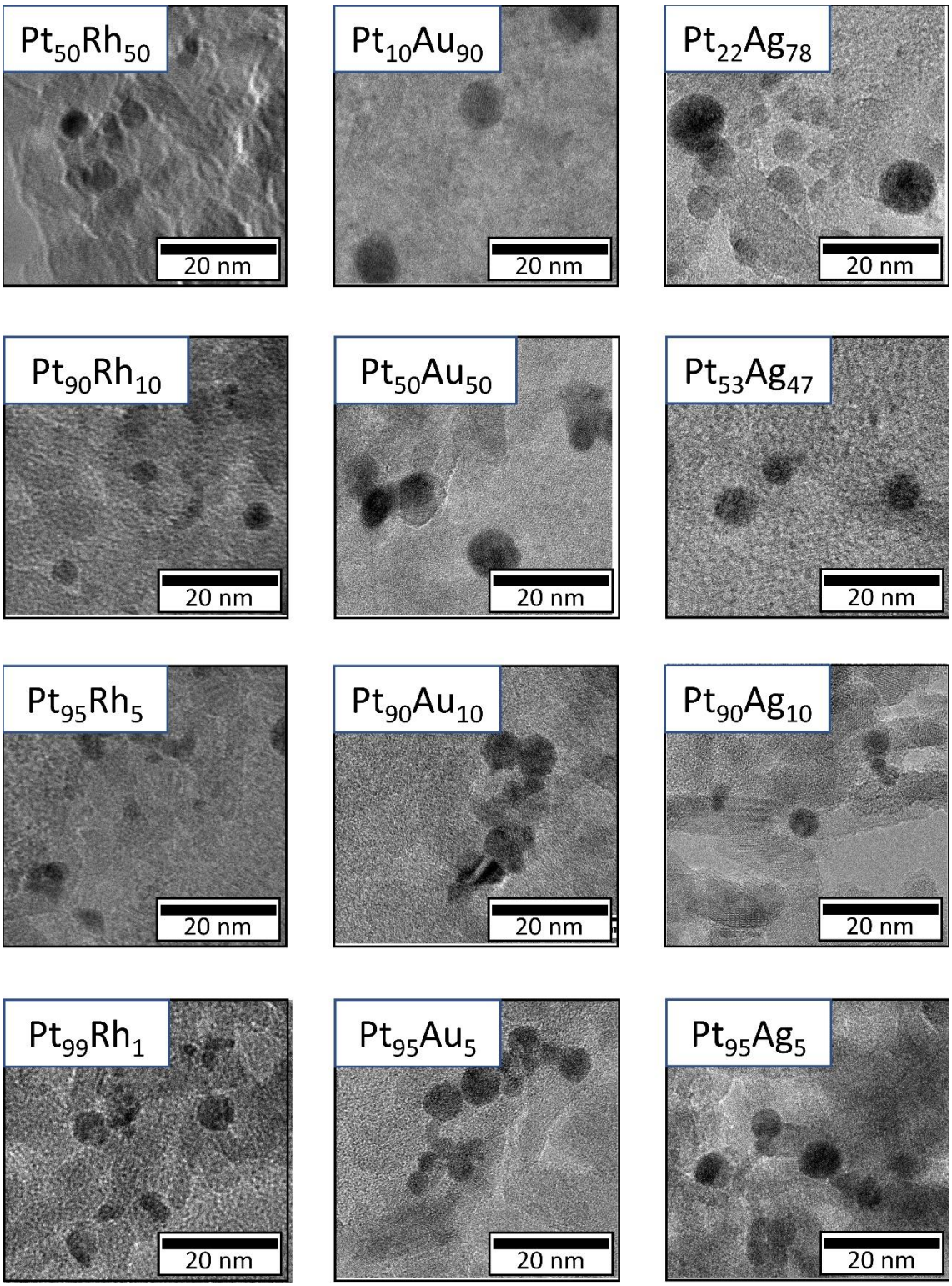

Figure 6 Exemplary STEM-Images of Pt-Rh, Pt-Au and Pt-Ag. Mixture ratios are given as nominal values.

S2.1.3. Pd-Cu, Pt-Fe, Pt-Mo

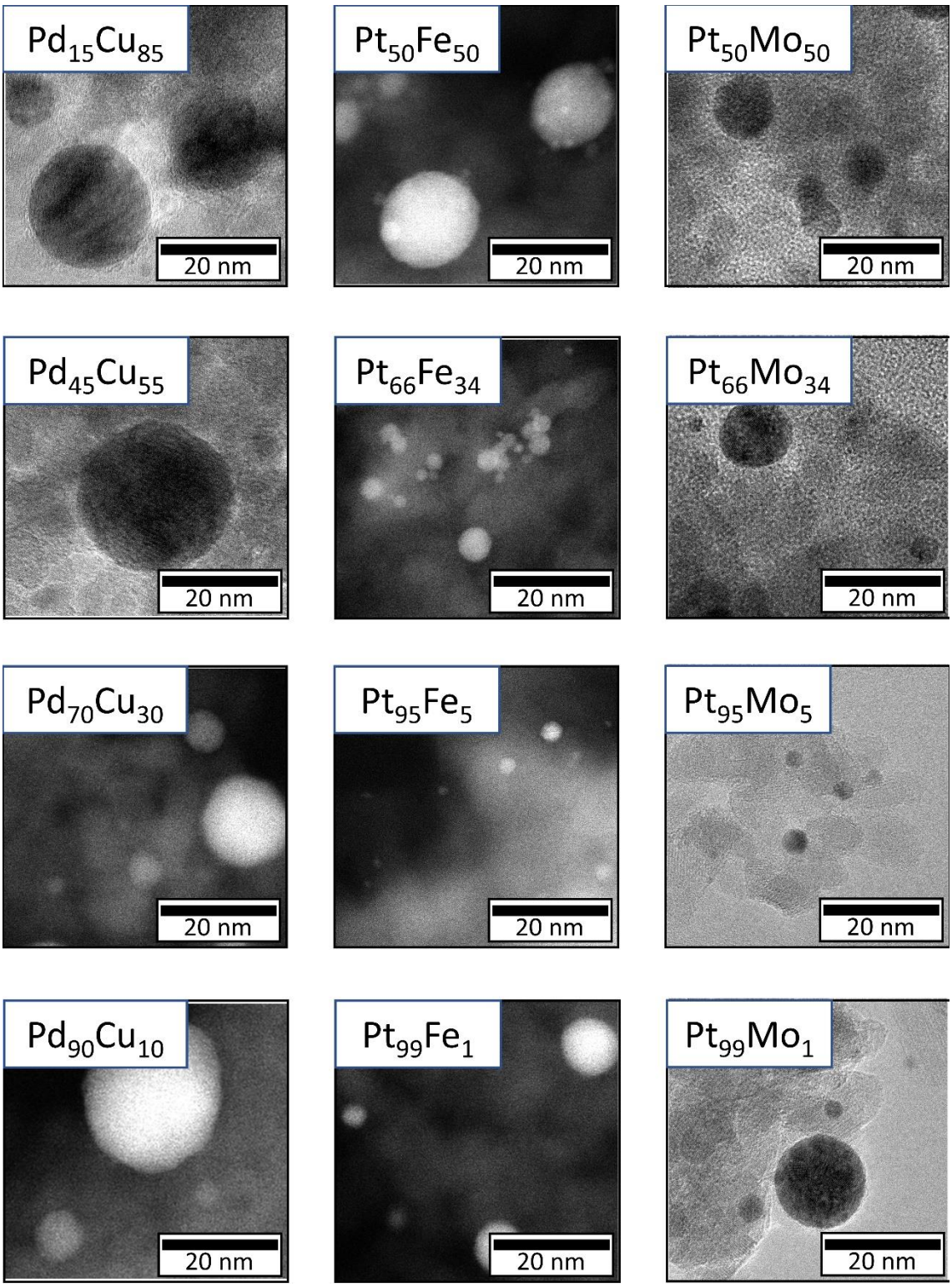

Figure 7 Exemplary STEM-Images of Pd-Cu, Pt-Fe and Pt-Mo. Mixture ratios are given as nominal values.

S2.1.4. Pt-Mn, Pt-Ru, Pt-Nb

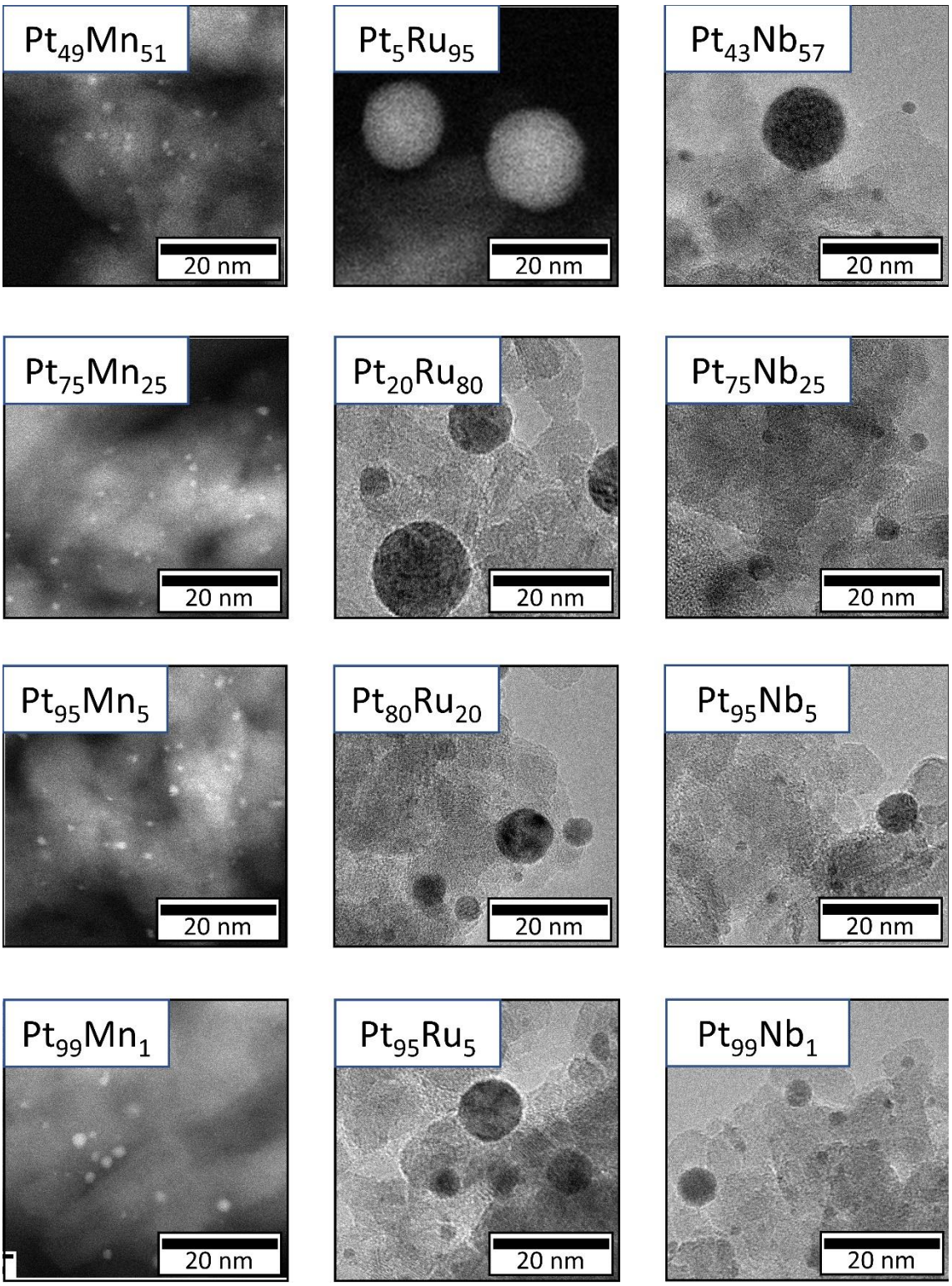

Figure 8 Exemplary STEM-Images of Pt-Mn, Pt-Ru and Pt-Nb. Mixture ratios are given as nominal values.

S2.2. Size Distribution

For measurement of particle size distribution, the slurry was diluted (in water for water-based samples, in acetone for solvent-based samples) and drop-casted onto lacey-carbon TEM grids. The substrate was chosen to not interfere with the sample (e.g., nickel grids for copper-containing samples, otherwise copper-grids). These grids were dried at room temperature and loaded into the TEM. Of the samples, 10 overview images (4 at 10000x, 6 at 30000) and 40 detailed images were taken (15 at 80000x, 25 at 200000x). The detailed images were chosen to measure the particle size by laying a circular shape upon them in FIJI. The particles were mainly identified by contrast and shape. This is possible because the alumina support particles comprise mainly rectangular particles of low density and the nanoparticles of mainly round particles with high density. The nanoparticles were overlayed with an elliptical shape best fitting the shape of the nanoparticle. Of this, the area was recorded and this was translated into the equivalent circle diameter. This data was then turned into a histogram and fitted with a lognormal distribution.

S2.2.1. Pt-Pd and Pt-Cu

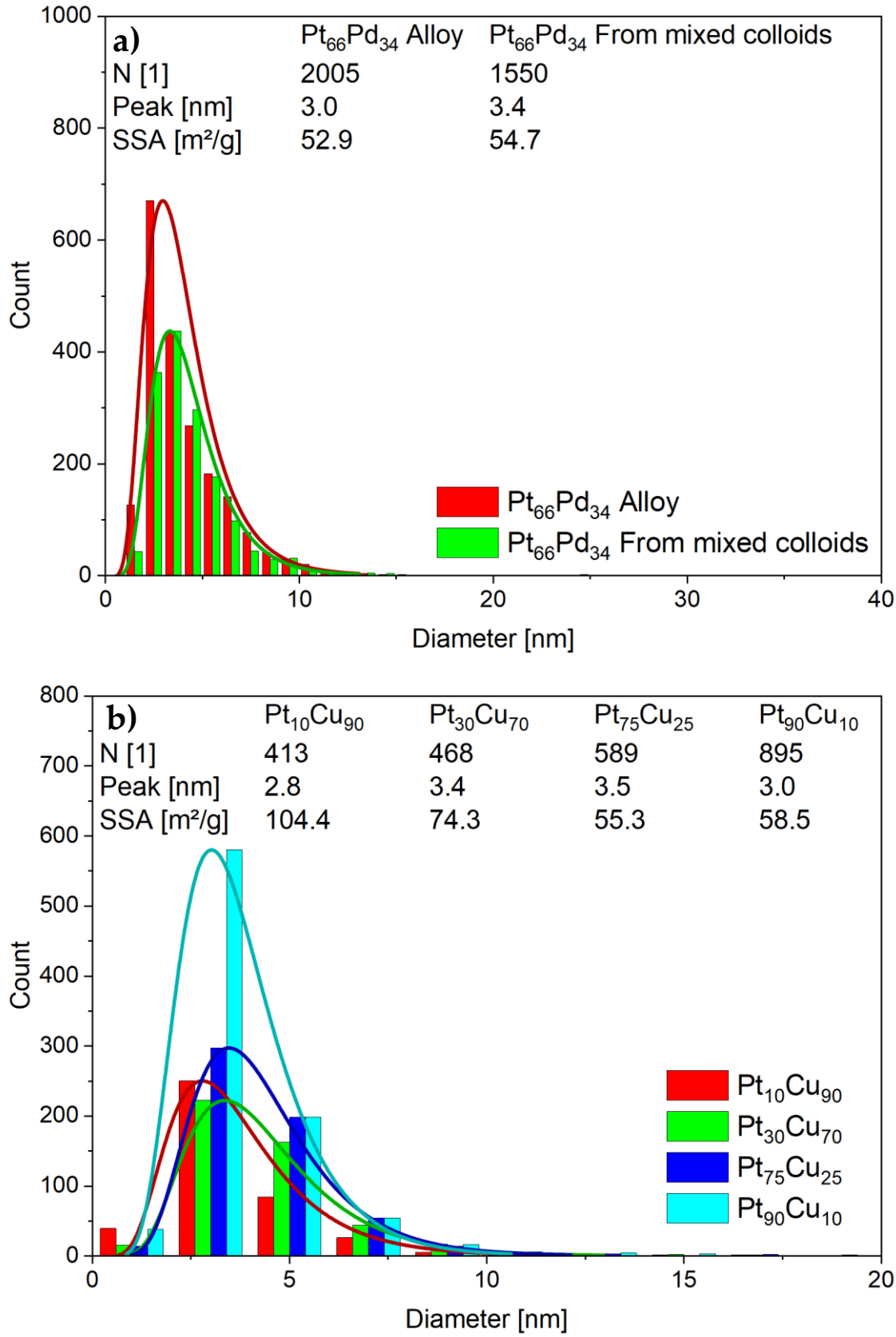

Figure 9 Particle size distributions from STEM of Pt-Pd (a) and Pt-Cu (b). Notice the differing x- and y-Axis scale for better visibility.

S2.2.2. Pt-Rh and Pt-Au

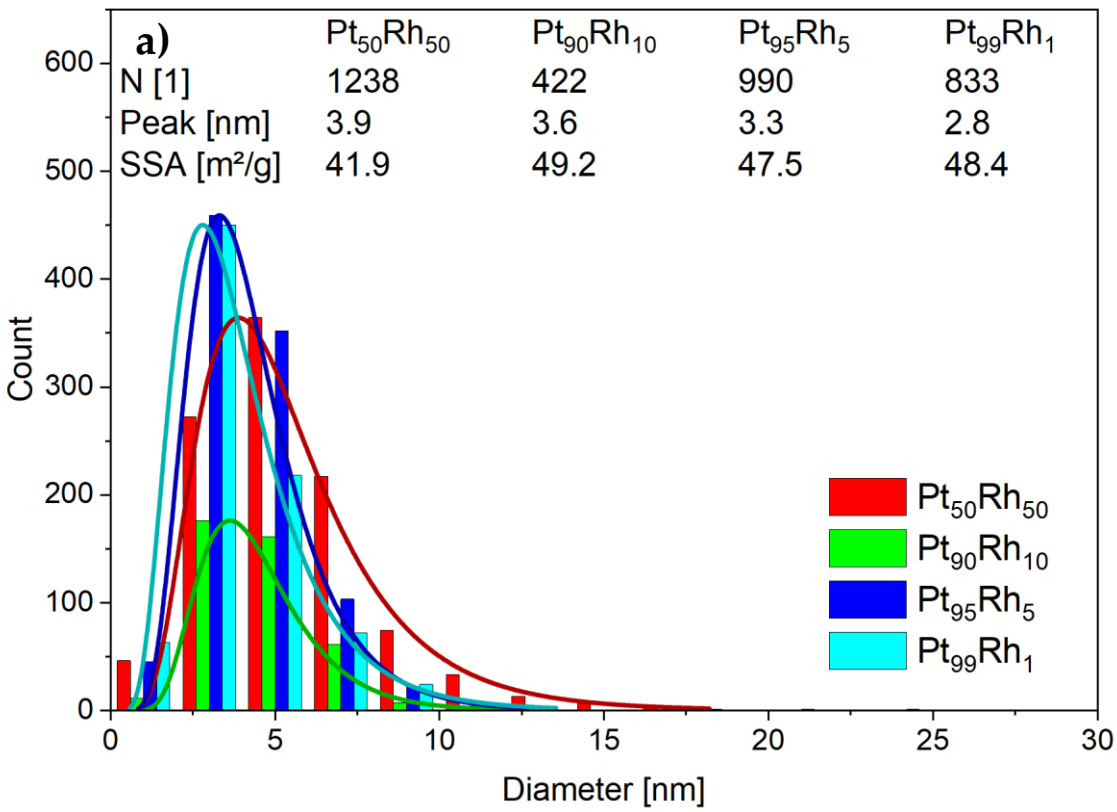

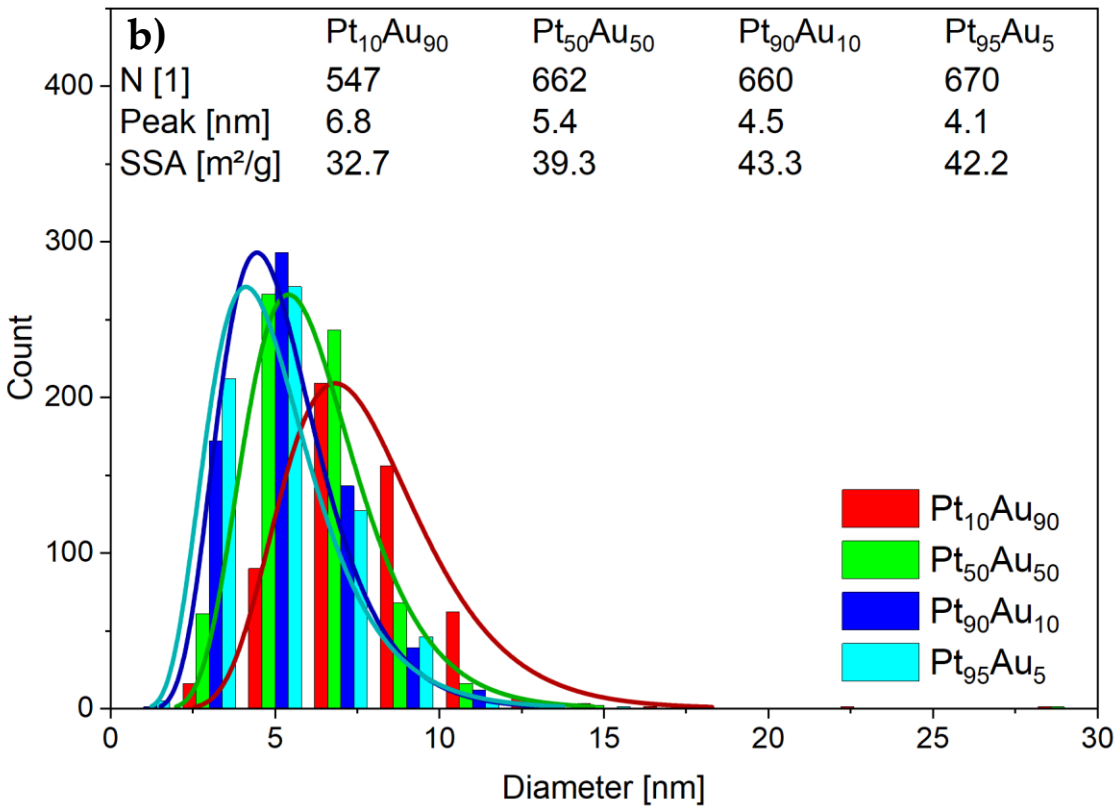

Figure 10 Particle size distributions from STEM of Pt-Rh (a) and Pt-Au (b). Notice the differing x- and y-Axis scale for better visibility.

S2.2.3. Pt-Ag, Au-Rh and Au-Ir

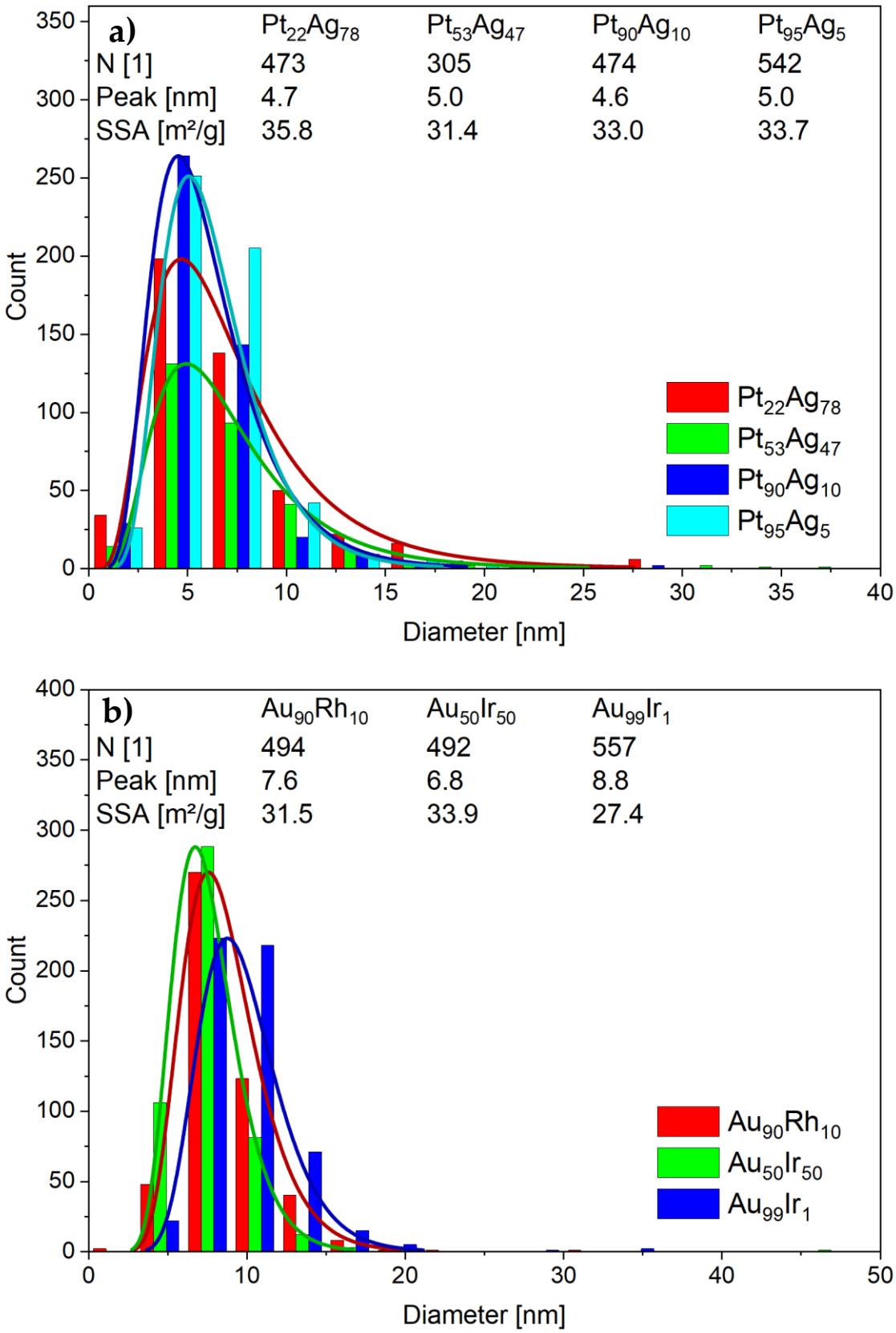

Figure 11 Particle size distributions from STEM of Pt-Ag (a) and Au-Rh and Au-Ir (b). Notice the differing x- and y-Axis scale for better visibility.

S2.2.4. Pd-Cu and Pt-Fe

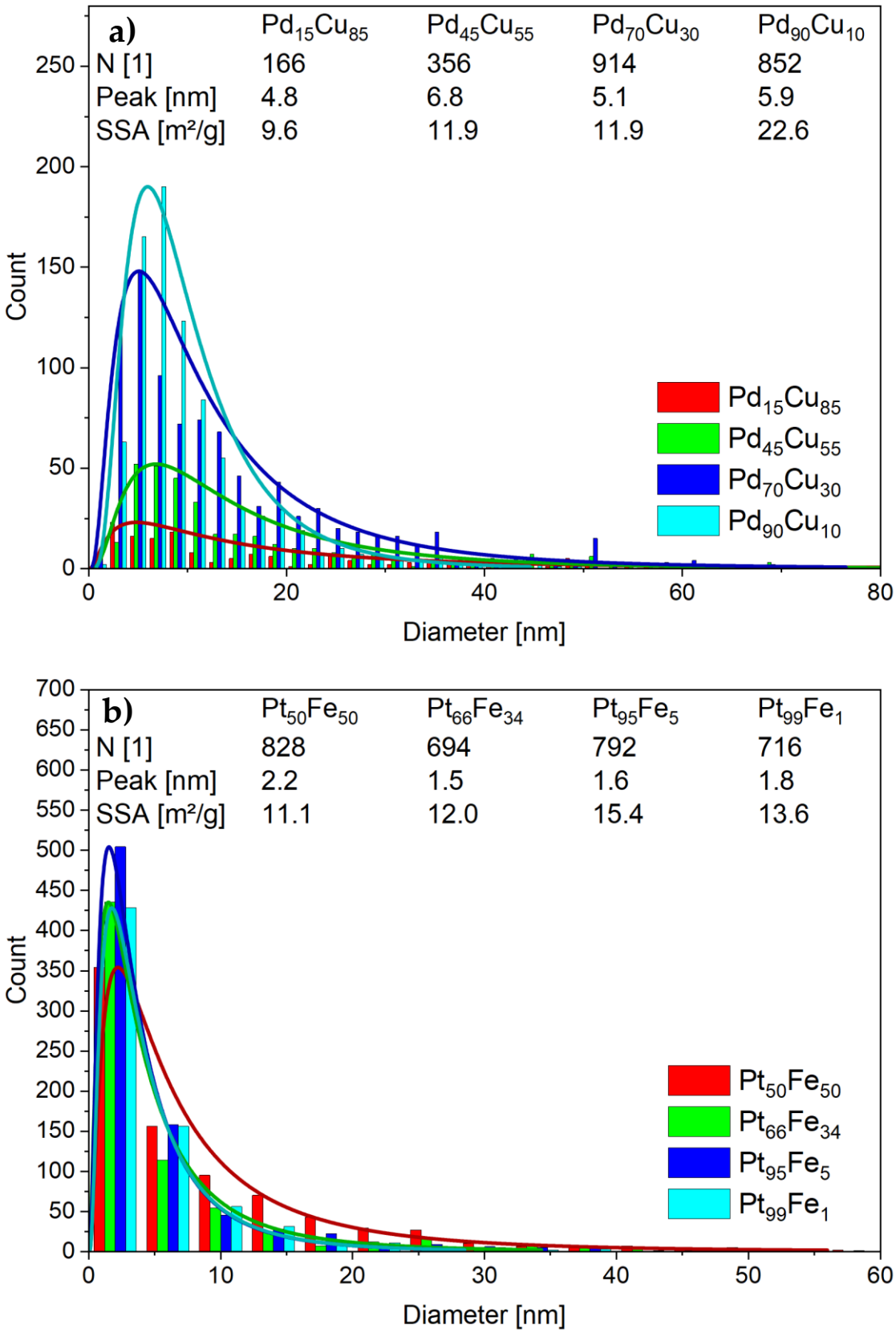

Figure 12 Particle size distributions from STEM of Pd-Cu (a) and Pt-Fe (b). Notice the differing x- and y-Axis scale for better visibility.

S2.2.5. Pt-Mo and Pt-Mn

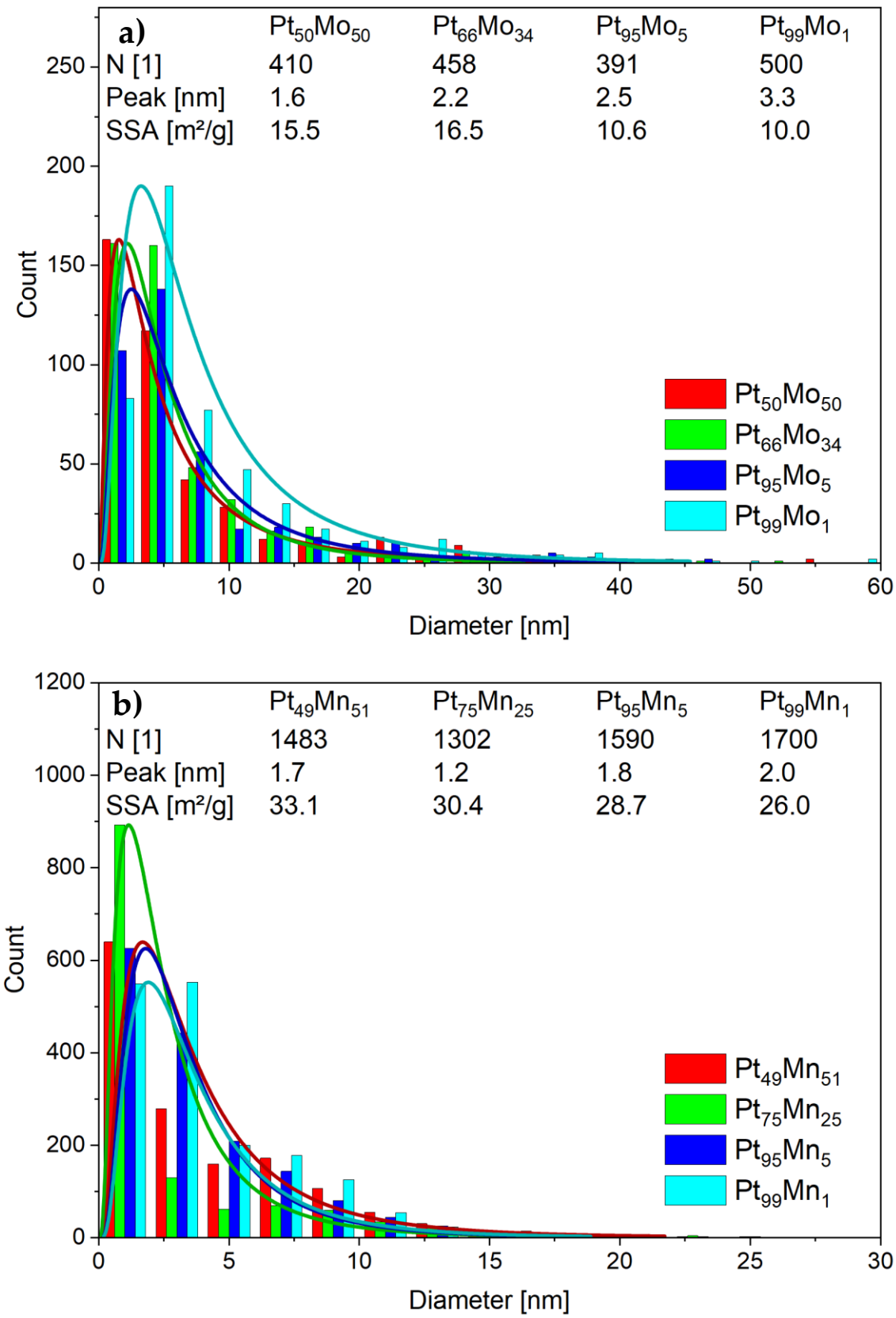

Figure 13 Particle size distributions from STEM of Pt-Mo (a) and Pt-Mn (b). Notice the differing x- and y-Axis scale for better visibility.

S2.2.6. Pt-Ru and Pt-Nb

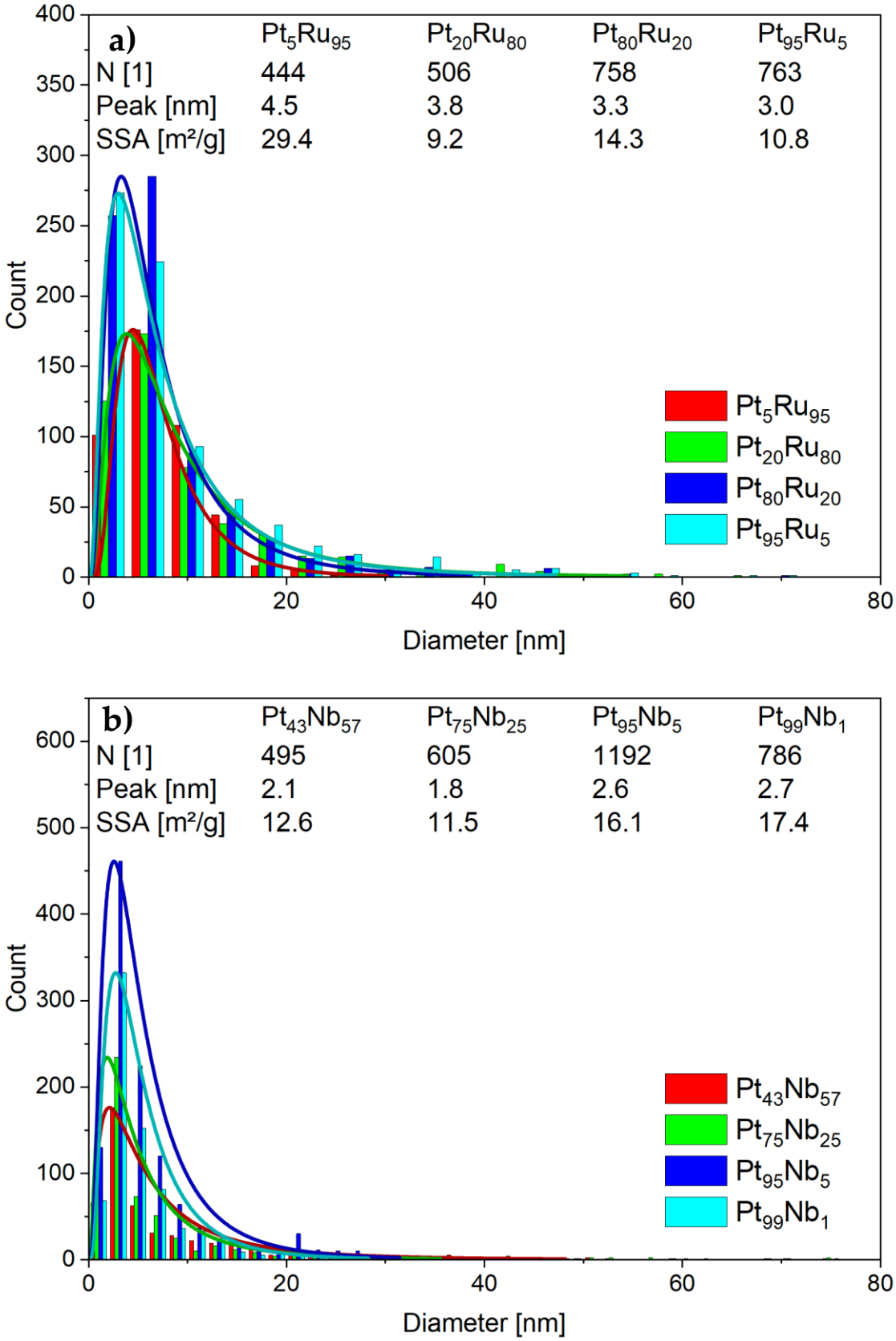

Figure 14 Particle size distributions from STEM of Pt-Ru (a) and Pt-Nb (b). Notice the differing x- and y-Axis scale for better visibility.

S2.3. Particle composition and support loading

Particle composition was verified using TEM-EDX and ICP-OES. EDX measurements comprised 10 line scans and 3 mappings. The obtained data was screened for significance by evaluating the signal-to-noise ratio. Only significant data was used for calculating the mean value and standard deviation of the measured composition. It was also evaluated whether an alloy formed. All particles containing a mixture of metals also showed homogeneous alloying throughout the particle. Nevertheless, also monometallic particles could be found, in particular for samples with a very high Pt (or Au/Pd) content (e.g., 95 at% and 99 at%). The obtained data was used to calculate a statistical error based on student distribution.

The ICP-OES data was also used to determine the factual support loading by also evaluating the support content.

S2.3.1. Pt-Pd and Pt-Cu

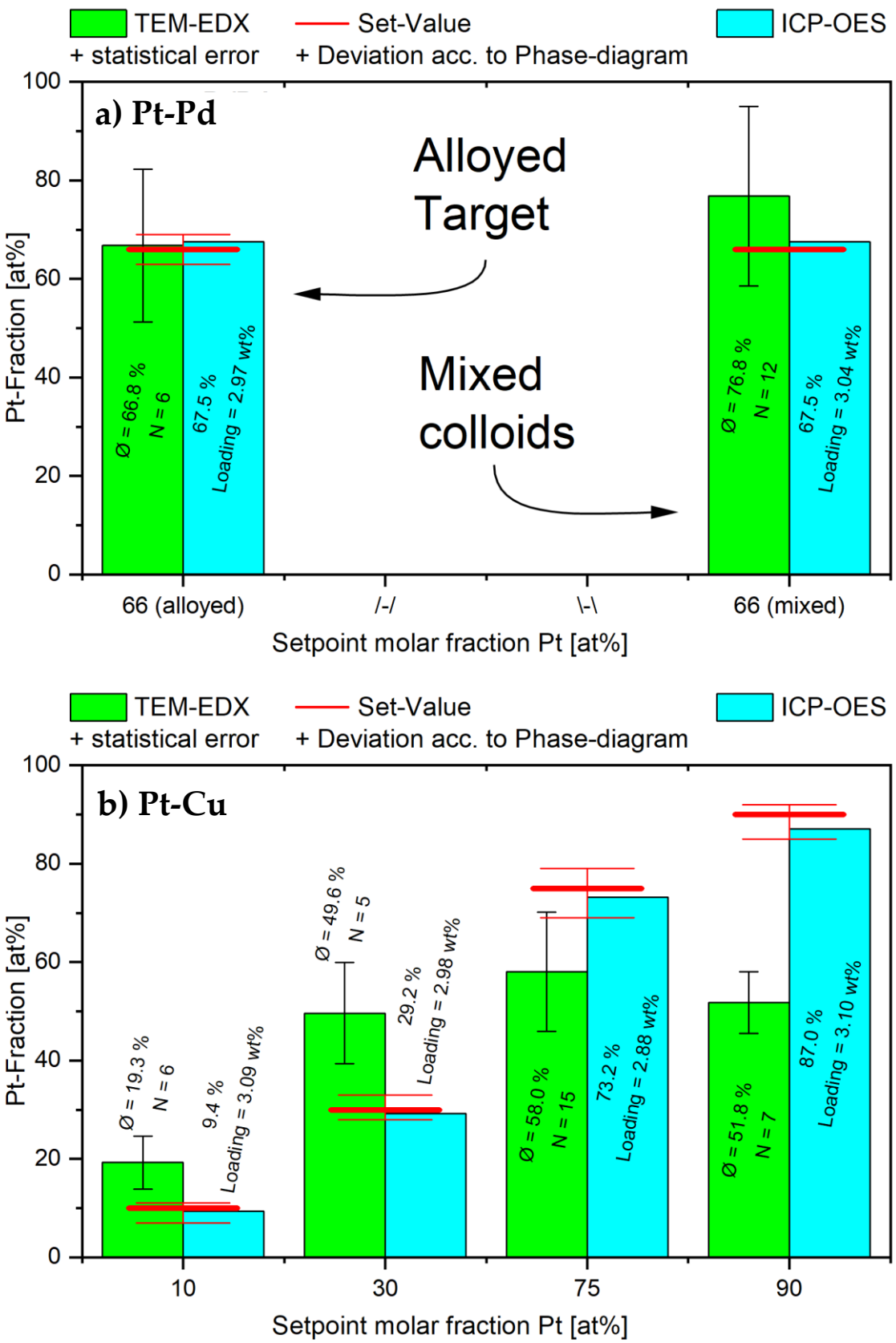

Figure 15 Sample composition from TEM-EDX and ICP-OES for Pt-Pd (a) and Pt-Cu (b).

S2.3.2. Pt-Rh and Pt-Au

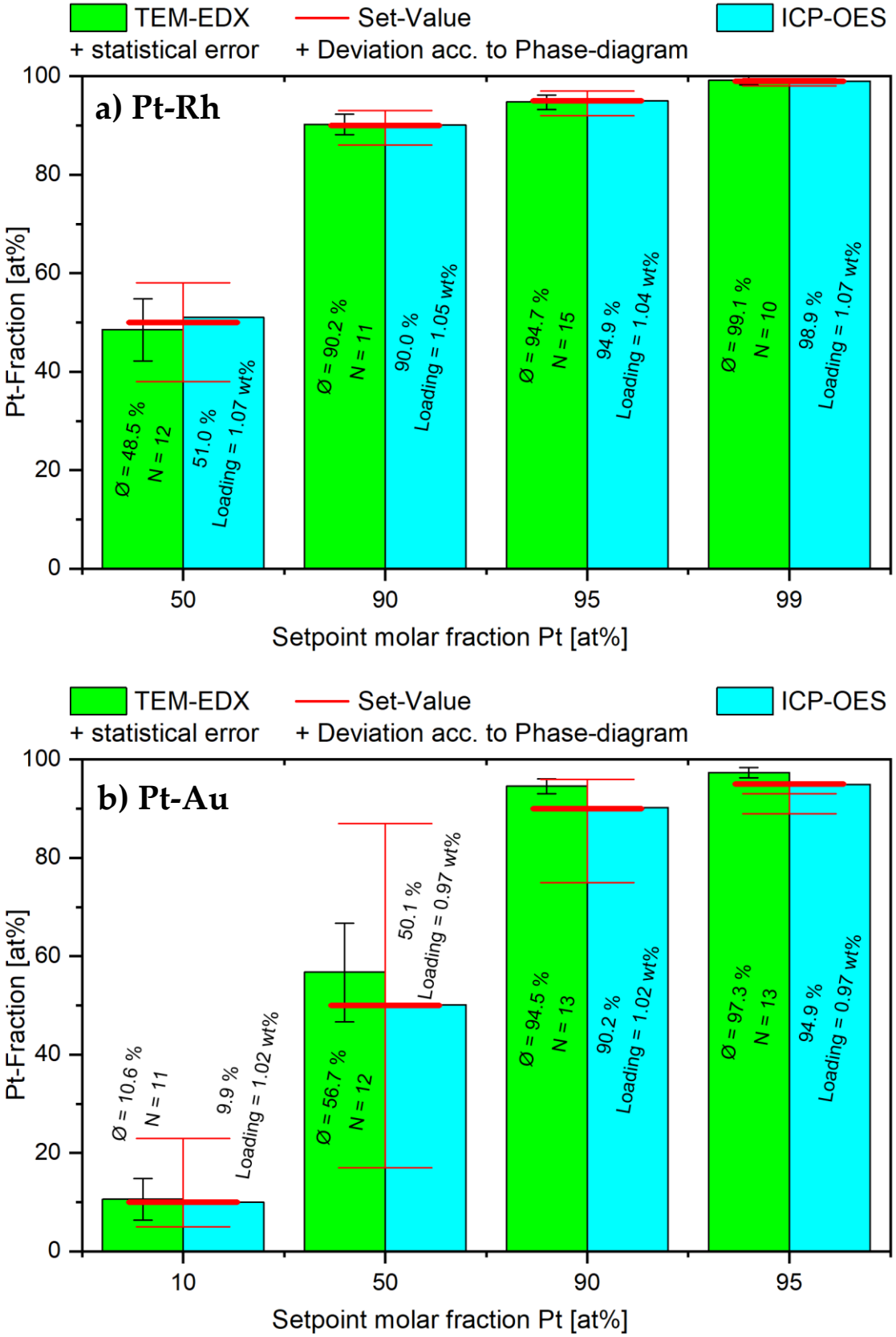

Figure 16 Sample composition from TEM-EDX and ICP-OES for Pt-Rh (a) and Pt-Au (b). Gold is very difficult do distinguish from platinum using EDX, due to the very similar characteristic X-Rays. Therefore EDX-Data is not very reliable for a mixture of Pt and Au.

S2.3.3. Pt-Ag, Au-Rh and Au-Ir

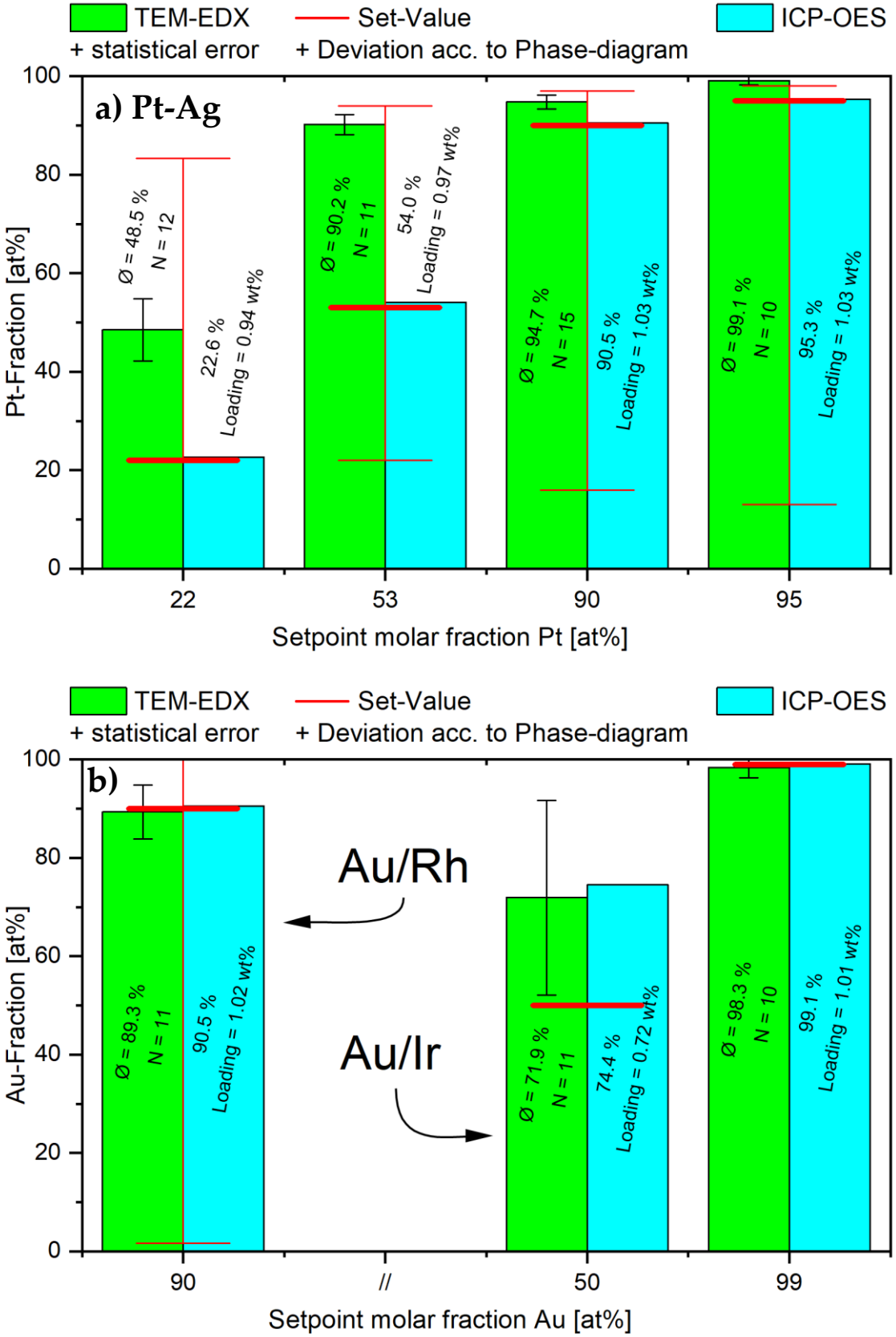

Figure 17 Sample composition from TEM-EDX and ICP-OES for Pt-Ag (a) and Au-Rh and Au-Ir (b).

S2.3.4. Pd-Cu and Pt-Fe

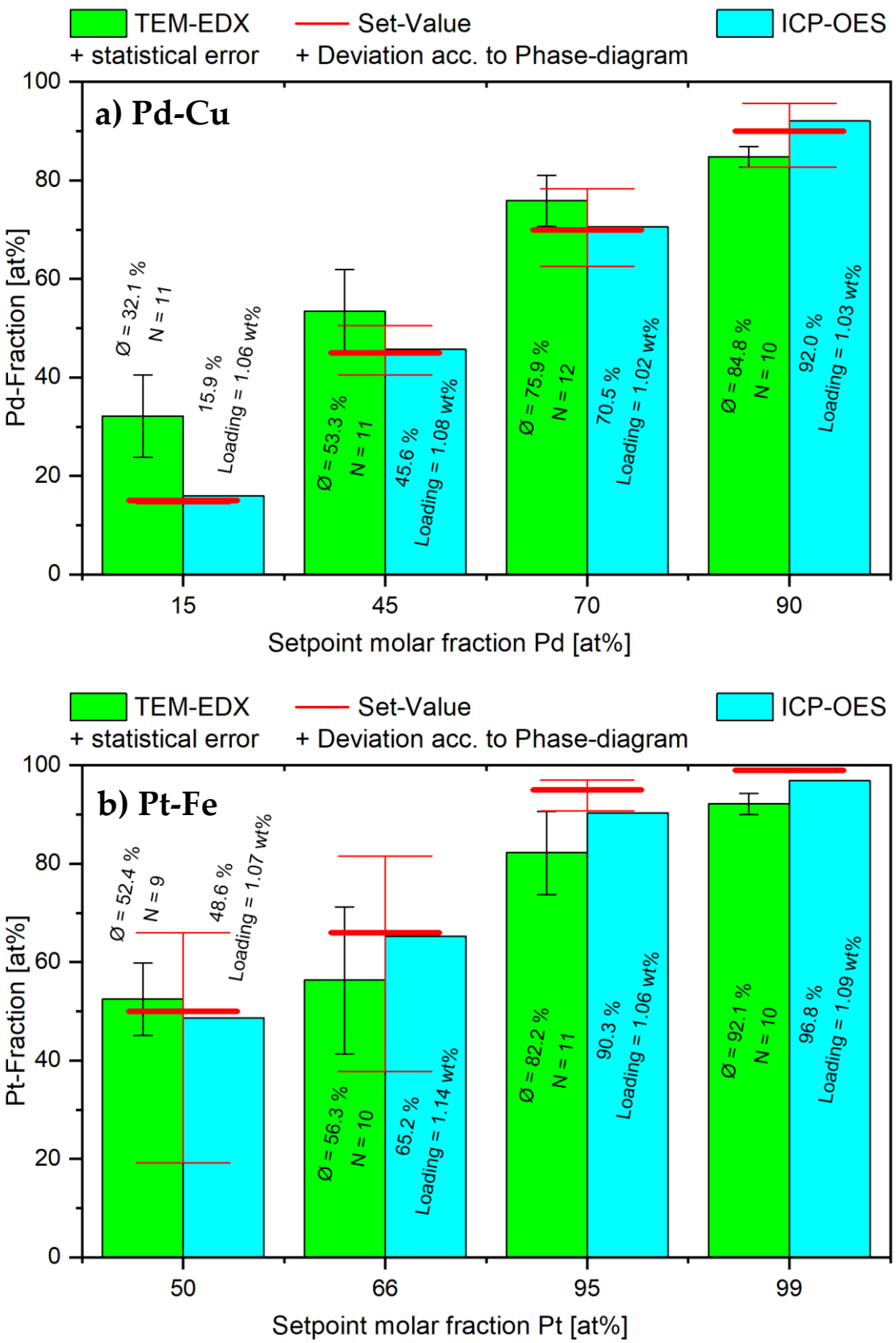

Figure 18 Sample composition from TEM-EDX and ICP-OES for Pd-Cu (a) and Pt-Fe (b).

S2.3.5. Pt-Mo and Pt-Mn

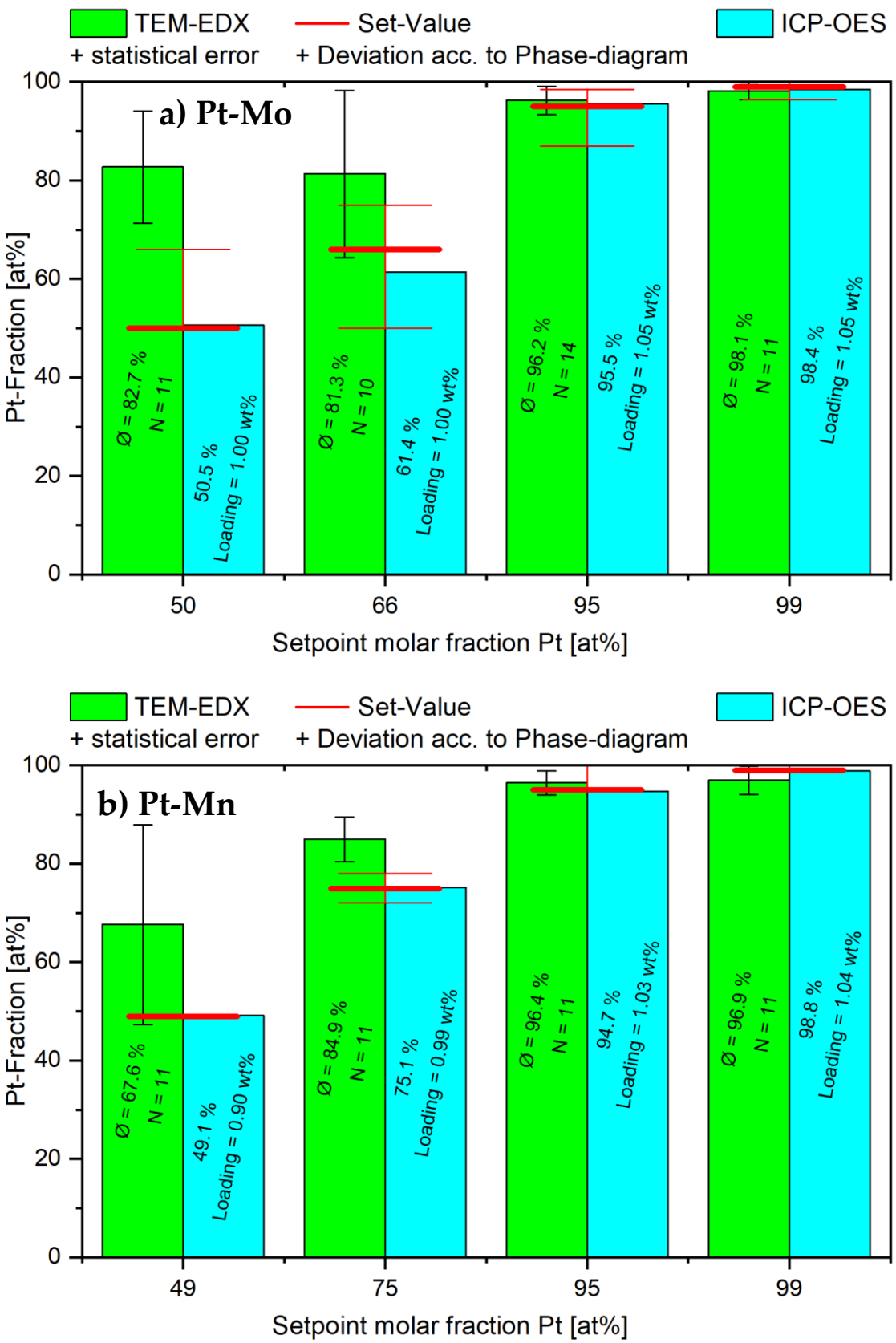

Figure 19 Sample composition from TEM-EDX and ICP-OES for Pt-Mo (a) and Pt-Mn (b).

S2.3.6. Pt-Ru and Pt-Nb

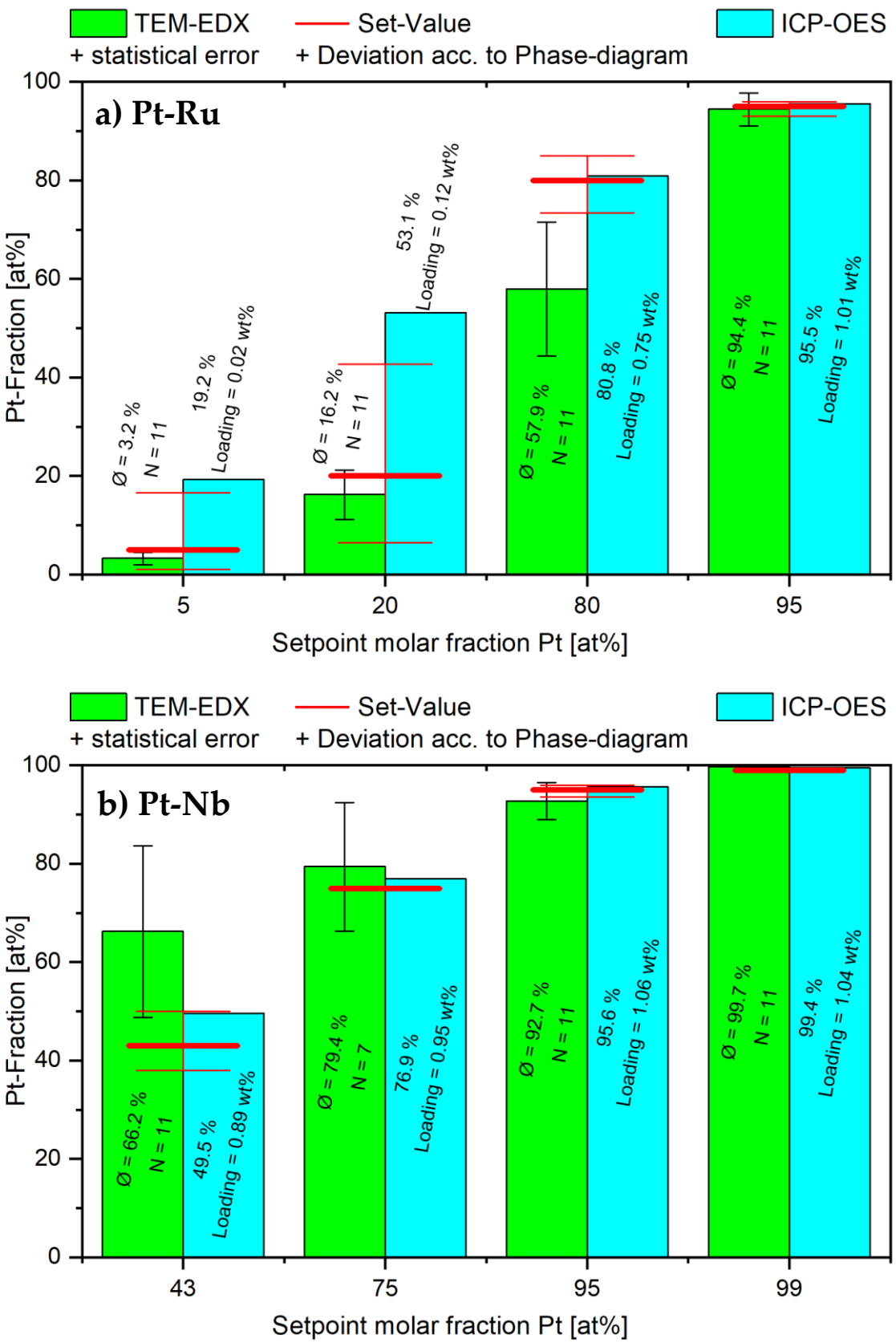

Figure 20 Sample composition from TEM-EDX and ICP-OES for Pt-Ru (a) and Pt-Nb (b).

S2.4. Selected EDX line scans of Pt-Pd, Pt-Cu and Pt-Mo

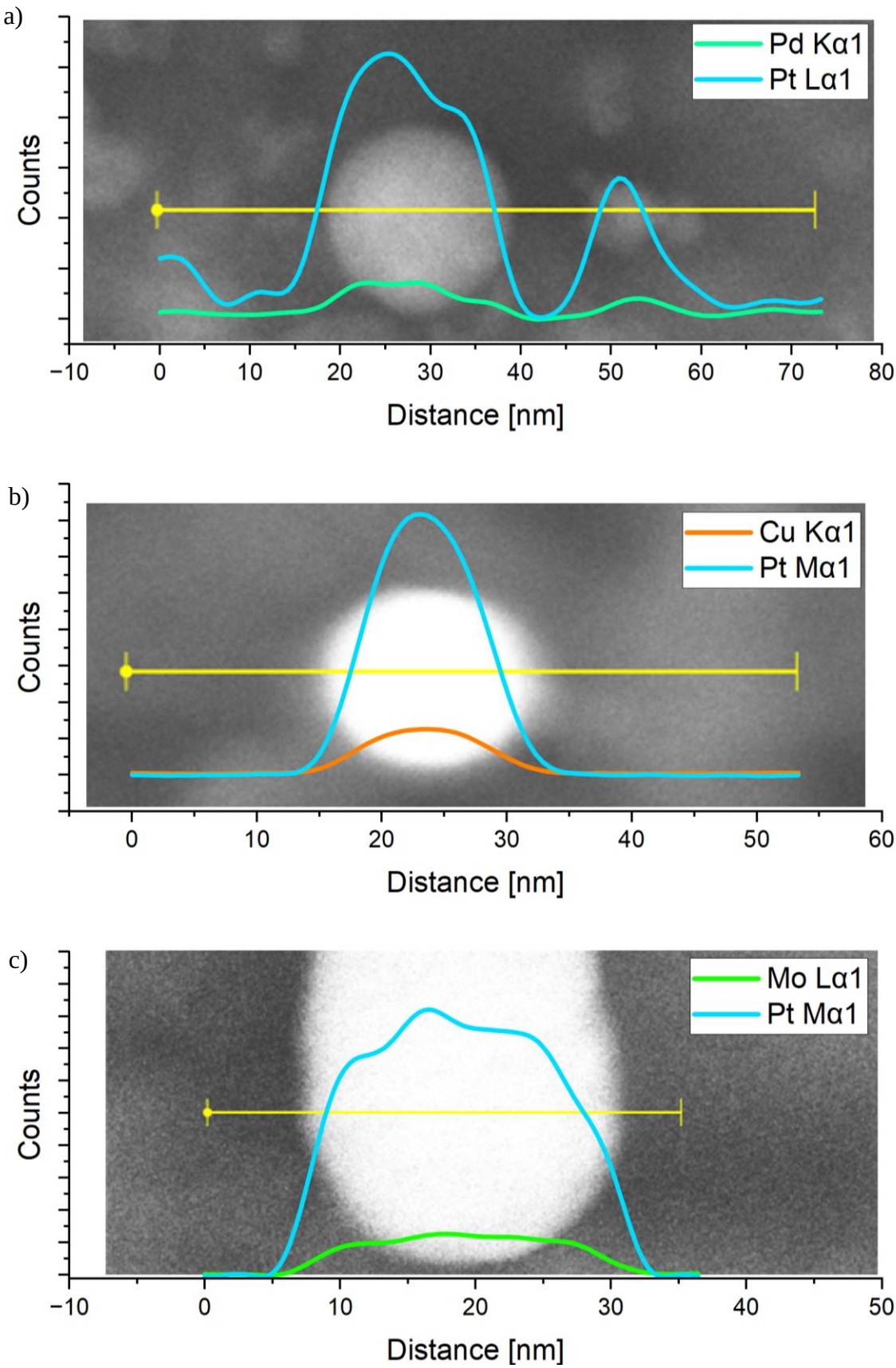

Figure 21 Example EDX line scans of Pt-Pd (a), Pt-Cu (b) and Pt-Mo (c). All line scans have been smoothed using the FFT filter in Origin-Pro with 5 points within the smoothing window to provide a better overview by reducing some noise.

S3. Crossover measurements

To ensure comparability between the measurements of the coated cordierite reactor and the powder reactor, crossover measurements were performed. For this measurement, the water-based slurry was prepared in a manner comparable to the preparation of the powder samples (dried, pressed, broken up etc.). Subsequently, the samples were then tested in the same environment as the solvent-based samples. For the comparison, only the mildly aged samples (16H650) were chosen. The DOC results are shown in Figure 22 and the ASC results in Figure 23. While the reactors do not produce identical values, the results are still very comparable. Especially the ranking of the samples stays the same, which is of the highest importance in this study. The only outlier is Pt-Pd when testing for the temperature where 20 ppm N_2O are generated in the ASC measurement with NO present (cf. Figure 23 b)). With every other measurement, the ranking is kept between reactors. If considering, that the most inactive samples (e.g. Au-Ir) show the largest deviation, even the values for the most active catalysts become partly comparable. Thus, the comparison of samples between the reactors should be possible.

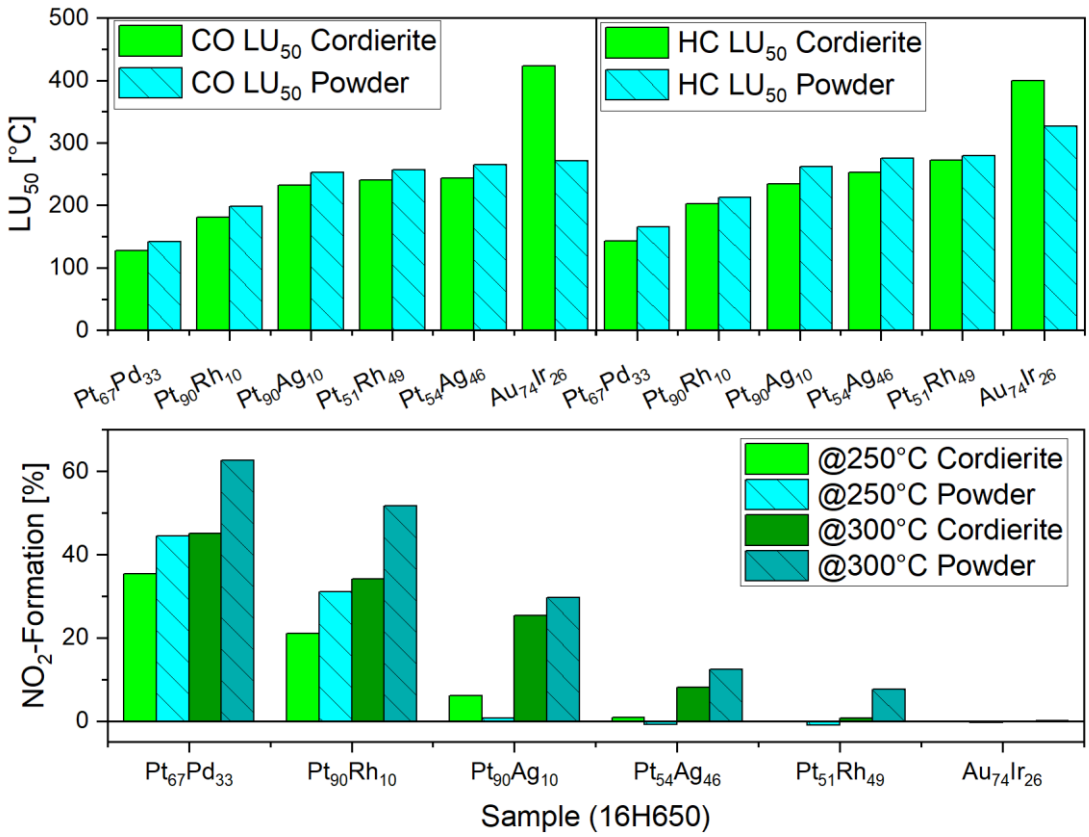

Figure 22 DOC Crossover measurements. Head-to-head comparison of Cordierite and Powder reactor for CO LU_{50}, HC LU_{50} and NO_2-Formation at 250°C and 300°C.

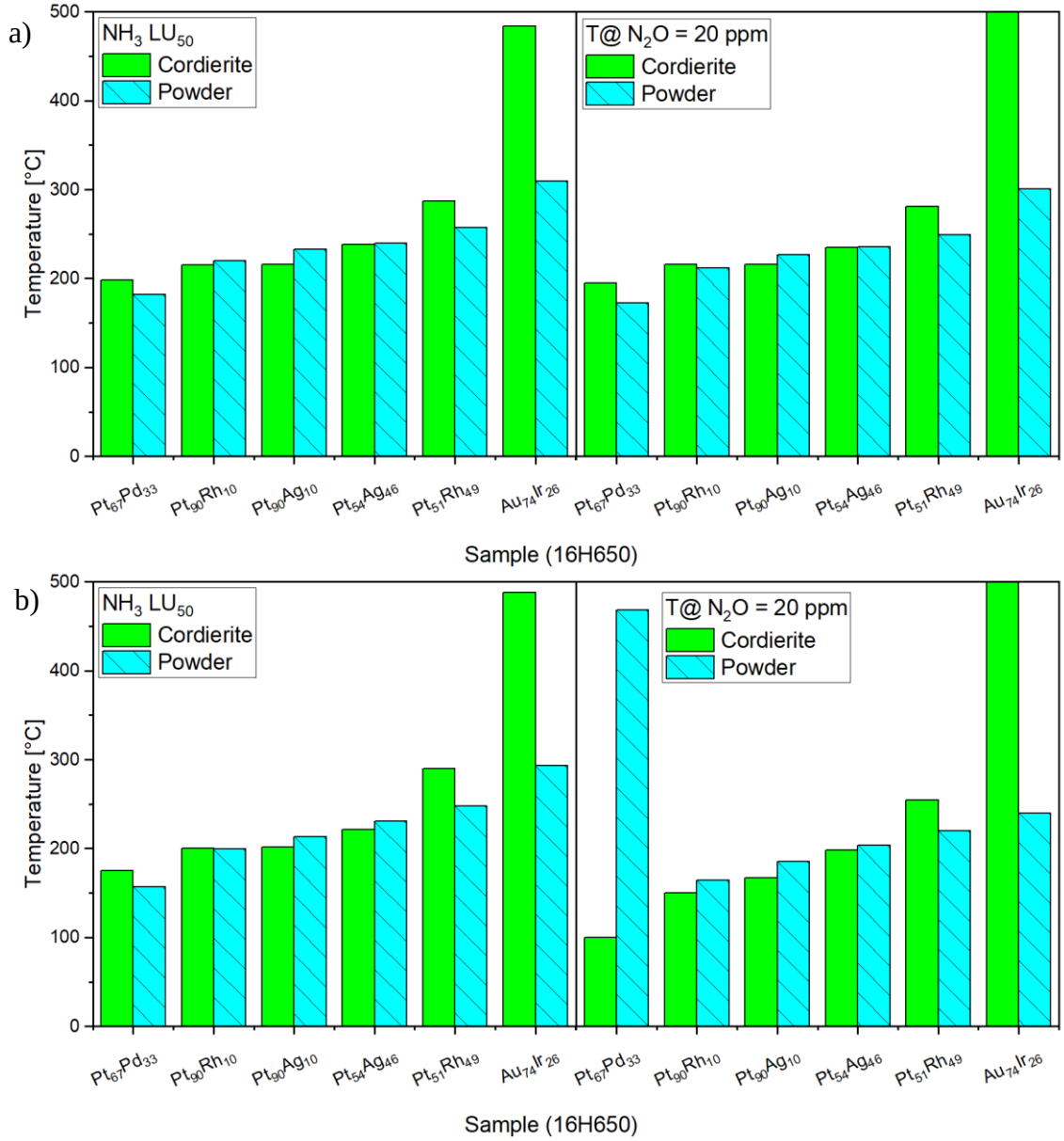

Figure 23 ASC crossover measurements. Head-to-head comparison of NH_3 LU_{50} and Temperature at which N_2O concentration was 20 ppm. Note that the Gold/Iridium-sample did not reach 20 ppm.

S4. Adsorption enthalpies

To evaluate the catalyst performance based on the heat of adsorption of the reactants, an extensive literature review was conducted. The results of this are shown in the following tables to provide a full list of references.

S4.1. Adsorption enthalpy CO

Metal	Mean Adsorption Enthalpy [eV]	Lowest Enthalpy [eV]	Highest Enthalpy [eV]	Source	Notes
Pt	-2.10	-1.87	-2.33	[70]	Initial Mean value between hex and unreconstructed (1x1)
Pd	-1.24	-0.95	-1.52	[71]	Mean between large particles and nanoparticle-clusters
Cu	-0.88			[72]	Copper sheet, 0°C, low coverage
Rh	-1.55			[73]	low coverage Rh (111)
Au	-0.56			[74]	Gold-Nanoparticles on TiO_2, low coverage
Ag	-0.69	-0.60	-0.79	[75]	Mean value of two configurations on Ag^0-site of Ag/Al_2O_3 catalyst at low coverage
Fe	-2.07			[76]	Initial heat of adsorption, 10nm sputtered iron film
Mo	-2.64			[77]	@25% coverage, calculated for Mo(100); Dissociative
Mn	//			None	
Ru	-1.59			[78]	Ru(0001), Low coverages, 300K
Nb	//			None	

S4.2. Adsorption Enthalpy NO

Metal	Mean Adsorption Enthalpy [eV]	Lowest Enthalpy [eV]	Highest Enthalpy [eV]	Source	Notes
Pt	-1.58	-1.20	-2.14	[79]	Mean value of all factettes, >= 300K
Pd	-1.76	-1.29	-2.17	[79]	Mean value of all factettes, >= 300K
Cu	-0.65	-0.57	-0.73	[80]	Estimation from desorption at 150K, NO adsorption is dissociative [81]
Rh	-2.85	-1.35	-4.35	[79]	Mean value of all factettes, >= 300K
Au	-0.55			[82]	On Au^4-clusters, very little literature as gold does not oxidise easily and no adsorption is detected above 95K [80, 83].
Ag	-0.68			[79]	
Fe	-0.62			[84]	Estimated from Data at 85K, for higher T, NO dissociates
Mo	-0.66	-0.47	-0.85	[79]	Mean value for two adsorption states
Mn	//			None	
Ru	-1.16	-1.07	-1.24	[79]	Mean value of all factettes, >= 300K
Nb	-2.49			[85]	Mean value of all geometrical possibilities on Nb(110)

S4.3. Adsorption Enthalpy O

Metal	Mean Adsorption Enthalpy [eV]	Source	Notes
Pt	-2.11	[34]	M12 Clusters
Pd	-1.51	[86]	experimental, polycrystalline
Cu	-2.04	[34]	M12 Clusters
Rh	-2.31	[86]	experimental, polycrystalline

Metal	Mean Adsorption Enthalpy [eV]	Source	Notes
Au	-0.60	[34]	M12 Clusters
Ag	-0.83	[86]	experimental
Fe	-3.18	[87]	Fe(100), experimental, 100% surface coverage
Mo	-4.02	[86]	experimental, polycrystalline
Mn	//	None	-
Ru	-2.91	[86]	experimental, polycrystalline
Nb	-4.51	[86]	

S5. DOC Details

S5.1. Gas Mixtures

	Coated Cordierite	Powder Reactor
CO	250 ppm	250 ppm
Propene (as C1)	180 ppm	180 ppm
NO	750 ppm	750 ppm
O_2	10%	10%
H_2O	7,5%	7,5%
CO_2	7%	7%
N_2	Rest	Rest
Space Velocity	50,000 1/h	similar conditions as cordierite samples, but due to fluctuations in packing density, no meaningful space velocity can be defined.

S5.2. Result Overview DOC

S5.2.1. CO LU_{50}

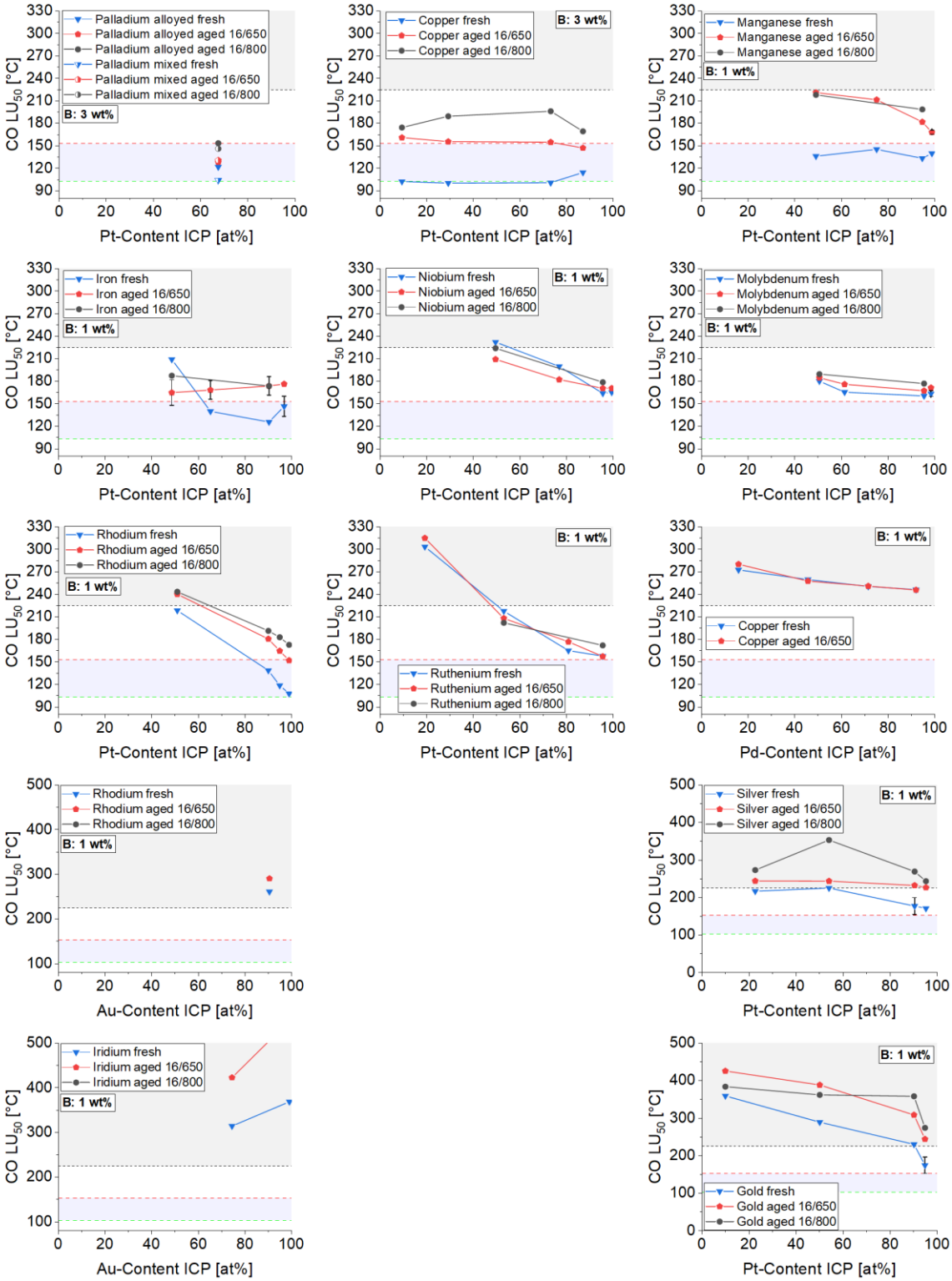

Figure 24 CO LU_{50} evaluated based on the Pt, Pd or Au content of the catalyst. Blue and red areas are a guide to the eye, to ease comparison.

S5.2.2. HC LU_{50}

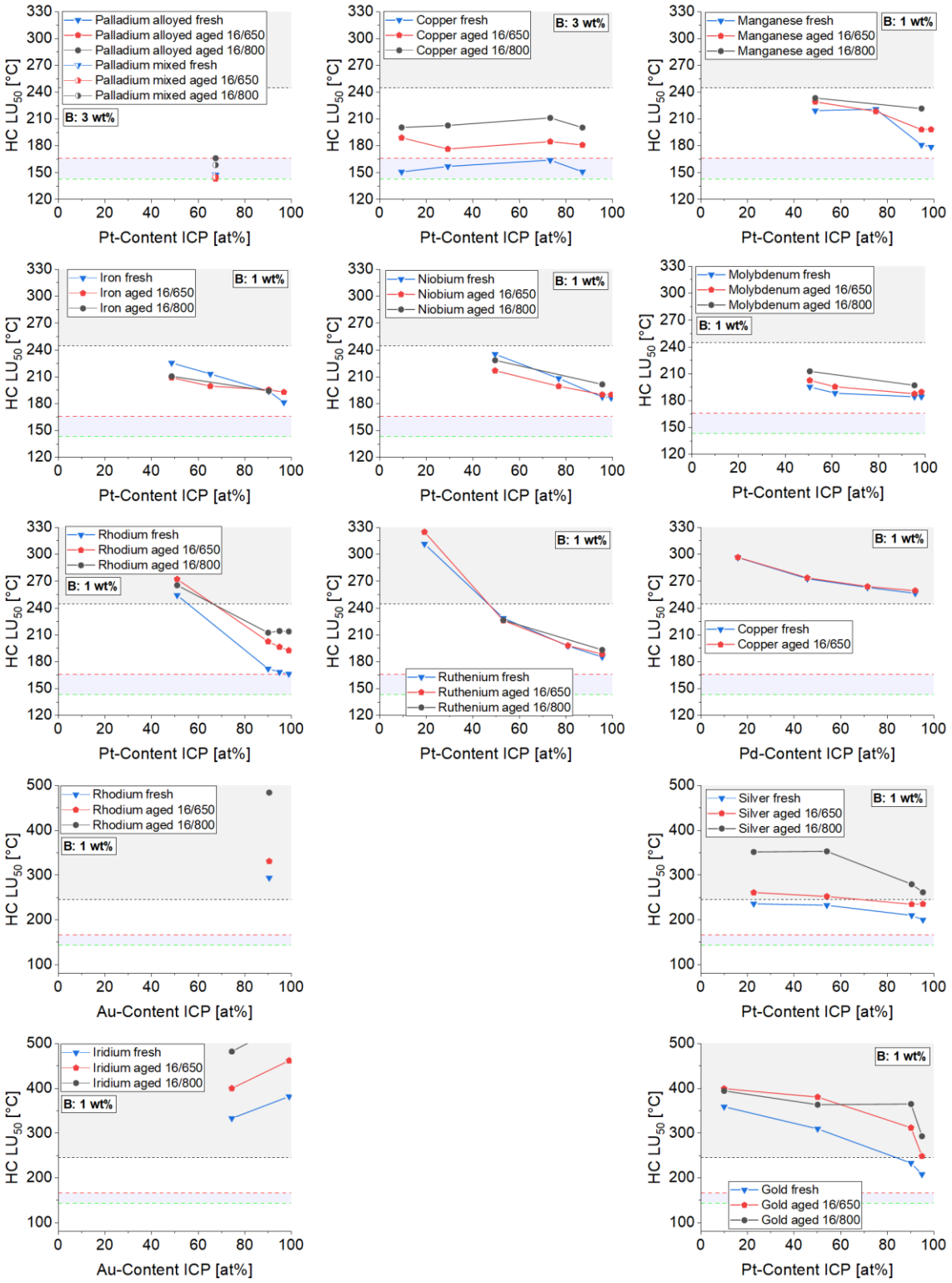

Figure 25 HC LU_{50} evaluated based on the Pt, Pd or Au content of the catalyst. Blue and red areas are a guide to the eye, to ease comparison.

S5.2.3. NO_2 Formation at 250 C

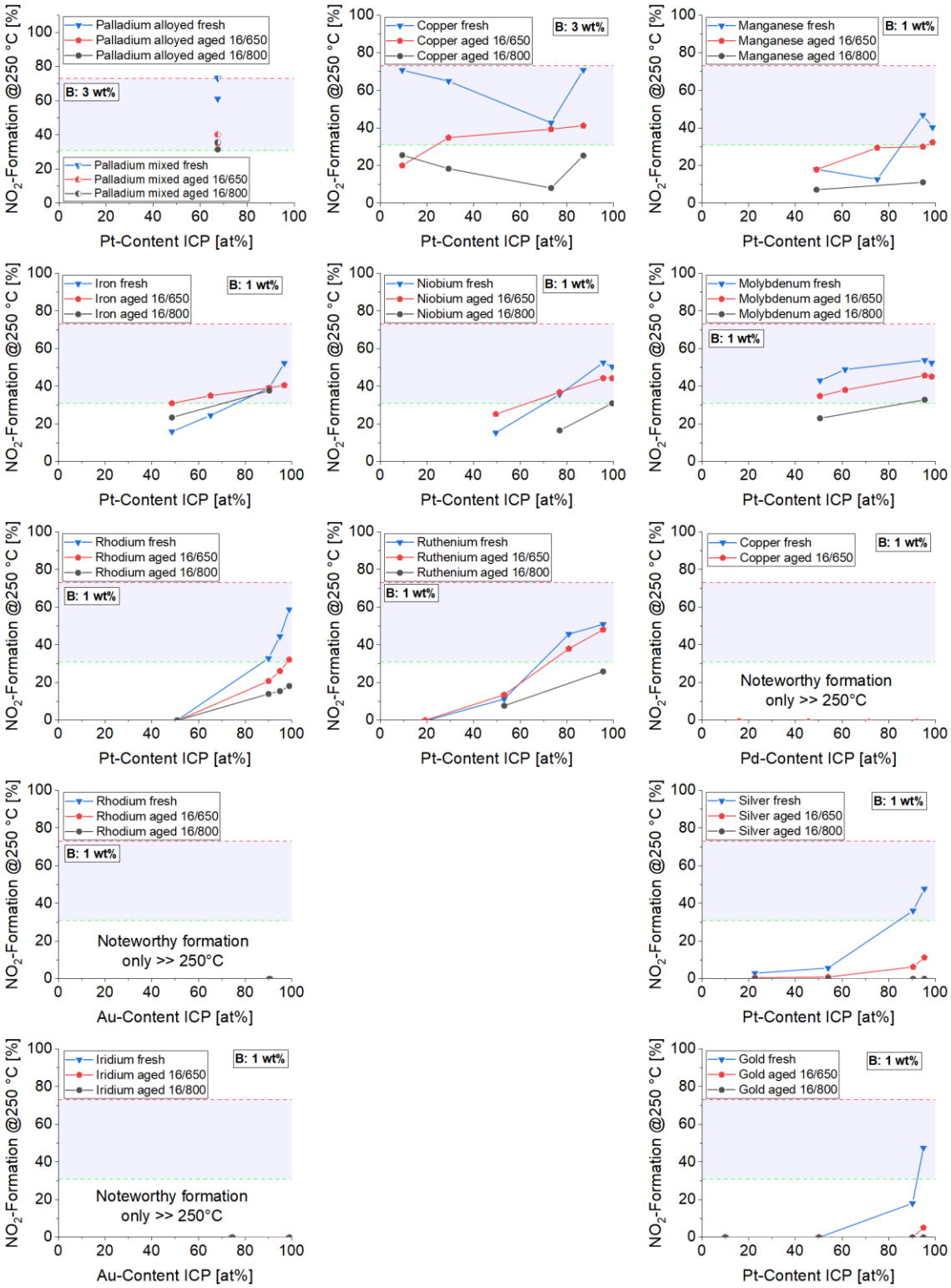

Figure 26 NO_2 formation evaluated based on the Pt, Pd or Au content of the catalyst. Blue and red areas are a guide to the eye, to ease comparison.

S5.2.4. Average N_2O concentration

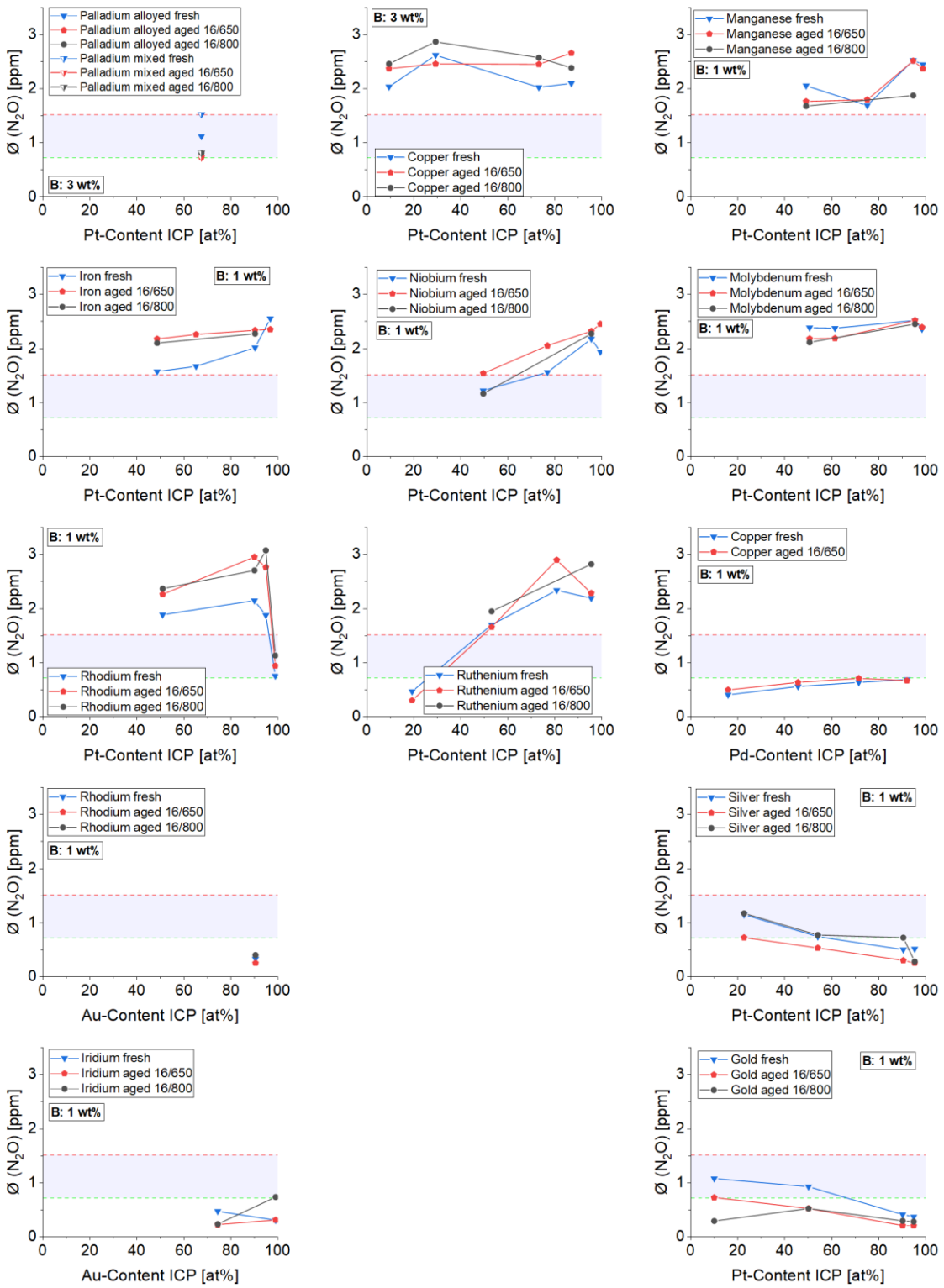

Figure 27 Average N_2O concentration evaluated based on the Pt, Pd or Au content of the catalyst. Blue and red areas are a guide to the eye, to ease comparison.

S5.3. Remaining Correlation curves DOC

S5.3.1. CO-Oxidation LU_{50} vs. CO adsorption energy

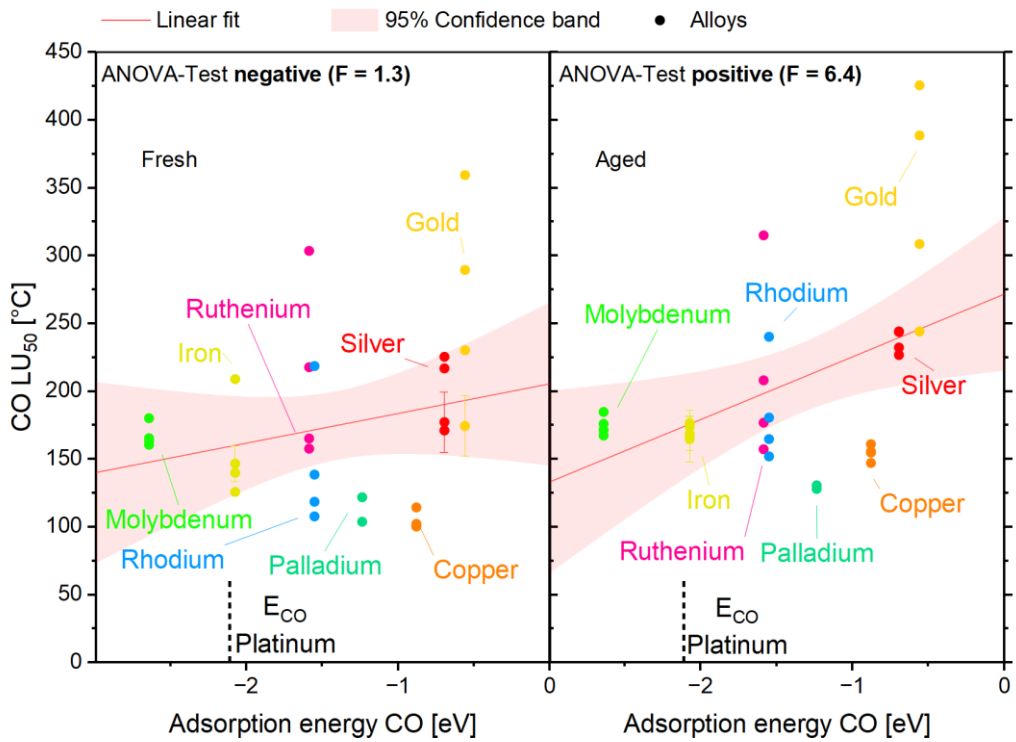

Figure 28 Scaling relation of CO-LU_{50} of laser-generated alloy catalysts in the CO-oxidation reaction.

S5.3.2. Propene-Oxidation

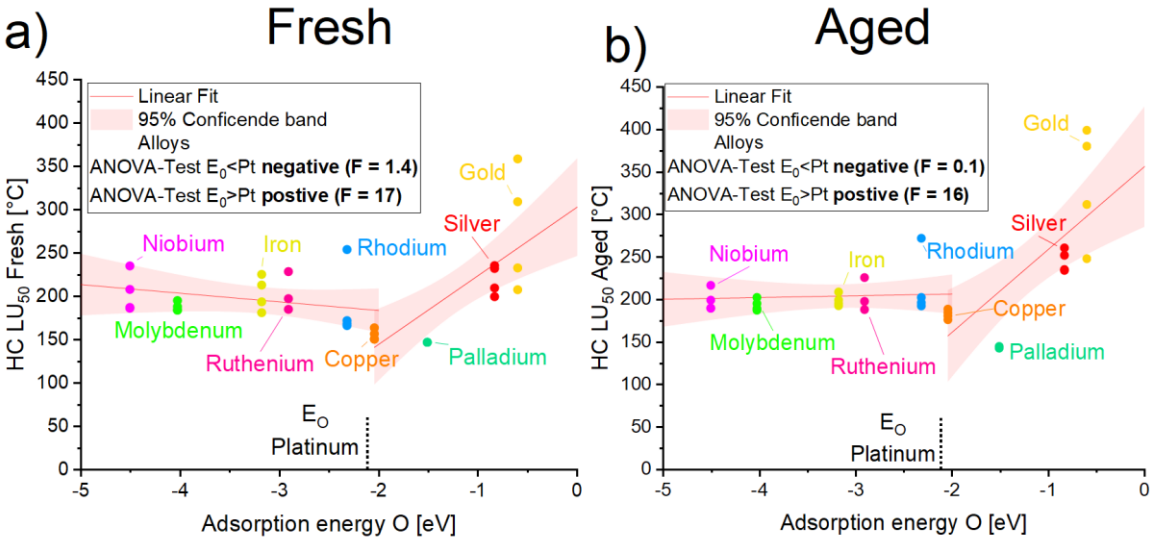

Figure 29 LU_{50} of laser-generated alloy catalysts in the propene oxidation reaction.

S5.3.3. NO_2-Formation

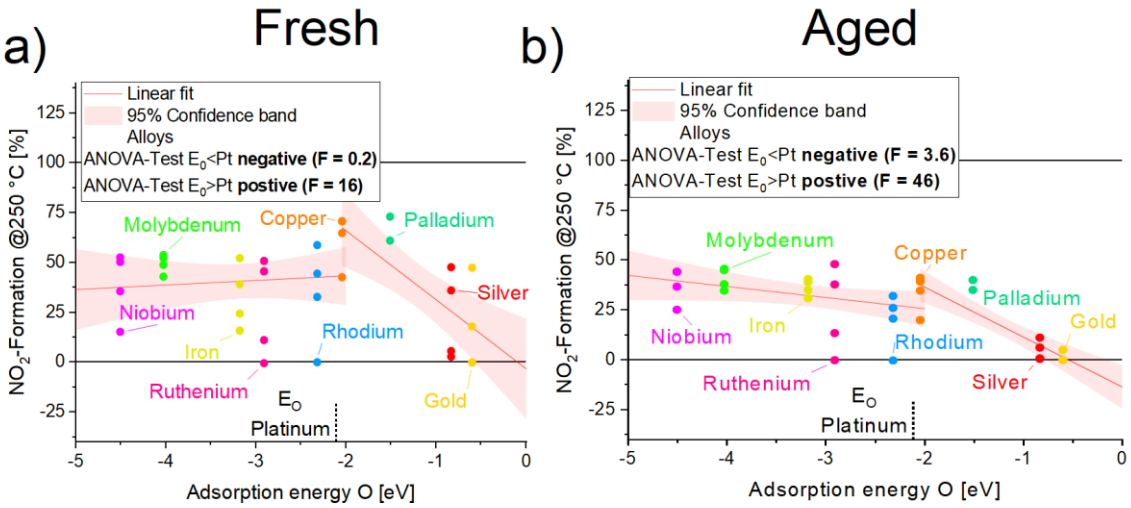

Figure 30 NO_2-Formation of laser-generated alloy catalysts in the NO_2-formation reaction.

S5.3.4. N_2O-Formation

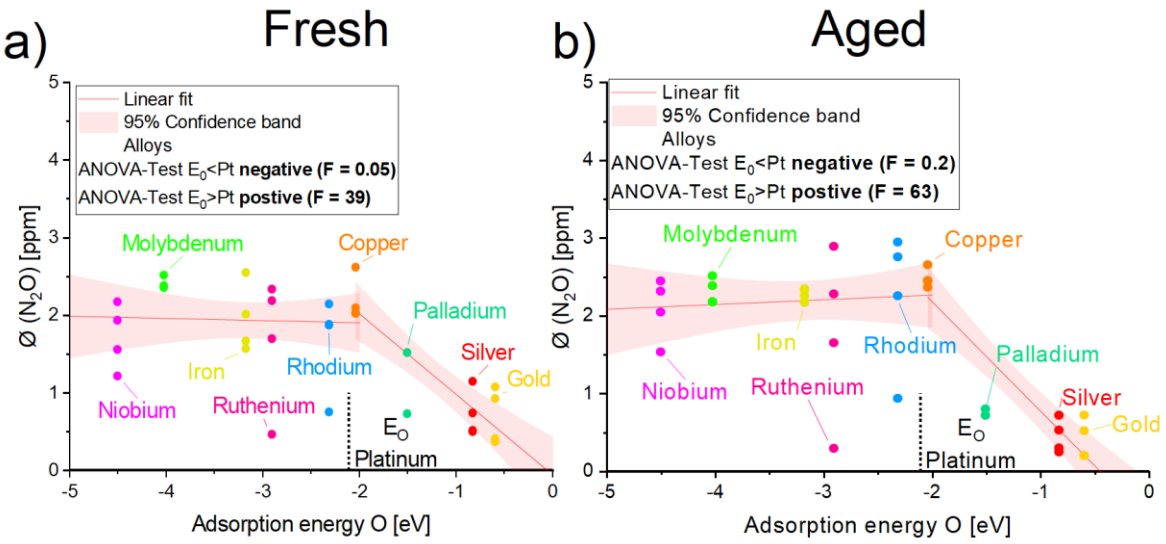

Figure 31 Concentration of N_2O of laser-generated alloy catalysts in the N_2O-formation reaction.

S5.4. Remaining ageing curves DOC

S5.4.1. Propene-Oxidation

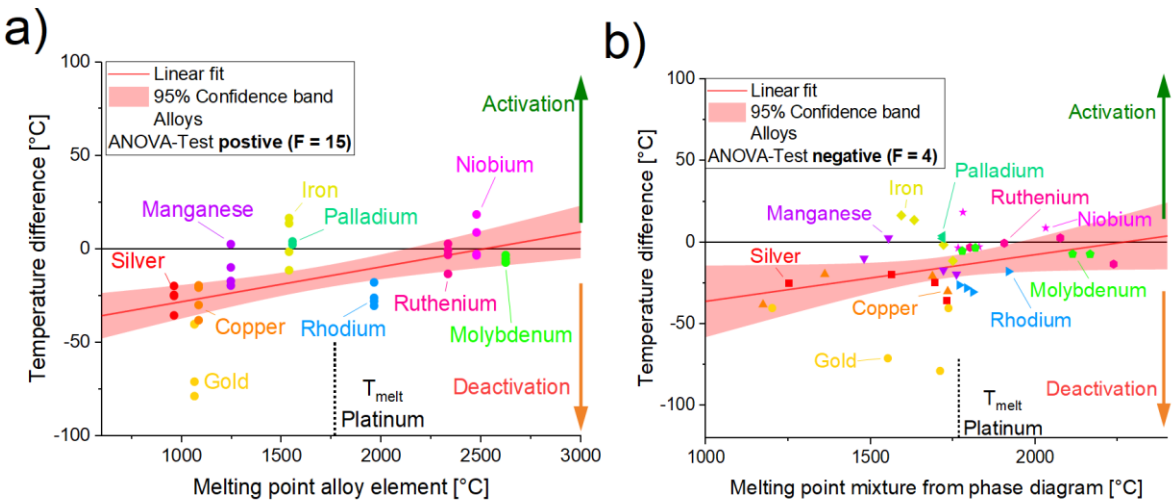

Figure 32 Difference between LU50 (Fresh minus Aged) of laser-generated alloy catalyst in the propene oxidation reaction. Comparison to melting point of alloy element (a) and to melting point of the mixture taken from the underlying bulk phase diagrams (b).

S5.4.2. NO_2-Formation

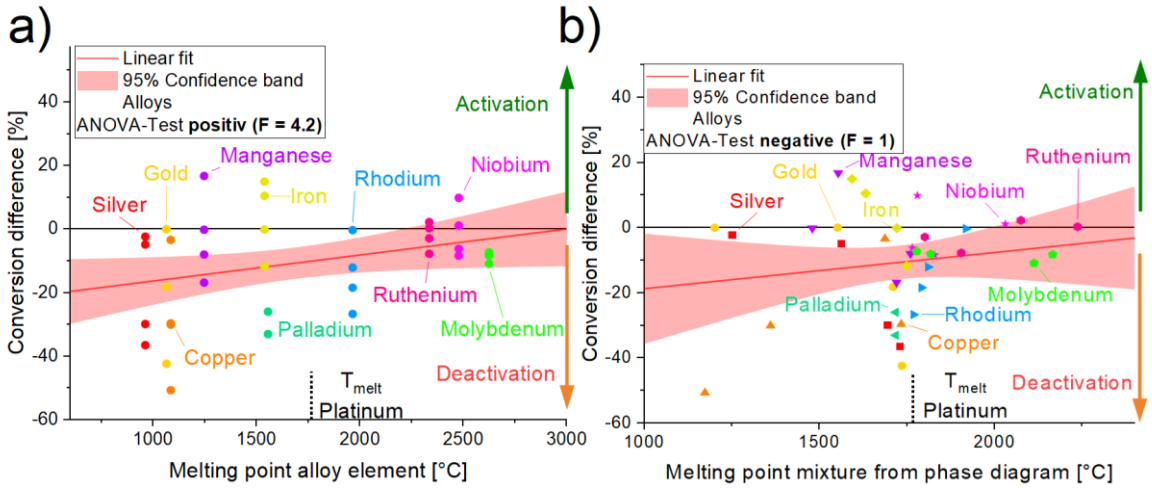

Figure 33 Conversion difference between (Fresh minus Aged) of laser-generated alloy catalyst in the NO_2-formation reaction. Comparison to melting point of alloy element (a) and to melting point of the mixture taken from the underlying bulk phase diagrams (b).

S5.4.3. N_2O-Formation

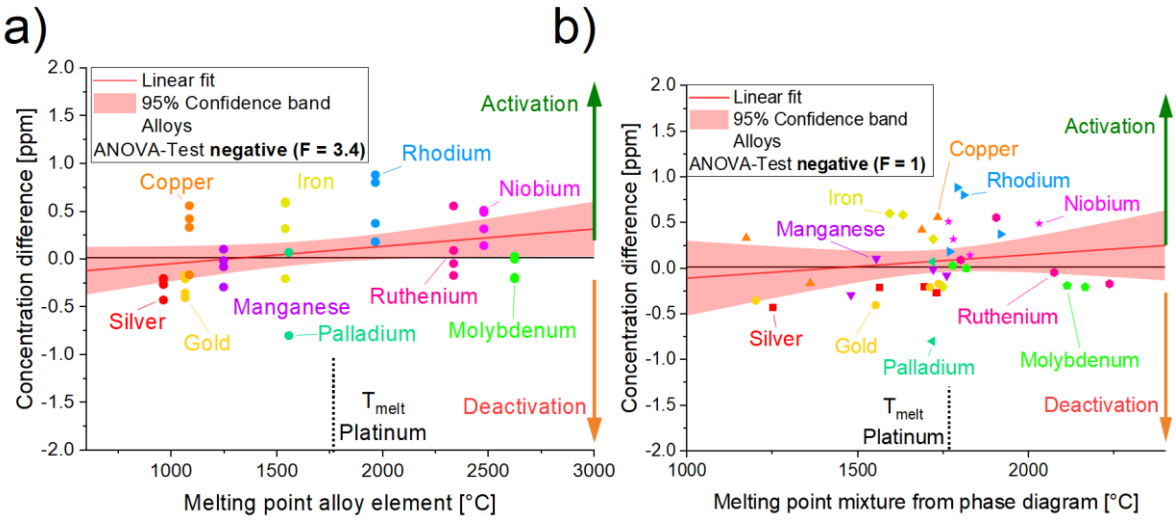

Figure 34 Concentration difference (Aged minus Fresh) of laser-generated alloy catalysts in the N_2O-formation reaction. Comparison to melting point of alloy element (a) and to melting point of the mixture taken from the underlying bulk phase diagrams (b).

S6. ASC Details

S6.1. Gas Mixtures

	Coated Cordierite		Powder Reactor	
	ASC wo/ NO	ASC2 w/ NO	ASC wo/ NO	ASC2 w/ NO
NO	0 ppm	200 ppm	0 ppm	200 ppm
NH_3	300 ppm	300 ppm	300 ppm	300 ppm
O_2	5%	5%	5%	5%
H_2O	5%	5%	5%	5%
N_2	Rest	Rest	Rest	Rest
Space Velocity	200,000 1/h	200,000 1/h	similar conditions as cordierite samples, but due to fluctuations in packing density, no meaningful space velocity can be defined.	

S6.2. Result Overview ASCI (without NO)

S6.2.1. NH_3 LU_{50}

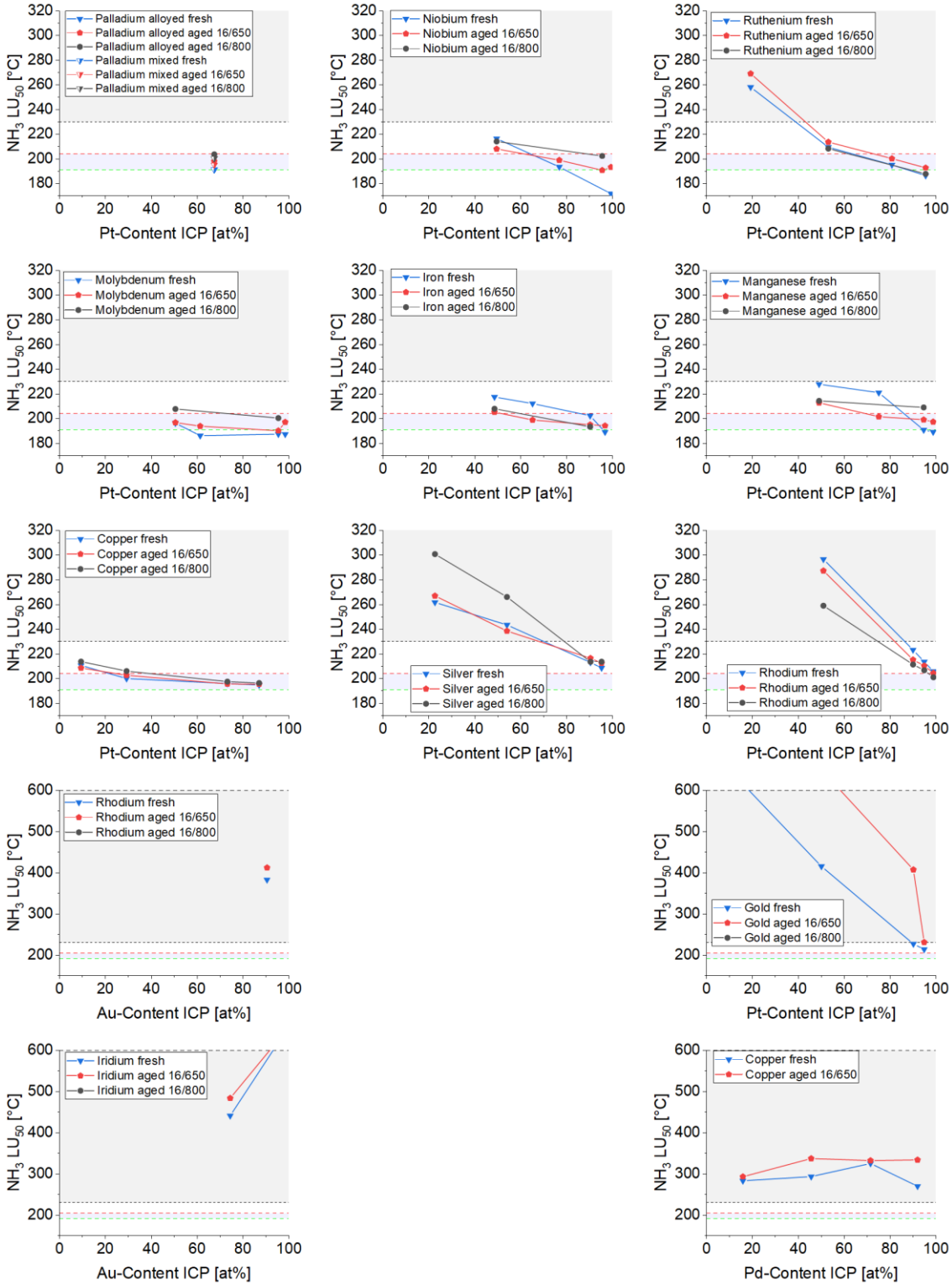

Figure 35 NH_3 LU_{50} evaluated based on the Pt, Pd or Au content of the catalyst. Blue and red areas are a guide to the eye, to ease comparison.

S6.2.2. Average NO_2 concentration

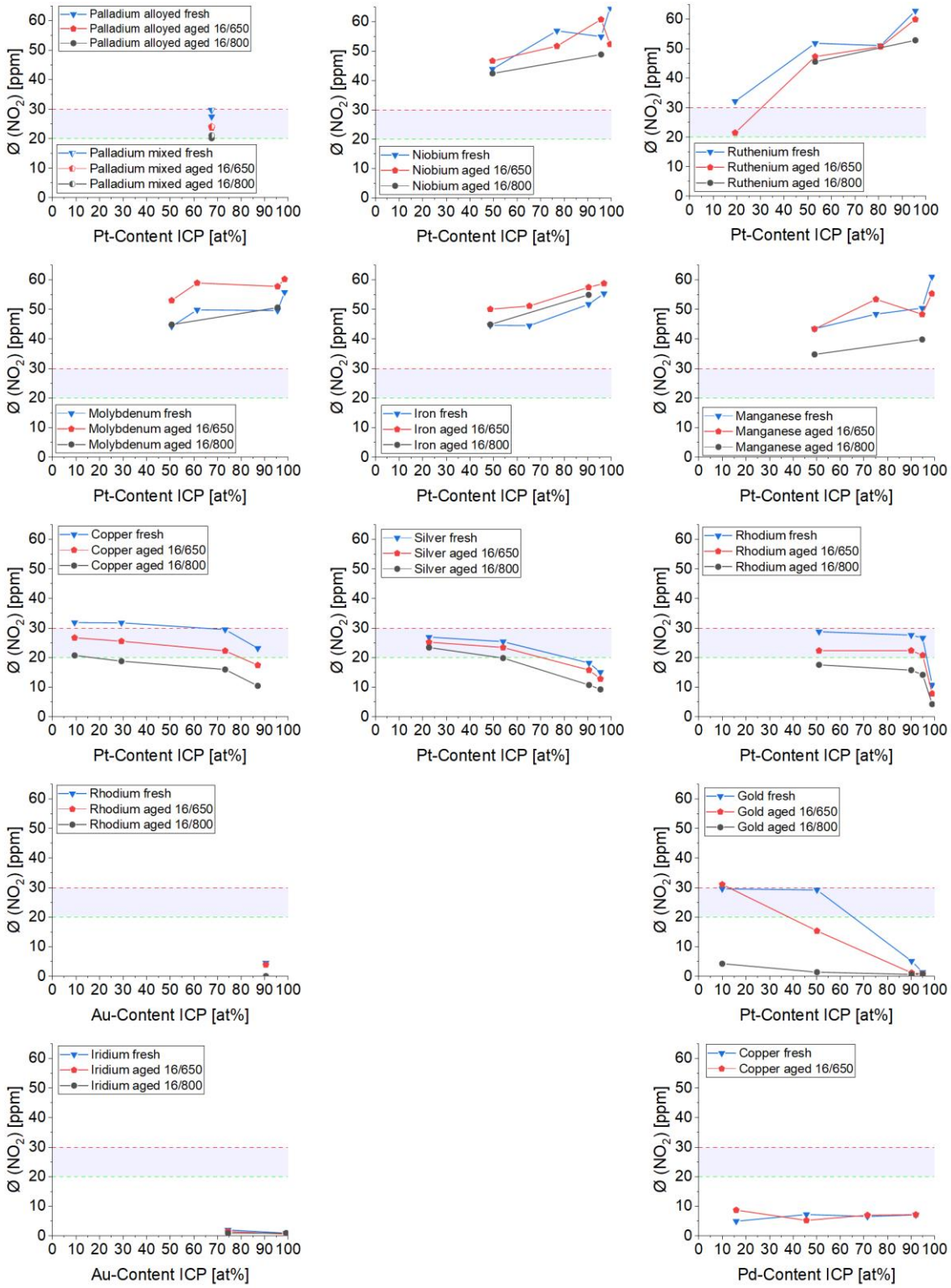

Figure 36 Average NO_2 concentration evaluated based on the Pt, Pd or Au content of the catalyst. Blue and red areas are a guide to the eye, to ease comparison.

S6.2.3. Average NO concentration

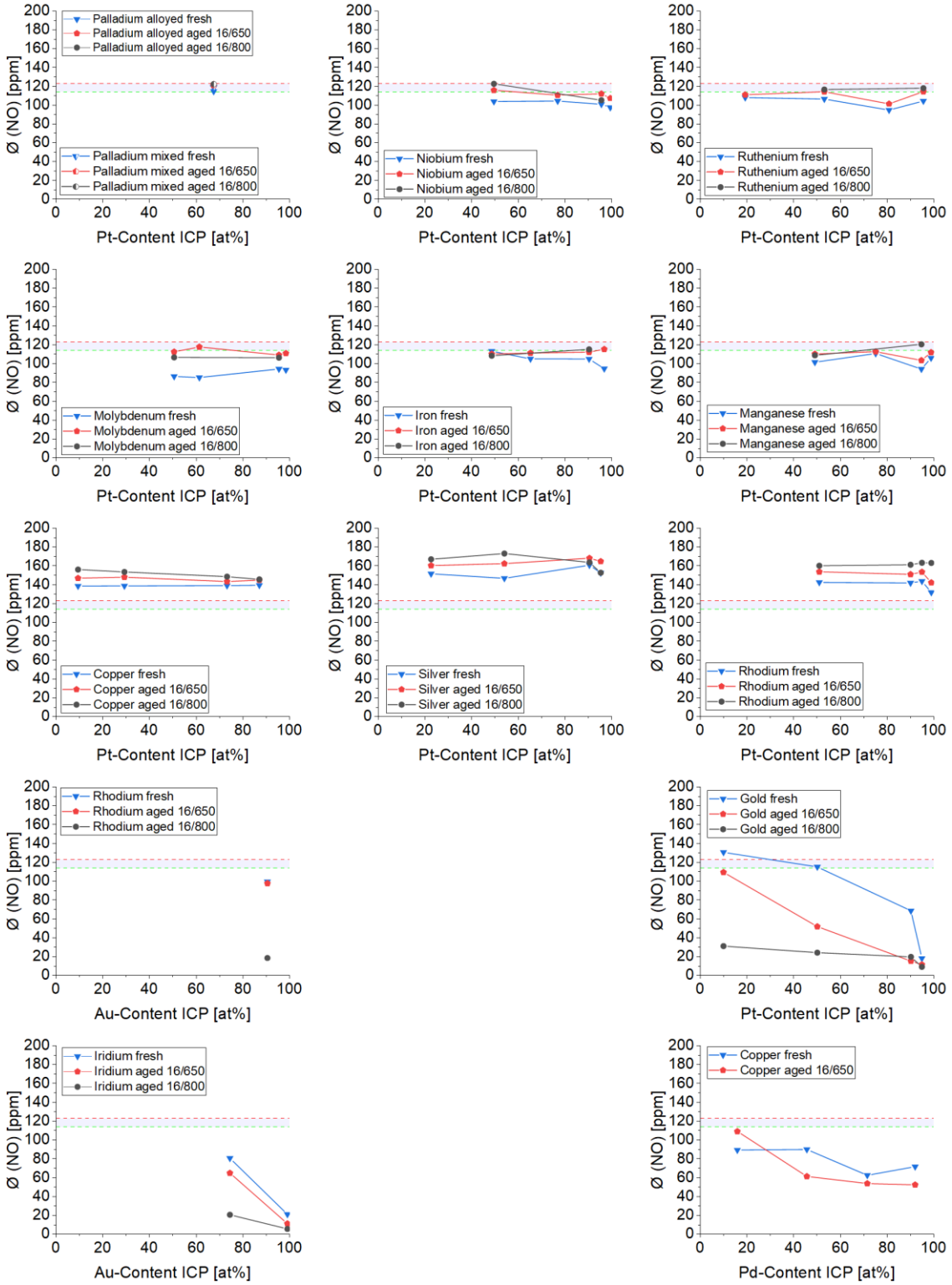

Figure 37 Average NO concentration evaluated based on the Pt, Pd or Au content of the catalyst. Blue and red areas are a guide to the eye, to ease comparison.

S6.2.4. Average N_2O concentration

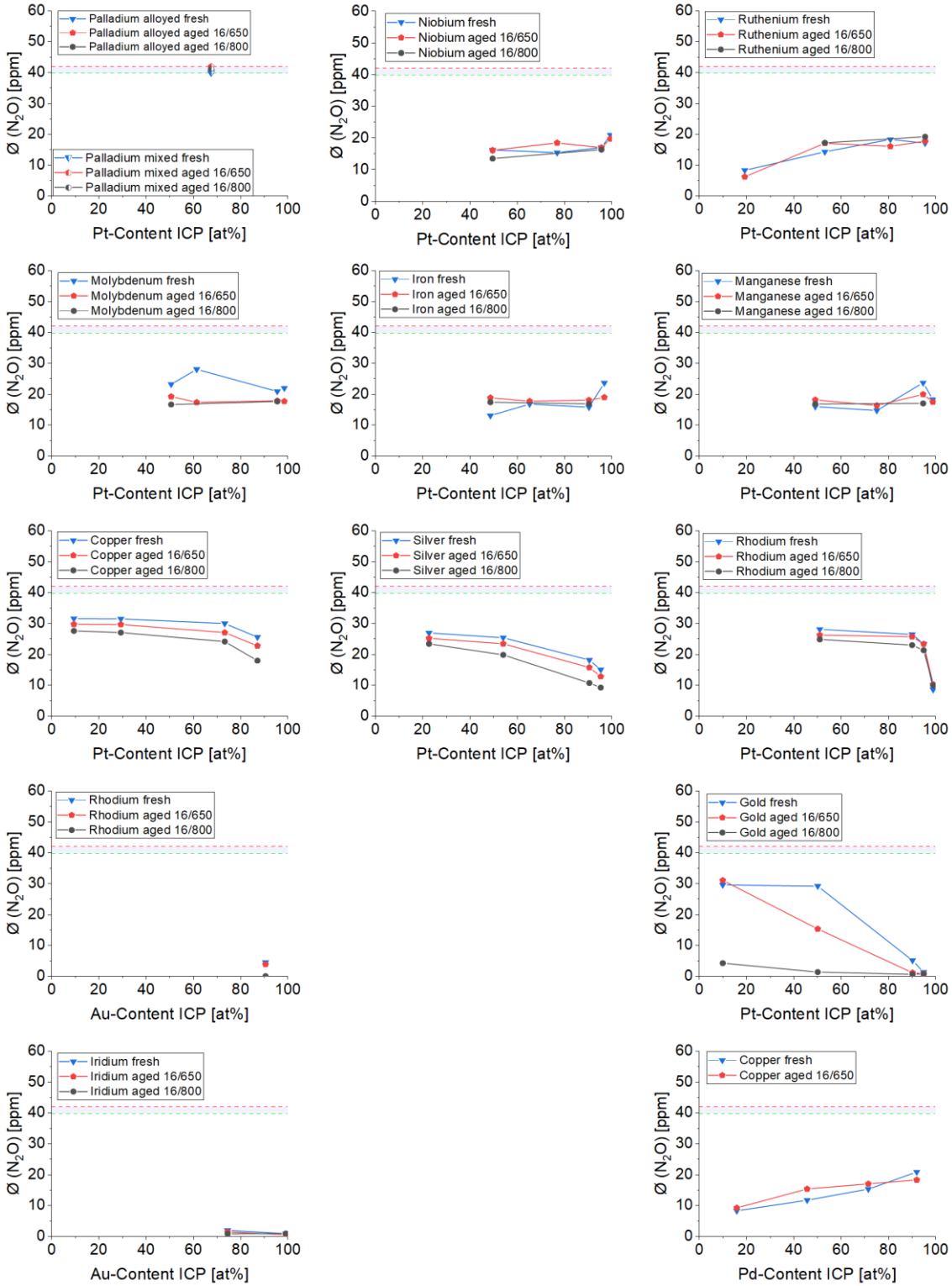

Figure 38 Average N_2O concentration evaluated based on the Pt, Pd or Au content of the catalyst. Blue and red areas are a guide to the eye, to ease comparison.

S6.2.5. Average formed N

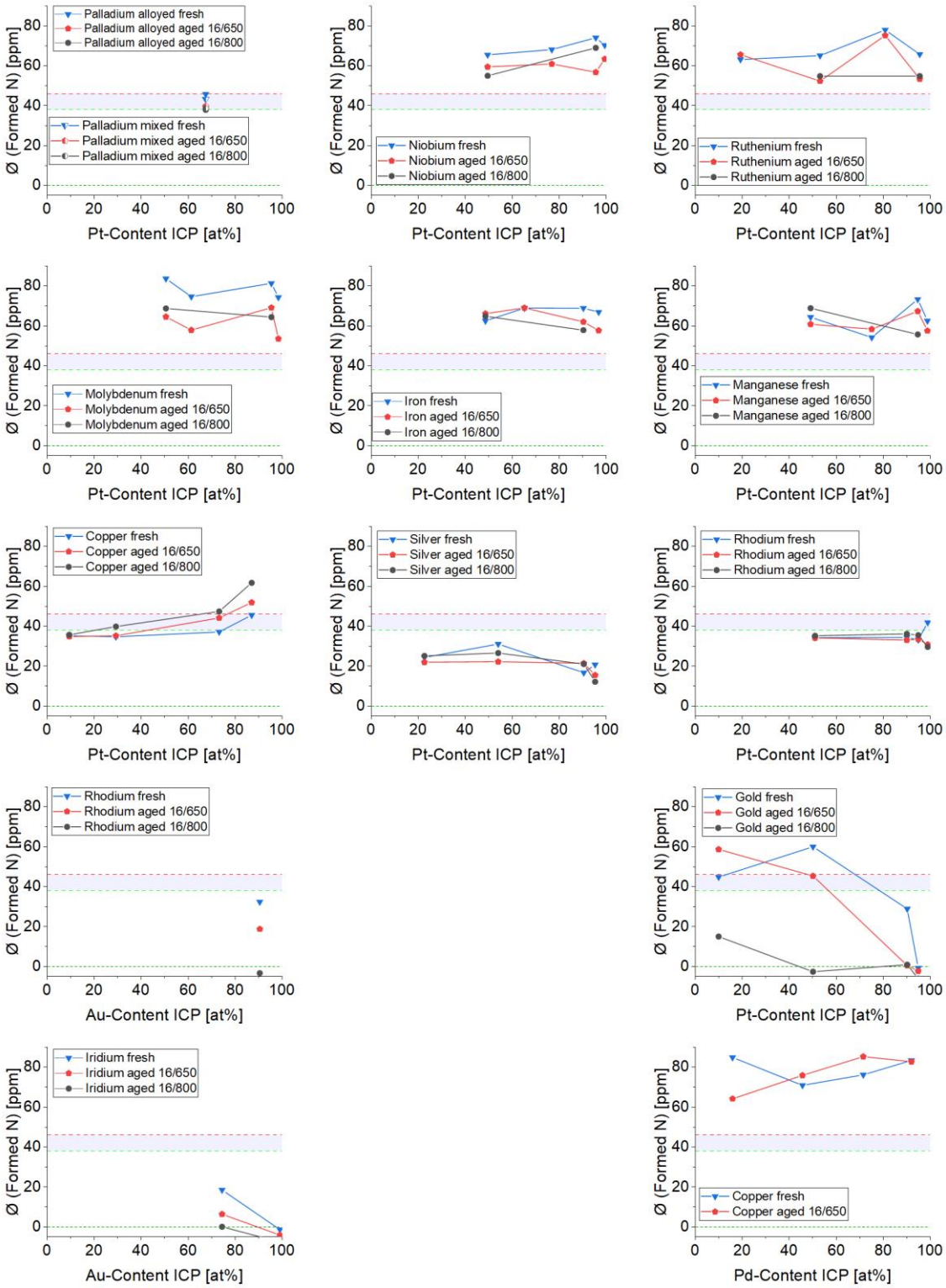

Figure 39 Average formed N evaluated based on the Pt, Pd or Au content of the catalyst. Blue and red areas are a guide to the eye, to ease comparison.

S6.3. Remaining Correlation Curves ASCI (without NO)

S6.3.1. LU_{50}-NH_3 vs. Adsorption enthalpy NO

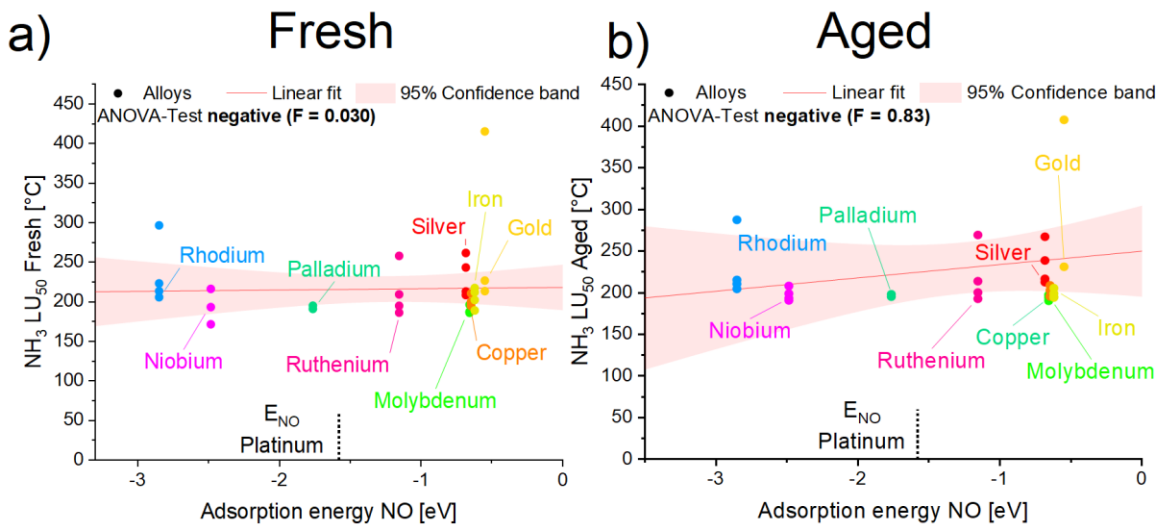

Figure 40 LU_{50} of laser-generated alloy catalysts in the NH_3-oxidation reaction.

S6.3.1. LU_{50}-NH_3 vs. Adsorption enthalpy O

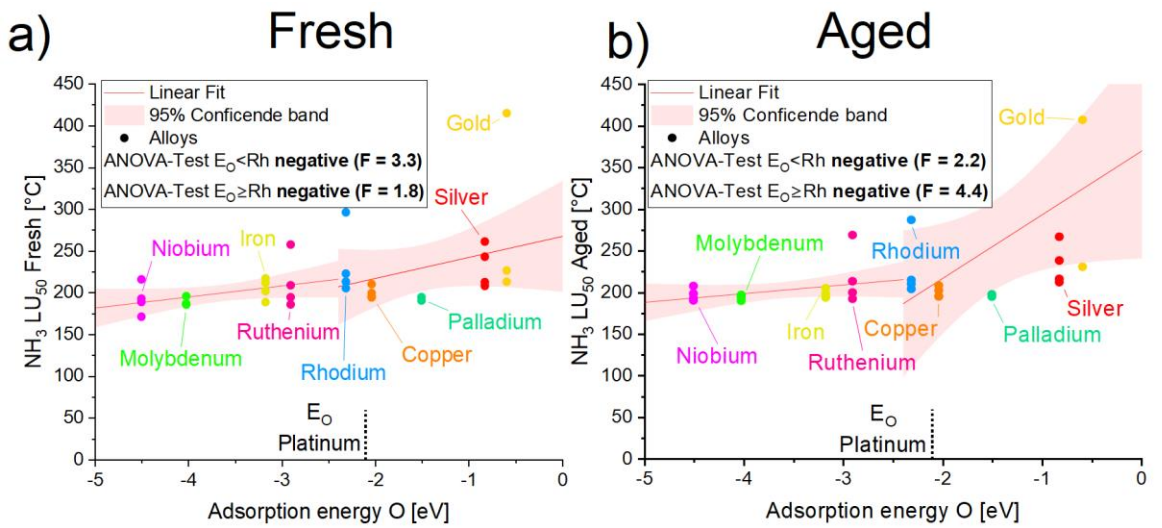

Figure 41 LU_{50} of laser-generated alloy catalysts in the NH_3-oxidation reaction.

S6.3.2. N_2O-Formation

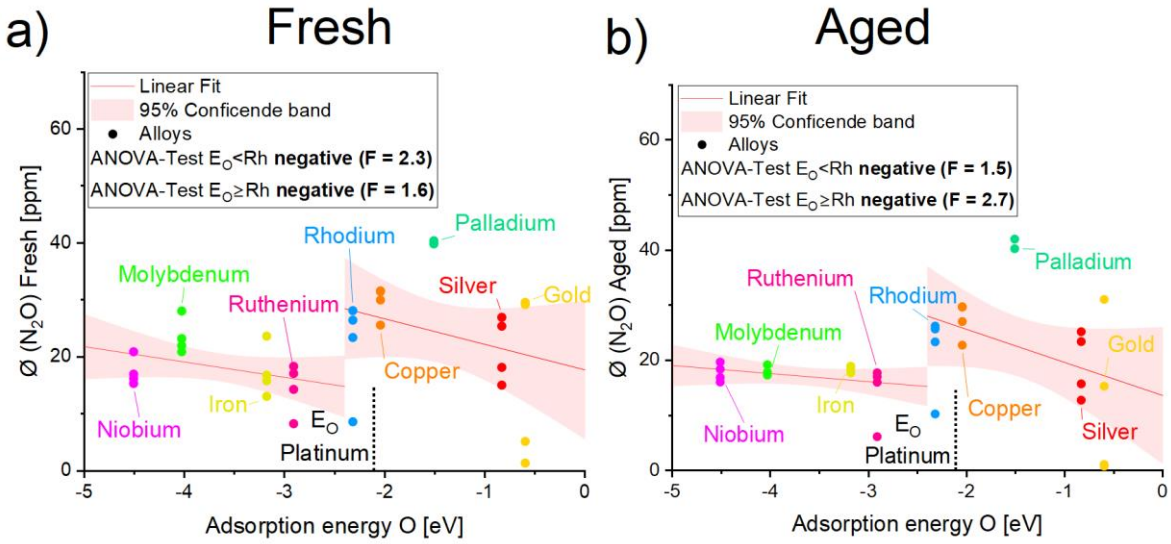

Figure 42 Average N_2O-Concentration of laser-generated alloy catalysts.

S6.3.3. NO_2-Formation

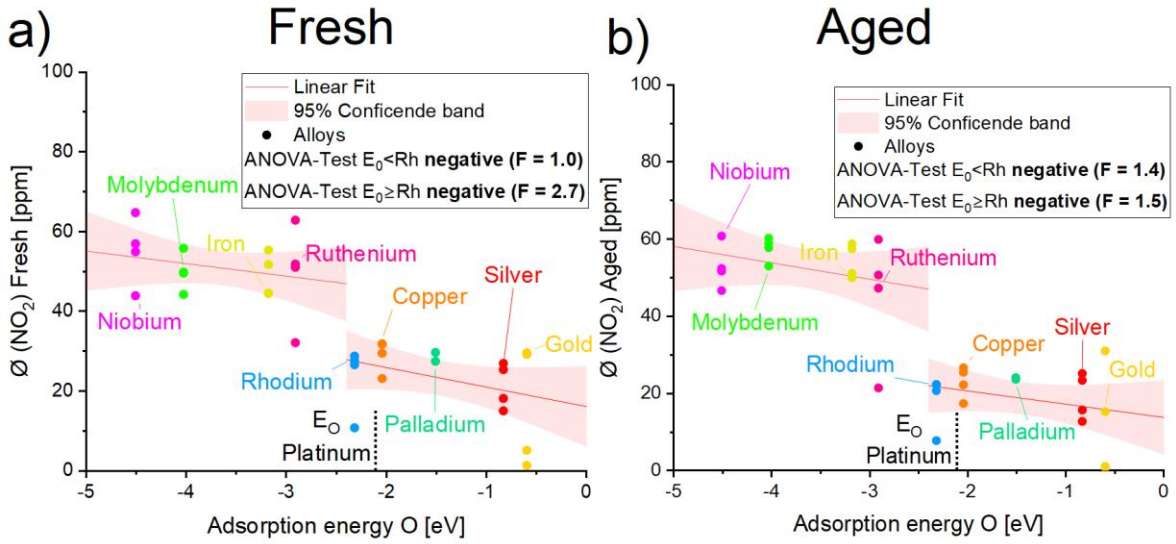

Figure 43 Average NO_2-Concentration of laser-generated alloy catalysts.

S6.3.4. N-Formation

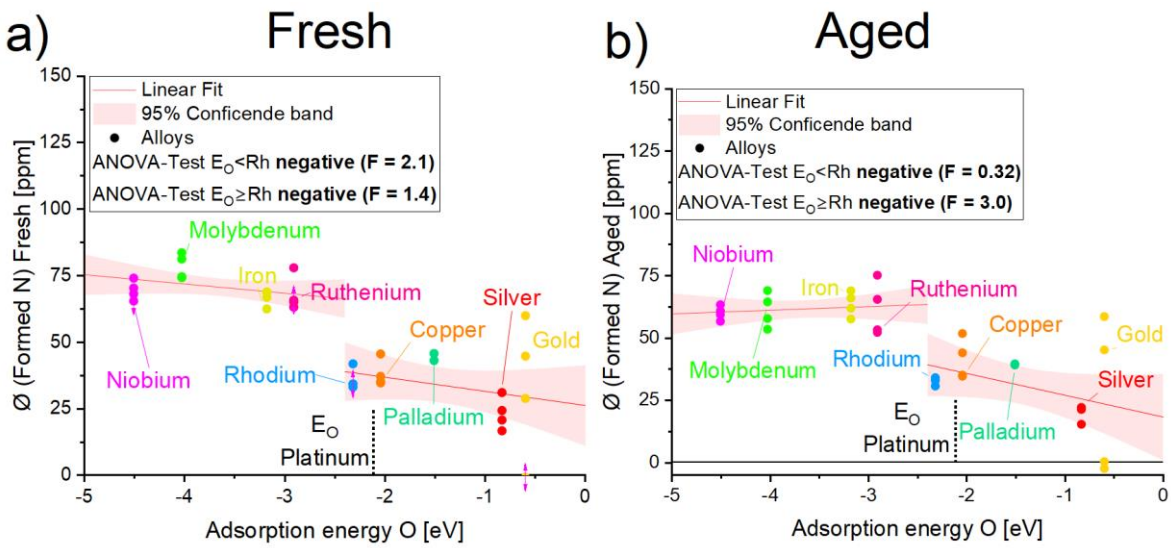

Figure 44 Average formed nitrogen concentration of laser-generated alloy catalysts.

S6.4. Ageing curves ASC I (without NO)

S6.4.1. NH_3-Oxidation

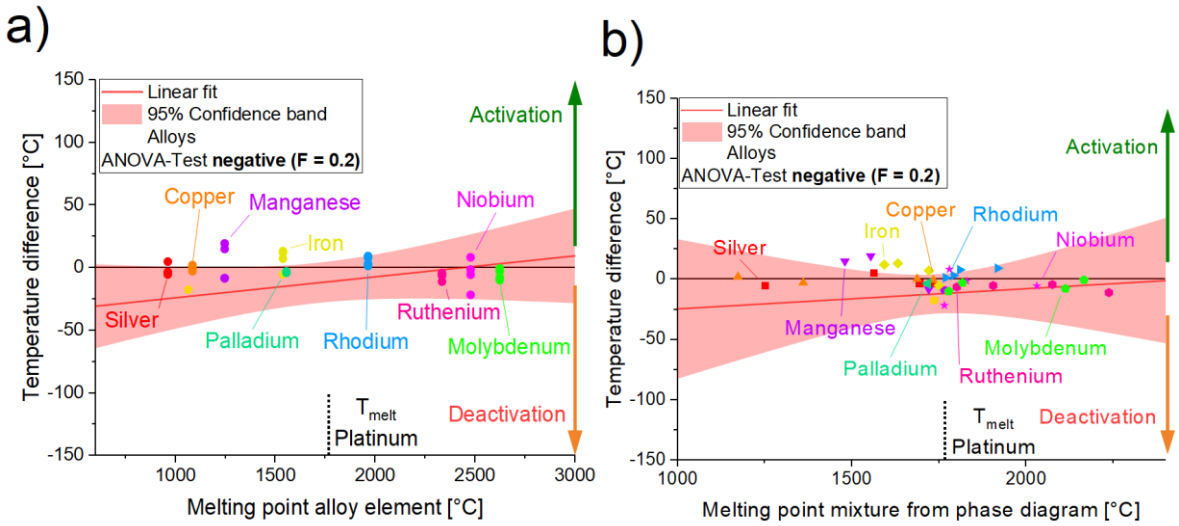

Figure 45 Difference of LU_{50} (Fresh minus Aged) of laser-generated alloy catalysts in the NH_3 oxidation reaction. Comparison to melting point of alloy element (a) and to melting point of the mixture taken from the underlying bulk phase diagrams (b).

S6.4.2. NO_2-Formation

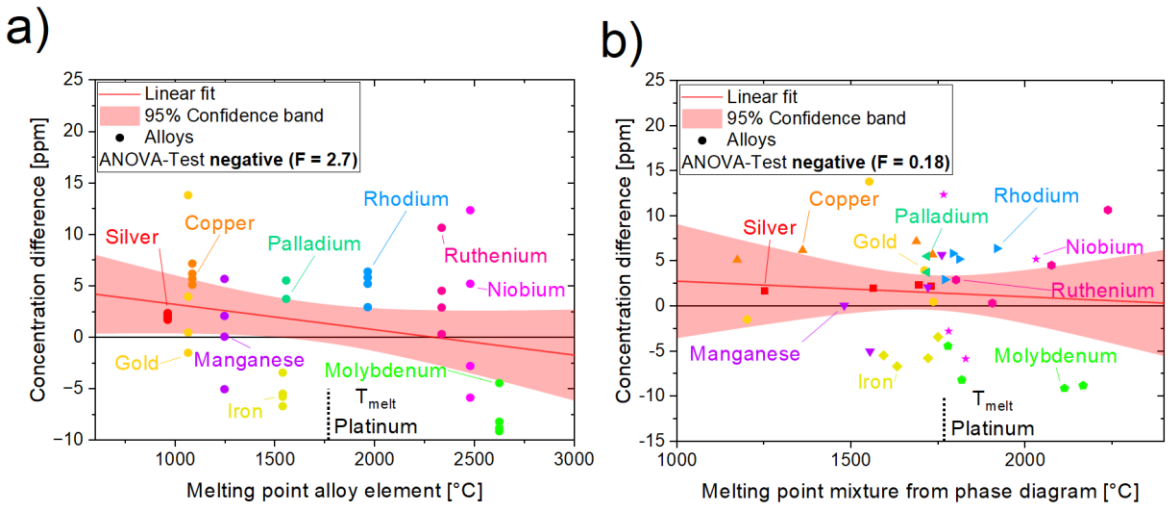

Figure 46 Difference in concentration (Fresh minus Aged) of laser-generated alloy catalysts in the NO_2-formation reaction. Comparison to melting point of alloy element (a) and to melting point of the mixture taken from the underlying bulk phase diagrams (b).

S6.4.3. NO-Formation

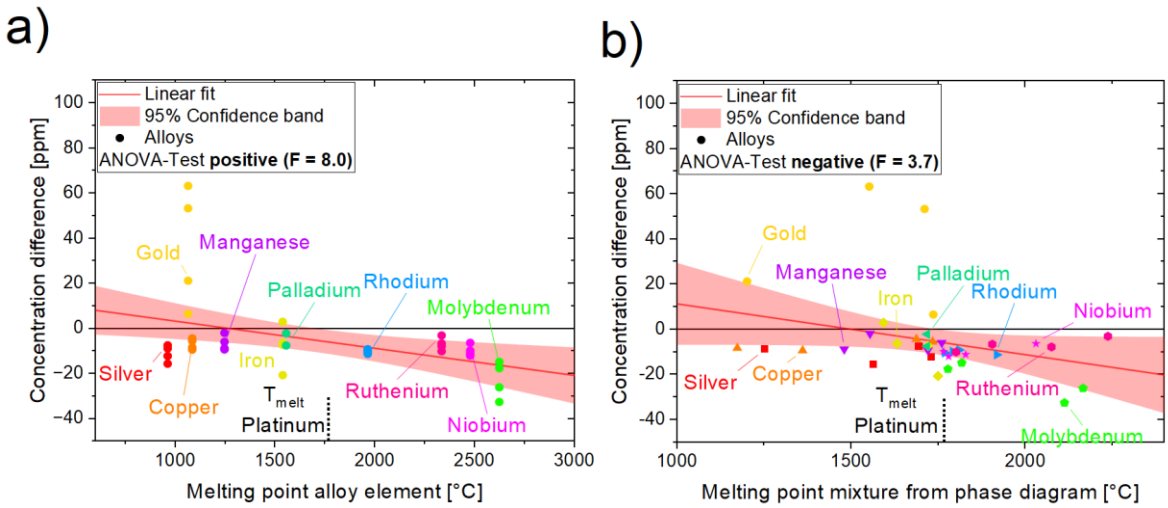

Figure 47 Difference in concentration (Fresh minus Aged) of laser-generated alloy catalysts in the NO-formation reaction. Comparison to melting point of alloy element (a) and to melting point of the mixture taken from the underlying bulk phase diagrams (b).

S6.4.4. N_2O-Formation

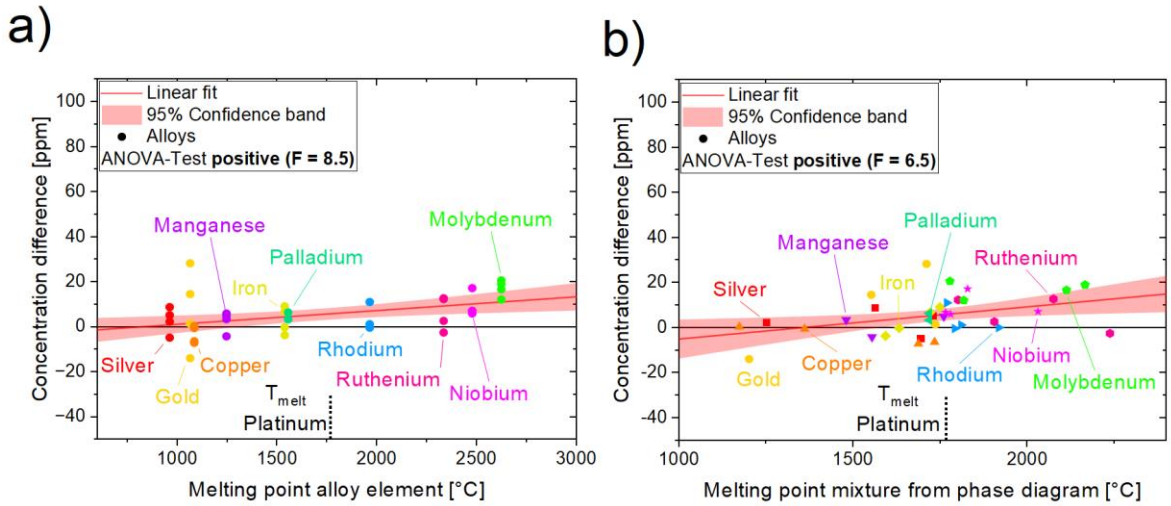

Figure 48 Difference in concentration (Fresh minus Aged) of laser-generated alloy catalysts in the N-formation reaction. Comparison to melting point of alloy element (a) and to melting point of the mixture taken from the underlying bulk phase diagrams (b).

S6.4.5. N-Formation

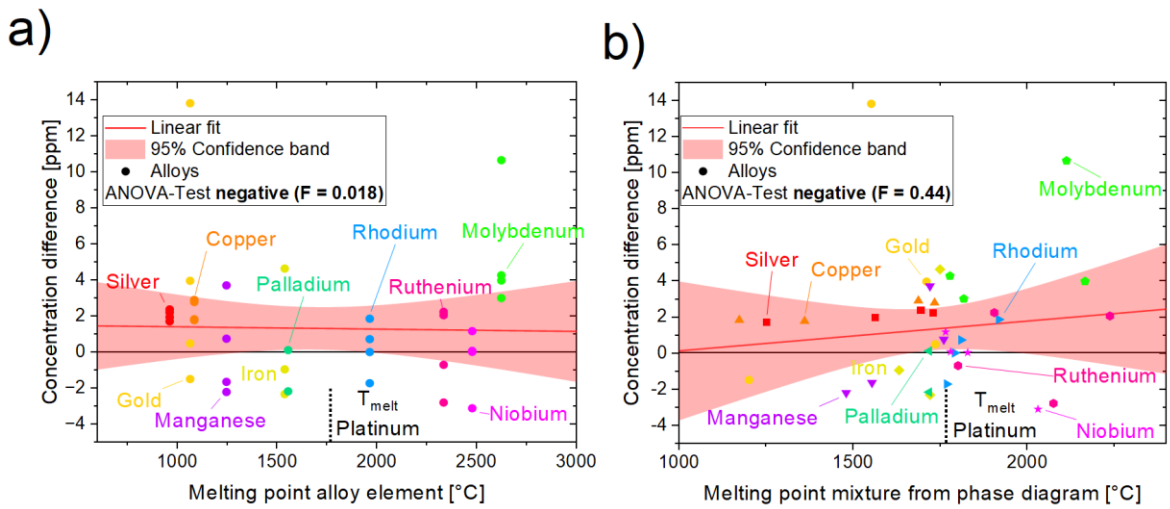

Figure 49 Difference in concentration (Fresh minus Aged) of laser-generated alloy catalysts in the N_2O-formation reaction. Comparison to melting point of alloy element (a) and to melting point of the mixture taken from the underlying bulk phase diagrams (b).

S6.5. Result Overview ASCII (with NO)

S6.5.1. NH_3 LU_{50}

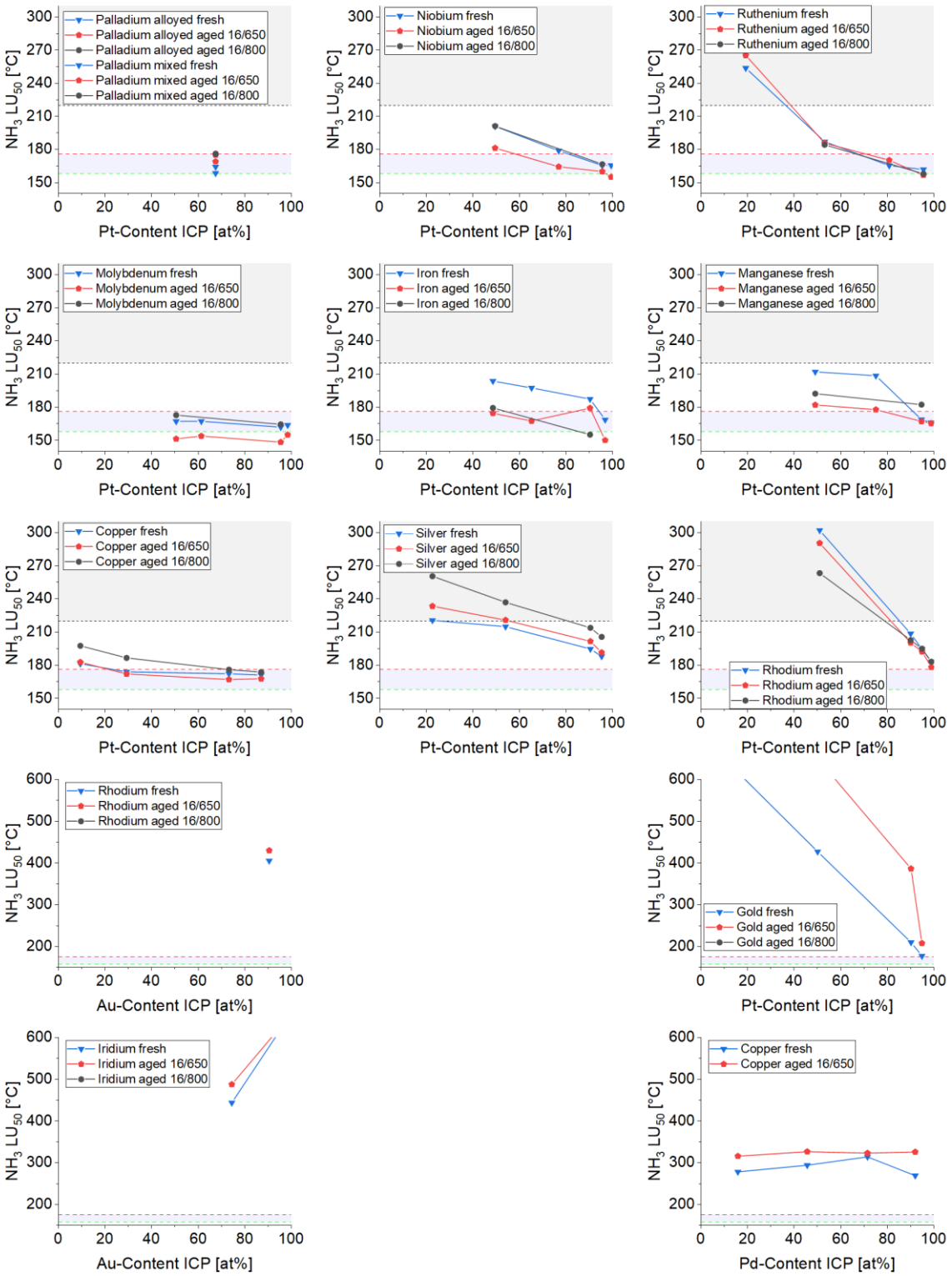

Figure 50 NH_3 LU_{50} evaluated based on the Pt, Pd or Au content of the catalyst. Blue and red areas are a guide to the eye, to ease comparison.

S6.5.2. Average NO_2 concentration

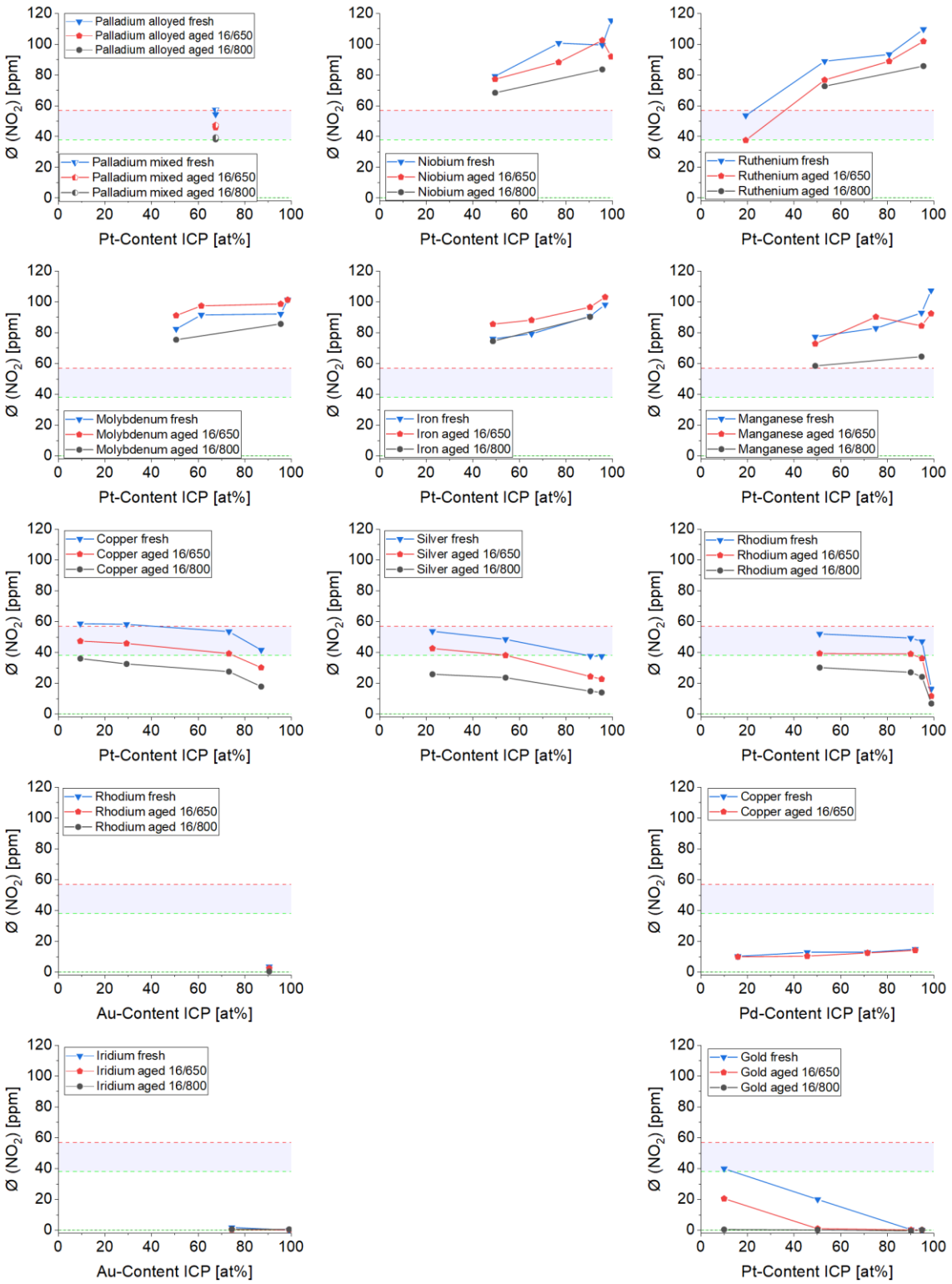

Figure 51 Average NO_2 concentration evaluated based on the Pt, Pd or Au content of the catalyst. Blue and red areas are a guide to the eye, to ease comparison.

S6.5.3. Average NO concentration

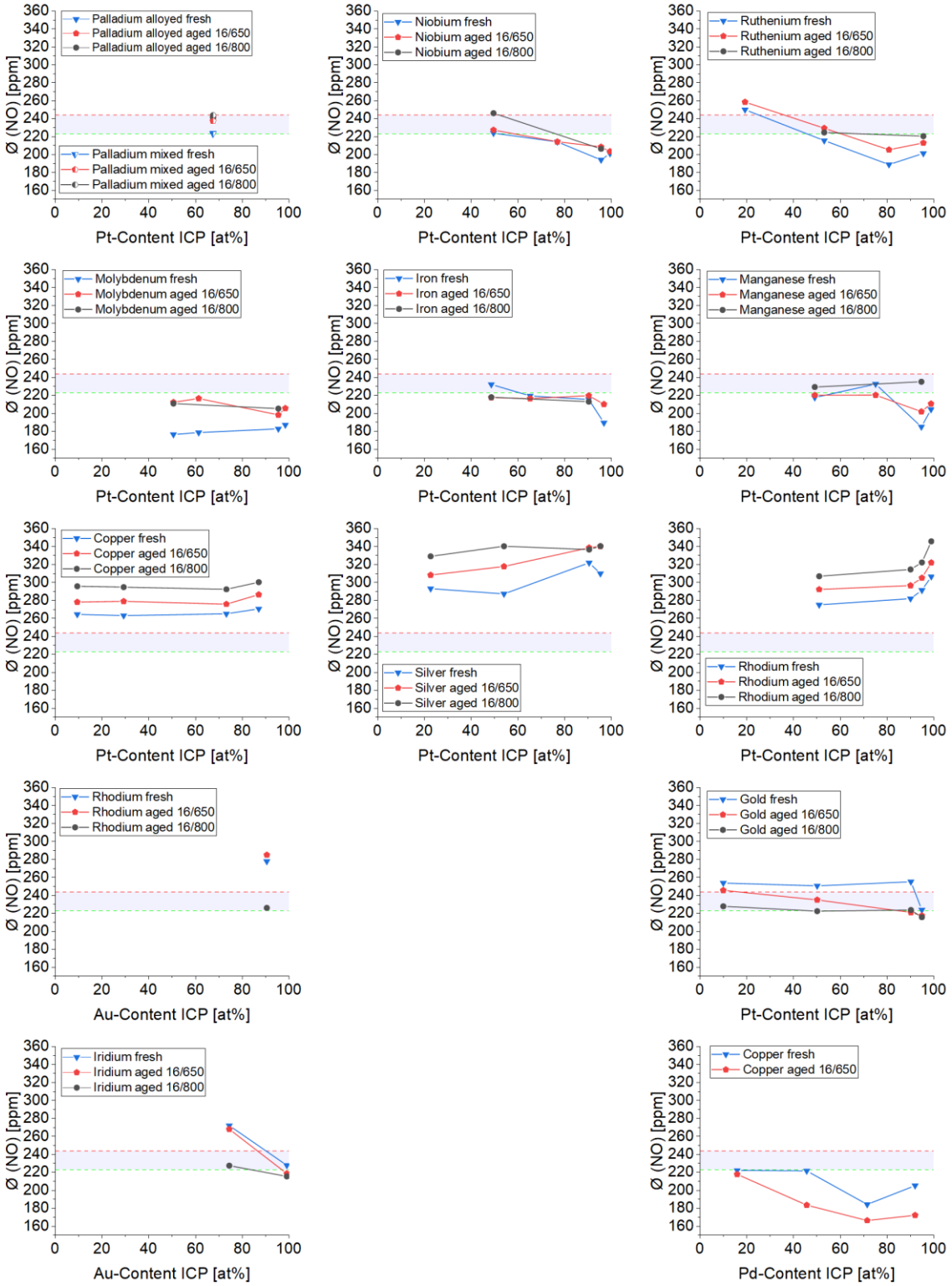

Figure 52 Average NO concentration evaluated based on the Pt, Pd or Au content of the catalyst. Blue and red areas are a guide to the eye, to ease comparison.

S6.5.4. Average N_2O concentration

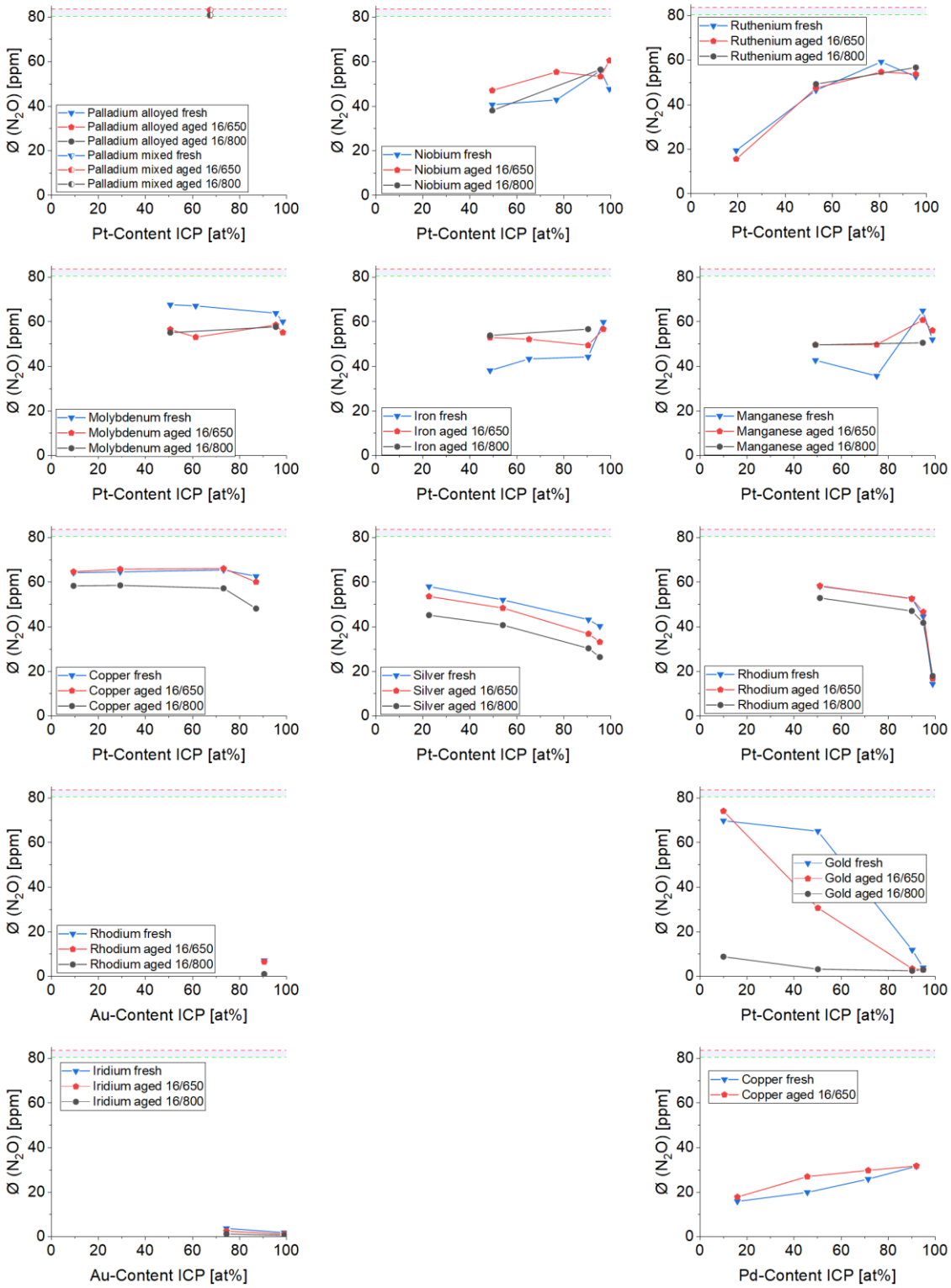

Figure 53 Average N_2O concentration evaluated based on the Pt, Pd or Au content of the catalyst. Blue and red areas are a guide to the eye, to ease comparison.

S6.5.5. Average formed N

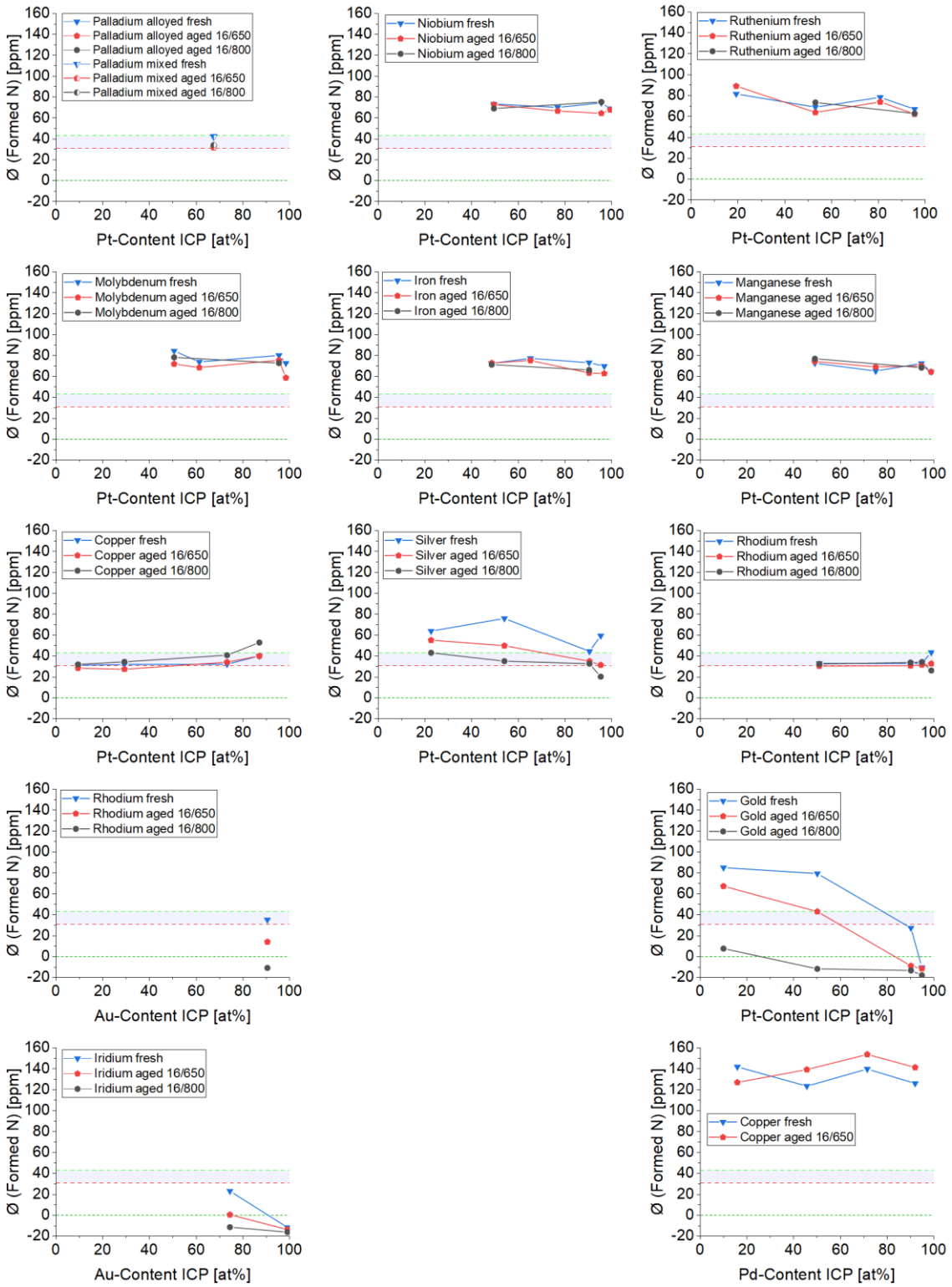

Figure 54 Average formed N evaluated based on the Pt, Pd or Au content of the catalyst. Blue and red areas are a guide to the eye, to ease comparison.

S6.6. Correlation Curves ASCII (with NO)

S6.6.1. LU_{50}-NH_3 vs. Adsorption enthalpy NO

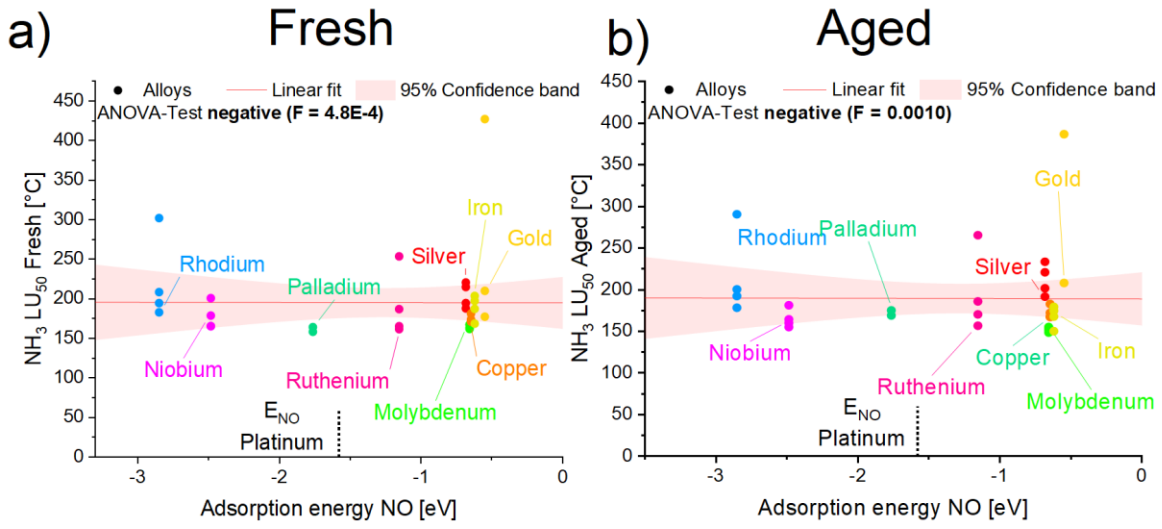

Figure 55 LU_{50} of laser-generated alloy catalysts in the NH_3-oxidation reaction.

S6.6.2. LU_{50}-NH_3 vs. Adsorption enthalpy O

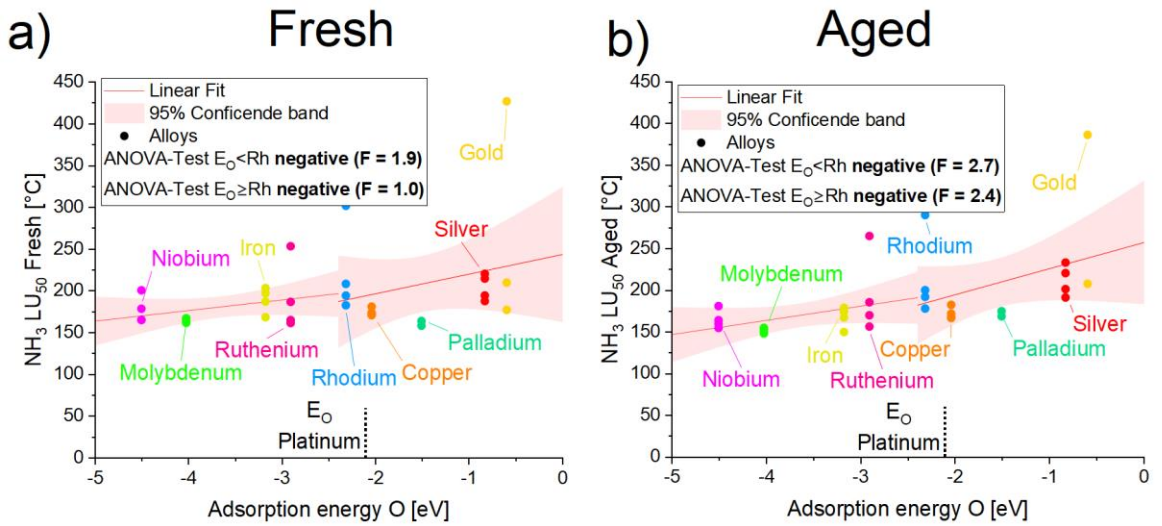

Figure 56 LU_{50} of laser-generated alloy catalysts in the NH_3-oxidation reaction.

S6.6.3. NO_2-Formation

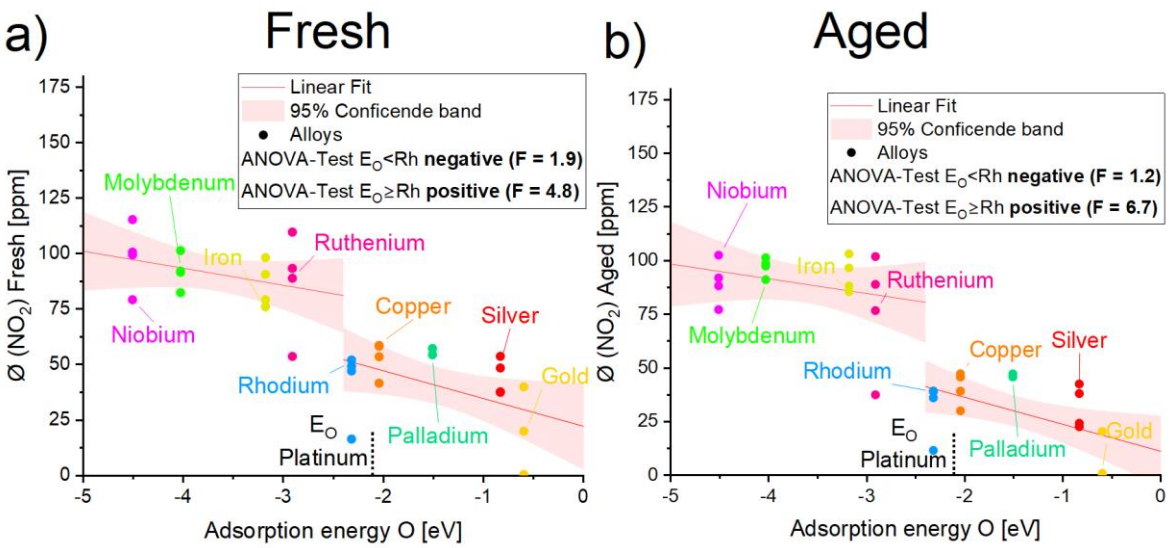

Figure 57 Average NO_2-Concentration of laser-generated alloy catalysts.

S6.6.4. N_2O-Formation

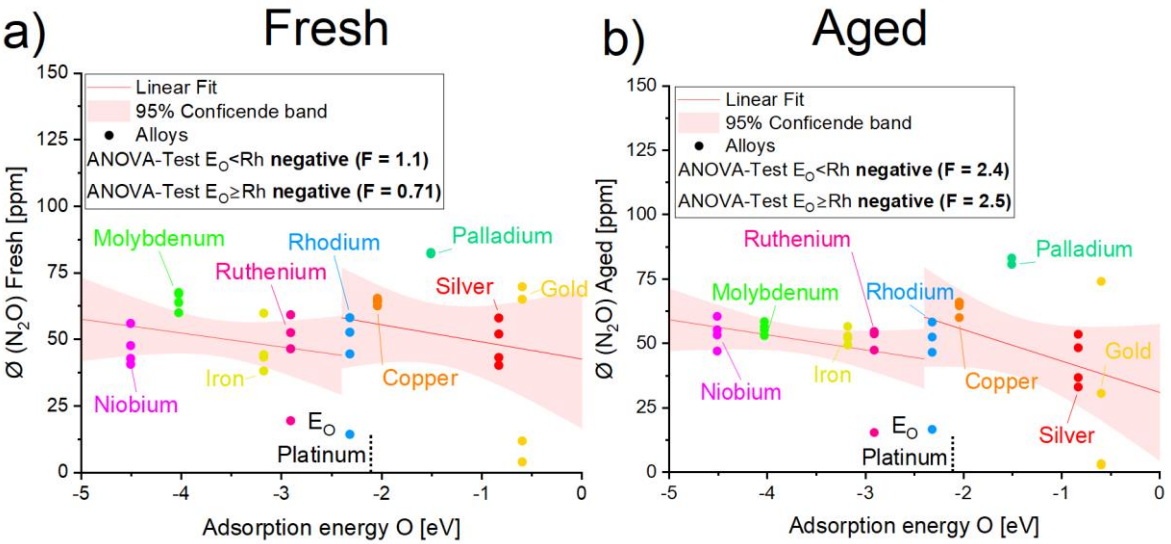

Figure 58 Average N_2O-Concentration of laser-generated alloy catalysts.

S6.6.5. NO-Formation

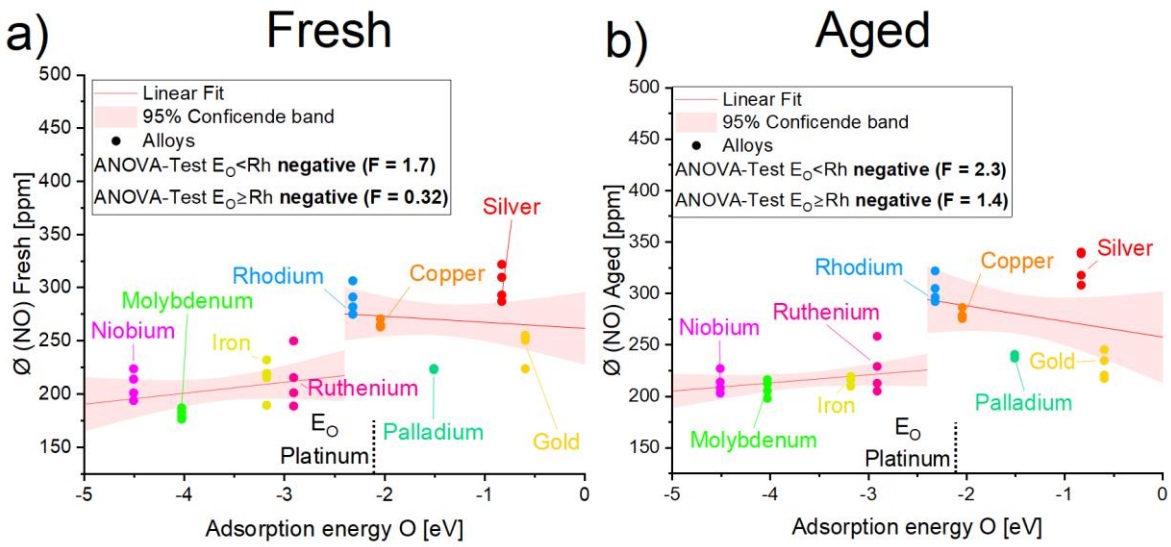

Figure 59 Average NO-Concentration of laser-generated alloy catalysts.

S6.6.6. N-Formation

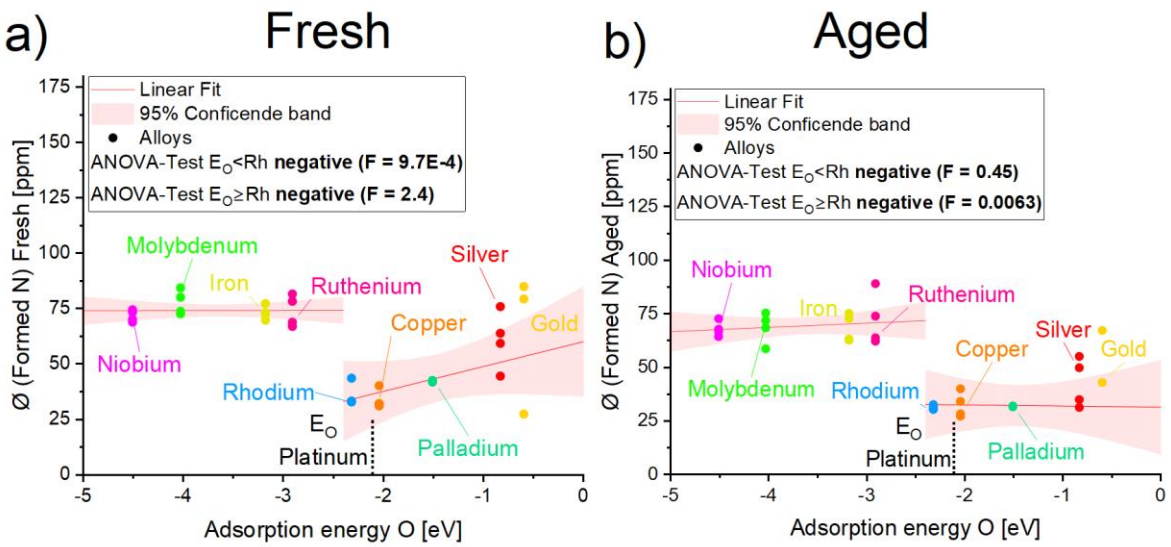

Figure 60 Average formed nitrogen concentration of laser-generated alloy catalysts.

S6.7. Ageing curves ASCII (with NO)

S6.7.1. NH_3-Oxidation

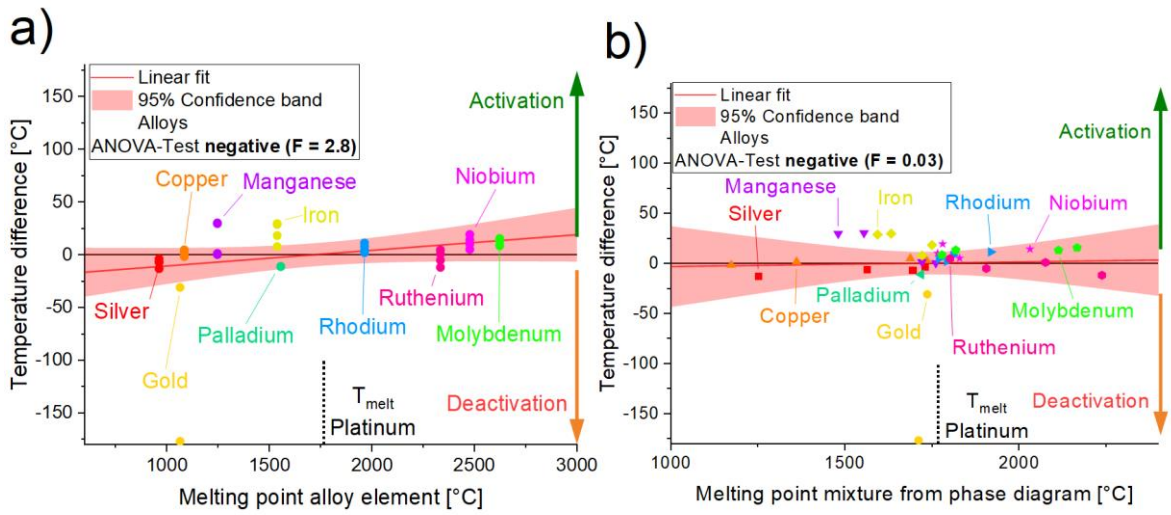

Figure 61 Difference between LU50 (Fresh minus Aged) of laser-generated alloy catalyst in the NH_3 oxidation reaction. Comparison to melting point of alloy element (a) and to melting point of the mixture taken from the underlying bulk phase diagrams (b).

S6.7.2. NO_2-Formation

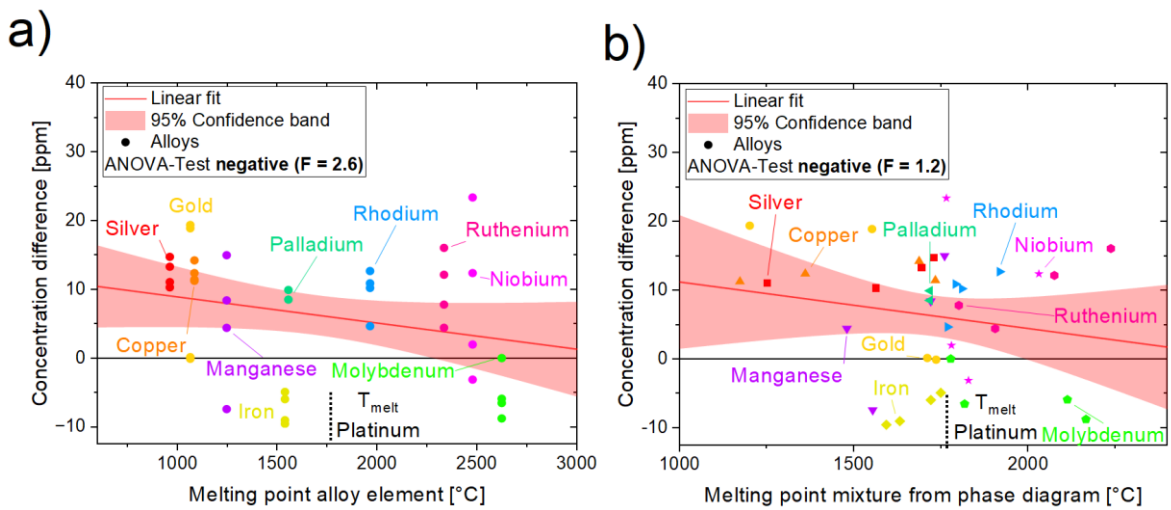

Figure 62 Difference in concentration (Fresh minus Aged) of laser-generated alloy catalysts in the NO_2-formation reaction. Comparison to melting point of alloy element (a) and to melting point of the mixture taken from the underlying bulk phase diagrams (b).

S6.7.3. NO-Formation

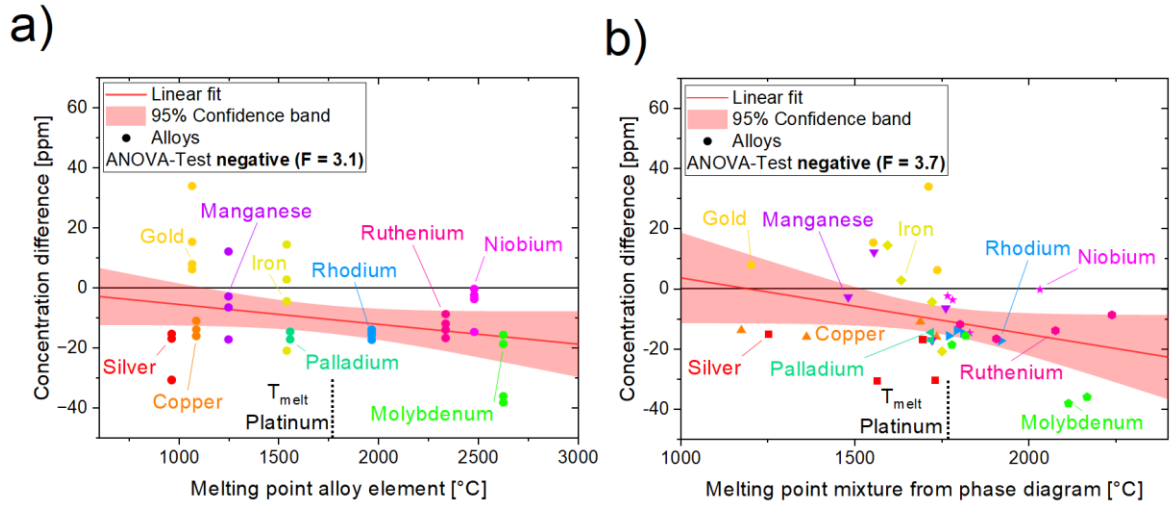

Figure 63 Difference in concentration (Fresh minus Aged) of laser-generated alloy catalysts in the NO-formation reaction. Comparison to melting point of alloy element (a) and to melting point of the mixture taken from the underlying bulk phase diagrams (b).

S6.7.4. N_2O-Formation

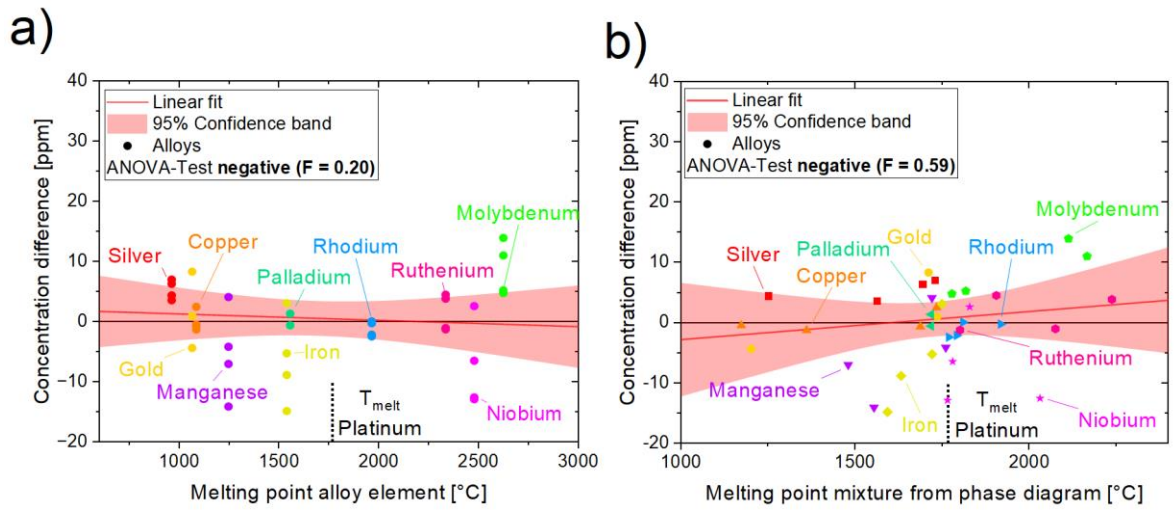

Figure 64 Difference in concentration (Fresh minus Aged) of laser-generated alloy catalysts in the N_2O-formation reaction. Comparison to melting point of alloy element (a) and to melting point of the mixture taken from the underlying bulk phase diagrams (b).

S6.7.5. N-Formation

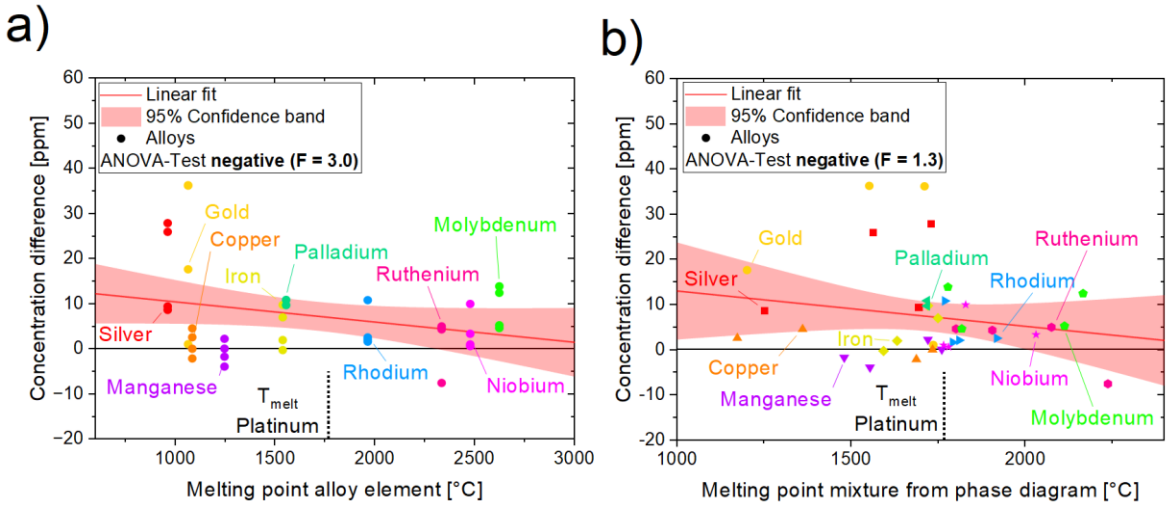

Figure 65 Difference in concentration (Fresh minus Aged) of laser-generated alloy catalysts in the N-formation reaction. Comparison to melting point of alloy element (a) and to melting point of the mixture taken from the underlying bulk phase diagrams (b).

Curriculum Vitae

The CV is not included in the online version
for reasons of data protection.

Publications and conference contributions

Peer-reviewed journals

[1] S. Siebeneicher, F. Waag, M. Escobar Castillo, V. V. Shvartsman, D. C. Lupascu, B. Gökce, *Laser Fragmentation Synthesis of Colloidal Bismuth Ferrite Particles*, *Nanomaterials* **2020**, *10*, 359, DOI: 10.3390/nano10020359.

[2] S. Siebeneicher, S. Reichenberger, C. Hengst, F. Dornhaus, B. Wittek, S. Barcikowski, *ChemCatChem* **2023**, DOI 10.1002/cctc.202300563, DOI: 10.1002/cctc.202300563.

Patents

[1] S. Siebeneicher, J. Paskuda, *Verfahren Zur Herstellung geträgerter Metallnanopartikel*, **2020**, DE 10 2020 004 878 A1.

Conference contributions

Presenting author marked with asterisk.

[1] S. Siebeneicher*, G. Marzun, H. Bönnemann, C. Lehmann, B. Spliethoff, C. Weidenthaler, S. Barcikowski, *A Study on the Origin of Oxygen in Particles Synthesized by Laser Ablation in Liquids*, Advanced Nanoparticle Generation and Excitation by Lasers in Liquids (ANGEL), Lyon, France, June 2018.

[2] S. Siebeneicher*, *Laser-based synthesis of mixed-metal nanoparticles for catalyst screening*, Research and Development Colloquium Umicore, Bad Orb, Germany, June 2019.

[3] S. Siebeneicher*, F. Waag, M. Escobar Castillo, V. V Shvartsman, D. C. Lupascu, B. Gökce, *Laser Fragmentation Synthesis of Colloidal Bismuth Ferrite Particles*, CENIDE Conference, Bergisch Gladbach, March 2020.

[4] S. Siebeneicher*, F. Waag, M. Escobar Castillo, V. V Shvartsman, D. C. Lupascu, B. Gökce, *Laser Fragmentation Synthesis of Colloidal Bismuth Ferrite Particles*, NRW Nano Conference, Online, April 2021.

List of student works

[1] Jasmin Beverungen (geb. Paskuda), *Auswirkungen eines Basentauschs in der laserbasierten Partikelsynthese auf Partikelgrößenverteilung und kolloidale Stabilität*, Analytikpraktikum (08.2018 - 11.2018)

[2] Jasmin Paskuda, *Trägerung von lasergenerierten metallischen Nanopartikeln auf oxidischen Trägermaterialien in organischen Lösungsmitteln*, Masterarbeit (05.2019 - 10.2019)

[3] Manuel Matten, *Einfluss von Sauerstoff und Wasser auf die Bildung metallischer Nanopartikel bei der gepulsten Laserablation in Propylencarbonat*, Vertiefungsarbeit (10.2019 - 03.2020)

[4] Manuel Matten, *Thermokatalytische Degradation von Schadstoffen mittel lasergenerierter Metallnanopartikel*, Masterarbeit (08.2020 - 03.2021)

[5] Moritz Materna, *Einfluss der pH-Wert induzierten Auflösung des Trägermaterials im Trägerungsprozess auf die Homogenität der Abscheidung von Nanopartikeln am Beispiel von Aluminiumoxid, Titandioxid und Gold*, Bachelorarbeit (05.2021 - 09.2021)

Eigenständigkeitserklärung (Declaration)

Hiermit versichere ich, dass ich die vorliegende Arbeit mit dem Titel

„Diesel waste gas abatement using alloyed nanoparticles“

selbst verfasst und keine außer den angegebenen Hilfsmitteln und Quellen benutzt habe, und dass die Arbeit in dieser oder ähnlicher Form noch bei keiner anderen Universität eingereicht wurde.

Ort, Datum	Simon Hartwig